UNIVERSITY OF CALIFORNIA SAN DIEGO

Galaxies and Their Environment Before Reionization

A dissertation submitted in partial satisfaction of the
requirements for the degree Doctor of Philosophy

in

Physics

by

William McNeill Hicks

Committee in charge:

Professor Michael L. Norman, Chair
Professor Michael J. Holst
Professor Dušan Kereš
Professor Julius Kuti
Professor Karin M. Sandstrom

2024

The Dissertation of William McNeill Hicks is approved, and it is acceptable in quality and form for publication on microfilm and electronically.

University of California San Diego

2024

EPIGRAPH

Happiness can be found, even in the darkest of times, if one only remembers to turn on the light.

Albus Dumbledore

TABLE OF CONTENTS

LIST OF FIGURES

LIST OF TABLES

ACKNOWLEDGEMENTS

First and foremost, I would like to thank Professor Michael L. Norman, whose patient approach to advising helped me flourish into an independent researcher. His seemingly endless wealth of knowledge, experience, and infectious passion for astrophysics and scientific computing has been an invaluable resource during my time at UCSD. I would also like to thank another of Mike's students, Azton Wells, for inspiring much of this work and for always being willing to lend a hand. Thanks also to the developers of `Enzo`, `Enzo-E`, `Grackle`, and `YT` for building the tools that made all of this possible. Specifically, thanks to James Bordner, John Wise, John Regan, Britton Smith, Greg Brian, and Brian O'Shea.

I would like to thank my parents, Kate and Glenn, for inciting in me a love for science that has somehow managed to carry me all the way to a Ph.D. Thanks also to my office-mate and friend, Jayke Nguyen, for all the coffee breaks and for helping me escape the Grad Cave into an office with a window. Thanks also to my childhood friend, John Burke, for living across the street from me growing up and coincidentally moving to San Diego shortly after I did. Thanks also to Don Cayabyab for driving down to San Diego just to skate with me on numerous occasions. Finally, thanks to Aya Reckless for being my connection to the "real world" outside of the academic bubble during the final, hectic phases of graduate school. If anyone is actually reading this, check out Aya on Instagram (@needlestoskin)—she is an insanely talented tattoo artist. Also Sal Elias (@sal_elias).

Chapter 2, in full, is a formatted reprint of the material as it appears in Hicks, Wells, Norman, Wise, Smith, & O'Shea (2021), "External Enrichment of Minihalos by the First Supernovae", *The Astrophysical Journal*, 909:70. The dissertation author was the primary investigator and author of this paper.

Chapter 4, in full, has been submitted for publication of the material as it may appear in Hicks, Norman, Wells, & Bordner (2024), "Galaxies and Their Environment at $z \gtrsim 10$—I: Primordial Chemical Enrichment, Accretion, Cooling, and Virialization of Gas in Dark Matter Halos", *The Astrophysical Journal*. The dissertation author was the primary investigator and author of this paper.

Chapter 5, in part, is currently being prepared for submission for publication of the material as it may appear in Hicks, Norman, Wells, & Bordner (2024), "Galaxies and Their Environment at $z \gtrsim 10$—II: The Role of Radiative and Kinetic Feedback in Protogalaxy Formation", *The Astrophysical Journal*. The dissertation author was the primary investigator and author of this paper.

VITA

2018	Bachelor of Science, University of California Riverside
2018–2020	Teaching Assistant, Department of Physics, University of California San Diego
2020–2024	Graduate Student Researcher, University of California San Diego
2024	Doctor of Philosophy, University of California San Diego

PUBLICATIONS

Hicks, Wells, Norman, Wise, Smith, & O'Shea (2021), "External Enrichment of Minihalos by the First Supernovae", *The Astrophysical Journal*, 909:70

Hicks, Norman, Wells, & Bordner (2024), "Galaxies and Their Environment at $z \gtrsim 10$—I: Primordial Chemical Enrichment, Accretion, Cooling, and Virialization of Gas in Dark Matter Halos", *The Astrophysical Journal*, submitted

Hicks, Norman, Wells, & Bordner (2024), "Galaxies and Their Environment at $z \gtrsim 10$—II: The Role of Radiative and Kinetic Feedback in the Protogalaxy Formation", in prep.

ABSTRACT OF THE DISSERTATION

Galaxies and Their Environment Before Reionization

by

William McNeill Hicks

Doctor of Philosophy in Physics

University of California San Diego, 2024

Professor Michael L. Norman, Chair

Recent observations suggest we do not fully understand how galaxies form at high redshifts. We use `Enzo` and `Enzo-E` cosmological simulations to study the transitional period between primordial star formation and the buildup of metal-enriched protogalaxies. We focus on metal enrichment, accretion, cooling, chemistry, and virialization of gas within dark matter halos before the Epoch of Reionization.

In Chapter 2, we analyze an `Enzo` cosmological simulation and find that the dominant mode of chemical enrichment in minihalos is the accretion of metals sourced from supernovae occurring outside of the virial radius. We find that stellar populations that form following external enrichment have low metallicity.

In Chapter 3, we document the code development and testing efforts that were made to prepare `Enzo-E`, `Enzo`'s highly scalable successor, for use in running large-scale cosmological simulations.

Necessary developments include primordial and metal-enriched star formation and feedback models, as well as a multigroup M1 closure radiative transfer solver. Comparisons between identical `Enzo` and `Enzo-E` simulations are also made.

In Chapter 4, we examine $\sim 12,000$ dark matter halos in the absence of metal-enriched star formation and feedback at $z \simeq 12$ in `Enzo-E` simulations. We find that 16% of halos are metal-enriched by $z \simeq 12$, and that metals in the most massive halo are sourced from at least 20 separate primordial stellar populations. Without heating from stellar feedback, gas virialization is supported by nonthermal bulk flows, and atomic cooling is inactive. We find that H_2 is the dominant coolant at the center of halos with $10^6\ M_\odot < M_{\rm vir} < 10^9\ M_\odot$.

In Chapter 5, we include metal-enriched star formation and feedback in our `Enzo-E` simulations and follow the evolution of a single halo under different feedback prescriptions until $z \simeq 18$. We find that radiative feedback controls the early star formation history of the protogalaxy through photoevaporative flows. H_2 remains the dominant coolant in the presence of stellar feedback due to H_2 formation in relic HII regions. Finally, we find that the virial temperature does not accurately describe the thermal state of the gas at any point in the halo's early lifetime.

Chapter 1

Introduction

As new generations of telescopes with ever-increasing resolving power are built, astronomers are able to peer further and further back in time towards the Big Bang. Up until now, study of galaxy formation at very high redshifts ($z \gtrsim 10$) has been largely the domain of computational astrophysicists who wield cosmological simulations to directly follow the formation of the first galaxies. With cosmological simulations, it is possible to obtain, relatively easily, a dynamical picture of the early universe just after the Big Bang by evolving simulations forward from a set of initial conditions. The simulator's woe, however, is that evolving a cosmological simulation down to low redshifts is often not feasible without making some serious compromises to account for the physical complexity of the system that inevitably arises. Observational astrophysicists encounter the exact opposite problem. For the observer, objects at low redshifts are very accessible for the simple reason being that they are closer to Earth. The early universe, however, is very difficult to observe with telescopes. Without observational data to compare results with, one could argue that studying the early universe using simulations is, in a sense, "firing blind". Recently, observers have used the *James Webb Space Telescope* to identify a number of luminous sources at high redshifts that are thought to be some of the first galaxies to have formed in the universe. While these objects are not yet well-resolved, this marks an important point in astronomy where simulators and observers are finally able to meet in the middle.

The history of the universe is typically portrayed using diagrams like Figure 1.1. Just after the Big Bang, the gas in the universe was a dense plasma. The plasma was so dense during this "hot soup" phase that any radiation produced internally was trapped. As the universe expanded, the plasma gradually diluted until radiation was able to decouple, thus allowing the gas to cool. With this cooling came the opportunity for protons and electrons, initially unbound, to combine to form neutral gas composed of

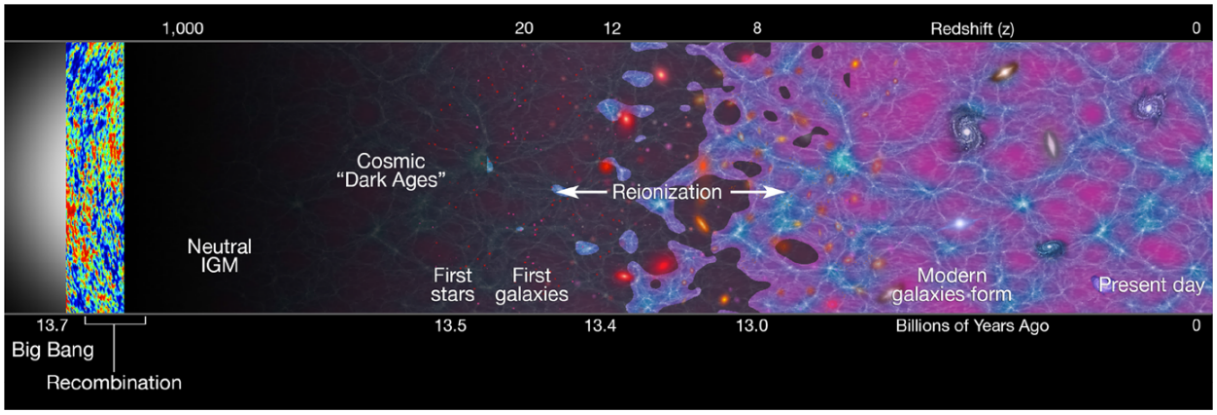

Figure 1.1. Cosmic timeline, taken from Gnedin & Madau (2022).

approximately 73% hydrogen and 27% helium, with trace amounts of lithium and deuterium that were formed during Big Bang nucleosynthesis.

For a few hundred million years, gas coalesced within the relatively shallow potential wells of dark matter minihalos until the very first generation of stars was born, commonly referred to as "Population III" stars (hereafter Pop III stars). Pop III stars were massive and short-lived. Nevertheless, they were the first sources of ionizing radiation in the universe, as well as the first sources of metal enrichment. A second generation of stars, referred to as "Population II" stars, formed in the wake of Pop III supernovae. Population II stars are metal-enriched, and long-lived in comparison to Population II stars, and make up the first galaxies. As the production of luminous objects increased, the ionizing radiation sourced from the objects gave rise to expanding ionization fronts. The initially isolated bubbles of ionized gas eventually met each other and continued to expand until almost all of the gas in the universe was once again reduced to a plasma, albeit now diffuse. This event is referred to as the "Epoch of Reionization", and is thought to have taken place around 1 billion years after the Big Bang.

This dissertation is largely concerned with the transitional period between the formation of the first stars and the first galaxies leading up to the Epoch of Reionization. In this Introduction, I briefly review the relevant physics and points of discussion as a primer for the chapters that follow. Chapter 2 analyzes a cosmological simulation run using the `Enzo` code, and identifies external enrichment by Pop III supernovae as the dominant enrichment process for dark matter minihalos. There is also some discussion of the properties of Population II stars that form as a result of external enrichment, as well as direct measurements of the time delay between Pop III supernovae and the first Population II star forming

event in merger trees. Chapter 3, where most of my time in graduate school was spent, documents my code development and testing efforts in preparing Enzo-E, Enzo's highly scalable successor, for use in simulating the formation of the first galaxies within cosmological simulations. My primary developments include porting, testing, and improving two star formation and feedback routines from Enzo into Enzo-E—(1) StarNet, a machine learning surrogate model for Pop III star formation and feedback, and (2) STARSS, a FIRE-2-like subgrid model for Population II star formation and feedback—and developing from scratch a multigroup M1 Closure solver for radiative transfer. Chapters 4 and 5 each use Enzo-E to run a suite of simulations with varying amounts of physical processes included. Chapter 4 focuses on primordial chemical enrichment, accretion, and cooling of gas in dark matter halos in the absense of Population II star formation and feedback. Chapter 5 then re-runs a subset of the simulations from the previous chapter with Population II star formation and feedback included and studies on the impact of radiative and supernova feedback on the early stages of protogalaxy formation.

1.1 The First Stars

1.1.1 Star Formation in a Metal-Free Environment

Heavy elements form in the cores of stars and are dispersed into the environment by stellar winds and supernovae. In the local universe, virtually all star formation takes place in gas that has been enriched with metals. This is important because gas can cool by fine structure lines of atomic species such as C and O, influencing how star formation occurs. This is not at all true during the formation of the very first generation of stars. By definition, Pop III stars form in pristine gas bound to minihalos that is devoid of all metals. For reasons explained below, Pop III stars are thought to be much more massive than the Population II/I stars that we observe in the local universe, which did form in metal enriched gas.

In order for gravitational collapse to occur, gas needs to cool to the point that gravity can overtake thermal pressure. Cooling can occur via a number of radiative processes, but the most relevant processes in this context involve the collisional excitation of a bound electron, immediately followed by de-excitation back the ground state. If the photon released during de-excitation is able to leave the system, then the gas has lost energy and has thus cooled. Generally speaking, the larger the number of possible electron transitions that are available in gas of a given composition, the more efficiently the gas is able to cool. In the absence of metals, the only available coolants are atomic hydrogen, helium, and molecular hydrogen.

Atomic cooling is only effective at $T \gtrsim 10^4$ K, which is an order of magnitude larger than typical virial temperatures associated with minihalos hosting Pop III stars. Instead, H_2 is the primary coolant in pristine gas. H_2 cooling is relatively inefficiant, and is active at temperatures down to $T \simeq 200$ K. In enriched gas, metal cooling is able to bring the gas to temperatures as low as $T \simeq 40$ K.[1]

The Jeans mass, the mass scale at which a gas cloud will experience gravitational collapse, is defined as

$$\begin{aligned} M_{\rm J} &= \frac{\pi}{6} \frac{c_{\rm s}^3}{G^{\frac{3}{2}} \rho^{\frac{1}{2}}} \\ &\sim T^{\frac{3}{2}} \rho^{-\frac{1}{2}}, \end{aligned} \tag{1.1}$$

where $c_{\rm s}$ is the sound speed and ρ is the baryon density. While the Jeans mass evolves during gravitational collapse, its strong positive correlation with gas temperature implies that gravitational collapse that starts in a ~ 200 K gas cloud will generally result in a much more massive star than collapse in a ~ 40 K gas cloud. Numerical simulations by Abel et al. (2002) found a characteristic Jeans mass of $\sim 600\ M_\odot$ in the gas at the centers of pristine minihalos. While it is very likely that Pop III stars existed in the early universe, the fact remains that no Pop III star has ever been observed directly, and thus Pop III stars remain purely theoretical objects. Because of this, the Pop III stellar initial mass function (IMF) is poorly constrained.

1.1.2 The Population III Stellar IMF

The fact that Pop III stars have not yet been observed is actually, in a way, a point of support for the assumption that Pop III stars were generally massive. Massive stars have short lifetimes, and any that formed in the early universe either blew up or fizzled out early on in cosmic history.[2] Understanding the

[1] In enriched gas, there is also the possibility of dust formation and cooling. The effects of dust are often argued away in discussions of primordial star and galaxy formation, with the argument being that dust production has not yet taken place in appreciable amounts by the time the first stars and galaxies begin to form. This is certainly true for the formation of the first stars, but the dust content of gas during the formation of the first galaxies is still an unknown.

[2] It is worth mentioning that any Pop III stars that may have survived in the local universe could be masquerading as Pop II/I stars. For one, stellar metallicity increases over time as heavy elements are produced in the star's core. Alternatively, a Pop III star could accrete metals produced and spread by a nearby supernova. In this case, it would be a difficult challenge observationally to disentangle which metals were produced internally from which were accreted. Nevertheless, the hunt for Pop III stars in nature remains a game of searching for stars with extremely low metallicities. This practice, along with the practice of connecting chemical abundances in metal-poor Pop II stars in the local universe to their possible Pop III progenitors is sometimes referred to as "stellar archaeology."

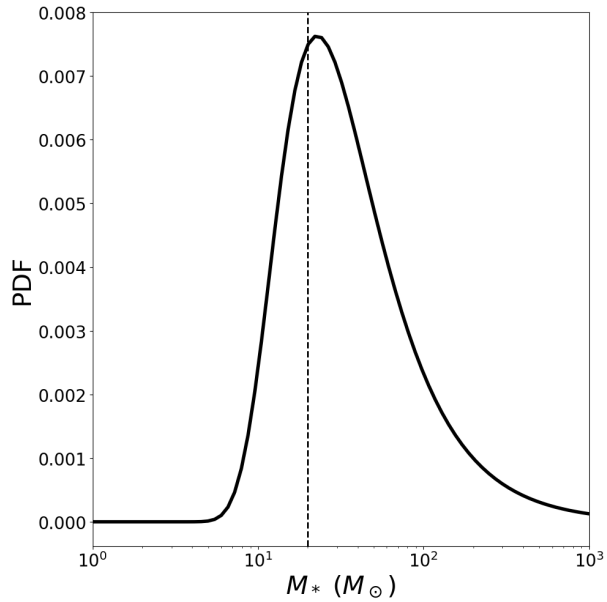

Figure 1.2. PopIII IMF computed using Equation 1.2, for $M_{\rm char} = 20\,M_\odot$. The vertical dashed line shows the value of $M_{\rm char}$.

Pop III IMF is vital to understanding the effects that Pop III stars have on their environment. It is probably true that Pop III stars were primarily massive, but just how massive were they? What is the value for the characteristic mass, $M_{\rm char}$? These are still very much open questions that require a highly detailed understanding of the physics and evolution of primordial protostellar disks to answer.

Simulating the evolution of protostellar disks is a challenge in itself with a wealth of literature dedicated to it. Pop III star formation occurs on a timescale of $\sim 10^6$ years. Once protostellar clumps collapse in a disk after $\sim 10^3$ years, the Courant condition (Courant et al., 1928) causes disk simulations to grind to a halt before radiation from the central protostar suppresses accretion. This can be circumvented by either artificially suppressing collapse below a certain gas density or by replacing dense clumps with sink particles, though both approaches come with the drawback of inaccurately capturing the internal shear forces within the clump. This can throw off predictions for whether a given clump would merge with the central protostar, remain in orbit, or be flung out of the disk via three-body interactions.

In cosmological simulations, the Pop III IMF is typically assumed to be top-heavy, with a behavior that exponentially tends towards a power law as mass increases above $M_{\rm char}$, but exponentially decreases

below $M_{\rm char}$. For example, Wise & Abel (2011a) assumes the following IMF:

$$f(\log M)dM = M^{-1.3}\exp\left[-\left(\frac{M_{\rm char}}{M}\right)^{1.6}\right]dM. \tag{1.2}$$

This form for the PopIII IMF is used for all simulations in that include Pop III star formation in this dissertation. The adopted value of $M_{\rm char}$ has varied over the years as the physics of primordial protostellar disks are better understood. The current values used for $M_{\rm char}$ in the literature are typically $10-20\,M_{\odot}$. Equation 1.2 is plotted in Figure 1.2 using $M_{\rm char} = 20\,M_{\odot}$. While most will have masses near $M_{\rm char}$, there will be some Pop III stars that form with hundreds of solar masses.

1.1.3 The Lyman-Werner Background

Issues with the primordial stellar IMF aside, the primarily large characteristic mass, whatever the true number may be, implies that Pop III stars are strong emitters of ultraviolet (UV) radiation. Of particular importance when discussing radiation from Pop III stars is Lyman-Werner (LW) radiation, which is a subset of UV radiation that has energy in the range $11.2-13.6$ eV. LW radiation has the effect of photodissociating H_2 via the two step Solomon process (Stecher & Williams, 1967). Because H_2 is the primary coolant available for primordial gas, Pop III star formation becomes self-regulating (**?**). Over time, LW radiation escapes from star-forming halos and permeates the IGM, gradually building into a global LW background (LWB) that works to delay further Pop III star formation (O'Shea et al., 2015).[3]

1.1.4 Primordial Metal Enrichment

When a Pop III star dies, its fate depends on its mass. According to stellar evolution models, dying Pop III stars will explode as Type II core collapse supernovae (SNe) between $10-20\,M_{\odot}$, hypernovae (HNe) between $20-40\,M_{\odot}$, and pair instability supernovae (PISNe) between $140-260\,M_{\odot}$ (Heger & Woosley, 2002). Pop III stars with masses between $40-140\,M_{\odot}$ will not explode, but will collapse into a black hole. Pop III star forming minihalos typically have virial mass $M_{\rm vir} \simeq 10^6\,M_{\odot}$. At such low masses, gas within the relatively shallow gravitational potential well is not very tightly bound to its halo. As such, extremely energetic PISNe are able to completely blow out all the gas in a minihalo (Whalen et al., 2008). SNe and HNe, while not as energetic, are more common than PISNe and contribute a similar combined

[3]It should be noted that Pop II/I stars also emit LW radiation, and thus contribute to the buildup of the LWB.

amount to the enrichment of the IGM as a whole. Following a Pop III supernova, gas will recollapse into metal-enriched Pop II stars on timescales of $10 - 100$ Myr.

1.2 The First Galaxies

When discussing the formation of the first galaxies, it is useful to define what exactly qualifies as a galaxy. The word galaxy often brings to mind images of a beautifully organized spiral structure, teeming with stars, gas, and dust–all bound within a disk. In contrast, the first galaxies were likely highly irregular in their structure. The Milky Way's dark matter halo has $M_{\rm vir} \simeq 10^{12}\ M_{\odot}$. The typical halo mass scale associated with the first galaxies is $M_{\rm vir} \simeq 10^{8}\ M_{\odot}$. This is for two reasons:

1. The gravitational potential in $\sim 10^{8}\ M_{\odot}$ halos is deep enough to retain outflows of photoionized gas.

2. The virial temperature is above 10^{4} K, which is temperature at which atomic cooling becomes relevant.

Reason 1 is important because it marks a point where gas that flows into a halo is generally retained, even in the event of an energetic supernova, marking a transition to a sustained star forming system at the center. Reason 2 is discussed in detail in Chapters 4 and 5. For the purposes of this dissertation, I loosely define a first galaxy as any metal-enriched star forming system in a $\sim 10^{8}\ M_{\odot}$ halo.

Gas flows into halos via "hot" and "cold" modes of accretion (Kereš et al., 2005; Kereš et al., 2009). In hot accretion, gas accretes spherically from the IGM and is shock-heated to the virial temperature somewhat near the virial radius. In cold accretion, gas is smoothly injected into the halo through denser filaments that trace out the cosmic web, and is not heated until it reaches the center. For the relatively low halo masses relevant to this discussion, we show in Chapter 4 that cold accretion is by far the dominant accretion vector. Still, the idea that gas will heat up to the virial temperature is central to the story that is often told when discussing the first galaxies. Recall that the Pop III stars form in halos with $M_{\rm vir} \simeq 10^{6}\ M_{\odot}$ due to the effects of H_2 cooling. These halos, which I refer to as "H_2 cooling halos", have virial temperatures of $T_{\rm vir} \simeq 10^{3}$ K. A halo with $T_{\rm vir} \gtrsim 10^{4}$ K is often referred to as an "atomic cooling halo" in the literature. As the name implies, atomic cooling halos are expected to be dominated by cooling via atomic hydrogen and helium. "Metal cooling halos" are also a part of this picture. Because if some

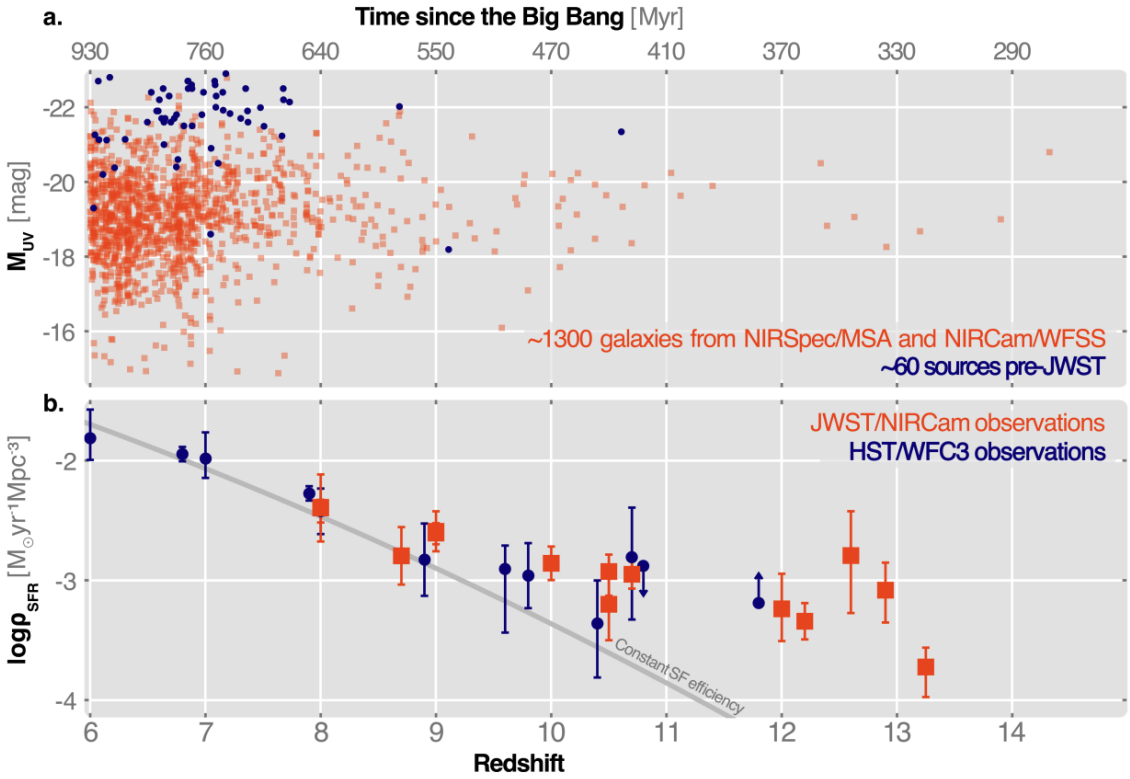

Figure 1.3. (*a*) Observed rest-frame UV magnitudes for spectroscopically confirmed galaxies. Orange points show galaxies observed by JWST, while blue points show HST observations. JWST has observed significantly more galaxies than HST at $z \gtrsim 6$. The ~ 60 high redshift HST galaxies included here are among the brightest of sources. (*b*) Cosmic SFR density over the first billion years after the Big Bang. The grey curve shows a model of constant star formation efficiency. The observed values notably diverge from the grey curve at $z \simeq 10$, which is during Reionization. Image credits: Adamo et al. (2024).

fraction of halos with $T_{\rm vir} < 10^4$ K are chemically enriched, it is possible for cooling via metals to induce Pop II star formation.

1.2.1 JWST and the "Impossibly Massive" Galaxies

Much of the radiation from young galaxies is emitted in the UV. By the time UV radiation from the early universe reaches Earth, it has been redshifted to infrared (IR) wavelengths. JWST is specifically designed to observe infrared radiation. Wide-field surveys are first taken with the Near Infrared Camera (NIRCam) at a few different wavelengths. From there, objects of interest can be identified, and their photometric redshifts can be attained using the Lyman break technique. A given object's spectral energy distribution (SED) can be inferred from the photometry to make coarse-grained estimates of stellar mass and star formation rate (SFR). High resolution observations of the SED can then be made on an

object-by-object basis using the Near Infrared Spectrograph (NIRSpec). An object that has been observed with NIRSpec has been "spectroscopically confirmed." Having access to an accurate SED for a galaxy is vital for accurately analyzing its properties. It is therefore important to distinguish galaxies that are spectroscopically confirmed from those that are not.

When results from JWST first hit news outlets, all computed properties of the observed galaxies were based on photometry. Some galaxies at $z_{\rm photo} \simeq 6$ were inferred to have $M_* \simeq 10^{11}\,M_\odot$. These galaxies were dubbed "impossibly massive" (Labbé et al., 2023) by many, as the number of galaxies with such a stellar mass in the survey volume beyond $z \simeq 2$ was expected to be effectively zero. A few $z_{\rm photo} \gtrsim 10$ galaxies, previously inaccessible to the *Hubble Space Telescope* (HST), have also been observed by JWST to have inferred stellar masses of $10^7\,M_\odot \lesssim M_* \lesssim 10^9\,M_\odot$. One by one, followup observations with NIRSpec have been made on these galaxies. To date, there are six spectroscopically confirmed galaxies with $z_{\rm spec} \gtrsim 10$.

Figure 1.3 shows observed rest-frame UV magnitudes for spectroscopically confirmed galaxies using data compiled from JWST and HST, as well as cosmic SFR density over the first billion years after the Big Bang derived from the observations. These results are taken from Adamo et al. (2024). From $z \simeq 6-10$, the observed cosmic SFR densities closely track the constant star formation efficiency model. Beyond $z \simeq 10$, the observed SFR densities deviate from the model. Harikane et al. (2023) finds that the observed values can be lowered to the constant SF efficiency curve by either assuming a top heavy stellar IMF or by assuming that there is no suppression of star formation by the UV background prior to Reionization. Whether or not this feature is caused by some misunderstanding in baryonic physics, its presence clearly shows that something is fundamentally different about galaxy formation before Reionization.

1.2.2 How to Extract Stellar Mass from Faint Red Blobs

A NIRCam/NIRSpec image of a galaxy at $z \gtrsim 10$, when projected on a screen, appears as a faint red dot only a few pixels wide. Computing a stellar mass for such an object is no trivial matter, and doing so requires a number of assumptions to be made about the object's makeup. A simplified prescription for such a calculation is as follows:

1. *Measure the object's redshift.* This is a game of picking out features from an observed SED that the

observer can identify with a known rest-frame photon energy. Photometric redshifts are typically determined using the Lyman break technique, where one identifies a distinct step-like feature in the object's spectrum that can be identified with absorption by neutral hydrogen at wavelengths below the Lyman limit. For a spectroscopically confirmed galaxy, the observer has better fidelity in the observed SED, which allows access to more identifiable features (e.g. emission lines in Lyα, HeII, CIV, OIII, MgII, etc.). Pre-Reionization observations come with the complication of requiring the observer to account for the fact that the radiation initially propagates through a largely neutral IGM that suppresses the observed SED at certain energies, particularly near the Lyman break.

2. *Fit photometric/spectroscopic data to a model SED.* The purpose of this step is to obtain a functional form for the SED, corrected for redshifting, that can be integrated to obtain rest-frame luminosities in the UV, IR, or any other energy range the observer may require. The process of obtaining a reasonable fit for a given observation typically includes comparing the incomplete observed spectrum with a number of model spectra generated using stellar population synthesis codes. This is a complex art form that requires careful consideration of a large number of input parameters. This means that some simplifying assumptions about the star formation history must be made about the galaxy. Unknowns of particular importance for $z \gtrsim 10$ galaxies include stellar IMF, star formation efficiency, stellar ages, photon escape fractions, metallicities, and dust-to-gas ratios. Potential errors in the stellar masses obtained for the observed $z \gtrsim 10$ galaxies so far would likely come from the assumptions made of one of these properties.

3. *Compute rest-frame UV luminosity.* Once a fit for the SED is obtained, $L_{\rm UV}$ can be computed by integrating the SED over UV wavelengths (100-400 nm)

4. *Convert $L_{\rm UV}$ to M_*.* Because young stars emit UV radiation, $L_{\rm UV}$ can directly be used to infer a star formation rate, and, thus, a stellar mass. Some care must be taken here because the relationship between $L_{\rm UV}$ and M_* is sensitive to the stellar IMF. If, for example, the stellar IMF is assumed to be a simple power law typical of stars in the local universe, but, in reality, the true IMF was top-heavy, the stellar mass that comes out of the calculation would be overpredicted because of the underpredicted per-star UV luminosity.

1.3 Cosmological Simulations with Enzo and Enzo-E

The simulations described in this dissertation were run using the Enzo (Bryan et al., 2014) and Enzo-E (Bordner & Norman, 2018) astrophysics codes. These are Eulerian, grid-based multiphysics applications that make use of adaptive mesh refinement (AMR) to dynamically increase or decrease the resolution where needed during a running simulation. The core physics modules are more-or-less identical in Enzo and Enzo-E, but their AMR structure and parallel backend are completely different, giving each code its own set of benefits and drawbacks. Comparisons between cosmological simulations run with identical initial conditions, physics methods, and parameters are presented in Section 3.0.1. I summarize the outcome of the analysis here.

Enzo's inherently patchy structured AMR (SAMR) approach (Berger & Colella, 1989a) makes it possible to efficiently run cosmological simulations with many levels of refinement–sometimes more than 20–providing grids with extremely high resolution that closely track the centers of halos. The resolution quickly drops off outside of halos, however, and the IGM is poorly sampled. On the other hand, Enzo-E's forest-of-octrees approach to AMR (Burstedde et al., 2011) produces refined regions that are much larger, providing excellent resolution in the gas flowing into and out of halos through filaments and from the IGM[4]. This comes with the cost of producing $\sim$ 20x more data than Enzo on average once the mesh has fully refined, making cosmological simulations with $\gtrsim 5$ levels of refinement memory-intensive with Enzo-E. Enzo-E is substantially more scalable than Enzo, though, meaning that one only needs to increase the number of processors to evolve an Enzo-E simulation down to a comparable redshift.

[4]The solution to the Poisson equation is also slightly more accurate outside of halos in Enzo-E than in Enzo because of the increased resolution in the IGM.

Chapter 2

External Enrichment of Minihalos by the First Supernovae

Recent high-resolution simulations of early structure formation have shown that externally enriched halos may form some of the first metal enriched stars. This study utilizes a 1 comoving Mpc^3 high-resolution simulation to study the enrichment process of metal-enriched halos down to $z = 9.3$. Our simulation uniquely tracks the metals ejected from Population III stars, and we use this information to identify the origin of metals within metal-enriched halos. These halos show a wide range of metallicities, but we find that the source of metals for $\gtrsim 50\%$ of metal-enriched halos is supernova explosions of Population III stars occuring outside their virial radii. The results presented here indicate that external enrichment by metal-free stars dominates the enrichment process of halos with virial mass between $10^{5.3}\,M_\odot$ and $10^{6.5}\,M_\odot$ down to $z = 9.3$. Despite the prevalence of external enrichment in low mass halos, Pop II stars forming due to external enrichment are rare because of the small contribution of low-mass halos to the global star formation rate. The enriched stars that do form through this process have absolute metallicities below $10^{-3}\,Z_\odot$. We also find that the fraction of externally enriched halos increases with time, $\sim 90\%$ of halos that are externally enriched have $M_{\rm vir} < 10^6\,M_\odot$, and that hypernovae are the predominant supernova type contributing to the external enrichment of halos; however, pair-instability supernovae contribute the most to the enrichment of the IGM as a whole for our choice of primordial IMF.

2.1 Introduction

In a quest to discover the characteristics of the first-generation of stars, we inevitably run into the inconvenient fact that there are no observable first-generation (Population III, Pop III) stars, so direct

constraints on their characteristics are lacking. This difficulty has given rise to galactic archaeology (i.e., Feltzing & Chiba 2013; Keller et al. 2014; Hernández et al. 2020; Frebel & Norris 2015) to determine the enrichment history of an object. Other observations attempt to constrain the Pop III initial mass function (IMF), number of enriching events and typical supernova energy (Welsh et al., 2019), or to detect the unique metal signature of massive Pop III supernovae (Bañados et al., 2019) by observing metal-poor damped Lyman-α (DLA) systems. In order to more fully understand the results from surveys measuring metallicity of presently observed stars or DLAs, it is imperative to understand how Pop III stars interacted with their environments. Prior works have investigated the effect of Pop III supernovae at the extreme small scale (Whalen et al. 2008; Cen & Riquelme 2008; Smith et al. 2015a; Chen et al. 2017). These studies illustrate that pristine minihalos can be enriched by external sources, such as Type II supernovae (SNe) from Pop III stars forming in nearby minihalos. Notably, these externally enriched minihalos could be the first sites of second-generation star (Pop II) star formation (Smith et al., 2015a). These prior simulations had extremely fine small-scale resolution, but were limited by the small simulation box size ($\sim$ 500 comoving kpc/h) and the low number of halos present in the volume. Further, Smith et al. (2015a) only considered the effects of 40 $M_\odot$ Pop III stars, whereas a more comprehensive IMF would include a variety of stellar endpoints: Type II SNe, hypernovae (HNe), and pair-instability supernovae (PISN). This study aims to extend Smith et al. (2015a) by making use of a simulation similar to that in Paper II of the *Birth of a Galaxy* series (Wise et al., 2012a) that has a larger box size (1 comoving Mpc) and includes PISN, HNe, and black hole collapse as Pop III endpoints.

The remainder of this paper is organized as follows: section 2.2 outlines the simulation design and reviews important stellar formation and feedback parameters. Sections 2.3 and 2.4 present our analysis on the prospects of external enrichment and star formation that occurs afterwards. Finally, Section 2.5 compares our results to other studies and Section 2.6 summarizes the main conclusions drawn from our analysis.

2.2 Simulation Setup

The simulation used for this analysis is a re-run of that described in Wise et al. (2012a), using a smaller Pop III characteristic mass of $20 M_\odot$ and a larger density threshold of $n = 10^6\,\mathrm{cm}^{-3}$ (proper) for star formation. It is the same simulation analyzed in Skinner & Wise (2020). Making use of the

AMR simulation code Enzo (Bryan et al., 2014; Brummel-Smith et al., 2019), the 1 Mpc box has a base resolution of 256^3 cells and particles with up to 12 levels of local refinement, which results in a maximum comoving resolution of 1 pc and a dark matter mass-resolution of $1840 M_{\odot}$. The simulation is initialized at $z = 130$ using cosmological parameters consistent with the Planck 2014 constraints (Ade et al., 2014): $\Omega_{\Lambda} = 0.6825$, $\Omega_M = 0.3175$, $\Omega_b = 0.049$, $h = 0.6711$, $\sigma_8 = 0.81$, and $n = 0.963$. The simulation is run until $z = 9.3$, when radiative transfer becomes prohibitively expensive. Its physics suite includes radiation hydrodynamics with adaptive-ray tracing (Wise & Abel, 2011b), the nine-species (H I, H II, He I, He II, H_2, e^-, H_2^+, H^-) non-equilibrium chemistry model from Abel et al. (1997), radiative cooling from primordial gas and metals, momentum transfer from ionising radiation, and an H_2-photodissociating Lyman-Werner background (LWB).

2.2.1 Stars and Feedback

The simulation includes prescriptions for forming individual Pop III stars and Pop II star clusters, described in detail in Wise et al. (2012b). Since star formation and destruction is instrumental in chemical evolution and enrichment, the details of how metals are calculated from stellar properties are restated here. When conditions for star formation are met in a cell, either a particle representing a single Pop III star (if $[Z/H] < -4$) [1] or a particle representing a cluster of Pop II stars (if $[Z/H] > -4$) is formed. The transition metallicity is chosen to be just below the metallicity where fine structure line cooling of C and O become important assuming solar abundances (Bromm & Loeb, 2003). If the particle is Pop III, the mass of the particle is sampled randomly from a modified IMF of the form

$$f(\log M)dM = M^{-1.3}\exp\left[-\left(\frac{M_{\rm char}}{M}\right)^{1.6}\right]dM \tag{2.1}$$

that behaves as a Salpeter IMF at high-mass, but is exponentially suppressed below $M_{\rm char} = 20\mathrm{M}_{\odot}$. The Pop III star particle is assigned zero metalicity despite the value in the cell that formed it. Alternatively, if $[Z/H] > -4$, a particle representing a coeval Pop II star cluster is formed assuming an unmodified Salpeter IMF. The particle's mass is taken to be 7% of the cold gas within a sphere of radius R_{cl} such that mean density inside R_{cl} is 10^3 cm^{-3} (see Wise & Cen (2009) for more details). An equivalent amount of gas is removed from cells within R_{cl} of the star forming cell. The star's metallicity is initialized to the

[1] For each cell, $[Z/H] = \log_{10}\left(\frac{M_Z}{M_{\rm H}}\right)_{\rm cell} - \log_{10}\left(\frac{M_Z}{M_{\rm H}}\right)_{\rm Sun}$

mass-weighted average of the metallicities of the surrounding cells, which can be below $[Z/H] = -4$ if the cell is at or slightly above threshold. As we wish the star cluster to sample the massive end of the Salpeter IMF, we require that its mass exceed a minimum mass of $10^3 M_\odot$. If it does not, R_{cl} is increased until the condition is met. After the Pop II star particle has lived for 4 Myr, it begins loosing mass by supernovae and deposits metals continuously into the finest AMR level at every time step according to

$$m_{\rm ej} = \frac{0.25\Delta t \times M_*}{t_0 - 4{\rm Myr}} \tag{2.2}$$

for $t \leq t_0 = 20$Myr (the lifetime of the particle), t is the age of the star, and Δt is the current time step. The ejecta has absolute metallicity $Z = 0.02$ and is tracked in a field dedicated to metals from Pop II stars.

Metals from Pop III stars are deposited impulsively by individual supernova events. After a Pop III star lives and radiates for its main sequence lifetime, it has different fates for different mass ranges. If $40{\rm M}_\odot < M_* < 140{\rm M}_\odot$ or $M_* > 260{\rm M}_\odot$, the particle collapses to an inert, collisionless black hole. Otherwise, the particles explode as supernovae with metal ejecta masses and energies taken from Nomoto et al. (2006). If $11{\rm M}_\odot < M_* < 40{\rm M}_\odot$, the star explodes with a metal ejecta mass given by

$$\frac{M_z}{M_\odot} = 0.1077 + 0.3383 \times \left(\frac{M_*}{M_\odot} - 11\right). \tag{2.3}$$

This applies to both Type II SNe ($11{\rm M}_\odot < M_* < 20{\rm M}_\odot$) and hypernovae (HNe) ($20{\rm M}_\odot < M_* < 40{\rm M}_\odot$). More massive stars in the range $140{\rm M}_\odot < M_* < 260{\rm M}_\odot$ will become PISNe (Heger & Woosley, 2002) and eject metal with a mass

$$\frac{M_z}{M_\odot} = \left(\frac{13}{24}\right) \times \left(\frac{M_*}{M_\odot} - 20\right) \tag{2.4}$$

at the end of their lifetime.

The blast wave is modeled by injecting the explosion energy and ejecta mass into a sphere of 10 pc, smoothed at its surface to improve numerical stability. Because we resolve the blast wave relatively well with several cells across at its initialization, the thermal energy is converted into kinetic energy and agrees with the Sedov–Taylor solution. After its destruction, the star is converted to a collisionless particle with negligible mass, and its metal contribution is logged into a separate metallicity field for Pop III stellar ejecta. Explosion energies are assigned as follows: Type II SNe have $E_{51} = 1$; HNe have

$10 \leq E_{51} \leq 30$ depending on their mass; and PISNe have $6.3 \leq E_{51} \leq 90$, according to Eq. 3 of Wise et al. (2012b). Here E_{51} is the explosion energy in units of 10^{51} erg. For our choice of Pop III IMF, the relative occurence of supernovae of different types are 38% Type II SNe, 55% HNe, and 7% PISNe. We chose a Pop III characteristic mass so that HNe would dominate the chemical enrichment process, as the chemical abundance patterns of Extreme Metal Poor stars are best fit by hypernova models (Nomoto et al., 2006).

2.3 Enrichment of Halos

For the following analysis, we define the variable,

$$f_3 \equiv \log_{10}\left(\frac{M_{Z_3,\mathrm{p}}}{M_{Z_3,\mathrm{a}}}\right), \tag{2.5}$$

to describe the enrichment of halos. Here, $M_{Z_3,\mathrm{p}}$ is the maximum mass of Pop III metals that could have originated from Pop III stars within the virial radius of each halo. $M_{Z_3,\mathrm{p}}$ is calculated using Equations 2.3 and 2.4, given the Pop III remnant particles inside the virial radius at the final redshift. $M_{Z_3,\mathrm{a}}$ is the Pop III metal mass within the virial radius that is directly measured from the simulation. We label a halo as "enriched" if it satisfies $\langle Z_2 \rangle + \langle Z_3 \rangle \equiv \langle Z_{\mathrm{total}} \rangle > 10^{-4} Z_\odot$, where $\langle Z_2 \rangle$ and $\langle Z_3 \rangle$ are the mass-averaged Pop II and Pop III metallicities inside the virial radius. Otherwise, the halo is labeled as "pristine." Using these definitions, $f_3 < 0$ corresponds to halos that contain more metals than could have come from internal sources, meaning that external enrichment must have occured; $f_3 = -\infty$ corresponds to halos that are enriched exclusively by external sources, and $f_3 > 0$ corresponds to halos that are primarily enriched by internal sources.

2.3.1 Externally Enriched Halos

The first question concerning external enrichment is simple: does external enrichment happen in an appreciable number of halos? To answer this question, halos are identified using ROCKSTAR (Behroozi et al., 2013), and the value of f_3 is calculated for each. We find that the number of both internally and externally enriched halos increases over time, and as redshift evolves, external enrichment becomes the most common enrichment vector. At the final output, $z = 9.3$, the simulation hosts 1864 halos with virial mass above our 100-particle resolution limit of $10^{5.3} M_\odot$ and 304 halos that are enriched to $\langle Z_{\mathrm{total}} \rangle > 10^{-4} Z_\odot$. Of the enriched halos, 168 (55.3 %) are found to have $f_3 < 0$.

Figure 2.1 shows a Pop III metallicity projection of the simulation at $z = 9.3$ indicating the location and virial radius of each halo and the location and type of all SN remnants. The regions with metallicities in excess of $Z_{\rm crit} = 10^{-4} Z_\odot$ tend to show more halo clustering. The halo-averaged Pop III and Pop II metallicity distribution functions are shown in Figure 2.2. Each distribution peaks near $Z_{\rm crit}$. This would occur even for different values of $Z_{\rm crit}$, as Pop II star formation proceeds beyond $Z_{\rm crit}$. The regions of high spatial density are where halos are more likely to be enriched externally. A calculation of the mean halo-to-halo nearest-neighbor distance gives a value of 0.6 proper kpc for externally enriched halos, whereas the mean nearest neighbor distance across all halos is around 1.7 proper kpc. There is one region near $(x, y) = (-35\,\mathrm{kpc}, -30\,\mathrm{kpc})$ of Fig. 2.1 that contains a particularly large volume of enriched gas that is the result of mixing between ejecta of many SN explosions. This region hosts the most massive halo in the simulation.

Figure 2.3 shows the f_3 cumulative probability distribution of enriched halos at $z = 9.3$ separated into five mass bins each containing the same number of halos between $10^{5.3} M_\odot$ and $10^{8.6} M_\odot$. The fraction of halos found to have been enriched purely externally increases with decreasing halo mass. Below $10^6 M_\odot$, the majority of halos are found to be enriched purely externally, while most of the halos above $10^6 M_\odot$ are enriched internally. There is a small minority of halos in the bins above $10^6 M_\odot$ that experience both internal and external enrichment by our measure, while the enrichment pathway for the remaining halos is either pure internal or pure external. In some cases (e.g., lower left-hand corner of Fig. 2.1), there is one high-mass halo that injects large amounts of metals into its surroundings and draws multiple low-mass satellites into the enriched region, turning them into externally enriched halos.

Figure 2.4 shows the evolution of various number fractions over time. While the fraction of all halos that are enriched above $Z_3 = 10^{-4} Z_\odot$ stays roughly constant, the fraction of those that are externally enriched increases over time. The externally enriched halo fraction follows the also-increasing volume fraction of enriched gas in the simulation, suggesting that the growing body of metal ejecta overtakes the halos over time or that the number of halos forming in the enriched IGM is increasing.

2.3.2 Pre-enriched vs. externally enriched?

So far, we have assumed that every enriched halo that is not internally enriched is externally enriched by a nearby supernova remnant. However, halos forming in an enriched region of the IGM will

accrete gas from the environment during virialization and become enriched that way. We call this kind of halo pre-enriched. As the volume fraction of enriched gas increases, we would expect more pre-enriched halos to form. Here we analyze the occurrence of pre-enrichment in our simulation. We flag halos as pre-enriched if their mass-weighted metallicity is above $10^{-4}Z_{\odot}$ in the first data output in which they appear; i.e., become resolved in our simulation. The time interval between data outputs is less than the lifetime of a Pop III star so it is unlikely we confuse an externally enriched halo with a pre-enriched halo.

Fig. 2.5 plots the ratio of the number of pre-enriched halos to all enriched halos versus redshift. The black line is for the entire volume, while the blue line is only for halos within 10 proper kpc of the most massive halo. We see that pre-enriched halos form predominantly near the most massive galaxy for $z > 12$, but form throughout the volume in increasing numbers at lower redshift. At $z = 9.3$, 13% of all enriched halos formed pre-enriched, implying that external enrichment by nearby supernova remnants remains the only channel for halos that are not internally enriched.

2.3.3 Contribution of Different SN Types

In order to characterize the contribution of each type of supernova in the simulation to the external enrichment process, we perform the following calculations. First, we identify the type of the nearest Pop III remnant to each externally enriched halo at the output when the halo first crosses the metal enrichment threshold of $10^{-4}\,Z_{\odot}$ and calculate the proper distance from the halo's center to the remnant at that output. We then calculate the total ejecta of all Pop III remnants within a 2 proper kpc radius of each externally enriched halo at the final output using Equations 2.3 and 2.4, and consider the type that has produced largest summed Pop III metal mass to be the dominant enricher of that halo. The mean distance from the externally enriched halo to all Pop III remnants of the dominant enriching type is then recorded. The results of these calculations are shown in Figure 2.6. The left panel shows the results of the first calculation, while the right panel shows the reults of the second.

As shown in the right panel of Figure 2.6, 52% of externally enriched halos are enriched primarily by HNe by the last output, while approximately 45% and the remaining 3% are enriched primarily by PISNe and Type II SNe, respectively. Taking into account the relative abundances of SN types set by the $20M_{\odot}$ Pop III characteristic stellar mass (54% are HNe, 38% are Type II SNe, and 8% are PISNe), it is unsurprising that HNe are the dominant enrichers of the largest fraction of halos. PISNe, however, are a

close second, enriching more halos per event on average, although the statistics on the latter is poor.

The most massive halo in the simulation is a significant source of metal enrichment, enclosing 62 HN, 45 Type II SN, and 7 PISN Pop III remnant particles by the last output. This is the most active region in the simulation, and the metallicity field surrounding the most massive halo is the result of mixing between many supernova remnants of different types. Halos that form in this environment could initially be labeled as externally enriched by our measure, and the type of Pop III supernova that contibutes the most to their enrichment is less clear. Because of this, the externally enriched halos that are within 10 proper kpc of the most massive halo by the final output are also identified in Figure 2.6. Of the 152 halos plotted in the right panel, 36 are within 10 proper kpc of the most massive halo. As seen in the right panel, the majority of halos nearby the most massive halo are identified as having been enriched primarily by PISNe by our measure. This makes sense because of the large concentration of PISN remnant particles in that particular region.

The median lines in Figure 2.6 give an indication of typical distances by which enrichment from each type of supernova can occur. In both panels, there is a clear stratification between distances to Type II SNe, HNe, and PISNe (listed in order of increasing distance). In the left panel, the median distance to the nearest Pop III remnant at the time of enrichment is 0.886 proper kpc for Type II SNe, 1.04 proper kpc for HNe, and 1.26 proper kpc for PISNe. In the right panel, the median distances are 0.559 proper kpc for Type II SNe, 1.02 proper kpc for HNe, and 1.26 kpc for PISNe. It should be noted that the Type II SNe bin in the right panel of Figure 2.6 only has four data points, so the median is less reliable for that one bin. The ordering in median distance to each type makes sense on energetic grounds, as PISNe are more energetic than HNe, which are more energetic than Type II SNe (see Sec. 2).

In order to further verify that the distances found in Figure 2.6 are reasonable, the following estimate is performed. The typical enriching radius of each type of supernova is calculated by considering the average volume that each type enriches to $Z_3 > 10^{-3}\,Z_\odot$. This is calculated as follows:

$$\langle V_{\rm enr}\rangle_{\rm type} = f_{\rm ej}\left(\frac{V_{\rm enr}}{N_{\rm type}}\right)$$

$$\langle r_{\rm enr}\rangle_{\rm type} = \left[\frac{3}{4\pi}\langle V_{\rm enr}\rangle_{\rm type}\right]^{1/3}$$

Here, $f_{\rm ej}$ is the fraction of the total mass of ejected metals from each type of SN by $z = 9.3$, $N_{\rm type}$ is the number of each type that has occured, and $V_{\rm enr}$ is the total volume of enriched gas at $z = 9.3$. By the final output, 93% of explosions that have occured are Type II core-collapse SNe or HNe, while the remaining 7% are PISNe. By $z = 9.3$, there are 169 Type II SNe, 240 HNe, and 32 PISNe that have occured. Interestingly, the few PISN explosions that occur contribute more metal ejecta than both of the other SN types combined. Using the ejecta Equations 2.3 and 2.4, these contribute $212.2\,M_{\odot}$, $1{,}494\,M_{\odot}$, and $2{,}753\,M_{\odot}$ of Pop III metal ejecta in each respective bin. Applying the formulae above, the calculation yields values of approximately 0.67 proper kpc, 1.0 proper kpc, and 2.5 proper kpc for the average enriching radius of Type II SNe, HNe, and PISNe respectively. These values are in good agreement with the simulations of Whalen et al. (2008), in rough agreement with the visual presented in Figure 2.1, and the distances in Figure 2.6. It should be noted that this calculation does not take into account the age of the remnants, as an older remnant has had more time to expand. The calculation also does not account for overlapping SN remnants, gas collapse, or mixing as a result of halo mergers. The radii derived above therefore must be viewed as rough upper limits. A more detailed calculation would use the individual mass of each SN progenitor, rather than assigning the average bubble size to all SNe that are labeled as a given type, while adjusting $V_{\rm enr}$ appropriately for gas dynamics. It should also be noted that these results are highly dependent on the IMF chosen for Pop III star formation.

2.4 Star Formation

2.4.1 The First Pop II Stars

Recall that in this simulation Pop II star particles represent coeval star clusters formed out of gas that has been enriched by Pop III supernovae and/or prior generations of Pop II star formation. One interesting question is how sensitive are the characteristics of the first Pop II stars to form to the type of the first Pop III supernova to occur in the host halo's history, as well as to the enrichment pathway leading to their formation. To shed light on this matter, for each halo, we compare the creation times of all Pop II particles and Pop III remnants within the halo's virial radius at the final output. We then select the earliest particle of each type for further examination. The explosion type of the first Pop III supernova is logged, and an additional check is performed to determine if the first Pop II star particle formed as a result of external enrichment. Here, a halo is considered externally enriched if it forms a Pop II star

particle without a Pop III remnant particle inside the virial radius. The metallicity requirement from Sec. 2.3 has been dropped because we only consider halos that form Pop II stars, and the formation of a Pop II star particle is a direct indication that the halo has been enriched by some process. If the first Pop II star particle forms inside a subhalo of a halo that contains Pop III remnants, then the Pop II particle is determined to have formed through external enrichment as long as none of the Pop III remnant particles are inside the subhalo at the time of the Pop II particle's formation. Some 28% of all externally enriched halos that are not pre-enriched are subhalos of larger halos.

Figure 2.7 shows the type of the first Pop III supernova, the metallicity of the first Pop II star cluster, and the time delay between the first Pop III supernova and the formation of the first Pop II cluster for each star-forming halo. Note that Pop II star particles exist with metallicities below $Z_{\rm crit} = 10^{-4} Z_{\odot}$ because they are assigned the mass-weighted average metallicity of their birth cloud, which can be less than $Z_{\rm crit}$. Because of our choice of 20 $M_{\odot}$ for the Pop III characteristic mass, 78% of the star-forming halos are originally seeded by hypernovae, which explains their prevalence. PISN are much rarer, again because our choice for the primordial IMF. The Pop II particles that form following a PISN tend to have higher metallicity, with an average of $10^{-2} Z_{\odot}$ compared to the average for particles forming after HNe and Type II SNe of $10^{-3} Z_{\odot}$. The first Pop II stars with the highest metallicities form < 5 Myr after a PISN. However, there are only 7 star-forming halos that are seeded by PISNe, and for 2 of these halos, the first Pop II star particles have metallicities below $10^{-4} Z_{\odot}$. Further study on this topic would require a larger sample size to draw reliable conclusions. Also shown in Fig. 2.7 are the halos that form their first stars through external enrichment. Of the 41 star forming halos in this sample, 5 formed their first Pop II stars through external enrichment. All of the clusters that formed through external enrichment, including those that form following PISN explosions, have metallicity below $10^{-3} Z_{\odot}$.

The Pop III and Pop II epochs of star formation are typically thought of as separate, sequential phases in a halo's history; however, it is possible for multiple progenitors within a merger tree to undergo star formation concurrently, with some living in the Pop II phase while others are still in the Pop III phase. This effective overlap between the phases is demonstrated in Fig. 2.8, which shows the time difference between each Pop III supernova and the formation of the first Pop II star cluster for each star forming halo in the simulation as identified in the final output. While most halos show little to no overlap between the phases, there are 7 halos in our sample with an overlap of over 100 Myr, with the longest overlap being

nearly 300 Myr. The 4 most massive halos continue to form additional Pop III star particles during this overlap phase. Figure 2.8 also provides a measure of the maximum time scale for the Pop III phase of the halos in this simulation, which is about 300 Myr. This time scale is entirely dependent on a halo's merger history, and is thus subject to change if the simulation progressed further and more halos were allowed the time to merge.

2.4.2 The Most Massive Halo

In order to assess the importance of external enrichment in the star formation history of the most massive halo in the simulation, a merger tree was created using Consistent Trees (Behroozi et al., 2013), and the most massive progenitor was tracked over time along with all of the stars that would eventually end up in the final halo. Figure 2.9 shows the Pop II star formation history and final stellar metallicity distribution function (MDF) for the most massive halo in the simulation ($M_v = 3.71 \times 10^8 M_\odot$), and distinguishes stars by whether or not they reside inside the most massive progenitor at a given redshift. Its first Pop II star cluster forms around $z = 20$ with a metallicity of about $10^{-3} Z_\odot$ outside of the most massive progenitor halo. Without double-counting due to stars forming within subhalos, the most massive halo has 5 separate Pop II star-forming progenitors. Stars that form through external enrichment are logged in the same way as was done for Figures 2.7 and 2.8 in the previous section; however, the most massive halo's history is devoid of externally enriched star formation. This is interesting because this halo contains 97% of the simulation's Pop II stellar mass and is a major source of enrichment for nearby externally enriched halos.

The right panel of Fig. 2.9 shows the Pop II stellar MDF for the most massive halo. For comparison, Fig. 2.10 shows the MDF for all Pop II particles in the simulation volume at the final output, and highlights those that form in externally enriched halos. The distribution peaks near $Z = 10^{-2.4} Z_\odot$, and falls off dramatically below $Z = 10^{-3} Z_\odot$ with a minimum value of $Z = 10^{-5.1} Z_\odot$. There is no contradiction that the minimum metallicity is below $Z_{\rm crit} = 10^{-4} Z_\odot$ for reasons discussed above. All of the externally enriched star formation exists in the long tail of the distribution below $10^{-3} Z_\odot$. The MDF for the most massive halo looks very similar, as it contains most of the Pop II particles in the simulation, but it has fewer particles in the low-metallicity tail.

2.5 Discussion

External enrichment phenomena are studied in Jeon et al. (2017), where external enrichment leads to extremely low-metallicity Pop II stars, and allows halos to form Pop II stars without ever hosting a Pop III star. This study corroborates that these halos can exist (i.e., Fig. 2.3) in appreciable quantities, but most of the externally enriched halos identified in this simulation are not massive enough to support Pop II star formation. In agreement with Smith et al. (2015a), the Pop II stars that do form through external enrichment form with very low absolute metallicity. However, we find such stars are absent from the merger tree of the most massive halo formed in this simulation. This finding could potentially be misleading, as this halo contains 97% of the Pop II stellar mass summed over the entire simulation volume by the final output and is thus the only halo to achieve a stellar mass $\gtrsim 10^5 M_\odot$ in this sample. A much larger sample of star forming halos is needed to accurately assess the role of external enrichment in the formation of more massive galaxies.

Jeon et al. (2017) also comments on the transition time between Pop III and Pop II star formation, finding that the transition takes a few tens of Myrs. This is in agreement with our findings, for which we find an average transition time of 63 Myr. Additionally, we find that there is not always a hard line separating the two phases of star formation, as there can be a period lasting up to $\sim 100\,\mathrm{Myr}$, during which both phases can exist simultaneously within separate halos in the merger tree of the final halo.

The search for metal-poor stars has been the focus of many observational surveys. Abohalima & Frebel (2018) compile an online database of stellar chemical abundance catalogs spanning searches from 1991 to 2016 that identified metal-poor stars located in the galactic halo, bulge, and dwarf galaxies in the Local Group. Currently, there are been over 900 unique stars that have been identified with $[\mathrm{Fe/H}] \leq -2.5$. While stars with $[\mathrm{Fe/H}] < -4.0$ are exceptionally rare, surveys continue to identify stars with lower and lower chemical abundances. The current record-holder is the carbon-enhanced SMSS J0313-6708, which has $[\mathrm{Fe/H}] < -7.3$ (Keller et al. (2014)). Despite its incredibly low iron abundance, the star's abundances of carbon and oxygen have upper bounds of $10^{-2.4}$ and $10^{-2.3}$ of solar, respectively. This places its total metallicity near the peak of Figure 2.10, which shows an MDF of all Pop II star clusters in the simulation by the final output. We observe very broad ranges of metallicity for Pop II stars; the lower bound here is a combined artifact of 1) our choice of critical metallicity to form Pop II stars, and 2) the limited sample

pool of Pop II stars in the simulation.

Table 4 in Kirby et al. (2013) summarizes the MDFs for a collection of dwarf galaxies in the Local Group. The most massive halo in the simulation has a similar stellar mass and average Pop II stellar metallicity dwarf spheroidal (dSphr) Milky Way satellite, Ursa Minor, which has a stellar mass of $10^{5.73\pm0.20} M_{\odot}$ and an average iron abundance ratio, $\langle [Fe/H] \rangle$, of -2.13 ± 0.01. The iron abundance ratio here is averaged over a sample of 190 stars that have been measured spectroscopically in the dwarf, and is thus a good indicator of the dwarf's total metallicity. Also similar is the dSphr, Sextans, with $M_{\star} = 10^{5.84\pm0.20} M_{\odot}$ and $\langle [Fe/H] \rangle = -1.94 \pm 0.01$, averaged over 123 unique stars within. These two dwarf galaxies are characterized by their primarily old, metal-poor stellar populations, with the only significant bursts of star formation occuring early on in their lifetime (Carrera et al. 2002; Bettinelli et al. 2018).

In agreement with metal-poor DLA studies (Cooke et al., 2017; Welsh et al., 2019), the star-forming galaxies in our simulation have only had a few enriching events. Welsh et al. (2019) places an upper limit of $\lesssim 70$ enriching Pop III supernovae. We find our galaxies ($\sim 10^3 - 10^4 M_{\odot}$) to have $\lesssim 20$ enriching events, with the outlier most massive galaxy ($M_* \approx 10^{6.3} M_{\odot}$) displaying > 100 events. We also find agreement in that most of the enriching events were HNe or SNe in stellar mass range $10 < M_*/M_{\odot} < 40$, which is entirely due to the characteristic mass chosen for this simulation. However, these DLA studies have not found evidence for highly energetic PISNe, which are included here. Therefore, the number of events we find here is likely to be a lower bound.

2.6 Conclusions

We have analyzed the formation and chemical evolution history of a sample of halos with mass $10^{5.3} \leq M_{vir}/M_{\odot} \leq 10^{8.6}$ derived from an Enzo AMR radiation hydrodynamic cosmology simulation which includes detailed models for Pop III and Pop II star formation and their chemical and radiative feedback within a 1 Mpc comoving box to a stopping redshift of z=9.3. The simulation is a re-run of Wise et al. (2012a) with 1,000 data outputs saved for subsequent analysis. By the final redhsift, 304 of the 1,864 halos analyzed are chemically enriched to $\langle Z_{total} \rangle > 10^{-4} Z_{\odot}$ where $\langle Z_{total} \rangle$ is the halo's mass-averaged metallicity from both Pop III and II stellar enrichment. With our high time resolution we can distinguish between 3 enrichment pathways: (1) internally-enriched: Pop III stellar remnants within the halo's virial

radius could have supplied the Pop III metals bound to it; (2) externally-enriched: Pop III stellar remnants within the halo's virial radius could not have supplied the Pop III metals bound to it, or contains no stellar remnants at all; (3) pre-enriched: a halo is born enriched with no Pop III stellar remnants. Based on our analysis, we can draw several conclusions:

1. Far from being the outlier, external enrichment is the dominant enrichment pathway that can provide enough metals to push the average metallicity of high redshift minihalos above the critical value required for Pop II star formation. Most halos that are enriched through this mechanism, however, are not massive enough to form stars. When external enrichment does trigger Pop II star formation, the resulting star particles have low metallicity.

2. Internal enrichment is the dominant pathway for halos forming Pop II stars. The majority of Pop II stars form in internally-enriched halos.

3. Only a small percentage of enriched halos form pre-enriched, increasing from 2% to 13% by the end of the simulation.

4. The fraction of halos that are externally enriched increases over time, and the majority of these halos have virial mass below $10^6 M_\odot$.

5. Hypernovae are the predominant supernova type contributing to the external enrichment of halos; however, pair-instability supernovae contribute the most to the enrichment of the IGM as a whole for our choice of primordial IMF.

6. The line between the Pop III and Pop II star formation phases in a merger tree is blurry, as a halo that is currently in the Pop II phase can merge with a halo that is still in the Pop III phase. The period of overlap, where both Pop III and Pop II star formation takes place within a merger tree, typically lasts around 100 Myr for the halos in this simulation.

We have found that during early star formation, the metal enrichment process is not exclusively local to the host halo, and must include the surrounding environment. The region that must be included will likely depend on many factors, e.g., halo mass, halo number density, baryon density between halos and enriching events, temperature, and the particular type of supernova. A future study may be able to study these variables more precisely to determine their effect on the enrichment process.

2.7 Acknowledgements

This research was supported by National Science Foundation CDS&E grant AST-1615848 to M.L.N. and B. S. A.W. gratefully acknowledges support from a MPS Graduate Research Supplement for Veterans (MPS-GRSV) fellowship to the above award. JHW is supported by NSF grants AST-1614333 and OAC-1835213 and NASA grants NNX17AG23G and 80NSSC20K0520. BWO acknowledges support from NSF grants PHY-1430152, AST-1514700, AST-1517908, and OAC-1835213, by NASA grants NNX12AC98G and NNX15AP39G, and by HST-AR-13261 and HST-AR-14315. The simulations were performed using ENZO on the Blue Waters supercomputer operated by the National Center for Supercomputing Applications (NCSA) with PRAC allocation support by the NSF (award number ACI-0832662). Data analysis was performed on the Comet supercomputer operated for XSEDE by the San Diego Supercomputer Center. Computations and analysis described in this work were performed using the publicly-available Enzo (Bryan et al., 2014; Brummel-Smith et al., 2019), yt (Turk et al., 2011), and ytree (Smith & Lang, 2019) codes, which is the product of a collaborative effort of many independent scientists from numerous institutions around the world.

Chapter 2, in full, is a formatted reprint of the material as it appears in Hicks, Wells, Norman, Wise, Smith, & O'Shea (2021), "External Enrichment of Minihalos by the First Supernovae", *The Astrophysical Journal*, 909:70. The dissertation author was the primary investigator and author of this paper.

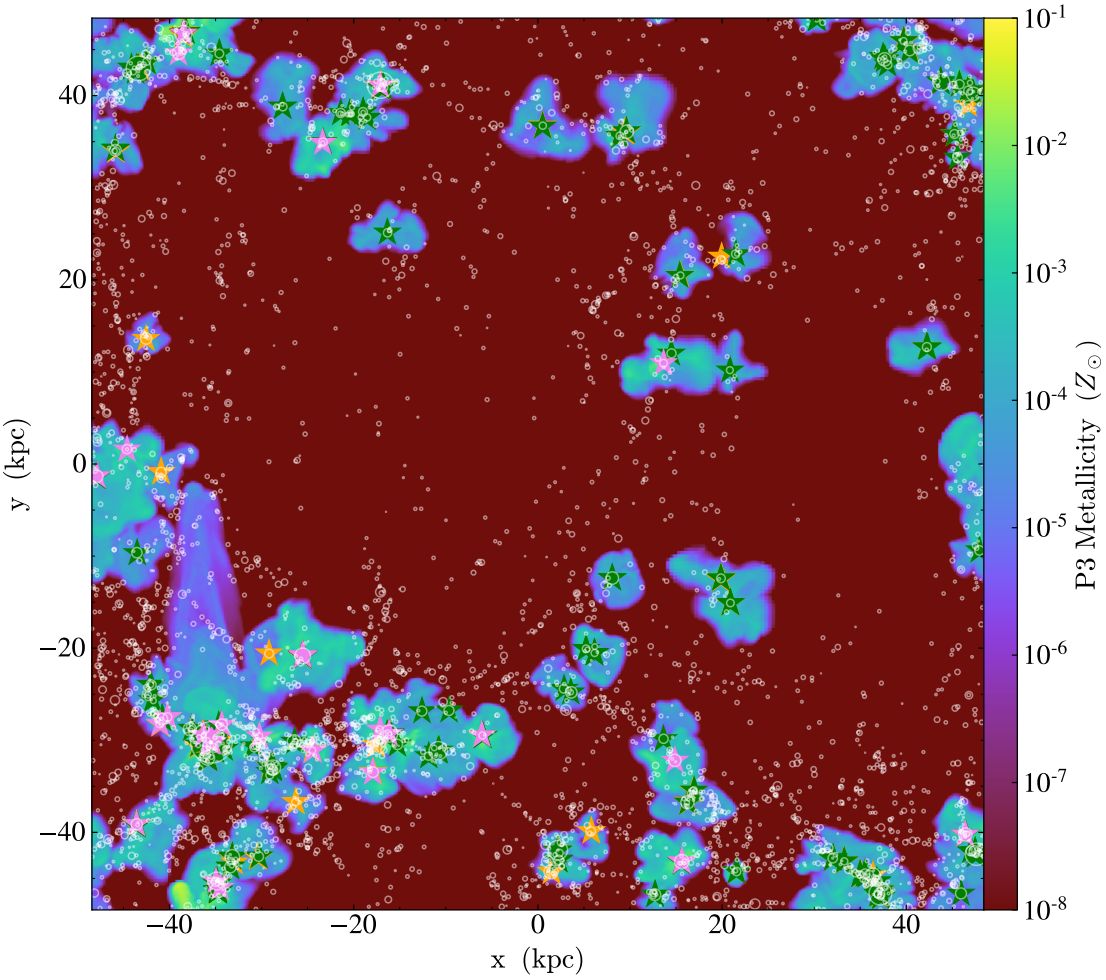

Figure 2.1. Pop III metallicity projection of the simulation at $z = 9.3$. The white circles outline the halos with virial mass greater than $10^{5.3} M_\odot$ identified with ROCKSTAR. The radius of each circle corresponds to the virial radius of the halo it represents. The stars label the Pop III SN remnants in the simulation (orange: Type II SNe, green: HNe, violet: PISNe). The distance scales here are in proper coordinates.

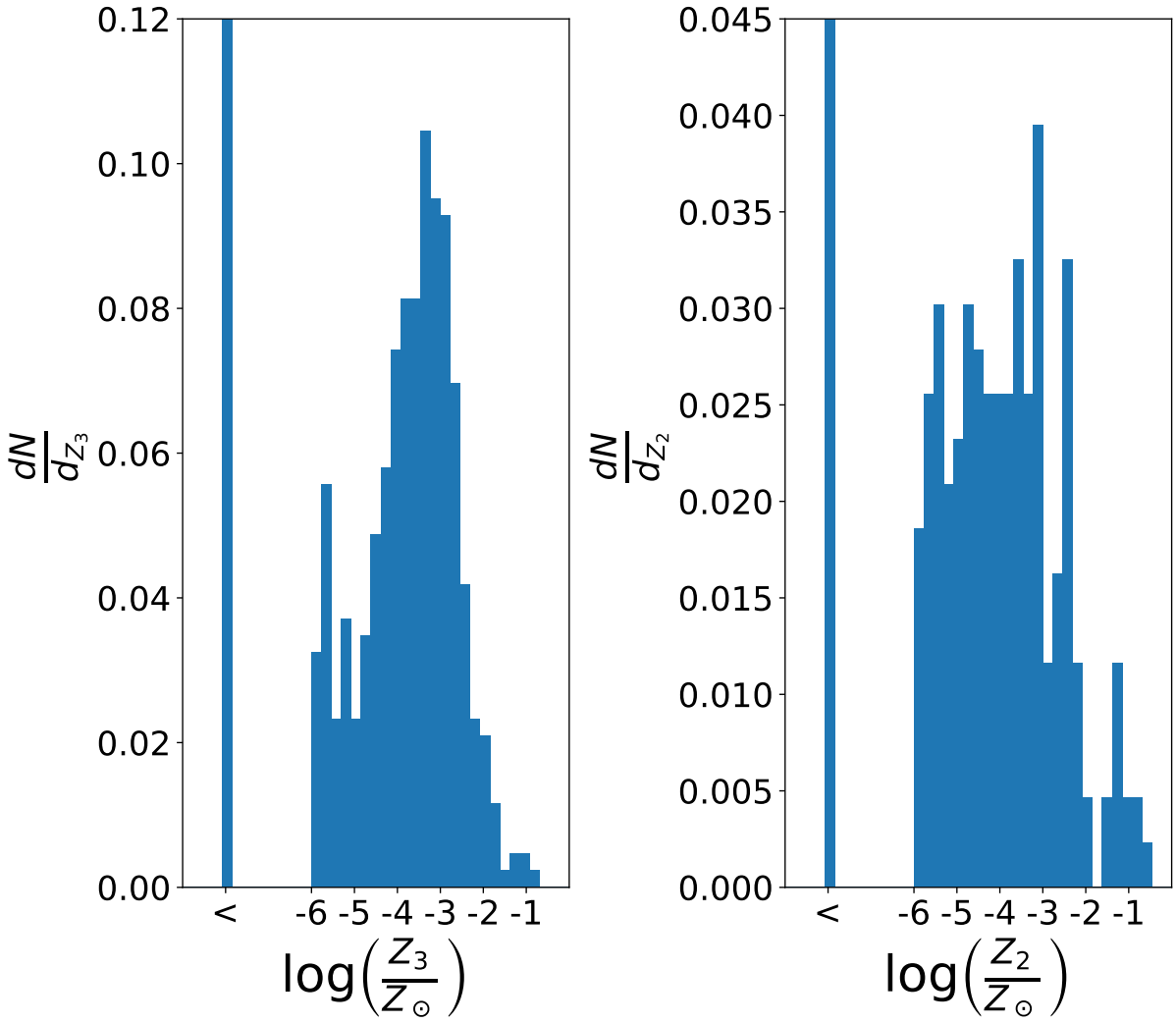

Figure 2.2. Halo-averaged Pop III and Pop II metallicity distributions at $z = 9.3$. The bin labeled '$<$' contains all of the halos with metallicity below $10^{-6} Z_\odot$. The median metallicities for the distributions are $[\langle Z_3 \rangle / \mathrm{H}] = -3.57$ and $[\langle Z_2 \rangle / \mathrm{H}] = -3.93$, respectively, for the sample of 304 enriched halos.

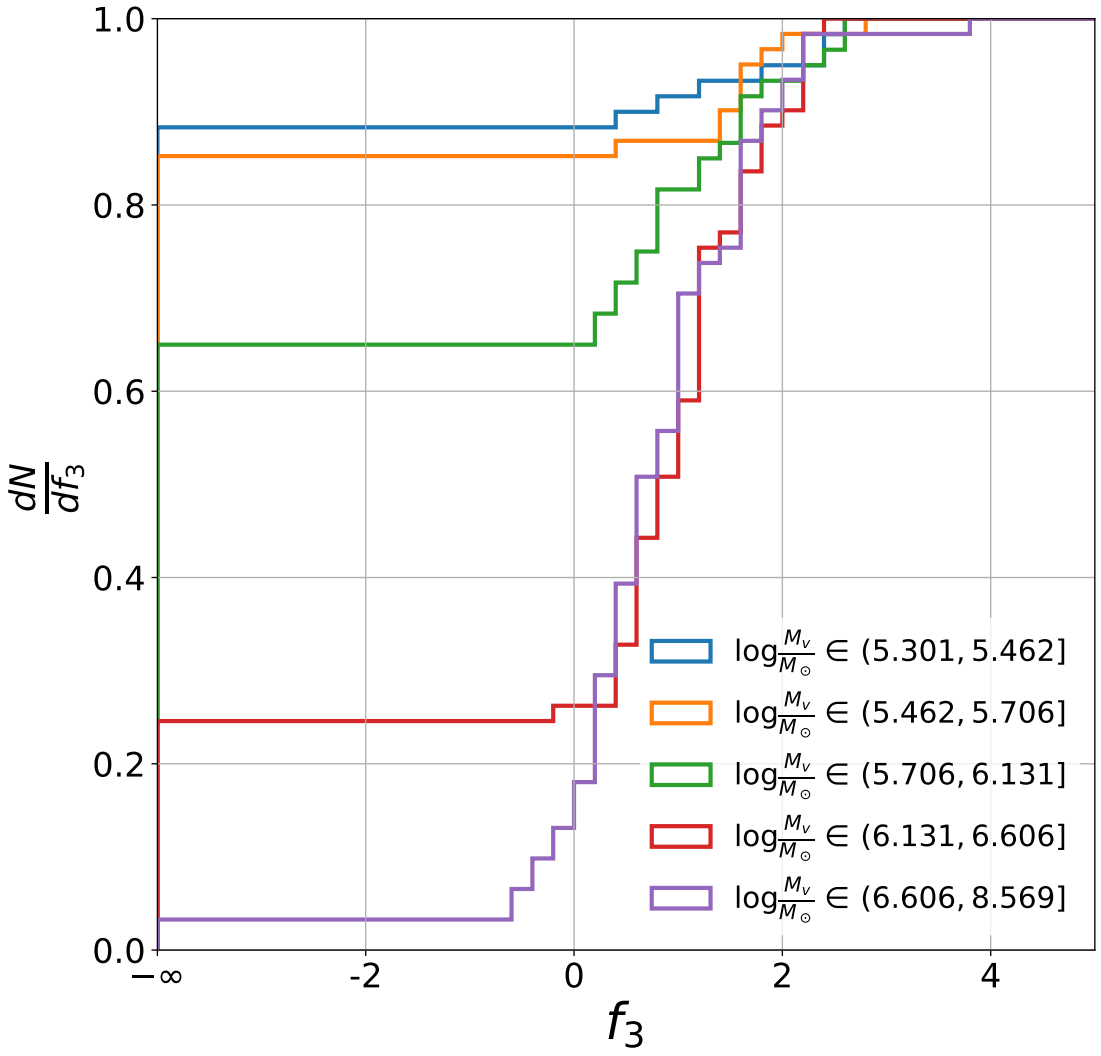

Figure 2.3. Cumulative distribution function of $f_3 \equiv \log_{10}(M_{Z_3,p}/M_{Z_3,a})$ for the 304 enriched halos in the simulation at the final redshift $z = 9.3$. The halos are binned according the virial mass such that each bin has the same number of halos. Because 304 is not evenly divisible by 5, the lowest-mass bin contains 60 halos, while the rest contain 61 halos. The majority of externally enriched halos ($f_3 < 0$) are enriched purely from outside sources ($f_3 = -\infty$). Additionally, most of the externally enriched halos have $M_{\rm vir} < 10^6 M_\odot$.

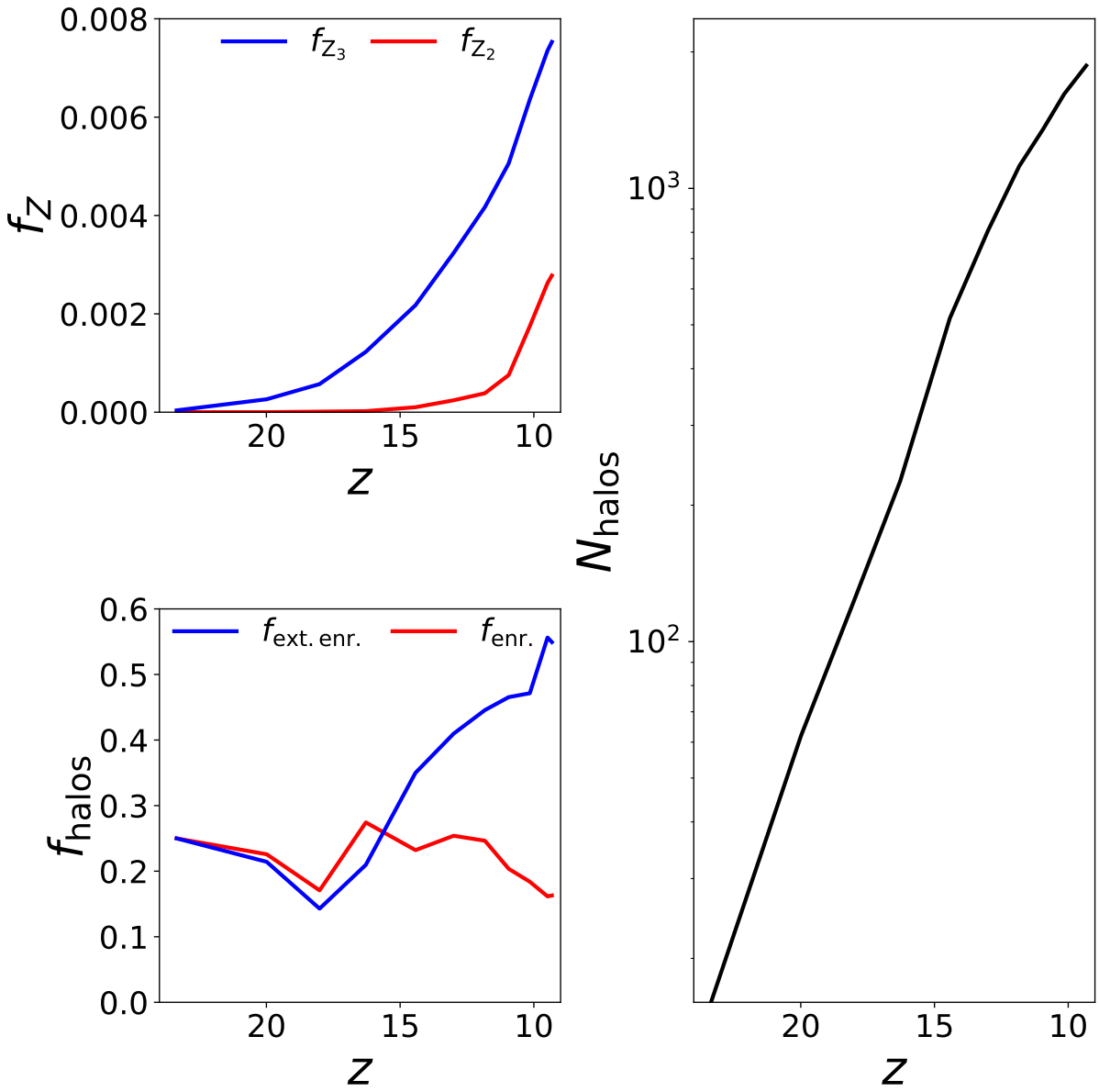

Figure 2.4. Number fractions of various quantities as a function of redshift. *Top left:* volume filling fraction for gas with $Z_3 > 10^{-4} Z_\odot$ (blue) and $Z_2 > 10^{-4} Z_\odot$ (red). *Bottom left:* The red line shows the fraction of all halos above our mass cutoff that are enriched. The blue line shows the fraction of enriched halos that are found to be externally enriched. It is pure coincidence that the lines start at the same point. *Right*: Number of halos above the minimum mass cut as a function of redshift.

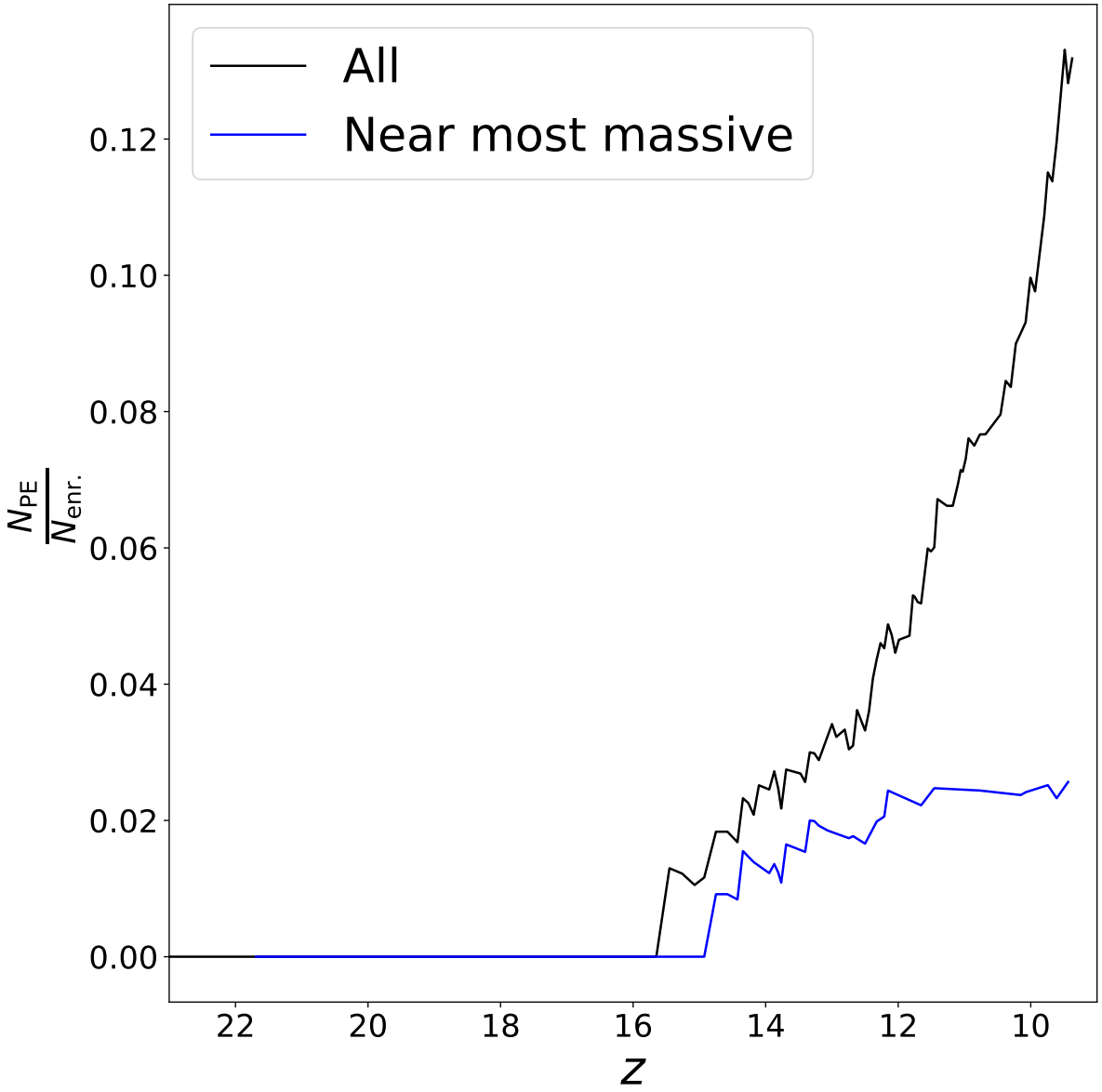

Figure 2.5. Formation of pre-enriched halos. Fraction of all enriched halos that were enriched when they were initially resolved versus redshift. Black line is for all halos in the volume; blue line is for halos within 10 proper kpc of the most massive halo's most massive progenitor. Pre-enrichment is a subdominant channel relative to internal and external enrichment of minihalos at all redshifts simulated, growing from a few percent at $z \sim 15$ to 13% at $z = 9.3$.

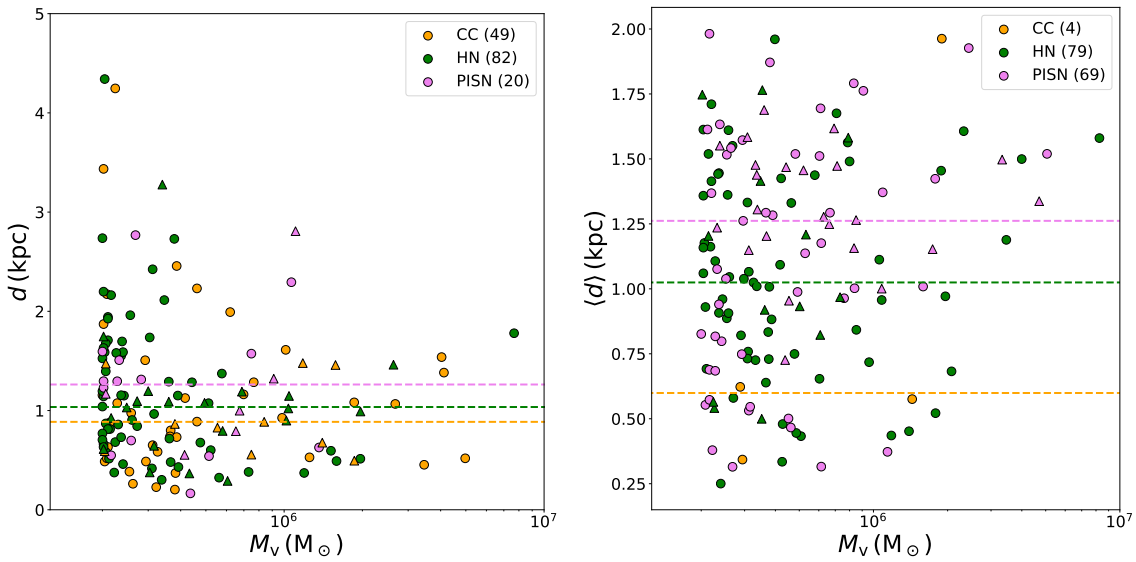

Figure 2.6. *Left:* Proper distance from each externally enriched halo, identified at the final output, to the Pop III remnant at the time it first reaches the metallicity threshold of $10^{-4}\,Z_\odot$ vs. virial mass at that time. *Right:* Mean distance to the Pop III remnants of the dominant enriching type within 2 kpc at the final output vs. virial mass at the final output. Halos that do not have any Pop III remnants within a 2 proper kpc radius are not plotted. Colors represent the type of Pop III remnant. The horizontal dashed lines represent median distances within the respective bins. Triangles represent halos that are within 10 proper kpc of the most massive halo at the final output. The parentheticals in the legends show the number of halos within each SN-type bin, without distinguishing between halos that are close to the most massive halo and those that are not.

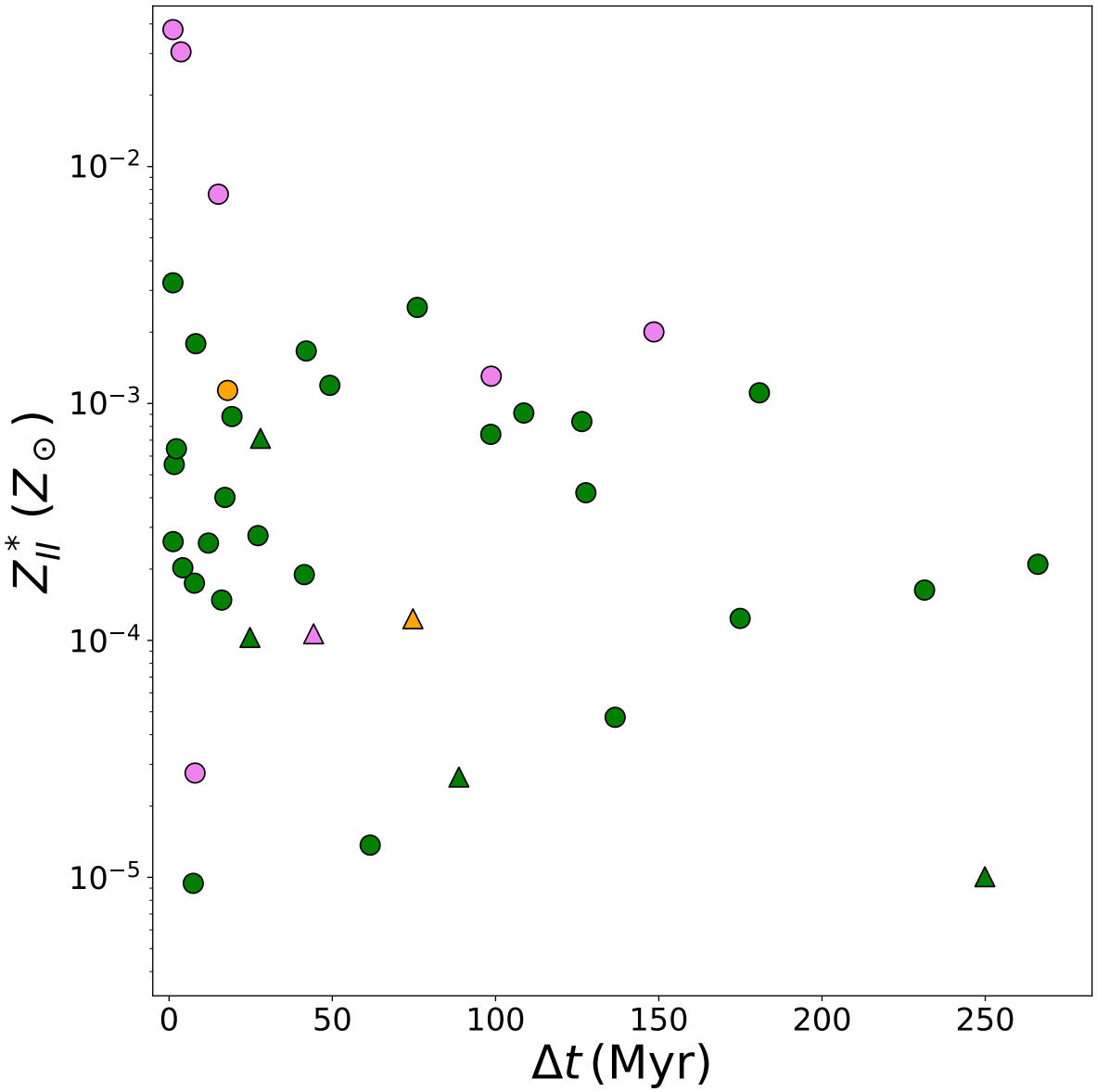

Figure 2.7. Metallicity and time delay of the first Pop II star cluster to form after the first Pop III supernova for each star-forming halo. The symbol shapes indicate the enrichment process leading to the formation of the first Pop II star cluster (circles: internal enrichment, triangles: pure external enrichment) and the symbol colors represent the supernova type of the first Pop III remnants that ends up in the final halo (orange: Type II SNe, green: HNe, violet: PISNe). The halos whose first Pop II stars form via pure external enrichment form in halos with $M_v < 10^6 M_\odot$, with metallicities below $10^{-3} Z_\odot$. Points corresponding to Pop II stars that form in halos below the minimum mass cut are not shown. The median time delay for all halos plotted, only internally enriched halos, and only externally enriched halos is 28, 19.3, and 59.5 Myr, respectively.

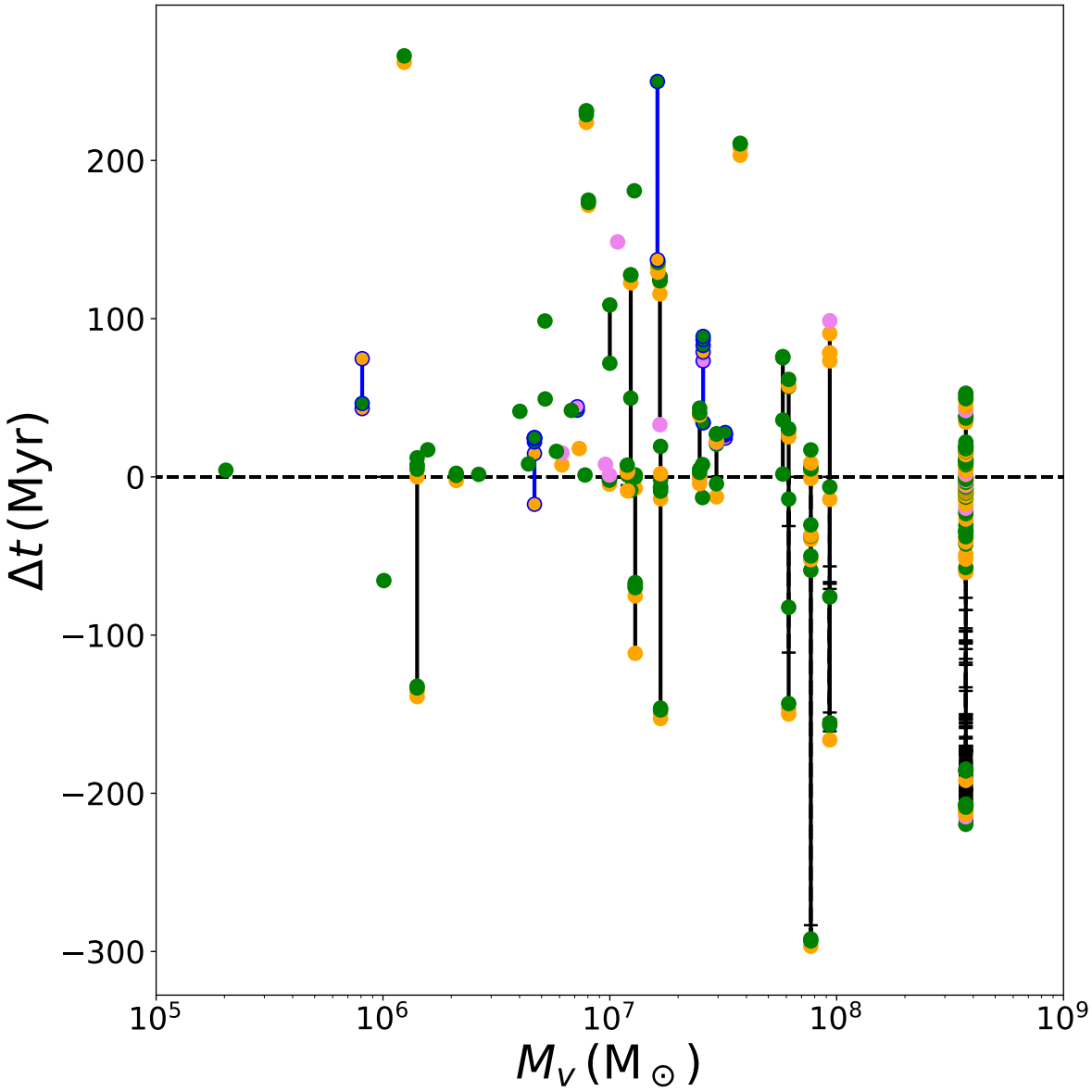

Figure 2.8. History of all Pop III supernovae in each Pop II star-forming halo's history, relative to the formation time of the first Pop II star cluster ($\Delta t \equiv t_{\rm II}^{\rm first} - t_{\rm III}$). Positive values correspond to events happening before the first Pop II star cluster's formation while negative values correspond to events happening after. Points connected by a vertical line are associated with the same final halo whose virial mass is indicated by the abscissa. The color of the points correspond to the type of each supernova (orange: Type II SNe, green: HNe, violet: PISNe). Horizontal dashes on the vertical lines show the times of further Pop II star formation during the Pop III-Pop II overlap phase. The points outlined in blue and connected with blue lines correspond to halos that form their first stars through external enrichment.

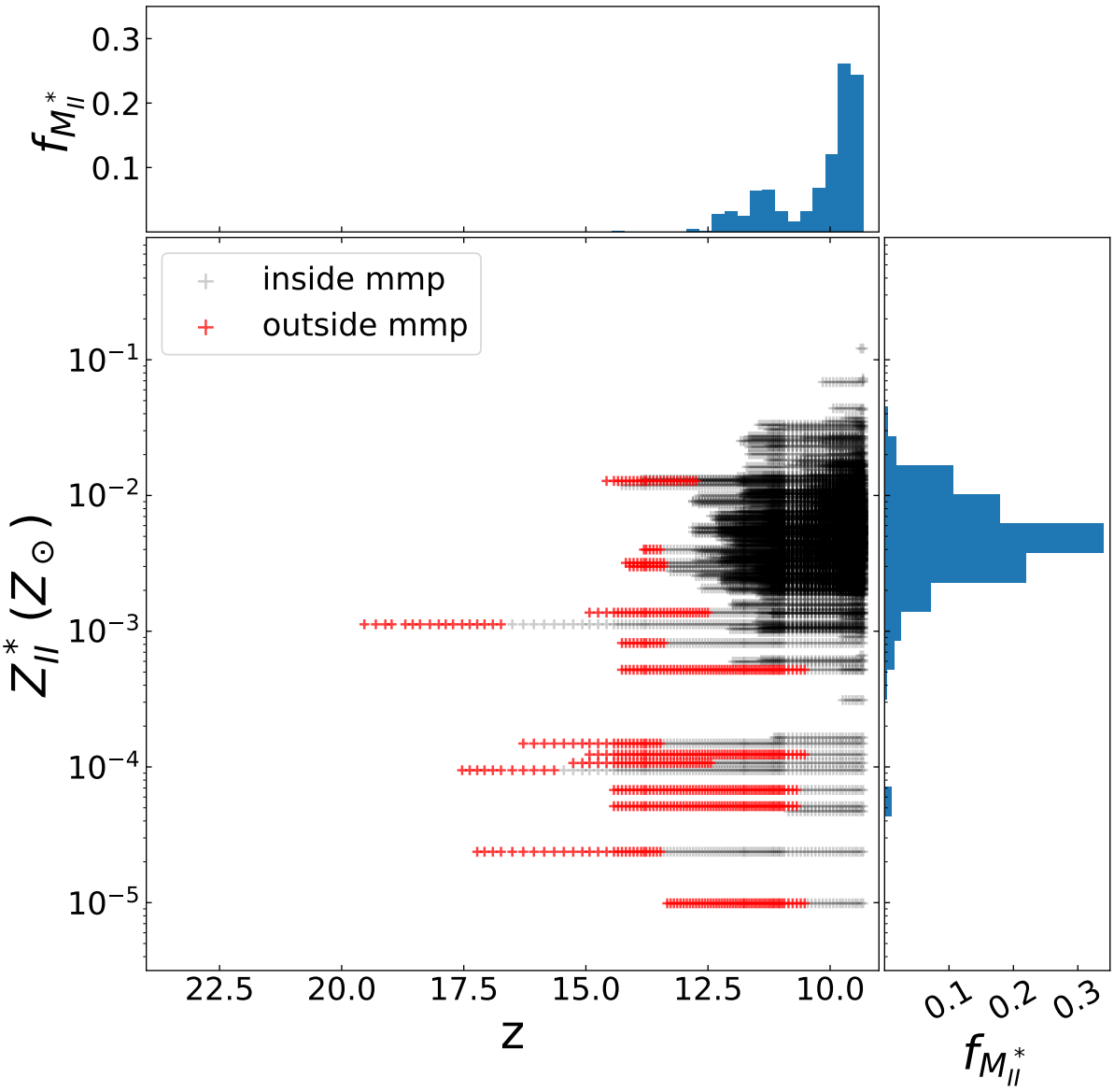

Figure 2.9. *Left:* Pop II formation history of the most massive halo in the simulation ($M_v = 3.71 \times 10^8 M_\odot$). Each data point represents a star particle in the merger tree. Red points correspond to star clusters that are outside the most massive progenitor, while black points correspond to star clusters that are inside. By the end of the simulation, the halo has a stellar mass of about $10^{6.3} M_\odot$. The discrete horizontal lines of points represent each individual star moving through time. *Right:* Stellar metallicity distribution of the halo at the final output. The variable, $f_{M^*_{II}}$, is the fraction of the halo's total stellar mass by the last output within each bin. The distribution peaks near $Z = 10^{-2.4} Z_\odot$. *Top:* Histogram of $f_{M^*_{II}}$ versus redshift of formation.

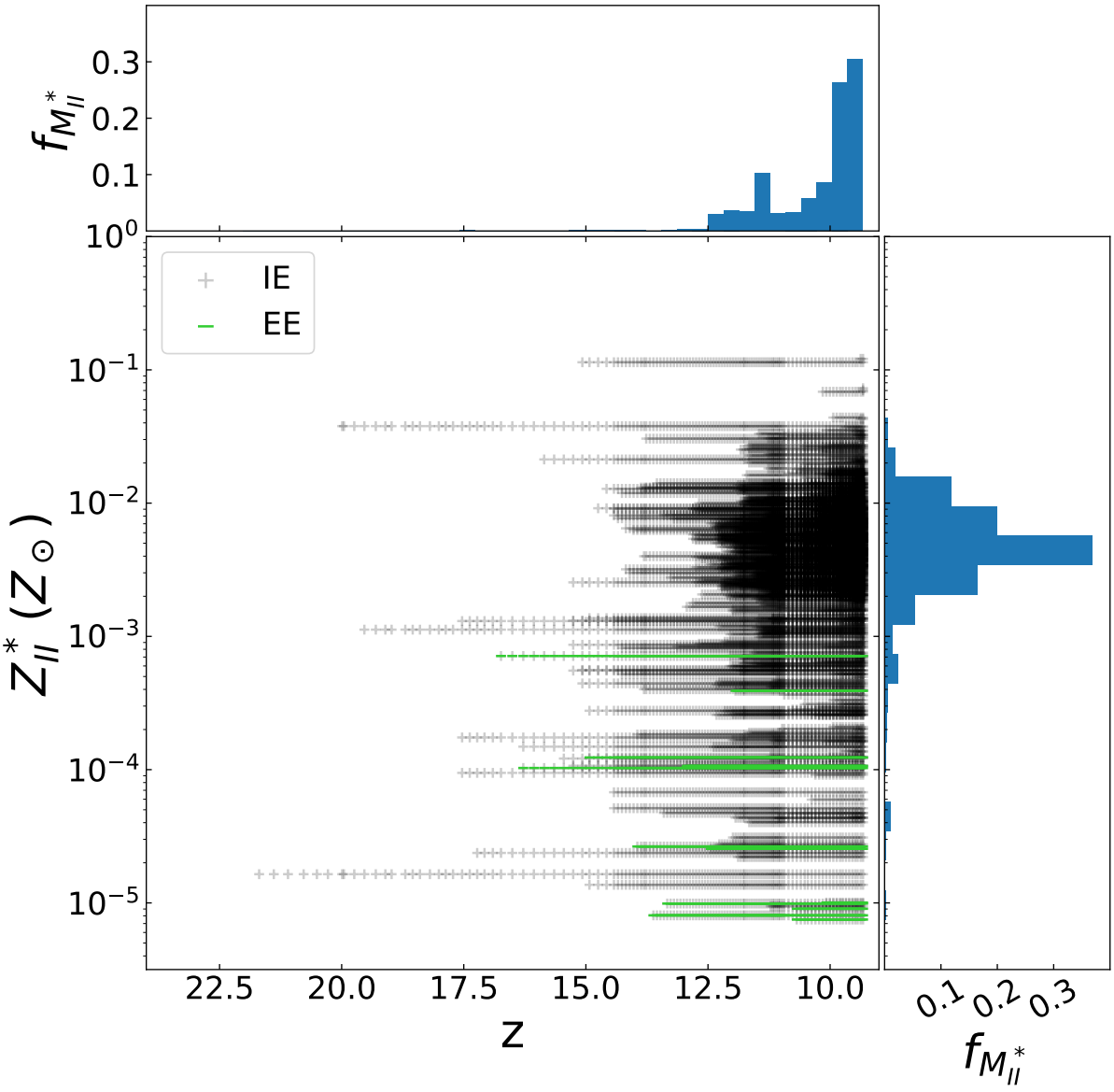

Figure 2.10. *Left:* Metallicity of all Pop II star particles in the simulation volume versus redshift. Each grey data point represents a star particle, with horizontally aligned points track the star over time. Stars that form in externally enriched halos are signified with green horizontal lines. *Right:* Metallicity distribution function by mass fraction of Pop II star clusters at $z = 9.3$. Even though the critical metallicity for Pop II star formation is $Z_{\rm crit} = 10^{-4}\,Z_\odot$, this distribution peaks near $Z = 10^{-2.4}\,Z_\odot$. All of the particles that form through external enrichment have metallicity below $10^{-3}\,Z_\odot$. Pop II particles are able to have metallicity below $Z_{\rm crit}$ because the metallicity is assigned to be the average in a sphere surrounding the densest cell that satisfies the star formation criteria. *Top:* Histogram of $f_{M_{II}^*}$ versus redshift of formation.

Chapter 3

Commissioning and Enhancing Enzo-E, a New Highly Scalable Version of Enzo

The focus of Chapter 2 is primarily on the chemical enrichment history of dark matter minihalos ($M_{\rm vir} \lesssim 10^7\ M_\odot$), with some additional exploration of the consequences of external enrichment on the properties of the first metal-enriched stars that form in the wake of the first supernovae. The following chapters will shift focus to the histories of larger halos (i.e. halos with $M_{\rm vir} \gtrsim 10^7\ M_\odot$) and the formation of the first galaxies. The simulation in Chapter 2 was performed using the `Enzo` code, and has a box size of 1 comoving Mpc. Across all the halos generated in the simulation, there is only one with $M_{\rm vir} > 10^8\ M_\odot$. The following chapters require a statistical sample of halos of this mass. To do this, we need to run a simulation with a much larger box size down to $z \sim 10$, while still accurately resolving all of the relevant physics. This is something that cannot be done feasibly with `Enzo`, as `Enzo`'s scaling is optimized for simulations that require $\lesssim 10^3$ processors.

The Chapters 4 and 5 make use of a new, highly scalable version of `Enzo` called `Enzo-Extreme` (`Enzo-E` hereafter) that can utilize up to $\gtrsim 10^6$ processors efficiently (Bordner & Norman, 2018). `Enzo-E` has been under active development in M. Norman's group since 2012. It became minimally operational for idealized cosmological simulations in 2019, about the time I joined the group. As the first graduate student to attempt to use `Enzo-E` for a Ph.D thesis, it first needed to be commissioned and significantly enhanced with additional physics capabilities to prepare the code to be useful in the context of large-scale galaxy-forming cosmological simulations. My code development work included:

- validating `Enzo-E` by direct comparison with results from `Enzo` on several cosmological test problems (3.0.2);

- debugging Enzo-E's interface to the externally-developed Grackle gas chemistry and cooling package (Smith et al., 2017) (3.0.2);
- porting and testing the StarNet deep-learning surrogate model for Population III star formation and feedback (Wells & Norman, 2022), originally developed in Enzo, into the Enzo-E framework (3.1);
- porting and testing the STARSS subgrid model for metal-enriched star formation and feedback (Wells & Norman, 2022), originally developed in Enzo, into the Enzo-E framework (3.2);
- developing from scratch a multigroup radiative transfer solver for Enzo-E based on the M1 closure method of Rosdahl et al. (2013), and extensively testing its performance and accuracy on a suite of standard test problems (3.3).

This work, which comprises a significant fraction of my dissertation research, is presented in this chapter in some detail, as it effectively documents and commissions Enzo-E for future research applications in cosmological structure formation. But first, we briefly describe the basic Enzo-E application, its object-oriented software architecture, the AMR infrastructure layer Cello, and the parallelization approach with Charm++.

3.0.1 Charm++, Cello, and Enzo-E

Enzo-E is a physics application that makes use of adaptive mesh refinement (AMR) to dynamically increase or decrease the resolution of subvolumes of a simulated region. The AMR backend of Enzo-E is its own standalone application called Cello (Bordner & Norman, 2018). Cello is a fully-distributed array-of-octrees AMR framework that is parallelized using Charm++ (Kalé, 2011). As a Charm++ application, Cello utilizes a series of C++ objects called *chares* as the parallel unit of work. Cello defines a chare to be an object, which is internally referred to as a *block*, that contains both field and particle data, and can execute physics methods.

Figure 3.1 shows the relationship between Charm++, Cello, and Enzo-E. Each Charm++ processing element (PE) spawns a Simulation object, which contains a series of subclasses for defining problem types, initializers, boundary conditions, etc., and is in charge of a number of blocks. The PE then serially loops through the blocks that are assigned to it, and calls a specified set of physics modules

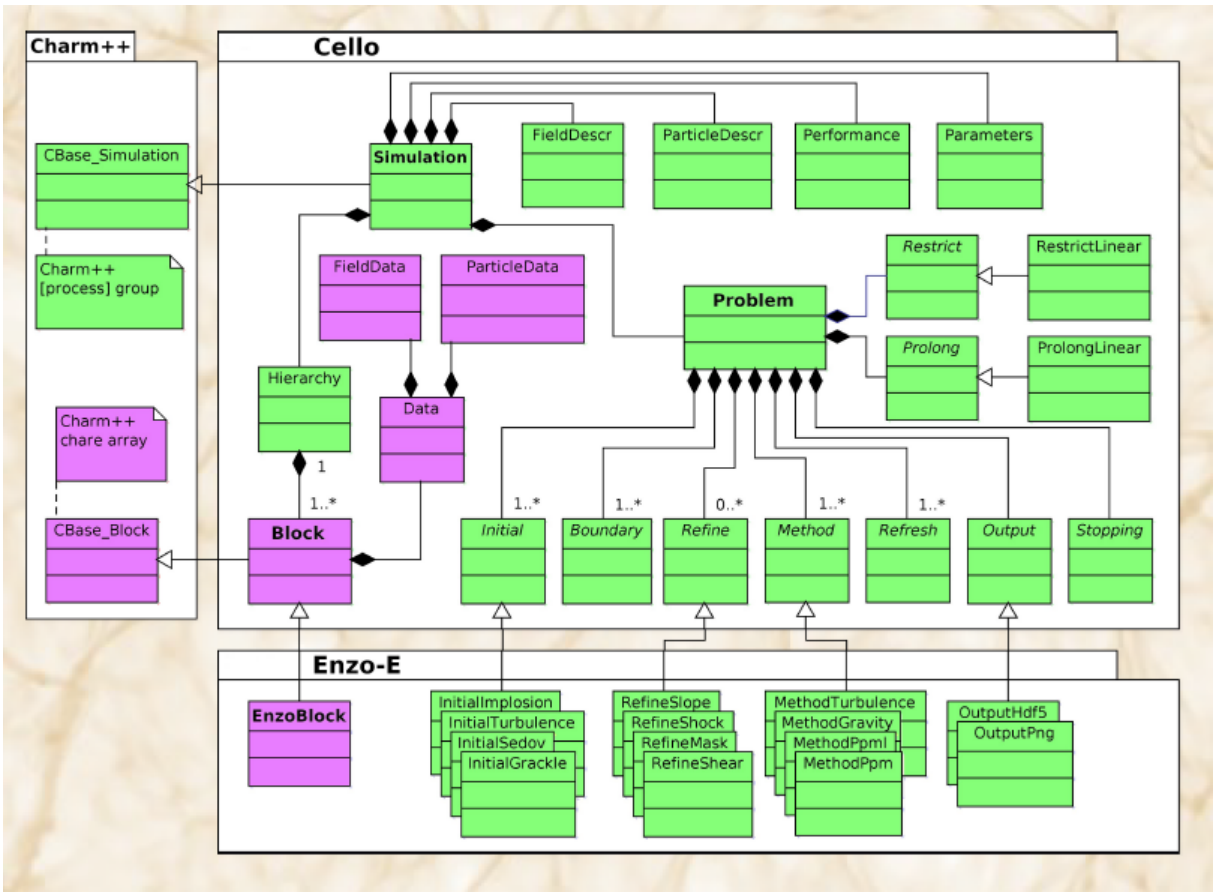

Figure 3.1. Class diagram showing the relationship between `Charm++`, `Cello`, and `Enzo-E`.

on each block. Physics modules within `Enzo-E` are implemented as classes that inherit from `Cello`'s `Method` class. Each block executes a number of physics `Methods` in a sequence, where the list of method types and the order in which they are called are specified in the parameter file.

For cosmological simulations, the number of cells per block is typically set to 16^3. To communicate field values between blocks, each block allocates an additional 4 layers of ghost cells that are periodically "refreshed" with updated values of the corresponding active cells in the neighboring blocks. Including ghost cells, the total number of allocated cells per block is 24^3. This number was empirically chosen to balance the time spent in a given solver in a block, which *increases* as the number of cells increases, with the additional time spent replicating data during ghost zone refresh, which *decreases* as the number of cells increases.

3.0.2 Comparisons with Enzo

Gravity is handled completely differently in Enzo and Enzo-E, owing to differences in the AMR mesh structures and timestepping. Enzo uses structured AMR (Berger & Colella, 1989b; Bryan et al., 2014), in which an adaptive hierarchy of overset grid patches of varying size and shape are evolved over a global root grid mesh. Patches at different levels of refinement are evolved with different timesteps according to a W-cycle schedule. Field data at different levels of refinement are kept consistent through conservative interpolation and restriction operators, as well as through flux correction. Enzo-E, on the other hand, uses a composite multiresolution adaptive mesh generated by array-of-octree refinement (Bordner & Norman, 2018). There are no overset meshes of lower resolution as in Enzo. Additionally every mesh patch regardless of level is cubic and of equal size (in terms of mesh points). Currently, the solution is evolved using a single global timestep, although work is underway on block-adaptive timestepping.

Given this background, we can now briefly describe how the Poisson equation (PE) is solved on the adaptive mesh to get the gravitational potential. In Enzo, first the PE is solved on the uniform, periodic root grid using fast Fourier transforms (FFTs). Then, all patches at the next level of refinement are evolved with a smaller timestep, and so on recursively until the finest level is reached with a W-cycle schedule. The gravitational potential on a refined patch is computed as an isolated PE problem using a geometric multigrid solve, interpolating its boundary conditions from its parent grid or root grid as the case may be. In Enzo-E, since global timesteps are used to evolve the solution at every level of refinement simultaneously, the PE must be solved everywhere on the multiresolution mesh. This is done in several steps. First, the density field is restricted to the root grid from the leaf nodes of the array-of-octree mesh. Second, the global PE is solved on the root grid using V-cycle geometric multigrid for the triply periodic domain. Third, the PE is solved on the multilevel mesh for each refined octree of the array using the BiCGStab algorithm, interpolating the global potential obtained in step 1 onto the boundary faces of the octree mesh. Fourth, a Jacobi smoothing step is applied to the global, multilevel potential. In both Enzo and Enzo-E, the density field is advanced a half timestep to properly time center the gravitational acceleration relative to the hydro solver. In both Enzo and Enzo-E, collisionless N-body dynamics is solved using the Particle-Mesh method with cloud-in-cell (CiC) spatial interpolation and leapfrog time integration. For both codes, ghost zones are included around grid boundaries to reduce artifacts in the

computed gravitational potential at the interfaces between grids.

Two sets of three cosmological simulations were run in order to compare the results and performance of `Enzo-E` with `Enzo` using simulations with identical parameters. First is an AMR simulation with a box size of 12 Mpc/h, a root grid of 64^3 cells, and a maximum refinement level of 4. Refinement is triggered in a block when a cell satisfies $M > \delta_{\text{thresh}}(\Delta x_{\text{root}})^3$, where $\delta_{\text{thresh}} = 8$ is the chosen overdensity threshold, including both the dark matter and baryon components. Hydrodynamic fields are evolved using a piecewise parabolic method (Bryan et al., 1995; Colella & Woodward, 1984). Additional density fields corresponding to six chemical species (HI, HII, HeI, HeII, HeIII, and e^-) are advected, and chemistry and cooling is performed using `Grackle` (Smith et al., 2017). A global UV background is implemented using photoionization and cooling rates from Puchwein et al. (2019).

Figure 3.2 shows density projections and phase diagrams at $z \sim 6$ for each run. The density projections have the AMR mesh overlaid, demonstrating the difference between the two approaches. Note each square or rectangle corresponds to the boundary of a mesh block, not a single cell. `Enzo`'s structured AMR creates high-resolution patches in regions of interest that vary in size and dimension. This can be seen in the top right panel of Figure 3.2. The `Enzo-E` mesh is notably much more regular in its structure (top left of Fig. 3.2). `Enzo-E`'s AMR approach also results in more refined volume overall. By $z \sim 6$, the `Enzo-E` simulation contains about 20 times more computational cells than the `Enzo` simulation. As a result, the phase diagram in the `Enzo-E` simulation is better sampled than the `Enzo` simulation, particularly in low-to-average-density regions. This comparison presents an important distinction: `Enzo-E` generates more data and can be more memory-intensive to use than `Enzo`, but it provides better resolution in regions at moderately high densities. Although `Enzo-E` generates more grid data, its parallel scaling in terms of memory is better than `Enzo`. This is because `Enzo`'s patchy grid structure requires dynamic reading and writing of AMR metadata for each grid patch (block center, dimensions, etc.). For sufficiently large problems, then, `Enzo-E` is actually less memory-intensive to use than `Enzo`. This, coupled with `Enzo-E`'s nearly ideal scaling makes `Enzo-E` ideal for large-box simulations that wish to resolve the physics of gas flowing into and out of dark matter halos (e.g. gaseous filaments, the CGM, etc.).

To assess the impact, if any, the differences in AMR approaches and linear Poisson solvers have on structure formation, a dark-matter-only simulation was run using each of the codes. This simulation has a 256^3 root grid, 4 levels of AMR, and a box size of 25 Mpc/h. Dark matter halos are identified using

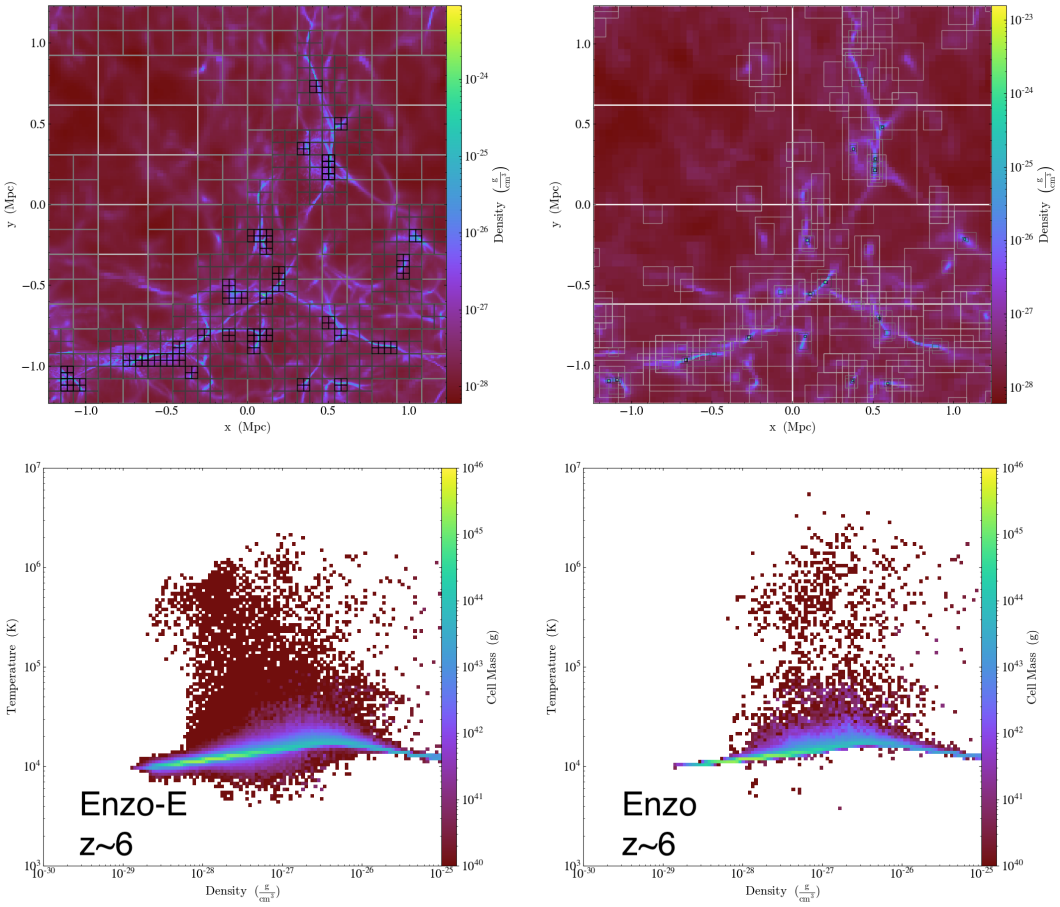

Figure 3.2. Comparison between `Enzo-E` (*left*) and `Enzo` (*right*) for a small cosmological simulation that includes a global UV background, showing density projections (*top*) and phase diagrams (*bottom*). The density projections have the grid overlaid to demonstrate the difference in AMR structure between the two codes. The `Enzo-E` simulation shows much more refinement overall, leading to better sampling of the density distribution, as shown by the phase diagrams.

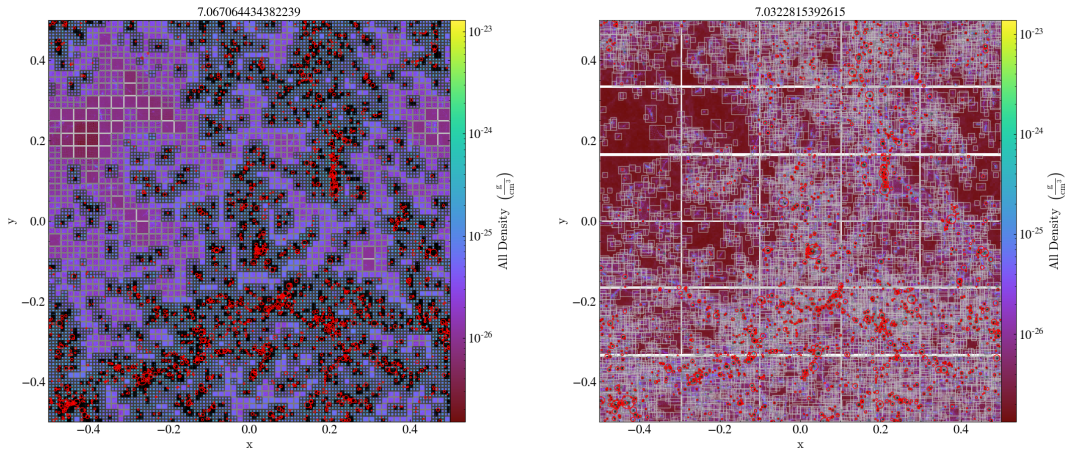

Figure 3.3. Dark matter density projections for identical 256^3 dark-matter-only simulations run with `Enzo-E` (*left*) and `Enzo` (*right*). For each projection, the computational blocks are overlaid to demonstrate the difference in AMR structure. Halos are annotated as red circles, with radius equal to the virial radius.

HOP (Eisenstein & Hut, 1998). Mesh projections at $z \sim 7$ are shown in Figure 3.3, with halos shown as red circles. The left panel of Figure 3.4 shows a dark matter power spectrum for the `Enzo-E` and `Enzo` versions of the simulation. The two curves show very good agreement, with some slight differences at large k (small scales). The differences at small scale can be seen more clearly in the right panel of Figure 3.4, which shows halo mass functions. The halo mass functions show that `Enzo-E` tends to generate more low-mass halos. This makes sense because the improved resolution in low-density regions due to `Enzo-E/Cello`'s AMR allows for a more accurate solution to the Poisson equation.

A unigrid simulation was also run to check that `Enzo-E` and `Enzo` agree under circumstances where the computational mesh is identical between the two codes. This simulation uses all the same physics methods and models used in the previous AMR simulation, but has a 128^3 root grid and a box size of 25 Mpc/h. Figure 3.5 shows the results of this unigrid simulation. The top left panel shows the median temperature of the box versus redshift. The temperature grows with time due to photoheating from the global UV background, with two features at $z \sim 7$ and $z \sim 3$ that coincide with the complete reionization of hydrogen ($z \sim 7$) and helium ($z \sim 3$) in the IGM. The decrease in temperature after reionization is primarily a result of cooling due to cosmological expansion. The top right panel shows this by plotting ionized fraction of hydrogen and helium versus redshift. The top left and right panels both show very good agreement between the `Enzo-E` and `Enzo` runs. The bottom left and right panels show phase diagrams of the `Enzo-E` (left) and `Enzo` (right) runs at $z \sim 2$, which are nearly identical.

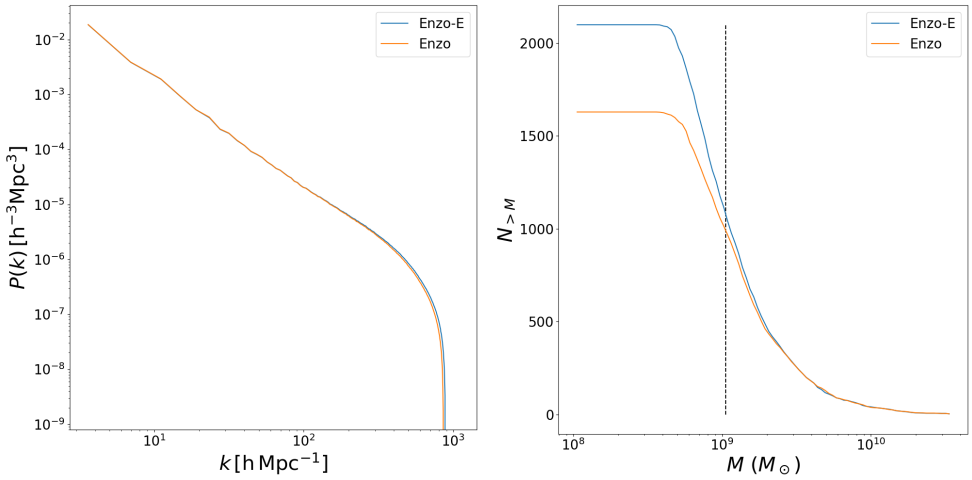

Figure 3.4. *Left:* dark matter density power spectrum comparing `Enzo-E` and `Enzo` in the 256^3 dark-matter-only simulations at $z \sim 7$. *Right:* Halo mass function for the same simulations at $z \sim 7$. The ordinate axis shows the number of halos with virial mass greater than the value denoted by the abscissa. The vertical dashed line denotes a mass that is equal to $100 M_\mathrm{p}$, where M_p is the dark matter particle mass. The difference in AMR approaches between the two codes shows some differences at small scales.

3.1 StarNet Surrogate Model for Primordial Star Formation and Feedback

`StarNet` is a surrogate model for Population III star formation and feedback that allows us to accurately simulate inhomogeneous primordial chemical enrichment on cosmological scales without a need for the strict spatial resolution required to model individual sites of star formation. `StarNet` is comprised of two parts:

1. `StarFind` (Wells & Norman, 2021) makes use of deep convolutional neural networks to identify Population III star-forming regions within a given volume. `StarFind` takes a two-stage approach. First, field data for a region is passed through a classifier network to determine if star formation will occur anywhere in the volume. If the stage 1 classifier determines that star formation will, in fact, occur, the region is passed through a 3D image segmentation network to determine specifically where in the volume the stars will form. Figure 3.7 shows three examplary `StarFind` predictions, with cells that are flagged as being part of the star-forming region shown as green squares. `StarFind` typically flags $3^3 - 5^3$ cells, depending on the size of the region.

2. `FBNet` uses linear regression models from Wells & Norman (2022) to predict the number of

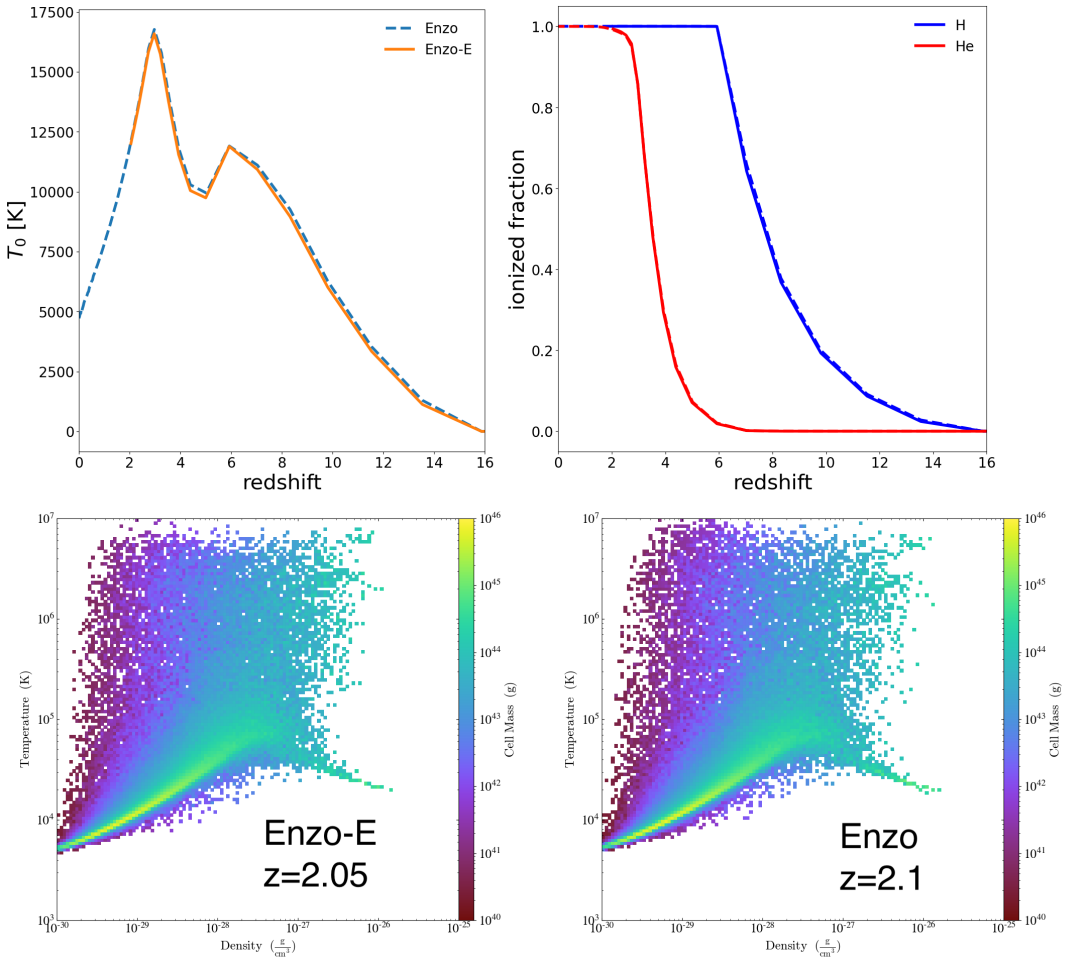

Figure 3.5. Unigrid comparison between `Enzo-E` and `Enzo` for a small cosmological simulation. *Top left:* average temperature at mean density vs. redshift. T_0 is calculated as the median temperature of the subset of cells with density within 1 percent of the mean. *Top right:* ionized fraction within the box for hydrogen and helium vs. redshift. Solid lines correspond to the `Enzo-E` simulation while the dashed line corresponds to the `Enzo` simulation. *Bottom left:* phase diagram at $z \sim 2$ for the `Enzo-E` simulation. *Bottom right:* phase diagram at $z \sim 2$ for the `Enzo` simulation.

Population III stars in a given region, metal yields, and the radius of the composite supernova remnant in its final evolved state. Population statistics are random—the number of stars and their masses (and thus, their metal yields), are pulled from distribution functions that are generated from the `Phoenix` simulations (Wells & Norman, 2022).

`StarNet` is designed to be called in a running simulation once every ~ 5 Myr. During a timestep where `StarNet` is called, the simulation domain is first be partitioned into ~ 10 kpc subvolumes with dimension 64^3. To reduce the number of regions to be processed, only regions containing a cell with overdensity > 3 are considered. If a ~ 10 kpc region of interest does not have dimension 64^3, as is often the case in an AMR simulation, the relevant field data is interpolated or coarsened as needed. The following five fields are then accessed and rescaled such that the average value is zero, and are passed into `StarNet`: `density`, `H2_density`, `metallicity`, `velocity_divergence`, and `total_energy`. A simplified flow-chart of a single `StarNet` iteration applied to a ~ 10 kpc region is shown in Figure 3.6. `StarNet` accesses the five fields described previously, and scans the domain for Pop III star-forming regions. If any cell within a predicted region has gas metallicity above $Z_{\rm crit} = 10^{-5.5}\ Z_\odot$, the prediction is thrown out. Once star-forming regions are identified, population statistics, metal yields, and the final radii of the evolved remnants are calculated. Metal yields are then deposited onto the mesh in uniform spheres of the predicted radii. The deposited metals are advected as the simulation progresses. The gas temperature of cells contained within the spherical region is set to $\texttt{max}(T_{\rm cell}, 10^4\ {\rm K})$. Optionally, all H_2 within the sphere is photodissociated, all HI is ionized, and all HeI is singly ionized. Photodissociations and ionizations are performed while conserving proton and electron counts.

Figure 3.7 shows example positive `StarFind` predictions acting on subvolumes of a cosmological simulation. The green squares show predicted star-forming regions. The predicted regions follow the density peaks of the gas distribution, and notably trace the shape of the dense gas. Figure 3.8 shows full-box projections of density and metallicity for a 256^3 cosmological simulation at $z \sim 11$. The only source of chemical enrichment in this simulation is the Pop III feedback predicted by `StarNet`. A number of metal bubbles can be observed in Figure 3.8 that coincide with the locations of dark matter halos. For more strenuous tests of `StarNet`'s predictions, see Chapter 4, which presents a detailed analysis of a set of production simulations similar to the one shown in Figure 3.8, within the context of high redshift ($z \gtrsim 10$) galaxy formation.

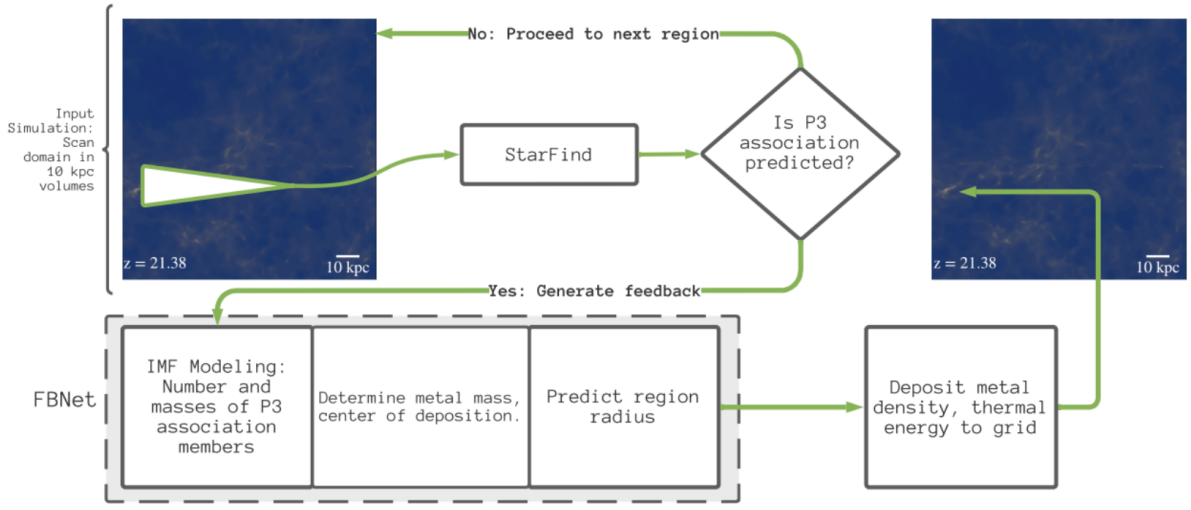

Figure 3.6. Flowchart of a single `StarNet` iteration. In a running simulation, this process is executed once every 5 Myr for every region of interest. This diagram is taken from Figure 11 of Wells & Norman (2022).

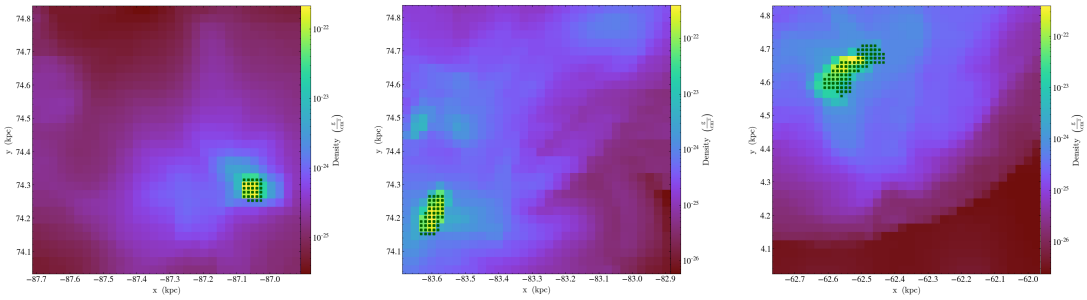

Figure 3.7. Examples of predicted star-forming regions using `StarFind`. Predictions are made at a resolution corresponding to one AMR level higher than the native maximum resolution. The green squares denote cells in the interpolated dataset that are identified as being part of the star-forming region.

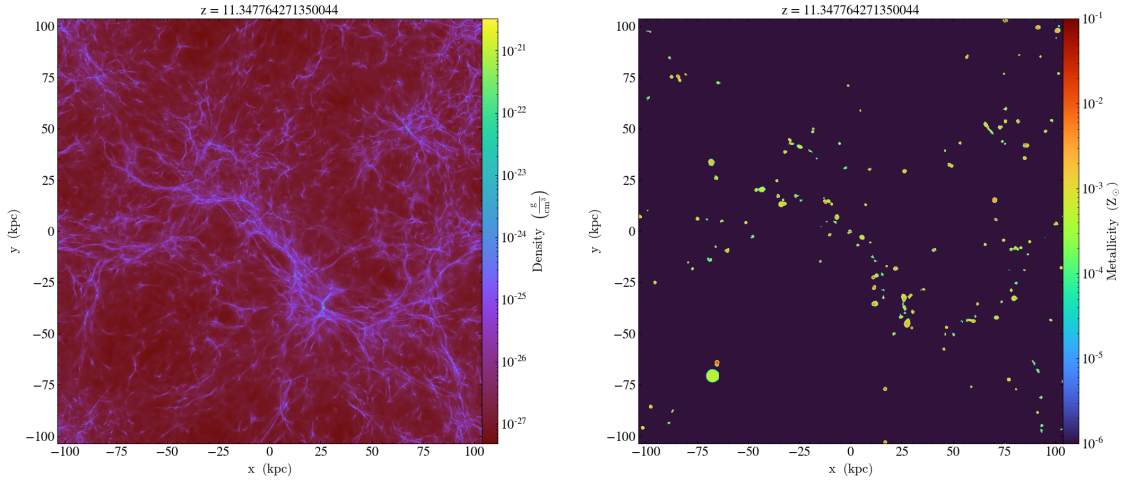

Figure 3.8. *Left:* Density projection of 256^3 cosmological simulation at $z = 11.3$. *Right:* Metallicity projection at the same redshift. The sources of metals are predictions of Pop III star formation and feedback made by `StarNet`.

3.1.1 Implementation in Enzo-E

`StarNet` was developed in `Enzo` using `Enzo`'s inline Python capabilities, where the `PyTorch` library was used to train and reference the networks. At the time of writing, `Enzo`'s inline python is deprecated, and is only compatible with Python version up to 2.7. On top of this, dynamic load balancing is inaccessible to `Enzo` simulations using inline Python. In cosmological simulations using AMR, where the computational mesh becomes highly imbalanced due to gravitational collapse, dynamic load balancing is essential. The implementation of `StarNet` in `Enzo-E` remedies both of these issues.

`StarNet` is implemented in `Enzo-E` as a part of the `EnzoMethodInference` class. `EnzoMethodInference` selects regions of interest according to very basic criteria (e.g. regions with overdensity above a given threshold) and accumulates block data around that region to construct an array of "inference blocks". For our purposes, the inference blocks are tuned to be ~ 10 proper kpc in width with a 64^3 computational cells. Inference blocks reference the pre-trained `StarNet` models on the using `LibTorch`, the `C++` frontend of `PyTorch`. It should be noted that `Enzo-E`'s Morton-curve-based load balancing method does not currently operate on the array of inference blocks; however, the inference array is expected to be sparse in cosmological contexts due to the relative scarcity of high-density regions. With the added fact that `StarNet` is called once every ~ 5 Myr, the contribution of calling `EnzoMethodInference` in a cosmological simulation to the total walltime is negligible.

Once StarFind identifies a star-forming region and the population statistics and remnant radii are calculated, a particle of type popIII_remnant is spawned at the center-of-mass of the star-forming region. The popIII_remnant particle stores information about the stellar population and final remnant in the following particle attributes: stellar_mass, num_SNe, num_HNe, num_PISNe, num_BH, yield_SNe, yield_HNe, yield_PISNe, and r. The stellar_mass attribute stores the total mass of Pop III stars that belong to the association. The num_<SNe/HNe/PISNe/BH> attributes store the number of stars in the population that reach their endpoint as a Type II core-collapse supernova (SNe), a hypernova (HNe), a pair-instability supernova (PISNe), or collapse into a black hole (BH). The yield_<SNe/HNe/PISNe> attributes store the metal ejecta mass from supernovae of each type, and the r attribute stores the final radius of the evolved remnant. The deposition of metal yields onto the mesh is handled by the EnzoMethodFBNetDeposit method, which accesses all of the popIII_remnant particles stored on a block, and deposits uniform metal spheres of the predicted size and mass at the center-of-mass of the star-forming regions.

Some complexity in the implementation is introduced by the fact that the volume taken up by the evolved remnants at deposition can, in general, span multiple blocks. This is a problem because a given block cannot directly access data stored on any other block, and the extent of the spheres makes transmitting the data via ghost zones infeasible. To counter this, a global list tracking all popIIIremnant particles that are formed in a cycle is assembled. A single copy of this list is stored on each PE. This is generally a fairly small list in cosmological simulations, as pristine regions undergoing gravitational collapse are sparse. Because of this, slowdowns in parallel in large simulations due to replication of data are not a concern.

3.2 STARSS Algorithm for Metal-Enriched Star Formation and Feedback

The **S**cale-**I**ntelligent **T**erminal-**M**omentum **A**lgorithm for **R**ealistic **S**tellar **S**ources (STARSS) was developed to reduce the resolution requirements needed to accurately model the formation and evolution of the first galaxies in AMR simulations. This model is based on the star formation and feedback routines in FIRE-2 (Hopkins et al., 2018b) and FIRE-3 (Hopkins et al., 2022), and is outlined in detail in Wells & Norman (2022). STARSS was originally developed for use in Enzo. It has been ported to

Enzo-E, making STARSS the first fully functional star formation and feedback routine implemented in the new code.

3.2.1 Star Formation

In the STARSS model, star particles represent coeval star clusters with masses $\sim 1000\,M_{\odot}$. A variety of criteria can be selected to pick out potential star-forming regions on the computational mesh:

1. **Velocity divergence:** $\nabla \cdot \mathbf{v}_{\rm b} < 0$.
2. **Virial parameter:** $\alpha < 1$, where $\alpha \equiv \frac{\text{gravitational potential}}{\text{specific energy}}$.
3. **Jeans mass:** $M_{\rm b} > M_{\rm Jeans}$, where $M_{\rm J} \equiv \frac{\pi}{6} \frac{c_{\rm s}^3}{G^{\frac{3}{2}} \rho^{\frac{1}{2}}}$.
4. **Cooling time:** $t_{\rm cool} < t_{\rm ff}$, where $t_{\rm ff} \equiv \sqrt{\frac{3\pi}{32G\rho}}$.
5. **Density threshold:** $\rho > \rho_{\rm thresh}$. One can choose between baryon number density or baryon overdensity (defined as $\rho_{\rm b}/\overline{\rho}_{\rm b}$).
6. **Temperature threshold:** $T < T_{\rm thresh}$.
7. **Metallicity threshold:** $Z > Z_{\rm thresh}$.

The recommended combination of criteria are options 1, 2, 3, and 4. A cell that satisfies the chosen criteria is flagged as a potential star-forming site. The probability that a fraction of the gas contained in the cell will be converted into star particles is given by

$$P_{\rm SF} = 1 - \exp\left[-f_s \frac{dt}{t_{\rm ff}}\right], \tag{3.1}$$

where $t_{\rm ff} \equiv \sqrt{\frac{3\pi}{32G\rho_{\rm b}}}$ is the local free-fall time and f_s is the H_2 self-shielded fraction calculated using fits from Krumholz & Gnedin (2011). If it is ultimately determined that a star particle will form in a given timestep, the newly formed particle is assigned the metallicity of the host cell and a mass

$$M_* = \eta_{\rm SF} M_{\rm b}, \tag{3.2}$$

where $\eta_{\rm SF}$ is a user-defined conversion fraction that is typically set to 0.05. The initial position is taken to be the center of the host cell, and the velocity is the center-of-mass velocity of the gas contained within

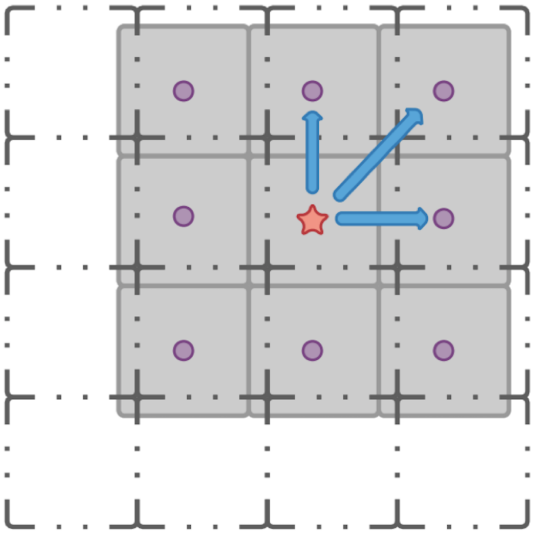

Figure 3.9. 2D diagram demonstrating the position of coupling particles (purple circles), relative to the position of the star particle (orange star) for a given feedback event. The dash-dotted grid outlines the computational mesh, while the solid grey grid shows the CiC deposition region. This diagram is taken from Figure 2 of Wells & Norman (2022).

a sphere of radius 3 cell-widths centered on the host cell. It should be noted that the inclusion of the constant conversion fraction, $\eta_{\rm SF}$, is a source resolution dependence that users must be wary of when setting up a parameter file.

3.2.2 Stellar Feedback

STARSS feedback considers Type II and Type Ia supernovae, stellar winds, and radiation. Recall that star particle in the STARSS model represent coeval star clusters with $M_* \sim 1000\,M_\odot$. The number of supernova events that a given particle is expected to experience in timestep Δt is determined for each Pop II star particle using rates from Hopkins et al. (2018b). To determine the number of SNe of each type, the values $P_{\rm II}$ and $P_{\rm Ia}$ are defined as

$$P_{\rm II} = R_{\rm II}(M_*\Delta t) \tag{3.3}$$

$$P_{\rm Ia} = R_{\rm Ia}(M_*\Delta t), \tag{3.4}$$

where $R_{\rm II}$ and $R_{\rm Ia}$ are the piecewise age-dependent rates presented in Appendix A of Hopkins et al. (2018b) for Type II and Type Ia supernovae, respectively, and M_* is the mass of the Pop II star particle. $P_{\rm II}$ and $P_{\rm Ia}$

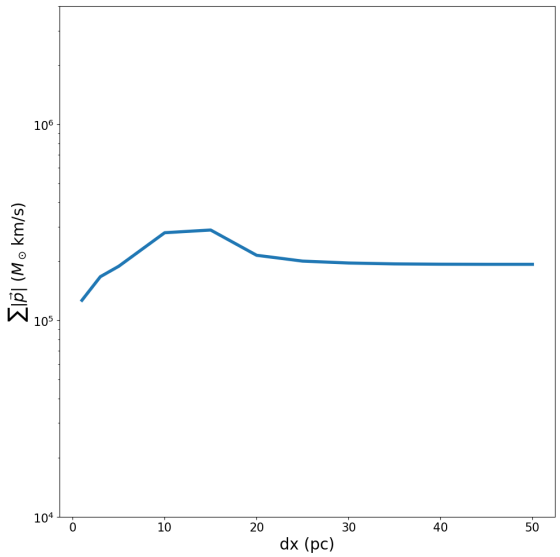

Figure 3.10. Terminal momentum versus cell width for the STARSS ideal resolution test. A perfect result would be a straight line at $p_{\rm term} = 2 \times 10^5\, M_\odot\, {\rm km\,s^{-1}}$.

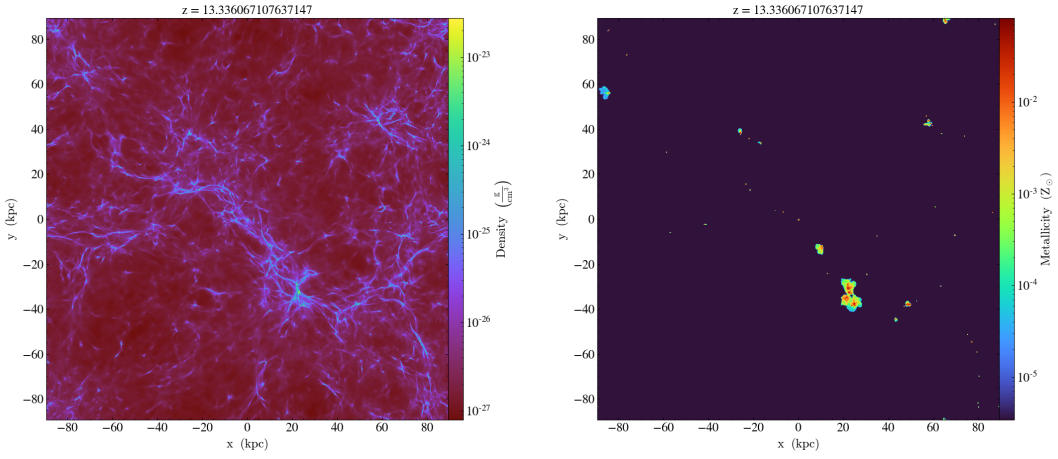

Figure 3.11. *Left:* Density projection of the 256^3 cosmology test with STARSS star formation and feedback at $z \sim 13.4$. *Right:* Metallicity projection at the same redshift, where the sources of metal enrichment are Pop II supernovae and stellar winds.

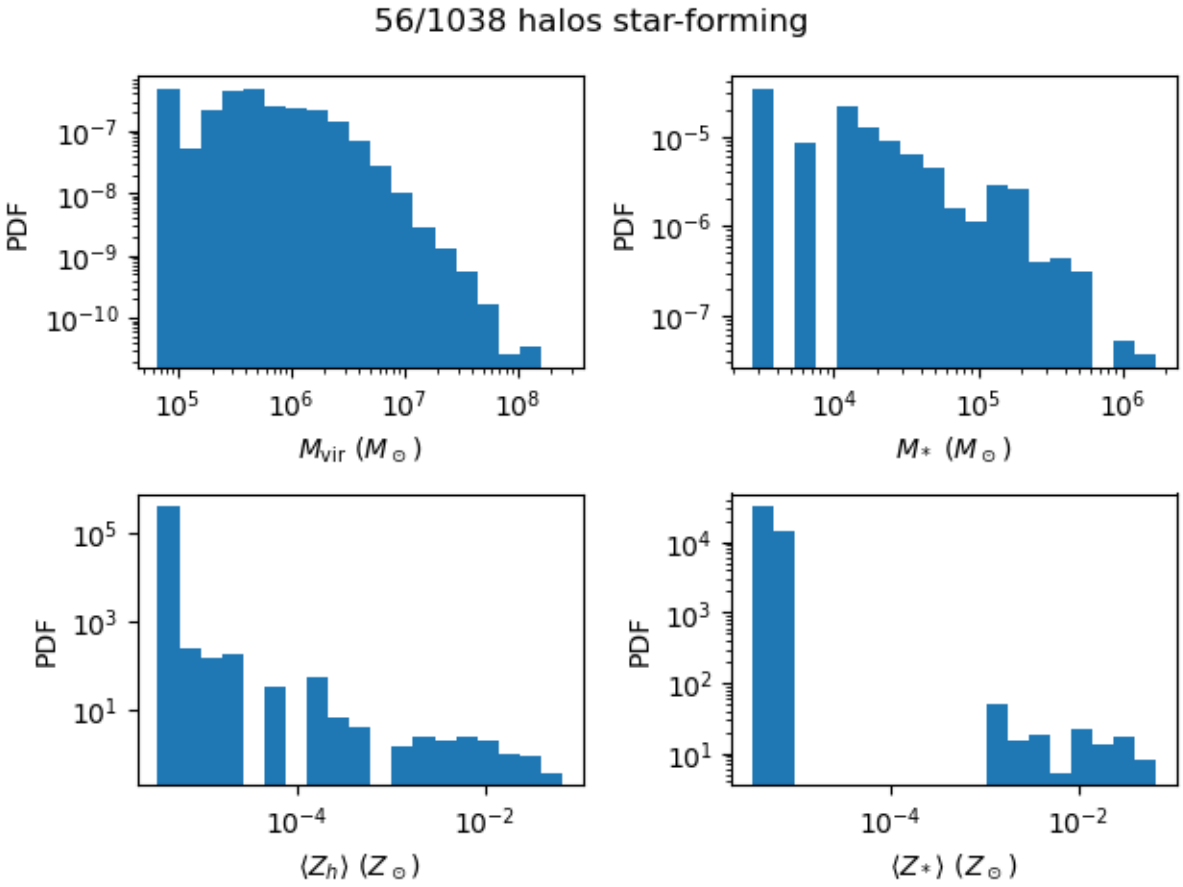

Figure 3.12. Halo statistics for the 256^3 cosmology test with STARSS star formation and feedback at $z \sim 13.4$. *Top left:* Halo mass function. *Top right:* Stellar mass distribution, where masses are taken to be the summed mass of star particles within the virial radius of a given halo. *Bottom left:* Halo-averaged metallicity distribution. For this, the halo's metallicity is taken to be the mass-weighted average metallicity of all cells within the virial radius. Halos that have not been affected by STARSS feedback have an average metallicity equal to the metallicity floor, $Z_{\rm floor} = 10^{-5.5} Z_\odot$. *Bottom right:* Halo-averaged stellar metallicity distribution, where average stellar metallicities are calculated as the arithmetic mean over all star particles within the virial radius. Halos with zero star particles are not included in this distribution. Star particles that form in un-enriched gas are assigned a metallicity equal to the metallicity floor.

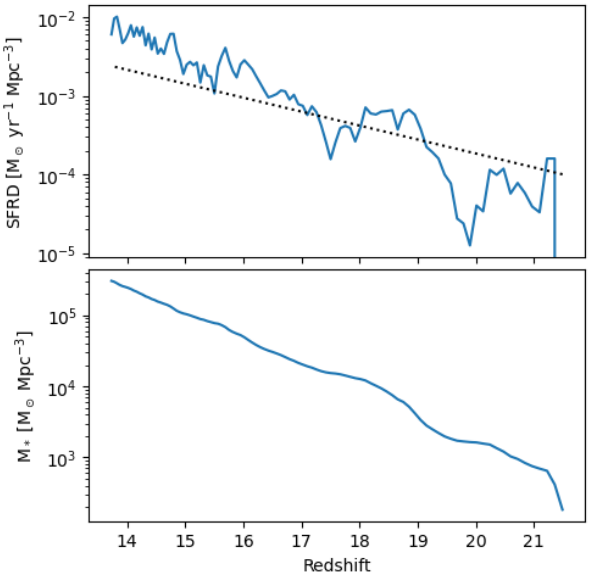

Figure 3.13. *Top:* Star formation rate density vs. redshift for the 256^3 cosmology test. The dashed line shows a fit from the *Phoenix Simulations* (Wells & Norman, 2022), which use an entirely different star formation and feedback prescription that is described in Wise et al. (2012b). *Bottom:* Stellar mass density vs. redshift.

are dimensionless non-integer values that are allowed to be > 1. The number of SNe, $N_{\rm II}$ and $N_{\rm Ia}$, are then computed:

$$N_{\rm II} = \texttt{floor}[P_{\rm II}] + f\left(P_{\rm II} - \texttt{floor}[P_{\rm II}]\right) \tag{3.5}$$

$$N_{\rm Ia} = \texttt{floor}[P_{\rm II}] + f(P_{\rm Ia} - \texttt{floor}[P_{\rm Ia}]). \tag{3.6}$$

The function $f(x)$ is defined as

$$f(x) = \begin{cases} 0 & x < \texttt{rand} \\ 1 & x \geq \texttt{rand}, \end{cases} \tag{3.7}$$

where `rand` is a random number between 0 and 1.

Each supernova produces 10^{51} erg of energy, and a fixed ejecta mass of either 10.5 $M_\odot$ for Type II, or 1.5 $M_\odot$ for Type Ia. Metal yields for Type II SNe depend on the metallicity of the star particle:

$$M_{\rm Z} = 1.91 + 0.0479\,\texttt{max}(Z_*,\ 1.65), \tag{3.8}$$

where Z_* is the metallicity of the star particle in solar units. Each Type Ia supernova produces 1.4 $M_\odot$ of metals.

Stellar winds are deposited every cycle, with mass and energy computed as

$$M_{\rm wind} = M_*(f_{\rm wind}\Delta t) \tag{3.9}$$

$$E_{\rm wind} = M_{\rm wind}(10^{12}\psi_{\rm wind}), \tag{3.10}$$

where $f_{\rm wind}$ and $\psi_{\rm wind}$ are piecewise age-dependent rates defined in Appendix A of Hopkins et al. (2018b). Wind energies are deposited as nonthermal kinetic energy.

Once supernova energies and ejecta masses are determined, values are deposited onto the mesh in sequence for each supernova occuring in each star particle. To do this, the relative fractions of thermal and nonthermal energies are first computed by determining which phase of evolution the expanding supernova remnant is in when it reaches a radius Δx, where Δx is taken to be a cell width at the AMR level at which the star particle resides. To determine the phase, the following radii are computed:

$$R_{\rm free} = 2.75\left(\frac{M_{\rm ej}}{3\,M_\odot}\right)^{1/3} n_{\rm b}^{-1/3}\ {\rm pc} \tag{3.11}$$

$$R_{\rm cool} = 28.4\left(\frac{E}{10^{51}\ {\rm erg}}\right)^{2/7} n_{\rm b}^{-3/7} f(Z_*)\ {\rm pc} \tag{3.12}$$

$$R_{\rm fade} = 66.0\left(\frac{E}{10^{51}\ {\rm erg}}\right)^{0.32} n_{\rm b}^{-0.37}\left(\frac{c_{\rm s}}{10\,{\rm km\,s^{-1}}}\right)^{-0.4}\ {\rm pc} \tag{3.13}$$

(Draine, 2011). The cell width, Δx, is then compared to these radii to determine the supernova phase. Specifically, the cases considered are:

1. $\Delta x < R_{\rm free}$ — Free expansion
2. $R_{\rm free} \leq \Delta x < R_{\rm cool}$ — Sedov-Taylor
3. $R_{\rm cool} \leq \Delta x < R_{\rm fade}$ — Terminal
4. $R_{\rm fade} \leq \Delta x$ — Fading (remnant has merged with the ISM).

As the supernova remnant evolves, energy in the medium will be smoothly transitioned between

the thermal and non-thermal components. The relative fraction of each component of energy depends on the phase of the evolving remnant at the time of deposition. The non-thermal kinetic energy of the gas is modified by updating the momentum of the gas in a manner consistent with the determined supernova phase according to analytic expressions for shell momenta. For the Sedov-Taylor phase (Kim & Ostriker, 2015):

$$P_{\rm ST} = 2.21 \times 10^4 \left(\frac{E}{10^{51}\ {\rm erg}}\right)^{4/5} n_0^{1/5} t_3^{3/5}, \tag{3.14}$$

where n_0 is the number density of the medium prior to the supernova event in cgs units, and

$$t_3 = \left(\frac{\Delta x}{5\ {\rm pc}\ \left(\frac{E}{10^{51}\ {\rm erg}}\right)^{1/5}}\right)^{5/2}. \tag{3.15}$$

For the terminal phase (Thornton et al., 1998):

$$P_{\rm term} = \sqrt{2 M_{\rm R} E_{\rm R}} = \begin{cases} 8.57 \times 10^5 \left(\frac{E}{10^{51}\ {\rm erg}}\right)^{13/14} n_0^{-0.12} & Z_* \leq 0.01\ Z_\odot \\ 2.73 \times 10^5 \left(\frac{E}{10^{51}\ {\rm erg}}\right)^{13/14} n_0^{-0.12} Z_*^{-0.14} & Z_* > 0.01\ Z_\odot. \end{cases} \tag{3.16}$$

$M_{\rm R}$ and $E_{\rm R}$ are defined in Equations 15, 21, 26, and 32 in Thornton et al. (1998) for the low and high metallicity cases. The momentum to couple to the mesh is then determined:

$$P_{\rm cpl} = \begin{cases} \texttt{min}\left(P_{\rm ST},\ \frac{\Delta x}{R_{\rm cool}} P_{\rm term}\right) \frac{\Delta x}{R_{\rm free}} & \text{Free expansion} \\ \texttt{min}\left(P_{\rm ST},\ \frac{\Delta x}{R_{\rm cool}} P_{\rm term}\right) & {\rm Sedov-Taylor} \\ \tanh\left(\frac{\Delta x}{R_{\rm cool}}\right) P_{\rm term} & \text{Terminal} \\ \tanh\left(\frac{\Delta x}{R_{\rm cool}}\right) P_{\rm term} \left(1 - \tanh\left(\left(\frac{5}{4}\frac{\Delta x}{R_{\rm fade}}\right)^2\right)\right) & \text{Fading.} \end{cases} \tag{3.17}$$

The expressions for coupling momenta are chosen to ensure a smooth transition between the different supernova phases. As an example, for the case of $\Delta x = R_{\rm cool}$, $\texttt{min}\left(P_{\rm ST},\ \frac{\Delta x}{R_{\rm cool}} P_{\rm term}\right) = \tanh\left(\frac{\Delta x}{R_{\rm cool}}\right) P_{\rm term} = P_{\rm term}$. In the limit of $\Delta x \to 0$ (i.e. infinite resolution), $P_{\rm cpl} \to 0$, in which case the energy would be deposited as completely thermal over a small volume. This leads to a large temperature gradient, which drives the initial expansion. In the opposite limit of $\Delta x \to \infty$, $P_{\rm cpl} \to 0$ as well. The poor resolution case also

results in mainly thermal energy being deposited, but distributed over a large volume. The temperature gradient after energy deposition in this case is small, and the remnant is assumed to have fully merged with the surrounding medium. The intermediate resolution cases lead to varying fractions of thermal and non-thermal energy. Finally, the momentum associated with stellar winds, $P_{\rm wind} = \sqrt{2 M_{\rm wind} E_{\rm wind}}$, is added to $P_{\rm cpl}$ to obtain the total momentum to deposit.

Now that all values to deposit onto the mash have been computed, it is time to do the actual deposition. For this, the computed baryon mass, metal mass, momentum, and thermal energy is distributed over 26 "coupling particles", which are placed in a cube with a side length of 3 cell widths centered on the star particle. The values associated with each coupling particle are then Cloud-in-Cell (CiC) deposited using the cell width Δx as the cloud radius. Figure 3.9 shows a projected 2D diagram which illustrates this process. A negative CiC "deposition" is performed to subtract the baryon mass that is swept up into the expanding shell, $M_{\rm swept}$, from the central cell width centered on the star particle. This mass is then redistributed outwards among the coupling particles to simulate the formation of a dense shell. The mass of swept up gas is computed as

$$M_{\rm swept} = \begin{cases} 0 & \text{Free expansion} \\ \frac{4}{3}\pi(\Delta x)^3 \rho & \text{Sedov} - \text{Taylor} \\ 4.89 \times 10^4 \left(\frac{\left(\frac{E}{10^{51}\,\text{erg}}\right)^{6/7}}{n_{\rm b}^{0.24}} \right) & \text{Terminal; } Z \leq 0.01 \\ 1.41 \times 10^4 \left(\frac{\left(\frac{E}{10^{51}\,\text{erg}}\right)^{6/7} Z_*^{0.27}}{n_{\rm b}^{0.24}} \right) & \text{Terminal; } Z > 0.01. \end{cases} \tag{3.18}$$

The expressions for the terminal case are taken from Thornton et al. (1998). The total mass that is deposited after this step is then $M_{\rm shell} = M_{\rm ej} + M_{\rm swept} + M_{\rm wind}$.

The final type of feedback considered by STARSS is radiative feedback from Pop II stars. The STARSS method does not directly deposit radiation onto the mesh, but simply calculates stellar luminosities following the method prescribed in Hopkins et al. (2018b). Specifically, the ionizing

luminosity for a Pop II star particle in units of $L_\odot/M_\odot$ is given by

$$\Psi_{\text{ion}} = \begin{cases} 500 & \text{age} < 3.5 \text{ Myr} \\ 60\left(\frac{\text{age}}{3.5\text{ Myr}}\right)^{-3.6} + 470\left(\frac{\text{age}}{3.5\text{ Myr}}\right)^{\gamma} & 3.5 \text{ Myr} \leq \text{age} < 25 \text{ Myr} \\ 0 & \text{age} \geq 25 \text{ Myr}, \end{cases} \tag{3.19}$$

where

$$\gamma = 0.045 - 1.82 \log(\text{age}), \tag{3.20}$$

and "age" refers to the age of the star particle in Myr. The actual deposition and transport of ionizing radiation is handled by `Enzo-E`'s M1 closure radiative transfer solver (see Section 3.3).

3.2.3 Implementation in Enzo-E

Star formation and feedback are implemented as two separate methods: `EnzoMethodStarMakerSTARSS` (star formation) and `EnzoMethodFeedbackSTARSS` (feedback). The former method inherits attributes from a parent `EnzoMethodStarMaker` class, while the latter is its own standalone method class. A star particle that is formed by `EnzoMethodStarMakerSTARSS` has the following unique attributes: `mass`, `creation_time`, `creation_level`, `lifetime`, `metal_fraction`, `number_of_sn`, and `luminosity`. The `number_of_sn` and `luminosity` attributes are updated in `EnzoMethodFeedbackSTARSS`. To handle the case of feedback depositions occurring at block boundaries, ghost zone refresh with an `accumulate` step is performed in `EnzoMethodFeedbackSTARSS` to add updated values to densities, energies, and momenta in ghost zones to the corresponding active zones of neighboring blocks. Apart from metallicity, all chemical concentrations (x_{HI}, x_{HII}, etc.) are held constant before and after supernova remnant deposition.

3.2.4 Resolution Test

In order to test the sensitivity of the STARSS feedback algorithm to grid resolution, a series of ideal test simulations were run. The setup of the test is as follows:

- 64^3 grid cells, where the cell width is varied from 0.5 - 50 pc
- Background medium is initially static and uniform, with $n_{\text{b}} \approx 60\,\text{cm}^{-3}$ and $T = 500$ K

- Primordial chemical composition, where gas is initially made up of 76% HI and 24% HeI
- Gas metallicity of $10^{-1}\ Z_{\odot}$, where $Z_{\odot} = 0.012$
- A single supernova is manually set off in the center of the box, on the corner of a block
- we run with six-species gas chemistry (HI, HII, HeI, HeII, HeIII, e^{-}) using `Grackle`

With this setup, the approximate resolution ranges corresponding to each supernova phase determined by Equation 3.17 are:

- $\Delta x \lesssim 1$ pc — Free Expansion
- $1\text{ pc} \lesssim \Delta x \lesssim 6$ pc — Sedov-Taylor
- $6\text{ pc} \lesssim \Delta x$ — Terminal

Each simulation is run for 1 Myr, and the terminal momentum is taken to be the peak value for the total shell momentum during the simulation. Figure 3.10 shows the obtained terminal momentum for each test versus cell width. The analytical value for p_{term} computed using Equation 3.16 is approximately $2 \times 10^5\ M_{\odot}\,\text{km}\,\text{s}^{-1}$. A perfect result would look like a straight horizontal line at $p_{\text{term}} = 2 \times 10^5\ M_{\odot}\,\text{km}\,\text{s}^{-1}$, where each supernova evolves to the same terminal momentum, regardless of the resolution. There is some deviation from the analytical value for $\Delta x < 20$ pc, a feature that can be attributed to difficulties in determining where the actual boundaries for the supernova phases are. These errors are within a factor of 2. In a running cosmological simulation, where the expansion of supernova remnants is surely not ideal, the error seen here is small enough to not cause any noticeable issues. Additionally, the intended maximum resolution for the simulations in which this code will be used in the chapters that follow is between $20 - 30$ proper pc, which is in the regime where the STARSS feedback algorithm is very well behaved in this resolution test.

3.2.5 Cosmological Simulation with Star Formation and Feedback

In order to test that the behavior of the STARSS star formation and feedback model within a running cosmological simulation, a test simulation was run. This simulation has identical initial conditions to the test cosmological simulation that was run in Section 3.1. In this case, however, we set a uniform

metallicity floor of $Z_{\rm floor} = 10^{-5.5}\ Z_\odot$ as the initial metallicity field. This is also the chosen value for the critical metallicity for Population II star formation. Of the possible criteria listed in Section 3.2.1, we use (1) $\nabla \cdot \mathbf{v}_{\rm b}$, (2) $\alpha < 1$, and (3) $M_{\rm b} > M_{\rm Jeans}$. We additionally set $Z_{\rm crit} = 10^{-5.5}\ Z_\odot$; however, because this value is the same as the chosen floor value, this criterion will always pass.

Figure 3.11 shows full-box projections of density and metallicity at $z = 13.3$. By this point, a number of isolated stellar populations have formed, the feedback effects from which can be seen in the metallicity projection. Comparing the two projections, it can be seen that the feedback bubbles are oriented along the dense filaments that can be seen in the density projection. Some simple halo statistics are shown in Figure 3.12, where dark matter halos were identifed using `ROCKSTAR` (Behroozi et al., 2013). By the final redshift, there are 56 star-forming halos, with stellar masses ranging between $3 \times 10^3\ M_\odot$ and $2 \times 10^6\ M_\odot$. Global star formation rate density (SFRD) versus redshift is shown in Figure 3.13. Importantly, the curve shows good agreement with the *Phoenix Simulations* (Wells & Norman, 2022), which use an entirely different model for Population II star formation and feedback. With this, we can say that the STARSS method in `Enzo-E` produces reasonable results.

3.3 M1 Closure Multigroup Radiative Transfer in Enzo-E

The general equation of radiative transfer can be written:

$$\frac{1}{c}\frac{\partial I_\nu}{\partial t} + \hat{n} \cdot \nabla I_\nu = -\kappa_\nu I_\nu + \eta_\nu. \tag{3.21}$$

Here, I_ν is the local radiation specific intensity, c is the speed of light, $\hat{n}$ is a unit vector, κ_ν is an absorption coefficient, and η_ν is the emissivity. Equation 3.21 can be expressed as a set of coupled conservation equations by taking the zeroth and first angular moments of I_ν:

$$\frac{\partial N_\nu}{\partial t} + \nabla \cdot \mathbf{F}_\nu = -\sum_j^{\rm HI,HeII,HeII} n_j \sigma_{\nu j} c N_\nu + \dot{N}_\nu^* + \dot{N}_\nu^{\rm rec} \tag{3.22}$$

$$\frac{\partial \mathbf{F}_\nu}{\partial t} + c^2 \nabla \cdot \mathbb{P}_\nu = -\sum_j^{\rm HI,HeII,HeII} n_j \sigma_{\nu j} c \mathbf{F}_\nu. \tag{3.23}$$

N_ν, $\mathbf{F}_\nu$, and $\mathbb{P}_\nu$ are the specific photon number density, photon flux, and radiation pressure tensor, respectively, and $\dot{N}_\nu^*$ and $\dot{N}_\nu^{\rm rec}$ are source terms corresponding to radiative point sources and recombination

radiation. $\sigma_{\nu j}$ is the photoionization cross-section for gas of species j with radiation of frequency ν. n_j denotes the number density of the gas of species j. Only three chemical species are considered for the attenuation and recombination terms – HI, HeI, and HeII. The discretized versions of N_ν and $\mathbf{F}_\nu$ can be defined by integrating over the frequency range that defines group i:

$$N_i = \int_{\nu_{i0}}^{\nu_{i1}} N_\nu d\nu, \qquad \mathbf{F}_i = \int_{\nu_{i0}}^{\nu_{i1}} \mathbf{F}_\nu d\nu. \tag{3.24}$$

With this, Equations 3.22 and 3.23 can be rewritten:

$$\frac{\partial N_i}{\partial t} + \nabla \cdot \mathbf{F_i} = -\sum_j^{\text{HI,HeII,HeII}} n_j \sigma_{ij} c N_i + \dot{N}_i^* + \dot{N}_i^{\text{rec}} \tag{3.25}$$

$$\frac{\partial \mathbf{F}_i}{\partial t} + c^2 \nabla \cdot \mathbb{P}_i = -\sum_j^{\text{HI,HeII,HeII}} n_j \sigma_{ij} c \mathbf{F}_i. \tag{3.26}$$

3.3.1 Implementation in Enzo-E

`EnzoMethodM1Closure` is implemented following the prescription of Rosdahl et al. (2013). The radiation is binned by energy, and equations 3.22 and 3.23 are solved separately for each bin using an operator splitting approach. The solution of Equations 3.25 and 3.26 is broadly decomposed into the following ordered steps:

1. **Photon Injection:** For a source of radiation with bolometric luminosity L, the component of L radiating into group i is calculated as $L_i = f_i * L$, where f_i is the energy fraction of radiation in group i according to a user-defined SED. The update to the N_i field, ΔN_i^* is calculated by partially solving Equation 3.25, considering only the time derivative and point source terms:

   $$\frac{\partial N_i}{\partial t} = \dot{N}_i^*. \tag{3.27}$$

   With this, $\Delta N_i \approx \dot{N}_i^* \Delta t$, where Δt is the timestep. ΔN_i^* is then cloud-in-cell deposited into the N_i field using a cloud radius of one cell width, Δx.

2. **Transport in Vacuum:** The right-hand-sides of Equations 3.25 and 3.26 are set to zero and solved

to update N_i and F_i:

$$\frac{\partial N_i}{\partial t} + \nabla \cdot \mathbf{F_i} = 0 \tag{3.28}$$

$$\frac{\partial \mathbf{F}_i}{\partial t} + c^2 \nabla \cdot \mathbb{P}_i = 0. \tag{3.29}$$

This is equivalent to solving the radiative transfer equations in vacuum. Equations 3.28 and 3.29 are solved using conservative finite differences. If we define the vectors $\mathscr{U}^t_{ijk} = (N,\, \mathbf{F})^t_{ijk}$ and $\mathscr{F}^t_{ijk} = \left(\mathbf{F},\, c^2\mathbb{P}\right)^t_{ijk}$ at cell index (i,j,k) and time t, we can write the solution at time $t+\Delta t$ as

$$\mathscr{U}^{t+\Delta t}_{ijk} = \mathscr{U}^t_{ijk} + \frac{\Delta t}{\Delta x}\left(\mathscr{F}^t_{i-\frac{1}{2},j,k} - \mathscr{F}^t_{i+\frac{1}{2},j,k}\right) + \frac{\Delta t}{\Delta y}\left(\mathscr{F}^t_{i,j-\frac{1}{2},k} - \mathscr{F}^t_{i,j+\frac{1}{2},k}\right) + \frac{\Delta t}{\Delta z}\left(\mathscr{F}^t_{i,j,k-\frac{1}{2}} - \mathscr{F}^t_{i,j,k+\frac{1}{2}}\right). \tag{3.30}$$

The half-integer indices correspond to face-centered, as opposed to cell-centered, field values. Face-centered values are calculated using the Global Lax Friedrich (GLF) flux function:

$$\mathscr{F}^t_{l+\frac{1}{2}} = \frac{1}{2}\left[\mathscr{F}^t_l + \mathscr{F}^t_{l+1} - c\left(\mathscr{U}^t_{l+1} - \mathscr{U}^t_l\right)\right]. \tag{3.31}$$

The radiation pressure tensor is approximated as $\mathbb{P} \approx \mathbb{D}N$, where $\mathbb{D}$ is the Eddington tensor,

$$\mathbb{D} = \frac{1-\chi}{2}\mathbf{I} + \frac{3\chi - 1}{2}\mathbf{n}\otimes\mathbf{n}. \tag{3.32}$$

$\chi = \chi(N,\mathbf{F})$ is a dimensionless value bounded between $\frac{1}{3}$ and 1 that represents the degree of isotropy of the radiation.

3. **Attenuation and Recombination:** Interactions with matter are included by solving the relevant components of Equations 3.25 and 3.26 corresponding the attenuation and recombination radiation,

ignoring divergence terms:

$$\frac{\partial N_i}{\partial t} = -\sum_{j}^{\text{HI,HeII,HeII}} n_j \sigma_{ij} c N_i + \dot{N}_i^{\text{rec}} \tag{3.33}$$

$$\frac{\partial \mathbf{F}_i}{\partial t} = -\sum_{j}^{\text{HI,HeII,HeII}} n_j \sigma_{ij} c \mathbf{F}_i. \tag{3.34}$$

From here, photoionization and heating rates are calculated as

$$\Gamma_j = \sum_{i=1}^{M} \sigma_{ij} c N_i \qquad \text{and} \qquad \mathscr{H} = \sum_{j}^{\text{HI,HeI,HeII}} n_j \sum_{i=1}^{M} \sigma_{ij} c N_i \left(\overline{\varepsilon}_i - \varepsilon_j\right), \tag{3.35}$$

where Γ_j is the photoionization rate for chemical species j, and $\mathscr{H}$ is the photoheating rate. $\overline{\varepsilon}_i$ is the group-mean energy, which depends on the user-defined SED, and ε_j is the ionization energy for chemical species j. The photoionization and heating rates are passed as fields into `Grackle` (Smith et al., 2017), where the energy equation is solved and the photochemistry is performed. There are ghost zone refresh operations after steps (1) and (2). The refresh operation after step (1) includes an `accumulate` step to add updated photon densities in ghost zones to the corresponding active zones of neighboring blocks to handle cases where radiating point sources are located on a block boundaries.

3.3.2 Notes on Timestepping

Much of the challenge in running radiative hydrodynamics (RHD) simulations comes from the stringent timestepping requirements put forth by radiative transfer solvers. The Courant condition in three dimensions dictates that the RT timestep must follow

$$\Delta t_{\text{RT}} \leq \frac{\Delta x}{3c}. \tag{3.36}$$

This presents a problem. In the case of a cosmological RHD simulation, there are many physical processes that act on a timescale that is much larger than the RT timescale. Evolving a cosmological simulation following the RT timestep defined in Equation 3.36 means increasing the number of global timesteps to reach an equivalent redshift dramatically. To get around this problem, we do two things.

First, we allow for the option to solve the RT equations using a reduced speed of light (RSOL). The RSOL approximation was first described in Gnedin & Abel (2001), and is now common practice in

astrophysical RHD codes. The speed of light is reduced by a user-defined factor, $f_{\rm r}$, such that

$$c_{\rm r} \equiv f_{\rm r} c, \tag{3.37}$$

where $c_{\rm r}$ is the RSOL. In the RSOL approximation, c is replaced by $c_{\rm r}$ in all of the equations relevant to RT decribed above, thus relaxing the timestep constraint in Equation 3.36 by a factor of $f_{\rm r}$. The major consideration for this approximation is choosing an appropriate value for the RSOL. The general rule of thumb is that the chosen speed of light must be much larger than the typical I-front speed through the simulated medium in order to maintain physical accuracy. Some example calculations of $f_{\rm r}$ in various contexts are presented in Rosdahl et al. (2013), and the use of the RSOL approximation in cosmological contexts is discussed in detail in Gnedin (2016). For cosmological simulations, there is a wide range of gas densities through which light can travel, resulting in a wide range of I-front propagation speeds. If one is mainly concerned with the physics of radiation in dense gas trapped within dark matter halos, one can get away with choosing values for $f_{\rm r}$ as low as 10^{-2}. If, however, one is concerned with resolving cosmic reionization at the correct redshift, Gnedin (2016) asserts that the value $f_{\rm r}$ must be no less than 10^{-1} to accurately capture the propagation of I-fronts through the diffuse IGM.

Second, we implement the ability to subcycle `EnzoMethodM1Closure` with respect to other physics methods that act on longer timescales. The number of RT subcycles per global timestep is defined as

$$N_{\rm sub} = \frac{\Delta t_{\rm glob}}{\Delta t_{\rm RT}}, \tag{3.38}$$

where $\Delta t_{\rm glob}$ is the global timestep, which is typically set to the hydrodynamic timescale. Because radiation physically drives chemistry, chemistry and cooling using `Grackle` is called once every RT subcycle to ensure that I-front propagation is able to keep up with the propagation of radiation. The speedup associated with subcycling RT in this way comes from the fact that the number of calls to other physics solvers is effectively reduced by a factor of $N_{\rm sub}$, with negligible effects on the physical outcome.

3.3.3 Notes on Cosmological Units

To avoid truncation errors during a running simulation, it is good practice to keep the numbers that are evaluated by the computer near unity when possible. `Enzo-E` uses the following cosmological

code unit definitions:

$$[\rho] = \frac{3H_0^2\Omega_{\rm m}}{8\pi G} \tag{3.39}$$

$$[T] = \frac{h}{H_0^2}\sqrt{\frac{2}{3\Omega_{\rm m}(1+z_i)^3}} \tag{3.40}$$

$$[V] = \left(\frac{1+z_i}{1+z}\right)\frac{[L]}{[T]}, \text{ where } [L] = L_{\rm box} \text{ in proper units} \tag{3.41}$$

$$[M] = [\rho][L]^3 \tag{3.42}$$

$$[a] = \frac{1+z}{1+z_i}, \tag{3.43}$$

where $[\rho]$, $[T]$, $[V]$, $[M]$, and $[a]$ are the conversions for density, time, velocity, mass, and cosmological expansion factor, respectively. The conversion for $[\rho]$ is chosen to be the mean comoving matter density to ensure that a typical density corresponds to a value near unity in code units. In similar fashion, $[T]$ is chosen to be the cosmological freefall time at the initial redshift, z_i.

During the Epoch of Reionization, the universe is "photon-starved", with the ratio of the number of ionizing photons emitted over the age of the universe to the number of hydrogen atoms having a value of just 1.5-3 Bolton & Haehnelt (2007). With this in mind, it makes sense to define the cosmological code unit conversion for the photon number density as proportional to the cosmological mean density. We choose the following conversions for photon number density and flux:

$$[N] = 0.76\frac{[\rho]}{m_{\rm H}} \tag{3.44}$$

$$[F] = [N]\frac{[L]}{[T]}, \tag{3.45}$$

where $[\rho]$ is defined in Equation 3.39. There is a subtle choice we have made in our definition of $[F]$. We have chosen to multiply $[N]$ by $[L]/[T]$ instead of by $[V]$, where $[V]$ and $[L]/[T]$ differ by a factor of $[a]$. Recall that $[L]$ is the *proper* box length, a value that evolves over time via the cosmological expansion factor (i.e. $[L] = aL_{\rm c}$). The additional factor of a introduced in the flux terms when switching to cosmology mode with these units causes all factors of a to cancel in Equations 3.25 and 3.26 when evaluated in code units, leaving the form of the RT equations unchanged.

3.3.4 Iliev Test 2: HII region expansion and the temperature state

This test is described in Iliev et al. (2006), and simulates the expansion of an HII region in a uniform, hydrostatic medium composed of pure hydrogen. The original test calls for a radiating particle to be placed at the corner of the box. For technical reasons, we instead place the particle at the center of the box. To maintain the integrity of the test, we double the box size while keeping the intended resolution the same. The setup is as follows:

- Initial neutral hydrogen number density is 10^{-3} cm^{-3}
- Initial temperature is 100 K
- 256^3 grid cells, with a box side length of 13.2 kpc
- 10^5 K blackbody placed at the center of the box
- Three radiation groups, with energy ranges 13.6-24.59 eV, 24.59-54.42 eV, and 54.52-100.0 eV, respectively
- RSOL fraction of 2.5×10^{-3}

Slices through the center of the box of HI fraction and temperature at $t = 10$ Myr, $t = 100$ Myr, and $t = 500$ Myr are shown in Figure 3.14. The simulated HII region is clearly spherical, and expands outwards with time. The position of the I-front, defined to be the radius at which $x_{\rm HI} = 0.5$, is tracked over time and plotted in Figure 3.15. The position is normalized by the Strömgren radius,

$$r_s = \left(\frac{3\dot{N}}{4\pi\alpha^{\rm B} n_{\rm H}^2} \right)^{1/3}, \tag{3.46}$$

where $\alpha^{\rm B} \approx 2.6 \times 10^{-13}$ cm$^3 s^{-1}$ is the case-B recombination rate coefficient at $T = 10^4$ K. The full definition for $\alpha^{\rm B}$ is listed in Appendix E2 of Rosdahl et al. (2013). Similarly, time is normalized by the recombination timescale,

$$t_{\rm rec} = \frac{1}{\alpha^{\rm B} n_{\rm H}}. \tag{3.47}$$

Overplotted on Figure 3.15 is the analytic expression for the I-front position vs. time in the isothermal case. Note that Iliev Test 2 is *not* isothermal, so some deviation from the ideal case is to be expected.

Because recombination rates decrease as temperature increases, the I-front reaches a terminal radius that is slightly larger than the ideal Strömgren radius. Figure 3.15 can be directly compared with the middle panel of Figure 14 in Rosdahl et al. (2013), where we find good agreement. We also find good agreement with Rosdahl et al. (2013) in Figure 3.16, which shows radial profiles of HI fraction, HII fraction, and temperature at $t = 10$ Myr, $t = 100$ Myr, and $t = 500$ Myr.

3.3.5 Iliev Test 3: I-front trapping in a dense clump and the formation of a shadow

This test simulates the self-shielding of a dense sphere of hydrogen due to incident radiation streaming in from one side. The sphere acts as a barrier for the radiation, resulting in the formation of a shadow behind the sphere. The setup is as follows:

- 128^3 uniform mesh, with a box length of 6.6 kpc
- A uniform, sphere is placed at $(z, y, z) = (5 \text{ kpc},\ 3.3 \text{ kpc},\ 3.3 \text{ kpc})$
- Outside the sphere, $n_{\text{H}} = 2 \times 10^{-4}$ cm^{-3}, and $T = 8000$ K
- Inside the sphere, $n_{\text{H}} = 4 \times 10^{-2}$ cm^{-3}, and $T = 40$ K
- Gas both inside and outside the sphere is initially fully neutral
- Inflow boundary conditions, with ionizing flux $F = 10^6$ s^{-1}cm^{-2} flowing in from the $x = 0$ boundary
- RSOL fraction of 10^{-1}

Due to our use of the notably diffusive GLF flux function, the formation of the shadow is not captured very well. This is to be expected. Nevertheless, we show slices of HI fraction and temperature at t = 1 Myr and t = 15 Myr. These slices show good visual agreement with the same test run with the GLF flux function in Figure 16 of Rosdahl et al. (2013). In Rosdahl et al. (2013), the authors prefer to use the Harten-Lax-van Leer (HLL) flux function Harten et al. (1983) for Iliev Test 3, as the HLL flux function is shows excellent behavior when simulating non-diffusive beams of radiation. However, the HLL flux function struggles to simulate the spherical propagation of radiation from point sources. For this reason, the authors prefer to use the GLF flux function for all other applications.

3.3.6 Iliev Test 4: Multiple sources in a cosmological density field

This test simulates the propagation of I-fronts in a hydrostatic cosmological density field. Initial conditions can be downloaded on the Cosmological Radiative Transfer Comparison Project website.[1]. This is a unigrid simulation with a box size of 500 comoving kpc/h and 128^3 cells. There are 16 radiative point sources with positions corresponding to the most massive halos in the simulation volume. Each source has a constant ionizing photon production rate given by

$$\dot{N}_\gamma = \frac{\Omega_b}{\Omega_0} \frac{M_h}{m_p} \frac{1}{t_s}, \tag{3.48}$$

where M_h and m_p are the halo and proton mass, respectively, $\Omega_0 = 0.27$, $\Omega_b = 0.043$, and $t_s = 3$ Myr represents the assumed lifetime of each point source.

Figure 3.18 shows slices of $x_{\rm HI}$ and temperature through the center of the box at 0.05 Myr and 0.4 Myr. These images agree well visually with Figure 19 of Rosdahl et al. (2013). Figure 3.19 shows the evolution of mass-weighted and volume-weighted mean ionized fractions over time for three different light speed fractions: $f_c = 1.0$, 0.1, and 0.01. There is a clear separation between the $f_c = 1.0$ curves and the rest. After 0.4 Myr, the simulation volume of the $f_c = 1$ is approximately 70 percent ionized, whereas the $f_c = 0.1$ and $f_c = 0.01$ volumes are only 10 percent and 1 percent ionized, respectively. The distribution for the mass-weighted averages by the end are roughly 70 percent, 20 percent, and 5 percent. The volume-weighted averages tend to lag behind the mass-weighted averages because the I-front propagation starts in dense gas, where it takes more time for the radiation to escape than in diffuse gas. The key takeaway from Figure 3.18 is that in order for the ionization of the diffuse IGM to proceed at the correct rate, the radiation transport solver must be called using the full speed of light.

3.3.7 Iliev Test 5: Classical HII region expansion

This test is described in Iliev et al. (2009), and is similar to Test 2, except that the medium is evolved hydrodynamically. This is a simple radiative hydrodynamics simulation that is meant to make sure that the radiative transfer and hydrodynamics solvers behave correctly when used together. The setup is as follows:

[1] https://astronomy.sussex.ac.uk/~iti20/RT_comparison_project/index.html

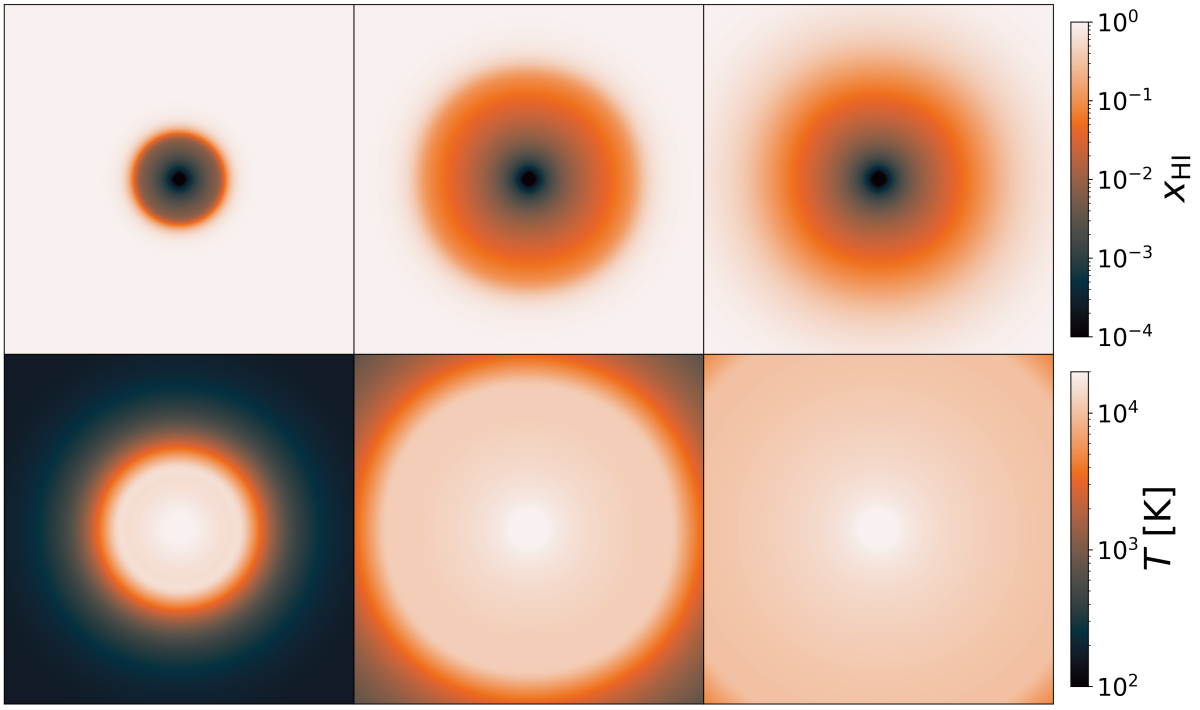

Figure 3.14. Slices through the center of the box at $t = 10$ Myr (*left*), $t = 100$ Myr (*middle*), and $t = 500$ Myr (*right*) for Iliev test 2. The top row shows neutral hydrogen fraction, while the bottom shows gas temperature.

- Initial neutral hydrogen number density is 10^{-3} cm^{-3}
- Initial temperature is 100 K
- 256^3 grid cells, with a box side length of 30.0 kpc
- 10^5 K blackbody placed at the center of the box
- Three radiation groups, with energy ranges 13.6-24.59 *e*V, 24.59-54.42 *e*V, and 54.52-100.0 *e*V, respectively
- RSOL fraction of 5×10^{-3}

Apart from the larger box size, the test setup is identical to that of Iliev Test 2. Slices of various fields through the center of the box at t = 10 Myr, 100 Myr, and 500 Myr are shown in Figure 3.20.

As in Test 2, the ionized sphere expands as it should, and the temperature within the sphere increases due to photoheating. Now that hydrodynamics is active, the increased pressure drives expanding

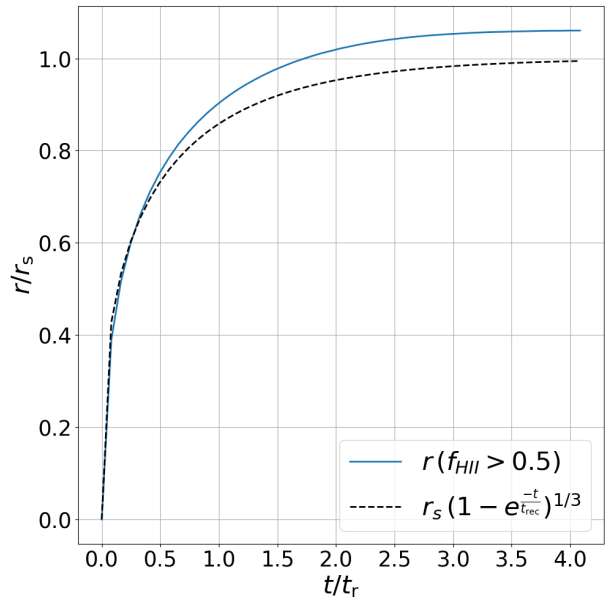

Figure 3.15. I-front position versus time in normalized units for Iliev test 2. Positions and times are normalized by the Strömgren radius and recombination time, respectively. The position of the I-front is defined to be the radius at which the gas is 50% ionized. The blue curve is obtained by `Enzo-E`, while the dashed black curve is the ideal solution for the isothermal case.

shock fronts, which are most noticeable in the hydrogen number density (third row) and mach number (fourth row) fields. There are initially two shock fronts, a feature that can be attributed to the fact that we are evolving multiple radiation groups. As a pure hydrogen simulation, the gas is optically thick to Lyα radiation. As such, the radiation in energy group 0, with energy 13.6-24.59 eV, initially lags behind the radiation in the other two groups. While radiation in groups 1 and 2 will not directly ionize the gas, it still produces non-zero photoheating rates. The outer shock front comes from photoheating by the streaming radiation of groups 1 and 2, while the inner shock front comes from the Lyα radiation in group 0. Eventually, as can be seen in the third column of Figure 3.20, the inner shock catches up with the outer shock by t = 500 Myr.

Figure 3.21 shows radial profiles of the same set of fields at t = 10 Myr, 100 Myr, and 500 Myr. The two shock fronts can be again observed as peaks in the density and mach number profiles. These profiles are meant to be compared with Figures 11-15 of Iliev et al. (2009). It should be noted that there is some small variation code-to-code between the precise positions and relative strength of the two density peaks in Iliev Test 5. Regardless, all profiles in Figure 3.21 show good agreement with those in Iliev et al. (2009).

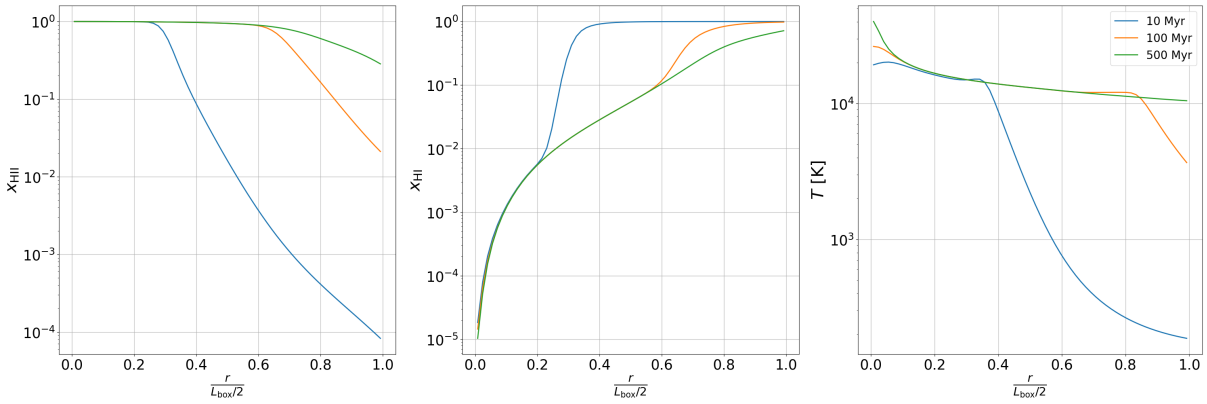

Figure 3.16. Radial profiles of neutral hydrogen fraction (*left*), ionized fraction (*middle*), and temperature (*right*) at $t = 10$ Myr (*blue*), $t = 100$ Myr (*orange*), and $t = 500$ Myr (*green*) for Iliev test 2.

3.3.8 Cosmological HII region expansion

This test is an alternate version of Iliev Test 2, where the box is allowed to expand as the simulation progresses. The purpose of this test is to verify that `EnzoMethodM1Closure` behaves correctly when running in cosmology mode. In particular, the primary concern is that the switch to cosmology mode is not accompanied by sudden unit conversion errors that cause completely unphysical results. The test setup is identical to Test 2, with the initial redshift set to 0. The comoving box length is set to 930 kpc, which corresponds to 30 kpc at $z = 30$.

As in Test 2, the position of the I-front is tracked over time and plotted as the blue curve in both panels of Figure 3.22. The solid black curve of the upper panel shows the I-front position over time in Test 2 (i.e. the static box case). The black dashed curve shows the position in the static box case, multiplied by the cosmological expansion factor. The black dashed curve lies on top of the expanding box curve. The fact that the two curves are so cleanly separated by the expansion factor is not a trivial result. Cosmological expansion dilutes baryon density and photon density over time, decreasing both photoionization rates and recombination rates. In this case, the photoionization and recombination rates decrease in such a way that I-front expansion rate in the comoving frame is approximately unchanged. In general, the expansion rate of cosmological HII regions is more compplicated than non-cosmological HII regions; however, the terminal radius differs by exactly the expansion factor for cosmological HII regions:

$$r_S(t) = a(t) r_{S,i}, \tag{3.49}$$

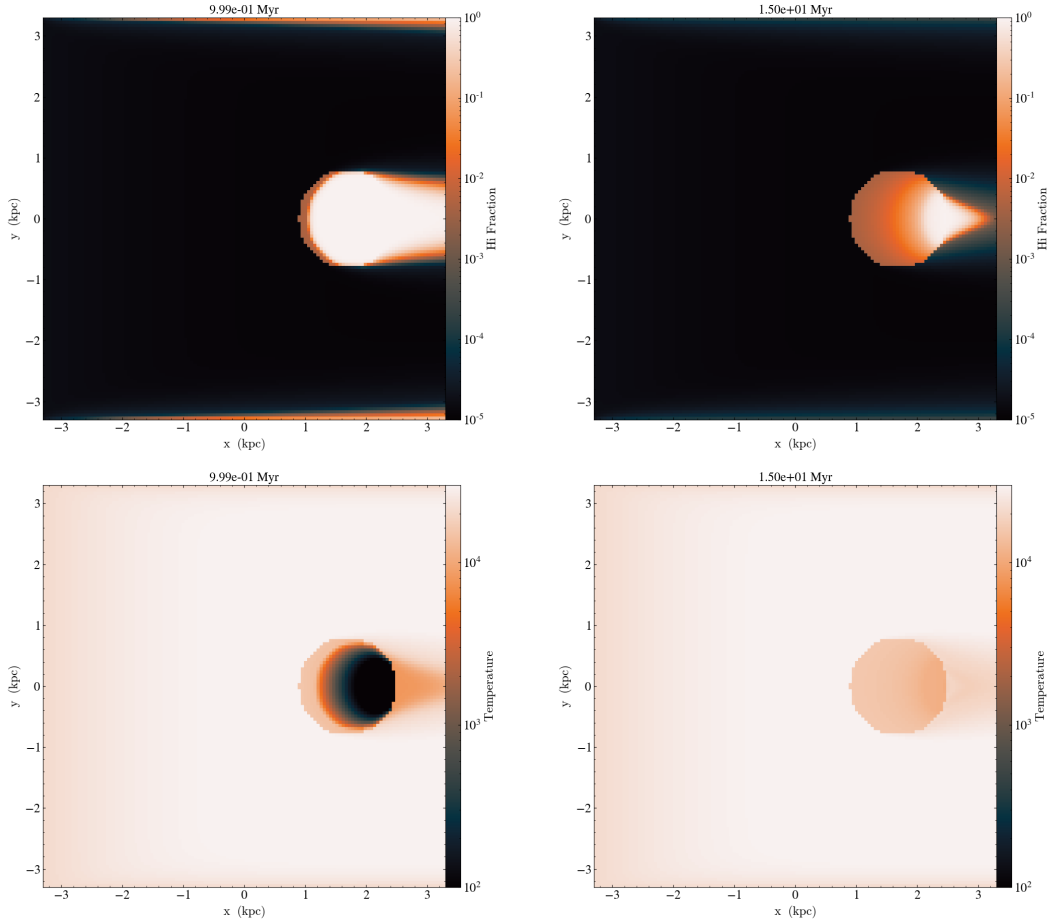

Figure 3.17. Slices through the center of the box of neutral hydrogen fraction (*top*) and temperature (*bottom*) at $t = 1$ Myr (*left*) and $t = 15$ Myr (*bottom*) for Iliev test 3.

where $r_{S,i}$ is the non-cosmological Strömgren radius (Shapiro, 1986). With this in mind, we can safely say that Figure 3.22 shows that `EnzoMethodM1Closure` behaves correctly in a box undergoing cosmological expansion.

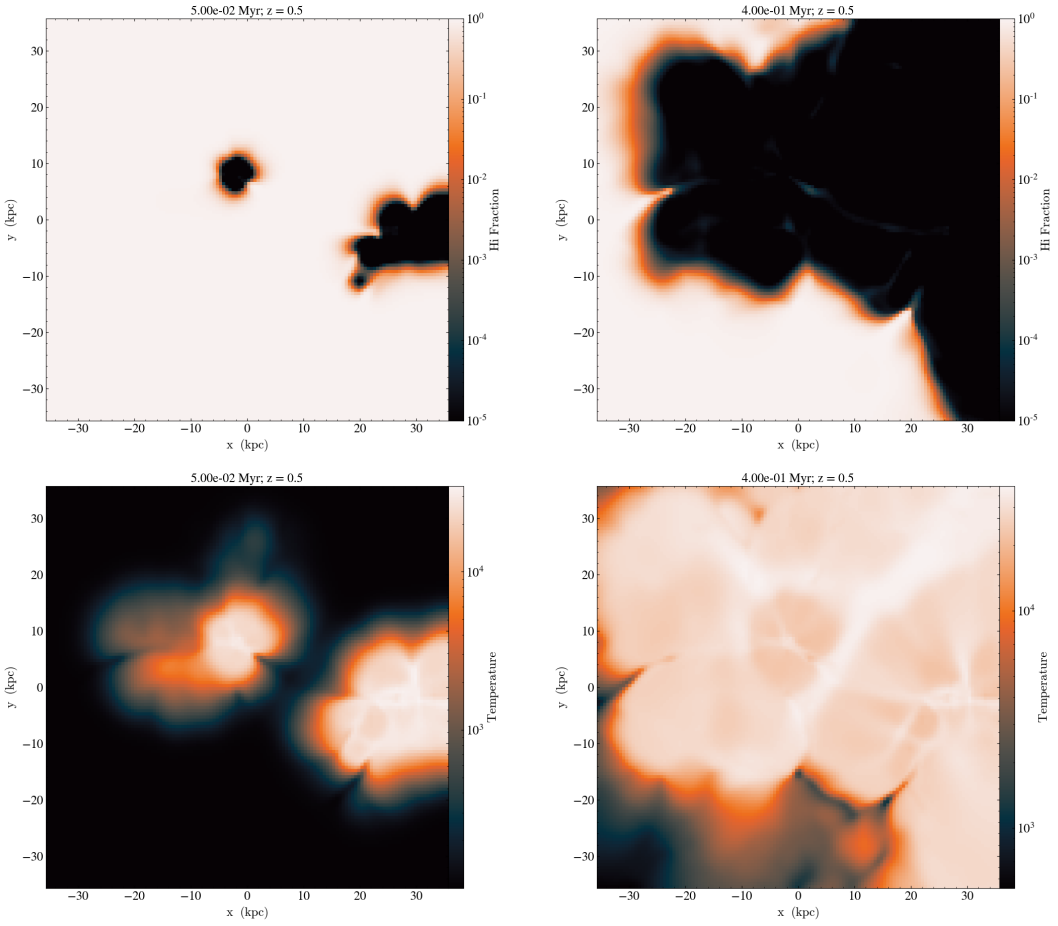

Figure 3.18. Iliev test 4. Slices through the center of the box are shown of HI fraction (*top*) and temperature (*bottom*) at 0.05 Myr (*left*) and 0.4 Myr (*right*).

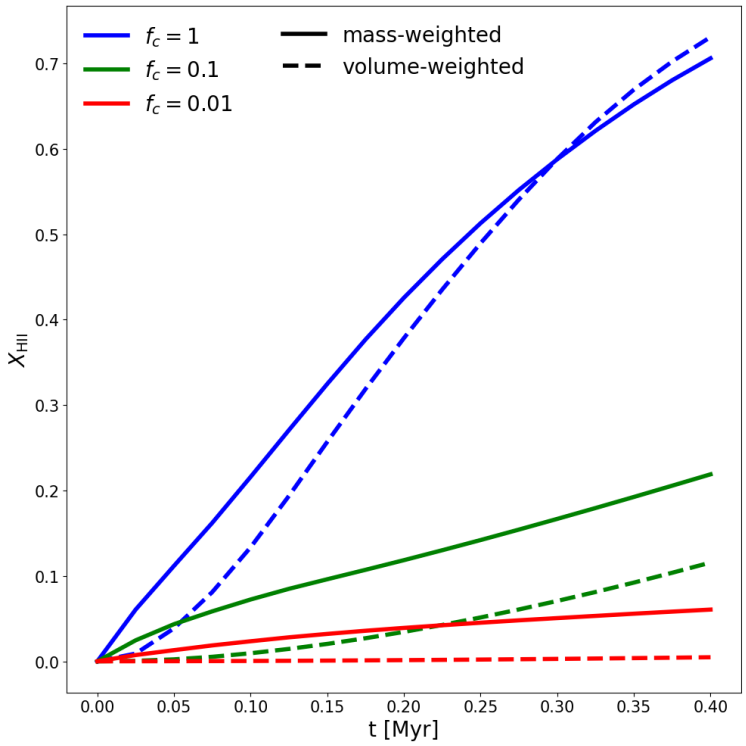

Figure 3.19. Mean ionized fraction in the box vs. time for Iliev test 4 for different choices for the reduced speed of light ($c_r = f_c\, c$). Solid lines indicate mass-weighted averages, which primarily samples dense gas. Dashed lines indicate volume-weighted averages, which is reduced to an unweighted arithmetic mean in the case of a unigrid simulation.

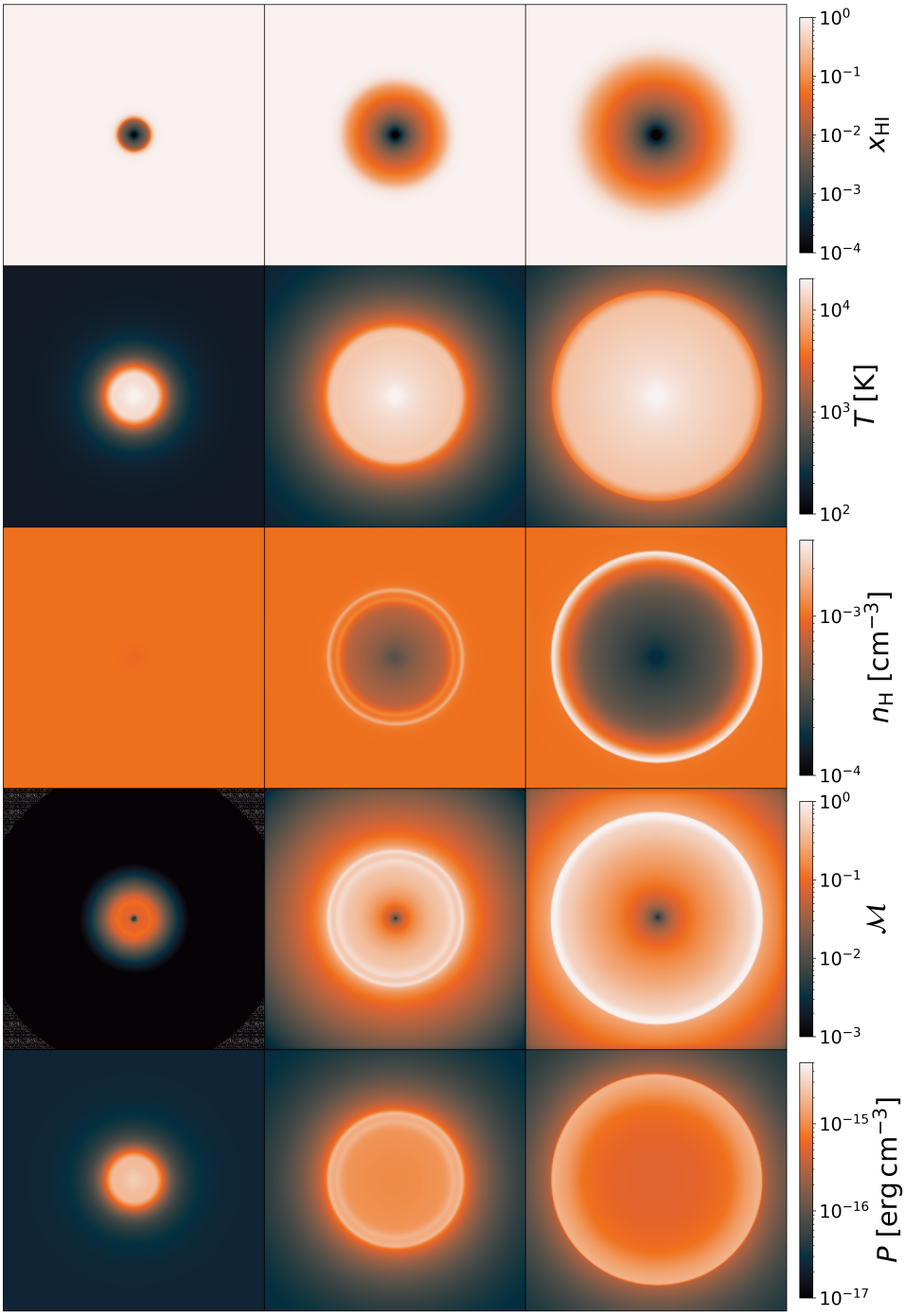

Figure 3.20. Iliev test 5. Slices through the center of the box of various fields at t = 10 Myr (*left*), 100 Myr (*middle*), and 500 Myr (*right*).

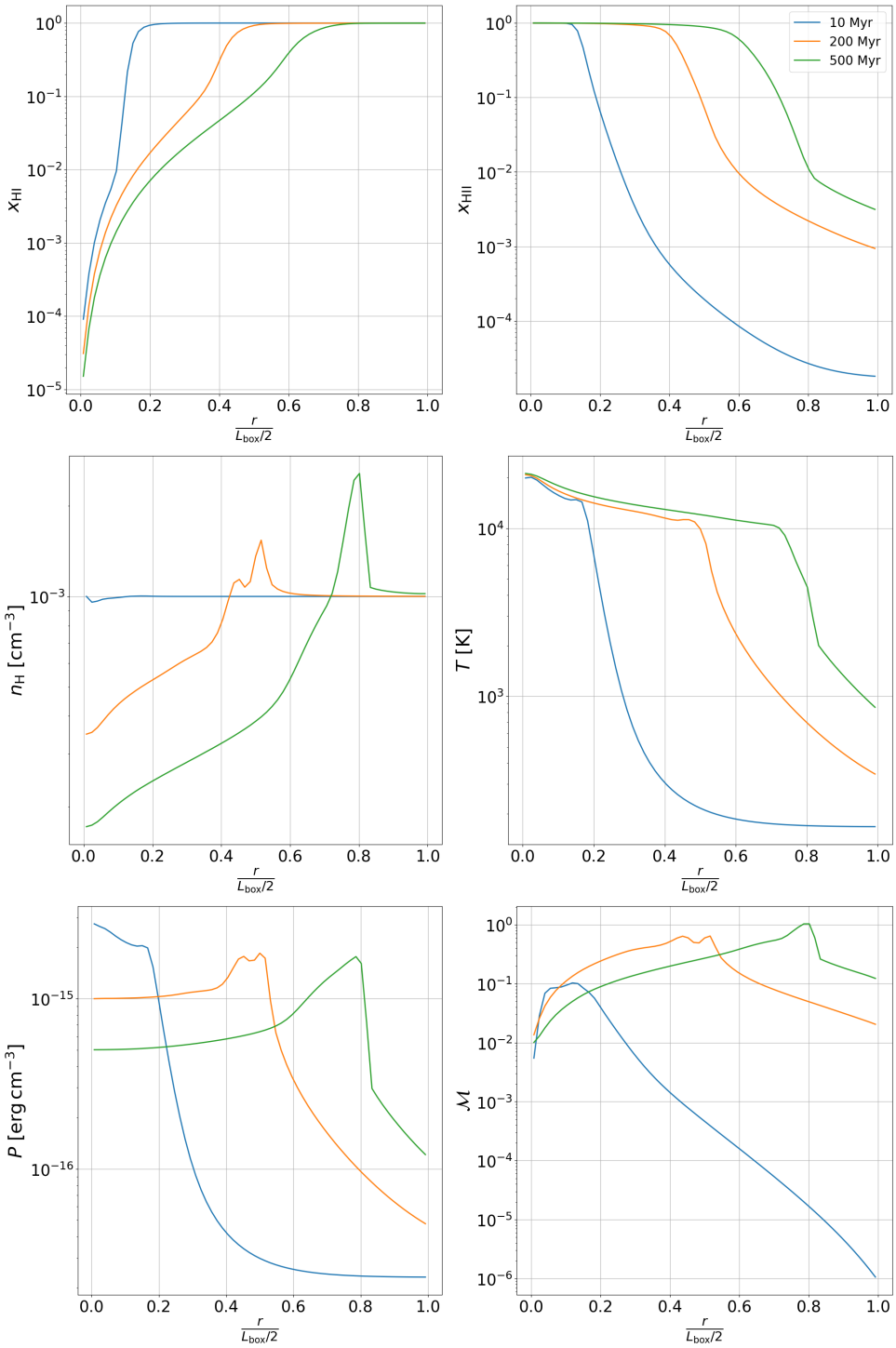

Figure 3.21. Iliev test 5 profiles. Each panel shows profiles for a different field at t = 10 Myr (*blue*), 100 Myr (*orange*), and 500 Myr (*green*).

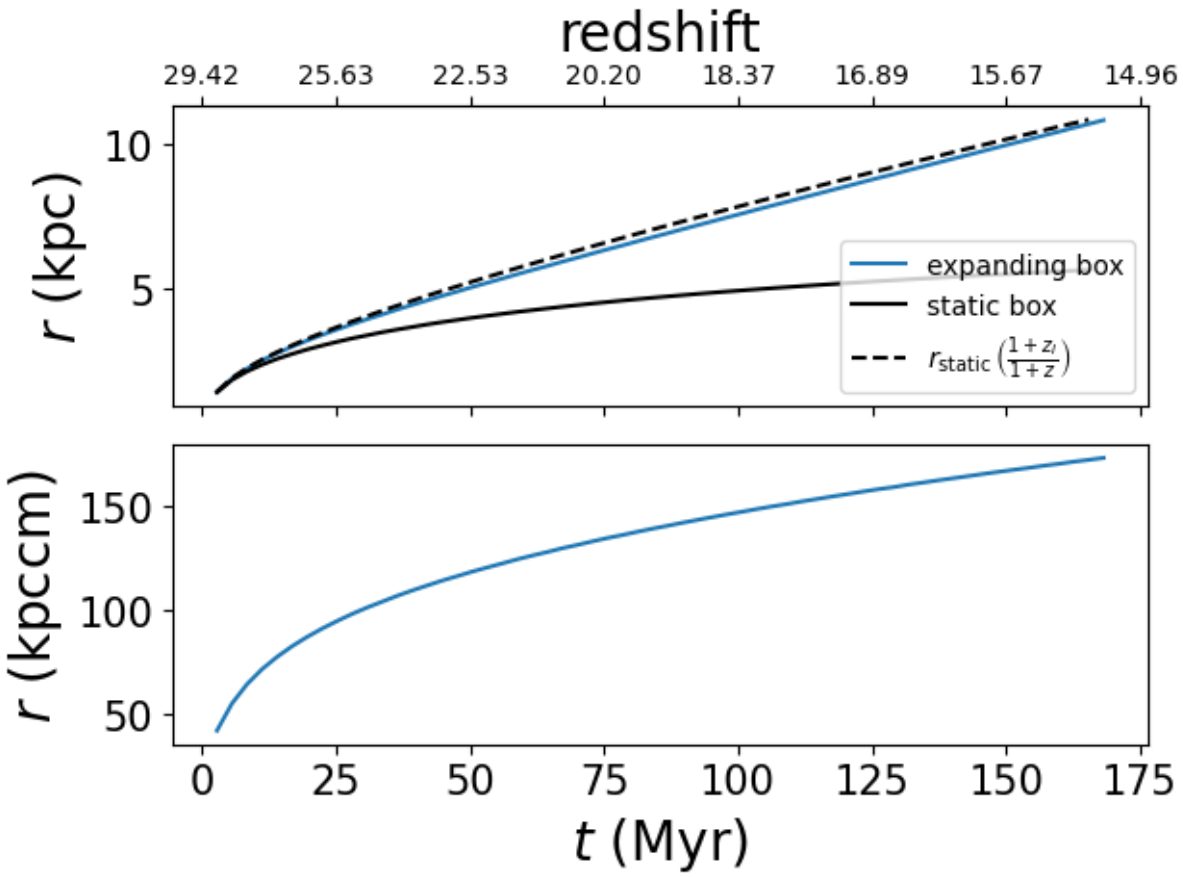

Figure 3.22. Iliev test 2 with cosmological expansion. *Top:* I-front position tracked over time for the static and expanding box cases in proper units. The top horizontal axis shows the redshift corresponding to the time given on the lower axis. The black and blue curves show the expanding and static box cases, respectively. The dashed curve shows the static box case, multiplied by the cosmological expansion factor. *Bottom:* Comoving I-front position vs. time for the expanding box case.

Chapter 4

Galaxies and Their Environment at $z \gtrsim 10$ — I: Primordial Chemical Enrichment, Accretion, Cooling, and Virialization of Gas in Dark Matter Halos

Recent observations made using the *James Webb Space Telescope* have identified a number of high-redshift galaxies that are unexpectedly luminous. In light of this, it is clear that a more detailed understanding of the high redshift, pre-reionization universe is required for us to obtain the complete story of galaxy formation. This study is the first in a series that seeks to tell the story of galaxy formation at $z \gtrsim 10$ using a suite of large-scale adaptive mesh refinement cosmological simulations. Our machine-learning-accelerated surrogate model for Population III star formation and feedback, `StarNet`, gives us an unprecedented ability to obtain physically accurate, inhomogeneous chemical initial conditions for a statistically significant number of galaxies. We find that of the 12,423 halos in the mass range of $10^6\,M_\odot < M_{\rm vir} < 10^9\,M_\odot$ that form in our fiducial simulation, 16% are chemically enriched by Population III supernovae by $z \sim 12$. Primordial hypernovae and pair-instability supernovae contribute in approximately equal amounts to the enrichment of halos as a whole, while Type II supernova enrichment is less important. The mean Population III metallicity of gas within a halo is $2 \times 10^{-3}\,Z_\odot$. We then profile and compare various cooling processes at the centers of halos, and find a complete absence of atomic cooling halos. All of our halos with central cooling gas are dominated by H_2 cooling, metal cooling, or a mixture of the two, even in the presence of a strong H_2-photodissociating Lyman-Werner background. We also find that accretion through the virial radius is not driven by cooling, as gas flowing in through filaments is typically not yet able to cool efficiently by the time it reaches a given halo. We then investigate the virialization state of the halos, and confirm that both the dark matter and the gas are virialized for

the halos in our sample. We find that gas virialization in halos with $M_{\rm vir} \gtrsim 10^7\ M_\odot$ is supported by bulk turbulent flows, and that thermal energy accounts for only a small fraction of the total kinetic energy. Because of this, the mean gas temperature is well below the virial temperature for these halos. We then compute the mass of gas that is available for Population II star formation, and infer star formation rates for each potential star-forming halo. We find good agreement in our inferred Population II statistics with the those in the *Renaissance Simulations*.

4.1 Introduction

The claim of the existence of "impossibly massive" galaxies observed by JWST at redshift $z > 10$ (Labbé et al., 2023) has spurred a re-evaluation of our standard model of cosmology and our understanding of the physics of galaxy formation and stimulated renewed interest in the earliest evolutionary stages of galaxies growth (Adamo et al., 2024). The high inferred stellar masses imply high star formation rates averaged over the entire formation history of the galaxy and its progenitors. It also implies high rates of mass accretion to feed the star formation process. Even if the stellar mass estimates are high due to unfounded assumptions about the stellar mass function or some other systematic, some high-z galaxies are nonetheless unusually luminous, which implies high star formation rates (Adamo et al., 2024). This raises two fundamental questions: (1) when does star formation become efficient in high redshift galaxy halos? and (2) how can high star formation rates be sustained in the presence of feedback?

Regarding the first question, the conventional wisdom is that star formation efficiency jumps in halos with a virial temperature above 10^4 K because then the gas can cool efficiently by Ly α emission. At z = 10, $T_{\rm vir} = 10^4$ K corresponds to a halo of mass of $M_{\rm vir} = 5 \times 10^7 M_\odot$ (Greif et al., 2008). According to the conventional wisdom, halos of lower mass (so-called minihalos) cool inefficiently by H_2 and HD if chemically pristine, and additionally by fine structure lines of C and O if chemically enriched by the first generation of stars (Bromm & Loeb, 2003). In either case, star formation would be inefficient in minihalos due to the low concentration of coolants.

Halos with $T_{\rm vir} > 10^4$ K are often referred to as *atomic cooling halos* (ACH) since they can cool by collisionally excited H and He lines. From a practical point of view, ACHs can be taken as the first galaxies and the building blocks of more massive galaxies (Greif, 2015). The reasoning is that minihalos would be starless after massive Population III stars (hereafter Pop III) have exploded or collapsed to

black holes, whereas ACHs have sufficiently deep potential wells to retain photoionized gas that can cool and form stars. If we want to understand the buildup of massive high redshift galaxies, it is therefore imperative that we understand the formation and properties of ACHs.

The first detailed cosmological simulations of ACHs were performed by Wise & Abel (2007) and Greif et al. (2008). They simulated the formation of an individual halo near the threshold mass of $M_{\rm vir} = 5 \times 10^7 M_\odot (\frac{1+z}{10})^{-3/2}$ using high resolution zoom-in simulations. In the absence of star formation and feedback but including primordial gas chemistry and cooling, they found that most of the gas accretes along filaments at $T < T_{\rm vir}$ and then virializes into fluid turbulence in the halo interior. Gas accreting directly from voids passes through an accretion shock near the virial radius and is heated to $T \approx 10^4$ K, where it becomes partially ionized, activating H line cooling. Hydrogen line cooling is found to be confined to just inside the accretion shock, while H_2 cooling dominates in the cooler, denser halo core. Greif et al. (2008) included deuterium chemistry in their primordial gas chemistry network, while Wise & Abel (2007) did not. The former authors found that HD is formed in appreciable concentrations in the warm, partially ionized gas near the halo's edge, and is efficiently mixed into the halo's interior by the turbulence. This is important because whereas H_2 cooling alone can only cool the gas to $T \approx 200$ K, HD can cool the gas to the CMB temperature floor, potentially reducing the Pop III stellar mass scale.

The stellar content of ACHs depends upon whether the gas is pristine or chemically enriched by Pop III supernovae and subsequent generations of metal-enriched star formation. This topic has received considerable attention by modelers and simulators in the past years. These investigations can be broadly divided into two related subjects: (1) the creation and survival of pristine halos, and hence Pop III star formation through cosmic time; and (2) the internal and external chemical enrichment of individual halos by stellar sources. Investigations of type 1 are typically carried out with semi-analytic models (SAMs) of increasing sophistication, while investigations of type 2 tend to employ hydrodynamic and radiation hydrodynamic cosmological simulations.

A pioneering study by Trenti & Stiavelli (2009) showed, using Press-Schechter modeling combined with a probabilistic model for self-enrichment, that Pop III stars could continue to form in pristine minihalos and ACHs to z=10. This is due to the fact that chemical enrichment is a local phenomenon, whereas hierarchical halo growth occurs everywhere in a largely pristine universe. A key uncertainty of their model is whether a pristine halo of ACH mass forms a single or multiple Pop III stars. They

investigated both cases, and found that if multiple Pop III stars form with a fixed star formation efficiency (defined as the fraction of baryons within the halo that are converted to stars), the Pop III star formation rate density (SFRD) dominates the Pop II SFRD to *lower redshifts* than the single star case because the former rate is boosted. Of course, increasing the production of Pop III stars increases the likelihood that one will explode as a supernova, enriching the halo and terminating any further primordial star formation.

More recent SAMs (e.g., Visbal et al. (2020)) use dark matter halo merger trees taken from N-body simulations and add analytic prescriptions to model the effects of H_2 photodissociation from Lyman-Werner (LW) radiation, suppression of star formation due to inhomogeneous reionization, and metal enrichment by supernova-driven winds. Visbal et al. (2020) computed both the Pop III and metal-enriched star formation histories from $z \approx 30$ to 6 using a novel grid-based method that places feedback spheres of different size for radiative and supernova feedback zones using the location of halos taken from the merger trees. They found that initially long-range LW feedback, local metal enrichment, and photoionization of halos control the Pop III SFRD, but that for $z \leq 15$, external enrichment of pristine halos by nearby star forming halos and inhomogeneous reionization begins to dominate. They find that the combination of reionization feedback and external enrichment reduces the Pop III SFRD at $z = 6$ by an order of magnitude compared to LW feedback alone. These results highlight the importance of including at least these three processes in models of high redshift galaxy evolution.

The first attempts to numerically simulate the formation of ACHs including Pop III and metal-enriched star formation and feedback (hereafter Pop II) were limited by small volumes and number statistics due to the severe range of scales present. In the *Birth of a Galaxy* simulations, Wise et al. (2012a,b, 2014) simulated a 1 cMpc^3 volume the with the AMR code `Enzo` including 9-species primordial gas chemistry, subgrid recipes for Pop III and II star formation and feedback, metal injection and cooling, EUV radiative transfer, and a LW background. With a dark matter mass resolution of 1840 $M_\odot$ and maximum spatial resolution of 1 comoving pc, the formation of several protogalaxies in halos of mass $M_{\rm vir} \approx 10^8 M_\odot$ were well resolved and evolved to $z = 7$. Assuming a top-heavy Pop III stellar IMF and pair-instability supernova (PISN) yields, they found that the transition from Pop III to Pop II star formation is sudden in halos of mass $M_{\rm vir} > 10^7 M_\odot$, which marks the transition from H_2 to metal line cooling. They found that a single PISN raises the halo metallicity to approximately $10^{-3} Z_\odot$, confirming and reinforcing earlier predictions (Bromm & Loeb, 2003; Greif et al., 2007; Wise & Abel, 2008).

The co-evolution of Pop III and Pop II star formation in larger volumes and more massive halos was investigated by Xu and collaborators with the *Renaissance Simulations* suite using `Enzo` running on the NCSA Blue Waters petascale supercomputer (Xu et al., 2013, 2014; Chen et al., 2014; O'Shea et al., 2015; Xu et al., 2016b,a,c). The *Renaissance Simulations* employed the same physical prescriptions as the *Birth of a Galaxy* simulations in a much larger volume of (40 cMpc)^3, with 3 zoom-in regions enclosing low, high, and average density environments referred to as Void, Rarepeak, and Normal. With a dark matter resolution of $2.34 \times 10^4 M_\odot$ and maximum spatial resolution 19 comoving pc, the evolution of halos over a mass range of $10^{6.5} < M_{\rm vir}/M_\odot < 10^9$ and their star formation histories, both primordial and enriched, could be simulated in detail.

Xu et al. (2013) examined the Pop III *multiplicity* as a function of halo mass in the Rarepeak simulation, and found that the majority of Pop III stars formed in halos of mass $10^7 < M_{\rm vir}/M_\odot < 10^8$ with a typical multiplicity of ~ 10. The most massive starless pristine halo was found to have a mass $M_{\rm vir} = 7 \times 10^7 M_\odot$, and every halo more massive than that was enriched with Pop III supernova ejecta.

The larger halo mass range and sample size of the *Renaissance Simulations* permitted a statistical analysis of the scaling properties of the first galaxies (Chen et al., 2014). They found star formation efficiency significantly increases at $M_{\rm vir} \sim 10^8 M_\odot$, which they attributed to the ACH threshold. However, this mass is significantly above the ACH threshold at that redshift, suggesting that the efficiency boost is driven by internal enrichment by Pop II feedback, and not by the onset of H line cooling.

In this paper we study the accretion, virialization, and cooling of intergalactic gas onto halos spanning the atomic cooling threshold in the absence of metal-enriched star formation and feedback. We employ a new, more scalable version of the `Enzo` code called `Enzo-E`, which provides more uniform mass resolution in the baryonic fluid in the vicinity of protogalactic halos, allowing us to better characterize the gas dynamics there. By virtue of `Enzo-E`'s parallel scalability, we also can survey larger cosmological volumes improving our statistical coverage. We take into account the pre-enrichment of protogalactic halos by Pop III supernovae using our recently developed machine learning-based surrogate model `StarNet` (Wells & Norman, 2022). We also take into account improved models for the evolving LW radiation background (Incatasciato et al., 2023) and H_2 self-shielding (Krumholz & Gnedin, 2011). We find that gas accretes onto halos predominantly by cold mode accretion and virializes via turbulence well below the halo's virial temperature for its given mass, in agreement with the results of Wise & Abel (2007) and

Greif et al. (2008). Consequently, hydrogen atomic line cooling is found to be unimportant to the thermal evolution of the gas in halos as massive as $5 \times 10^8\ M_\odot$. Rather, a combination of metal line cooling due to Pop III pre-enrichment and H_2 cooling are dominant across the halo mass range surveyed, calling into question the conventional notion we have of the importance of atomic cooling halos to galaxy formation and evolution.

The plan of the paper is as follows. In Sec. 4.2 we describe our suite of `Enzo-E` simulations and our numerical methodology, and summarize the salient features of `StarNet` as well as the *Phoenix Simulations* used to train the surrogate model. In Sec. 4.3, we present our main results. Sec 4.3.1 analyzes the statistics of the Pop III stellar associations produced by `StarNet` and compares our star formation rate density with the semi-analytic models of Visbal et al. (2020). Sec. 4.3.2 quantifies the chemical enrichment by Pop III supernovae of over 2,000 halos in our sample of 12,423 halos. In Sec. 4.3.3, we analyze the accretion and cooling of gas in our sample of halos; in Sec. 4.3.4, we discuss the topic of incomplete virialization of gas in halos and how that effects how the gas cools. In Sec. 4.3.5, we analyze the large scale environment from which the halos are accreting, and characterize it as a cosmic web of cool-warm filaments with a typical temperature 10^3 K. This result, coupled with incomplete virialization of gas, explains the absence of significant H and He line cooling in ACHs. In Sec. 4.3.6, we analyze the properties of 5 of the most massive halos in our sample. In Sec. 4.3.7, we estimate the Pop II stellar masses and star formation rates in our sample using a post-processing approach. Finally, in Sec. 4.3.8, we discuss the sensitivity of our results to variations in feedback and chemistry prescriptions. In Sec. 4.4, we discuss our key results and make comparisons to results in the published literature where relevant. Sec. 4.4 is organized according to key processes which have an effect on the formation and evolution of pre-galactic halos, and includes a discussion of the limitations and caveats of our models. A summary of our key results and conclusions are presented in Sec. 4.5.

4.2 Methodology

Our simulation suite is run using the `Enzo-E` code[1]. `Enzo-E` is a port of `Enzo` (Bryan et al., 2014) onto an entirely new parallel adaptive mesh refinement framework called `Cello` (Bordner & Norman, 2018). `Enzo-E/Cello` is parallelized with `Charm++` (Kalé, 2011). `Enzo-E` and `Cello` are developed in

[1] https://github.com/enzo-project/enzo-e

tandem, but are each their own separate application. `Cello` organizes the computational mesh as a fully distributed array-of-octrees, where the computational domain is decomposed into "blocks" of field data. Each block is a cubic Cartesian mesh of size n_b^3, where $n_b \geq 4$ is an input parameter. For our simulations, $n_b = 16$. Each block has an associated list of Lagrangian particles (dark matter, stars, etc.) which varies in length. When refinement is triggered in a block, 8 child blocks of the same dimension are spawned within the parent block's volume, and the field data is interpolated such that the resolution increases by a factor of 2 in the child blocks. Particles are always associated with the finest level block enclosing them.

`Enzo-E` encapsulates many of the physics solvers originally developed for `Enzo`. These include multispecies gas dynamics using a Piecewise Parabolic Method (PPM) adapted for cosmological flows (Bryan et al., 1995), collisionless N-body dynamics using the Particle-Mesh method, and various star formation and feedback recipes (see Bryan et al. (2014) for more details). The Poisson equation for gravity is solved using an entirely new method from that used in `Enzo`. The large-scale gravitational field is solved on the root grid using a V-cycle geometric multigrid method assuming periodic boundary conditions. The local gravitational field in each refined octree is then solved using the bi-conjugate gradient method taking as its boundary conditions the large-scale potential interpolated onto the external facets of the octree mesh. Nine-species (HI, HII, HeI, HeII, HeIII, H_2, H_2+, H^-, e^-) non-equilibrium chemistry and cooling is handled using the `Grackle` library (Smith et al., 2017). We include an H_2 photodissociating Lyman-Werner background (LWB) using fits derived in (Incatasciato et al., 2023). Specifically, we calculate the global H_2 photodissociation rate as $k_{H_2} = 1.38 \times 10^{-12} J_{21}$ s^{-1} (Abel et al., 1997), where J_{21} is given by equation 9 in Incatasciato et al. (2023). The H^- photodetachment rate and H_2^+ photodissociation rates are then calculated using equation 10, with the fitting parameters listed in Table 5 of Incatasciato et al. (2023). We also track metals sourced from primordial supernovae using an implementation of the machine-learning accelerated surrogate model for Pop III star formation and feedback, `StarNet` (Wells & Norman, 2022; Wells & Norman, 2022, 2021). Metal line cooling is computed in each enriched cell using precomputed tables assuming ionization equilibrium as described in (Smith et al., 2017). To demonstrate the similarities and differences between `Enzo` and `Enzo-E`, comparisons between two sets of identical cosmological simulations run with each code are presented and analyzed in Section 3.0.1.

In total, we perform 6 simulations in this study, the parameters for which are listed in Table 4.1. Our fiducial simulation, `N512_fiducial`, has 512^3 cells and dark matter particles on the root grid, up

to 5 levels of AMR, and a box of length 5.12 comoving Mpc on a side, providing a maximum spatial resolution of 312.5 comoving pc (26 proper pc at $z = 11$). Refinement is triggered in a block when the mass in a cell reaches a value of $M > \delta_{\rm thresh}(\Delta x_{\rm root})^3$. Here, $\delta_{\rm thresh} = 8$ is the chosen overdensity threshold, where $\delta = 1$ corresponds to the cosmic mean density at a given redshift, and $\Delta x_{\rm root}$ is the cell width on the root grid. Cosmological initial conditions are generated using `MUSIC` (Hahn & Abel, 2011) at $z = 199$ using the Planck 2014 (Ade et al., 2014) cosmological parameters: $\Omega_{\rm m} = 0.3111$, $\Omega_{\rm b} = 0.048975$, $\Omega_k = 0$, $\Omega_\lambda = 0.6889$, $H_0 = 0.6766$, $\sigma_8 = 0.811$, $n = 0.965$. With these parameters, the dark matter particle mass is $3.34 \times 10^4\ M_\odot$, which comparable to that in the *Renaissance Simulations*. The simulation is run to a final redshift of $z = 11.92$.

The remaining simulations listed in Table 4.1 are run with the same resolution settings, but with varied physics and box sizes. These are meant to test the sensitivity of our results to variations in our physics models, and to provide more statistics. `N256_fiducial` is a scaled-down version of `N512_fiducial` that includes all the same physics, but with the simulated volume and root grid both reduced by a factor of 8. `N256_noLWB` is a re-run of `N256_fiducial`, but without a LWB. `N256_adiabatic` is a version that does not include chemistry and cooling, and does not source metals from Pop III supernovae. `N256_6species` includes chemistry and cooling only for atomic hydrogen and helium species: HI, HII, HeI, HeII, HeIII, e^-. `N256_9species` includes the full nine-species chemistry network with metal cooling and a LWB, but metals are sourced using a uniform metallicity floor of $Z_{\rm floor} = 10^{-5.5}\ Z_\odot$.

This study focuses on the physical processes leading up to Pop II star and galaxy formation, and we thus do not include an explicit model for Pop II star formation and feedback in any of our simulations. This is done so that we may isolate the effects of primordial pre-enrichment on the accretion, virialization, and cooling gas in protogalaxies. It is also in the spirit of the pioneering simulations of Wise & Abel (2007) and Greif et al. (2008), who also did not include metal-enriched star formation and feedback. In a follow-up paper, we will re-run our simulation suite with the inclusion of Pop II star formation and feedback, and will discuss how the findings in this study are affected by the additional physics. We will also investigate the properties of the galaxies that form following enrichment by Pop III supernovae.

Table 4.1. List of relevant parameters for each of the simulations run for this study. From left to right, columns show simulation name, root grid dimension, box length in comoving Mpc, chemical species participating in chemistry and cooling with `Grackle`, the source of metals (either predicted with `StarNet`, set using a uniform metallicity floor, or no metals), final redshift, and the virial mass of the most massive halo at the final redshift. All simulations have a maximum AMR level of 5, and reach the same maximum spatial resolution of 312.5 comoving pc (26 proper pc at z=11). We use a dark matter particle mass of $3.34 \times 10^4\ M_\odot$. The column labelled "MMH" shows the virial mass of the most massive halo in each simulation. The 256^3 series of simulations start from identical cosmological initial conditions.

Simulations						
Name	Root	$L_{\rm box}$ [cMpc]	Species tracked	$Z_{\rm source}$	$z_{\rm final}$	MMH [$M_\odot$]
`N512_fiducial`	512^3	5.12	H, He, H_2, e^-, ions	`StarNet`	11.92	5.67×10^8
`N256_fiducial`	256^3	2.56	H, He, H_2, e^-, ions	`StarNet`	11.34	4.90×10^8
`N256_noLWB`	256^3	2.56	H, He, H_2, e^-, ions	`StarNet`	11.35	4.60×10^8
`N256_adiabatic`	256^3	2.56	None	None	11.58	5.62×10^8
`N256_6species`	256^3	2.56	H, He, e^-, ions	None	12.03	4.63×10^8
`N256_9species`	256^3	2.56	H, He, H_2, e^-, ions	$Z_{\rm floor} = 10^{-5.5}\ Z_\odot$	12.10	4.55×10^8

4.2.1 Primordial Chemical Enrichment with `StarNet`

Our simulations are scoped to generate a statistically significant number of halos with $T_{\rm vir} \gtrsim 10^4$ K while capturing inhomogeneous chemical enrichment from primordial supernovae. To accomplish this, we call the surrogate model, `StarNet` (Wells & Norman, 2022), once every 5 Myr. `StarNet` utilizes deep convolutional neural networks to identify Pop III star-forming regions within subvolumes of size 10 proper kpc throughout the computational domain. `StarNet` flags cells in the subdomain that are potential sites of Pop III star formation using the hydrodynamic fields as input. If any cell within a given predicted star-forming region has a metallicity above $Z_{\rm crit} = 10^{-5.5}\ Z_\odot$, the prediction is discarded. In this way, Pop III stellar associations only form in pristine gas. For more details, see (Wells & Norman, 2022).

Once the star-forming regions are identified, population statistics for each region are randomized following statistics from the *Phoenix Simulations* (see Sec. 4.2.2), and a simple linear regression model is used to predict the size of the composite supernova remnant once all stars within the population reach their endpoint. Metal yields are calculated based off of the masses of the stars within the population, and the metals are then uniformly deposited onto the mesh within a sphere of the predicted radius. The metal bubbles predicted by `StarNet` typically have radii of 1 to 3 kpc. The temperature of the gas within the sphere is set to `max(`T_i`, 10^4 K)`, where i denotes the cell index. In our implementation of `StarNet`, we also photodissociate all H_2 within the sphere, ionize all hydrogen, and singly ionize all helium (i.e. all chemical species are converted to HII, HeII, and e^-, while conserving proton and electron counts).

Details of each population (number of stars, stellar masses, metal yields, etc.) are saved in massless `popIII_remnant` particles that are free to move around the mesh after their corresponding supernova remnants are deposited. These particles are placed at the center of mass of the supernova remnant at the time of deposition. Because the `popIII_remnant` particles and the gas in their vicinity fall under the influence of the same gravitational potential, the `popIII_remnant` particles serve as tracers that generally follow the supernova remnants as the enriched gas is advected. With this, it is possible to analyze the stellar population statistics in post, as well as track the separate progenitor stellar populations as supernova remnants inevitably merge. For a detailed account of `StarNet`, its training, and its capabilities, we refer the reader to Wells & Norman (2021, 2022); Wells & Norman (2022).

4.2.2 The Phoenix Simulations

`StarNet` was developed in `Enzo` using training data from the *Phoenix Simulations* (Wells & Norman, 2022). All predictions from `StarNet` are thus consistent with those observed in the *Phoenix Simulations* (PHX hereafter). We briefly describe these simulations here. The PHX simulations are a set of three radiation hydrodynamic cosmological simulations run with the `Enzo` code — one with a root grid dimension of 512^3 and a box length of 5.21 comoving Mpc, and two with dimension 256^3 and box length 2.61 comoving Mpc. The PHX simulations have the same root grid resolution as our simulation suite, but are run with 9 levels of AMR. It should be noted that while the maximum resolution of the PHX simulations is much higher than the simulations considered in this study, the differences in AMR approaches between `Enzo` and `Enzo-E` make it such that the `Enzo-E` simulations obtain better resolution outside of halo centers.

The PHX simulations include direct models for both Pop III and Pop II star formation and feedback, as well as radiative transfer using the adaptive ray tracing algorithm, `Moray` (Wise & Abel, 2011b). It is found in (Wells & Norman, 2022) that Pop III stars form in associations with up to ~ 150 individual stars. A detailed analysis is then performed to connect Pop II star clusters to their progenitor Pop III supernova remnants, and the influence of different configurations of Pop III supernova type on the properties of the Pop II stars that form in their wake is explored. Finally, a piecewise linear regression model is fit to relate the size of a conglomerate Pop III supernova remnant to the number of stars, their masses, and their relative formation times in the association. This model is the very same model that is

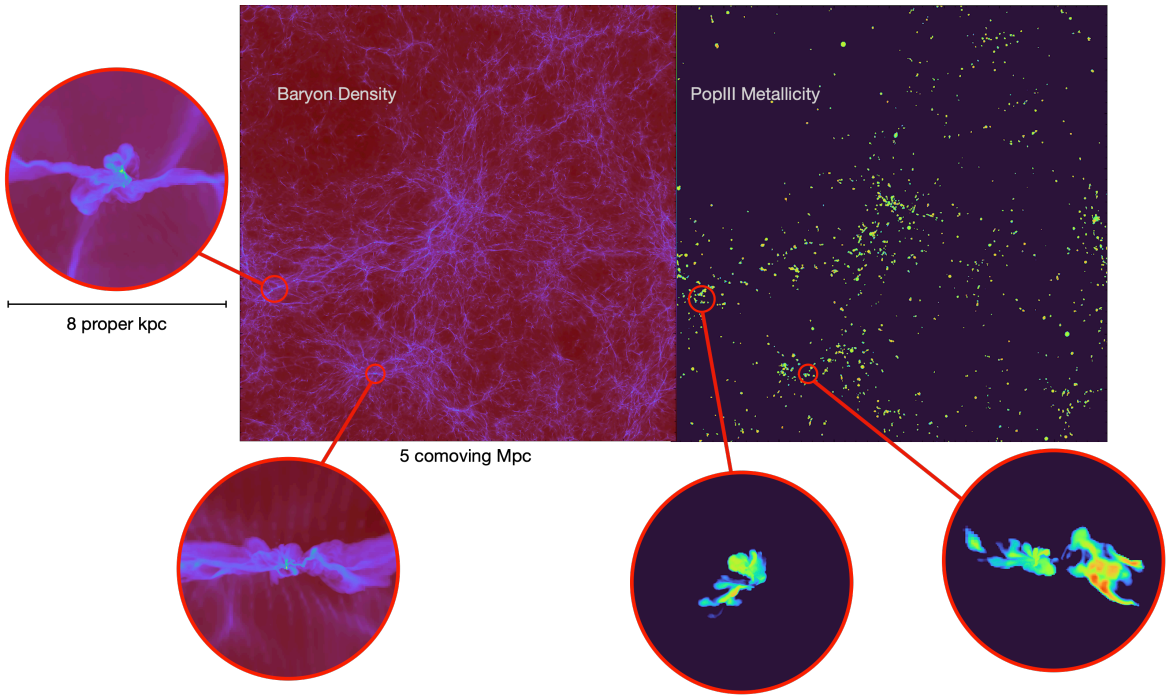

Figure 4.1. Full-box projections of baryon density and Pop III gas metallicity for the `N512_fiducial` simulation, which has a simulated volume of ~ 125 comoving Mpc^3. The small red circles show the locations of the two most massive halos in the box. Connected to the small red circles via red lines are slices through the center of the two most massive halos, for both baryon density and metallicity. The halos have virial radii of ~ 2 kpc. Metal enrichment in this simulation is purely from Pop III feedback predicted by `StarNet`.

used in `StarNet` to determine the radius of the evolved remnant, assuming it evolves spherically, once the location and properties of the association are predicted.

4.3 Results

4.3.1 Population III Statistics

We begin by discussing the Pop III star formation history in our fiducial simulation over the redshift range $23 \geq z \geq 12$. Fig. 4.1 provides a visual impression of their formation sites and feedback effects. Specifically, Figure 4.1 shows full-box projections of baryon density and metallicity for the

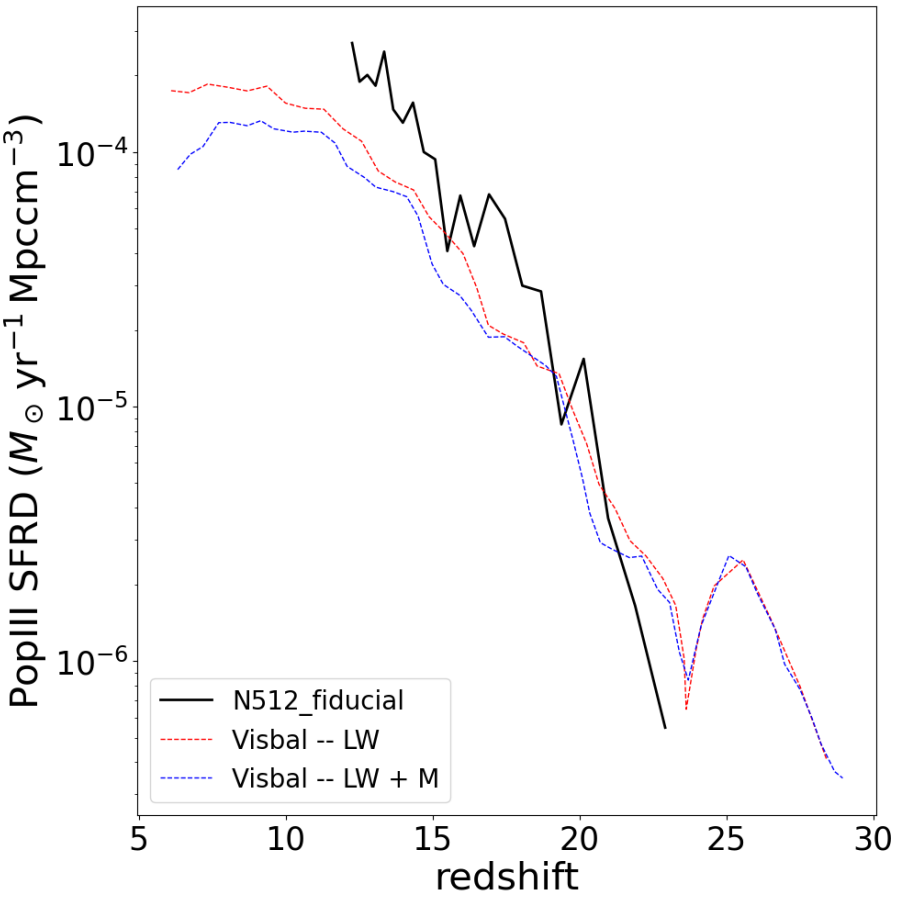

Figure 4.2. Global Pop III SFR vs. redshift for the `N512_fiducial` simulation. The red and blue dashed lines show the rates obtained in Visbal et al. (2020) for the LW and LW+M cases, respectively. LW refers to the semianalytic model that includes the LWB, and LW+M refers to the model that includes both the LWB and external enrichment. Our rates agree very well with those in Visbal et al. (2020) at early times, though our rates are higher at $z \sim 12$ by a factor of 2-3.

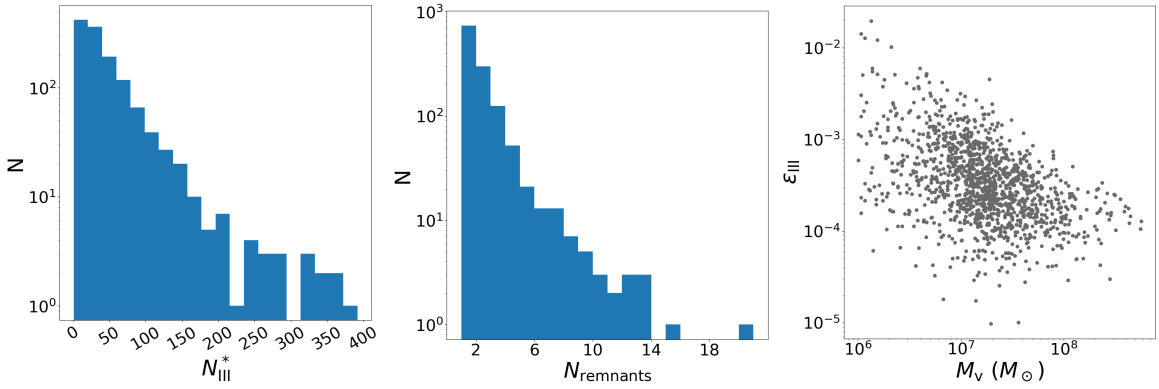

Figure 4.3. *Left:* Distribution of the number of Pop III stars associated with supernova remnants within the virial radius of each halo. Most halos are associated to $\lesssim 50$ Pop III stars, while some have $\gtrsim 300$. Note that the count for the number of Pop III stars here includes those in the mass ranges of $40\,M_\odot < M^*_{\rm III} < 140\,M_\odot$ or $260\,M_\odot < M^*_{\rm III}$ that do not explode as supernovae, but instead collapse into an inert black hole. *Middle:* Distribution of the number of `popIII_remnant` particles within the virial radius of each halo. The number of `popIII_remnant` particles is a measure of the minimum number of separate Pop III associations that contribute to the enrichment of the halo. The actual number of enriching associations could be higher than the number of `popIII_remnant` particles within the virial radius if the halo is externally enriched. *Right:* Pop III star-forming efficiency vs. virial mass for each halo, where the star-forming efficiency is defined as the ratio between Pop III stellar mass and baryon mass.

`N512_fiducial` simulation at $z = 11.92$, with zoomed-in slices through the centers of the two most massive halos shown around the perimeter. The collections of high-metallicity gas are entirely a result of primordial chemical enrichment with `StarNet`. Although metals are initially deposited in uniform spheres, the local morphologies of the deposited remnants lose their sphericity over time due to a combination of hydrodynamic mixing and tidal forces. Examples of the non-spherical morphologies of deposited remnants can be seen in the halo slice plots in Figure 4.1.

By the final output of the `N512_fiducial` simulation, there have been 2,009 separate Pop III star-forming events in the volume predicted by `StarNet` over the course of the simulation. The global Pop III star formation rate density (SFRD) is plotted versus redshift in Figure 4.2, assuming stellar populations predicted by `StarNet` form uniformly over a period of 10 Myr. By $z = 12$, SFRD $\approx 3 \times 10^{-4}\,M_\odot\,{\rm Myr}^{-1}\,{\rm Mpccm}^{-3}$. To verify that the SFRD is reasonable, we overplot two Pop III SFRD curves from Figure 2 of Visbal et al. (2020) for comparison. Our SFRD's generally agree with those in Visbal et al. (2020), though there is a difference of a factor of 2-3 at $z = 12$. This is likely due to our inclusion of H_2 self-shielding, which is not included in Visbal et al. (2020). In the absence of H_2 self-shielding, the LWB will suppress further Pop III star formation. This causes in a turnover of the Pop

III SFRD, which can be seen in the blue and red dashed lines of Figure 4.2. An effect of H_2 self-shielding is to cause a delay in the turnover of the Pop III SFRD, as it allows for efficient H_2 cooling to take place in star-forming cores that would not take place otherwise. Another explanation for the flattening of the SFRD at lower redshifts in the Visbal models is their inclusion of radiative and supernova feedback from Pop II star formation which we do not take into account. According to Visbal et al. (2020), growing spheres of photoionized and chemically enriched gas from normal star formation in protogalaxies exclude an increasing volume of the IGM from forming Pop III stars.

By inspecting the number of massless `popIII_remnant` particles within the virial radius of a given halo, we can obtain information about the number of separate supernova remnants that have merged within the halo. Because we explicitly throw out positive `StarNet` predictions in high metallicity gas, it is unlikely that a given halo would experience multiple internal star-forming events. Figure 4.3 shows histograms of the number of Pop III associations contributing to the enrichment of each halo, as well as the total number of stars belonging to the associations, and a plot of the Pop III star-forming efficiency for each halo. Halos are identified using the `ROCKSTAR` halo finder (Behroozi et al., 2013). While most of the halos contain < 5 `popIII_remnant` particles as expected, many halos contain > 10 `popIII_remnant` particles, with the most massive halo in the simulation containing 20 by the final output. This means that the enriched gas in this halo is the result of a merger between at least 20 separate supernova remnants, with the majority of remnants being deposited initially outside the most massive halo's virial radius and being accreted.

The Pop III star-forming efficiency shown in Figure 4.3 is defined as

$$\varepsilon_{\rm III} = \frac{M^*_{\rm III}}{M_{\rm b}}. \tag{4.1}$$

In this case, $M^*_{\rm III}$ refers to the total mass of stars associated with all remnants within the virial radius. Since these stars are assumed to have all reached their endpoint, $\varepsilon_{\rm III}$ is a direct measure of the fraction of gas within the halo that was once contained within Pop III stars. There is a wide scatter due to the stochastic nature of the population statistics, but there is generally a downwards trend as baryon accretion rates increase with halo mass. The geometric mean of $\varepsilon_{\rm III}$ is approximately 3×10^{-4}.

4.3.2 Chemical Enrichment

By the final output of `N512_fiducial`, there are 12,423 halos in the sample—2,018 (16%) of which are chemically enriched. Of the chemically enriched halos, 1,265 (63%) are enriched externally, where an externally enriched halo is defined to be a halo where

$$M_Z > M_{Z,\mathrm{p}}. \tag{4.2}$$

M_Z is represents the total metal mass within the virial radius, and $M_{Z,\mathrm{p}}$ represents the total mass of metals produced by internal supernovae. The fraction of enriched halos that are externally enriched is in agreement with Hicks et al. (2021), which achieves a similar result using an explicit model for Pop III star formation and feedback that tracks the formation and destruction of individual stars. Going further, 786 (62%) of the externally enriched halos are *primarily* externally enriched, meaning that $> 50\%$ of the metals observed inside the virial radius originate from external sources.

Figure 4.4 shows halo mass functions for each subset of halos previously discussed. While 10,405 (84%) of halos are pristine by the final output, only 10 pristine halos have $T_{\mathrm{vir}} > 10^4$ K. Apart from these 10, all halos with $T_{\mathrm{vir}} > 10^4$ K are chemically enriched. This is significant because the gas within halos with $T_{\mathrm{vir}} > 10^4$ K is expected to cool predominantly through radiative line transitions in atomic hydrogen and helium (Omukai, 2001). However, Figure 4.4 shows that metal-line cooling is almost always present in halos with $T_{\mathrm{vir}} > 10^4$ K.

`Enzo-E` uniquely tracks separate metallicity fields for each type of supernova considered by `StarNet`. As such, it is possible to disentangle the relative contributions to the enrichment of halos from each type of supernova. Figure 4.5 shows a phase diagram of halo-averaged metallicity vs. virial mass, where the set of fractional contributions from each type of supernova to the total metal mass within each bin are mapped to RGB color values (red = core-collapse SNe, green = HNe, blue = PISNe). The diagram is almost entirely shades of blue and green, meaning that enrichment is dominated by HNe and PISNe. There are many halos with equal contributions of HNe and PISNe metals. These results are highly dependent on the chosen characteristic mass of Pop III stars because it determines the relative fraction of supernovae of each type. The distribution of combined halo-averaged metallicities peaks at $10^{-3}\ Z_\odot$ (see right panel of Fig. 4.5), with halos at the high-mass end having a higher tendency towards this value.

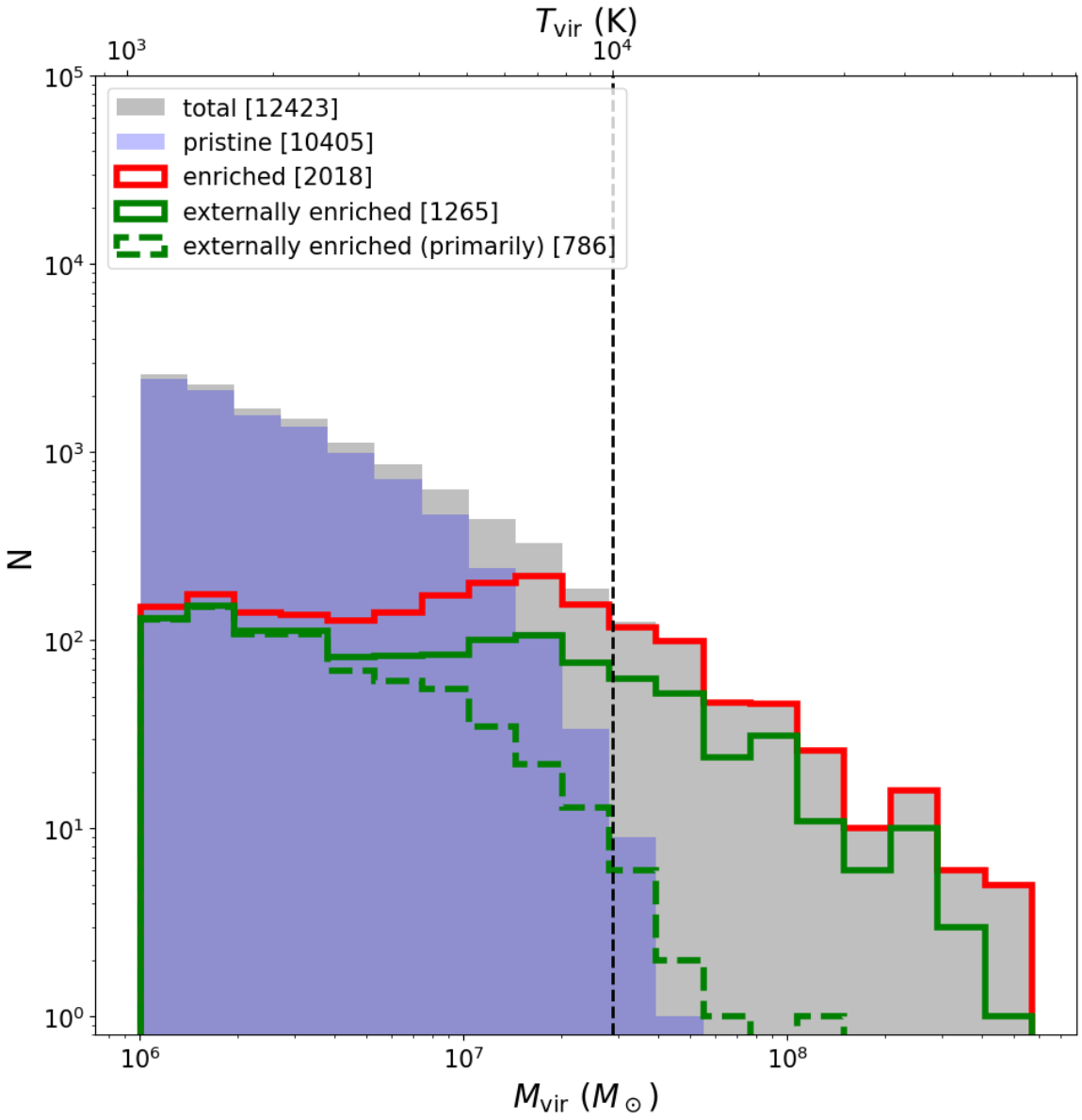

Figure 4.4. Halo mass functions for halos in the `N512_fiducial` simulation at $z \sim 12$. The grey filled histogram shows the mass function for all halos. The blue filled histogram shows the mass function for pristine halos (i.e. halos that have not been chemically enriched by Pop III supernovae). The red curve shows the mass function for halos that have been chemically enriched by Pop III supernovae. The green solid curve shows the mass function for the subset of enriched halos that have been externally enriched. The green dashed curve shows the mass function for the subset of externally enriched halos that have been enriched *primarily* by external sources. The bracketed numbers in the figure legend show the total number of halos for each label. The vertical dashed line shows the virial mass corresponding to a virial temperature of 10^4 K at the final redshift. All but 11 halos with virial temperatures above 10^4 K are chemically enriched by the final redshift.

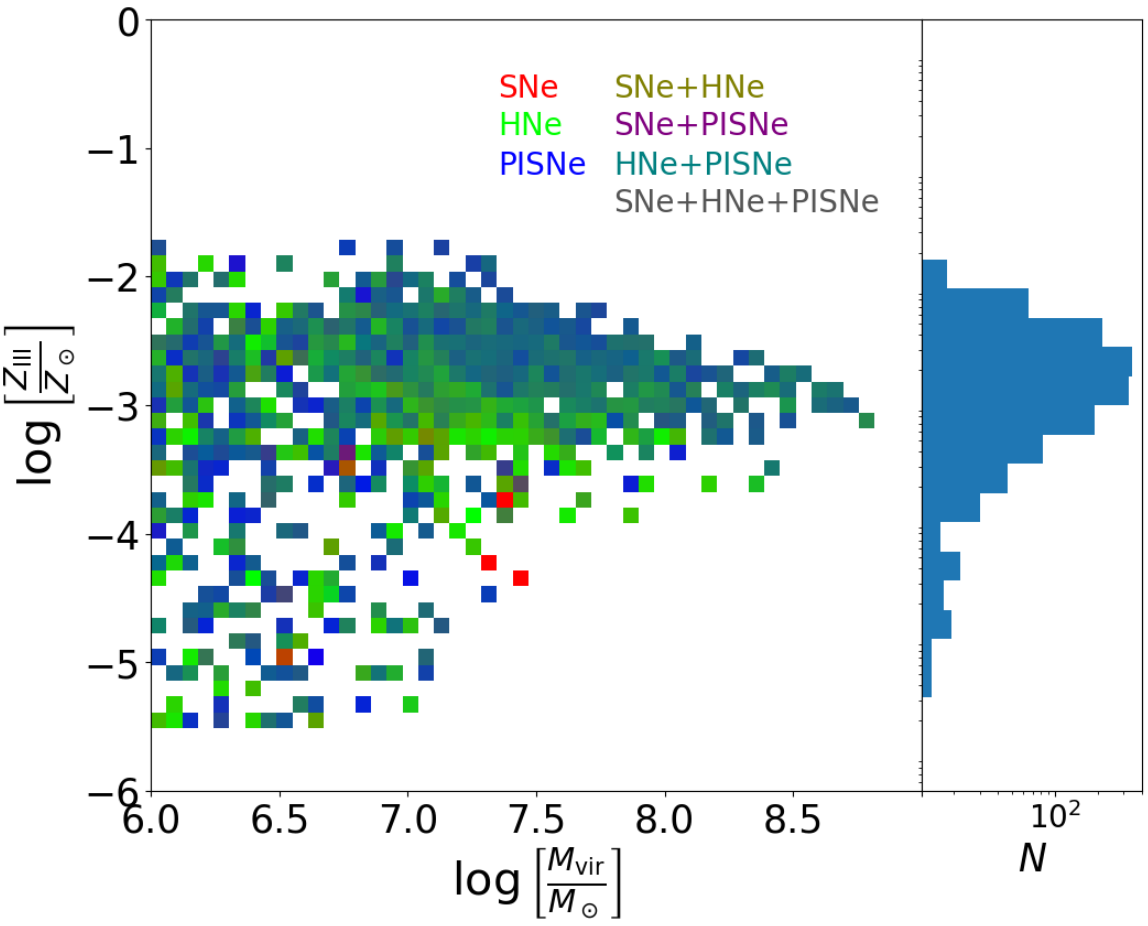

Figure 4.5. *Left:* 2D histogram of Pop III metallicity vs. virial mass for chemically enriched halos, where a given bin is colored by the relative contribution by type II SNe, HNe, and PISNe to the enrichment of halos within that bin. To compare the relative contributions in a bin, the total mass of metals sourced from supernovae of each type within the virial radius are summed separately over all halos within the bin. The masses are normalized by the total, and mapped to an RGB color index, given by, $\left(\frac{M_{\rm SNe}}{M_{\rm tot}}, \frac{M_{\rm HNe}}{M_{\rm tot}}, \frac{M_{\rm PISNe}}{M_{\rm tot}}\right)$, where $M_{\rm tot} = M_{\rm SNe} + M_{\rm HNe} + M_{\rm PISNe}$. Colors corresponding to various combinations of supernova contributions in equal amounts are shown in the text in the upper right-hand corner. The image is made up mostly of shades of blue and green, which suggests that enrichment is overall dominated by both HNe and PISNe. Subhalos are filtered out of the sample for this figure to avoid the double counting of metals. As halo mass increases, metallicities tend towards $10^{-3}\ Z_\odot$. *Right:* Distribution of the average halo metallicity within the virial radius. The distribution peaks at $2 \times 10^{-3}\ Z_\odot$.

4.3.3 Accretion and Cooling

For the following analysis, halos in the sample are classified as "cooling" if the average cooling time within R_{1000} is less than a Hubble time. Cooling rates and times are calculated in post using `PyGrackle`[2], the Python frontend of the `GRACKLE` chemistry and cooling library. We consider the following three modes of radiative cooling: (1) line transitions in atomic hydrogen and helium, (2) rovibrational line transitions in molecular hydrogen, and (3) metal-line transitions. The average volumetric cooling rate of each type is calculated within R_{1000} as

$$\overline{\Lambda} = \frac{\sum_i \Lambda_i \Delta x_i^3}{\sum_i \Delta x_i^3}, \tag{4.3}$$

where i denotes the cell index and Δx_i is the width of cell i. A corresponding cooling time is then calculated as

$$t_{\rm cool} = \frac{\overline{\varepsilon}_{\rm int}}{\overline{\Lambda}}, \tag{4.4}$$

where $\overline{\varepsilon}$ is the average volumetric internal energy density within R_{1000}. The cooling halos are then further classified as either (1) atomic cooling halos, (2) H_2 cooling halos, or (3) metal cooling halos, depending on which of the three averaged cooling rates is largest within R_{1000}.

For each halo, we compute the accretion rate as the baryon mass flux through the virial radius:

$$\dot{M}_{\rm acc} = -4\pi R_{\rm vir}^2 \frac{\sum_{i(r=R_{\rm vir})} \mathbf{p}_i \cdot \hat{r}}{\sum_{i(r=R_{\rm vir})} \Delta x_i^3}. \tag{4.5}$$

Here, $\hat{r}$ is the radial unit vector, centered at the halo's center of mass, and $\mathbf{p}_i$ is the gas momentum for a given cell, i, which is at the virial radius. The velocity used in computing the gas momentum is taken to be the value relative to the halo's center-of-mass velocity.

Figure 4.6 plots the accretion rates versus virial mass for halos in the `N512_fiducial` simulation. There is a clear positive correlation between the two quantities. The data for cooling and non-cooling halos are separately fit to power laws of the form $dM/dt \propto M^{\beta}$. The two curves have similar slopes, indicating the physics of accretion is independent of cooling. The cooling halo curve has a slope of $\beta = 0.92$, and the non-cooling curve has a slope of $\beta = 0.83$. The majority of halos with $M_{\rm vir} > 10^7\ M_{\odot}$

[2] https://grackle.readthedocs.io/en/latest/Python.html

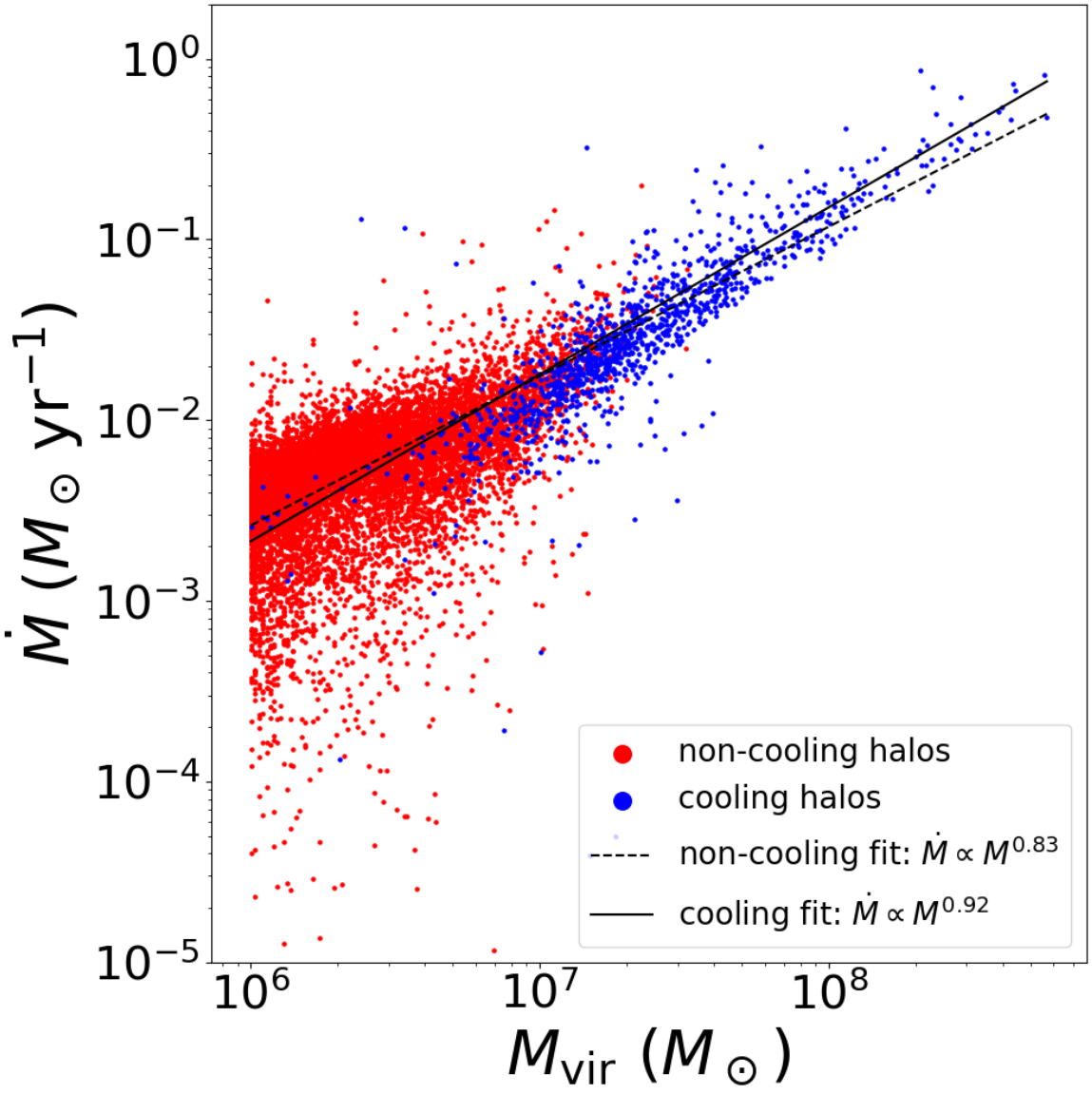

Figure 4.6. Accretion rate through the virial radius vs. virial mass for cooling halos (blue) and non-cooling halos (red). Each sample is fit separately to a power law. The slopes are 0.92 for cooling halos and 0.83 for the non-cooling halos. The similarity in the two slopes suggests that cooling does not drive gas accretion through the virial radius. For consistency, we have also made similar power law fits for H_2 cooling halos, metal cooling halos, and all halos. These additional fits are not plotted, but the slopes are 0.99 for H_2 cooling halos, 0.82 for metal cooling halos, and 0.92 for all halos. Subhalos are filtered out of the sample for this analysis.

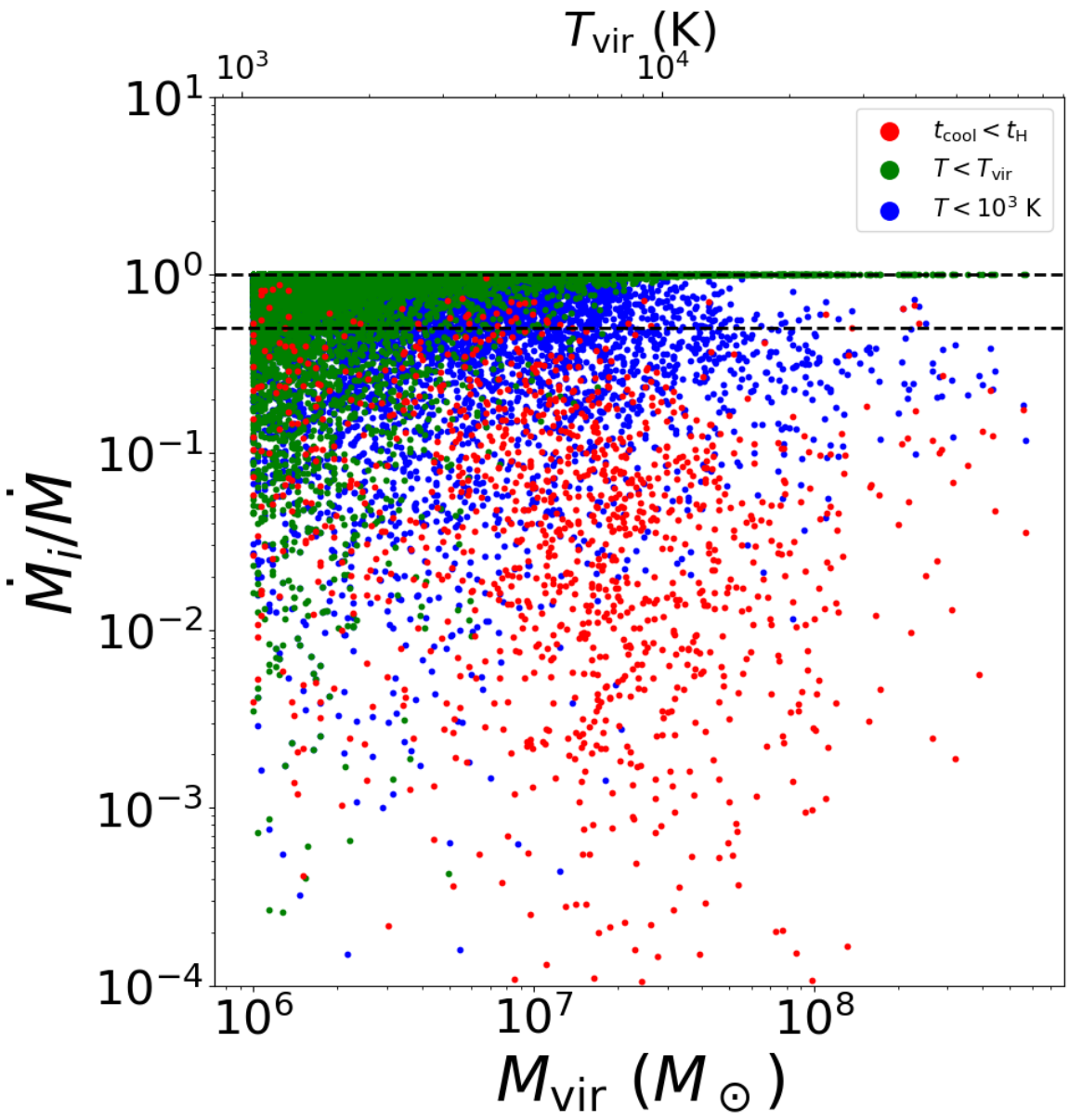

Figure 4.7. Fractional inflow rates for gas at the virial radius that is cooling (red), below $T_{\rm vir}$ (green), and/or below 10^3 K (blue). Horizontal dashed lines are at fractional rates of 0.5 and 1.0. Blue (green) dots between the horizontal lines show halos where most of the gas flowing into the virial radius has $T < 10^3$ K ($T < T_{\rm vir}$). Red dots between the horizontal lines show halos where the majority of the gas flowing into the virial radius is able to cool in less than a Hubble time.

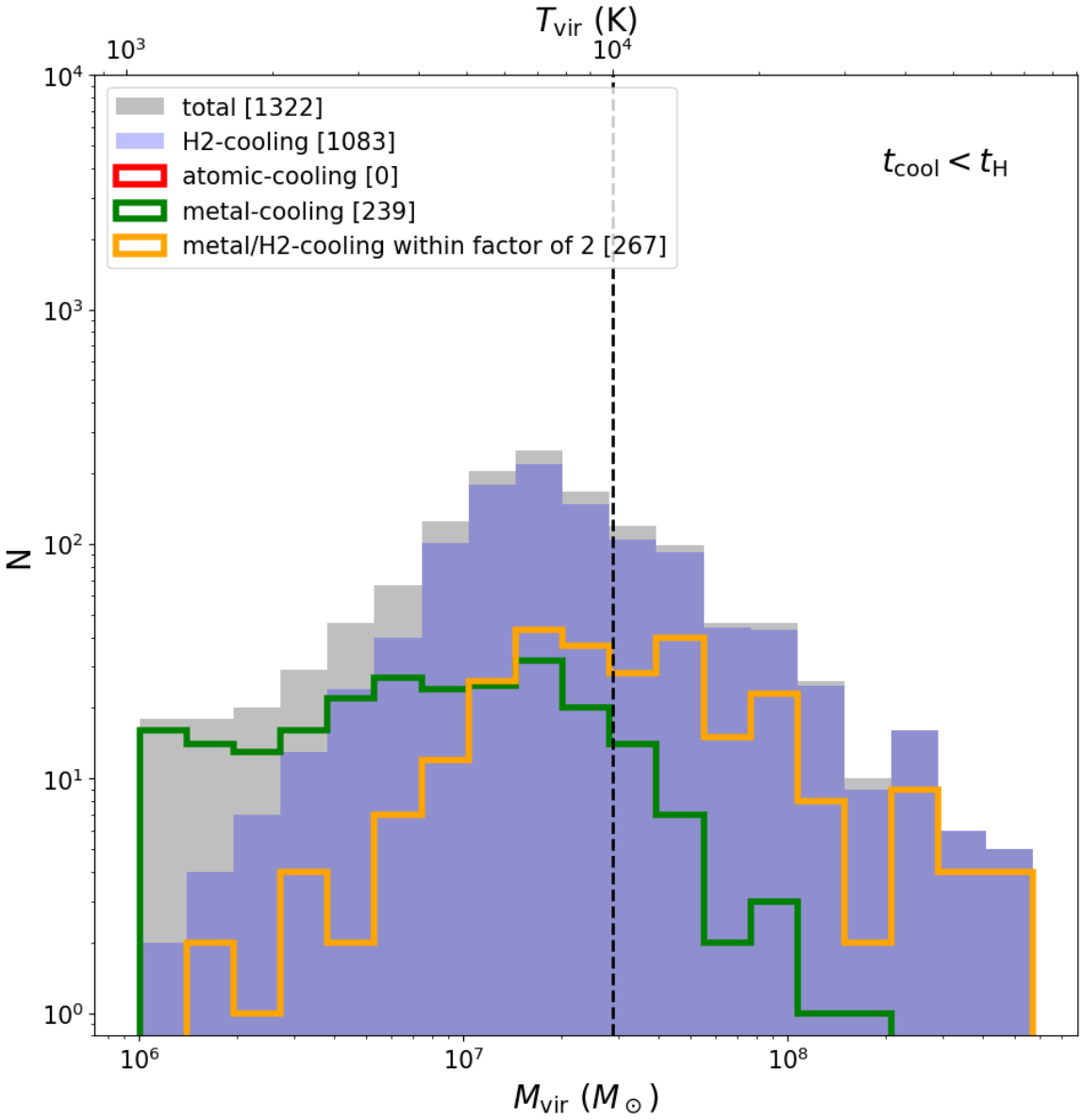

Figure 4.8. Halo mass functions for cooling halos. The grey histogram shows the mass function for all cooling halos. The blue histogram shows the mass function for H_2 cooling halos. The green curve shows the mass function for metal cooling halos. The orange curve shows cooling halos that have relative mean H_2 and metal cooling rates within R_{1000} that are within a factor of 2 of eachother. The vertical dashed line corresponds to a virial temperature of 10^4 K. The total number of each type of halo is placed in brackets in the figure legend. Atomic cooling halos would show up in this plot as a red curve; however, we find zero atomic cooling halos in the sample.

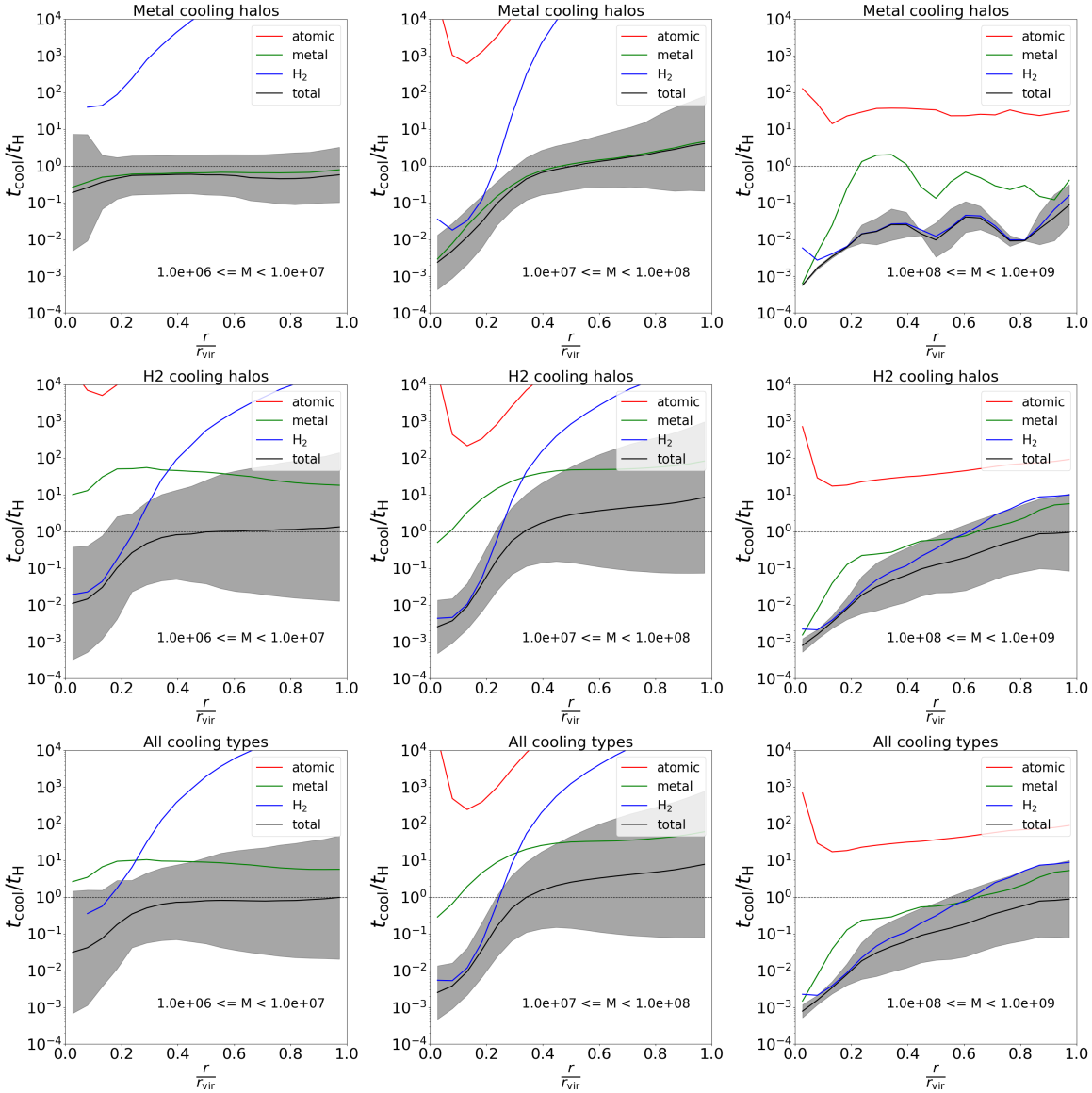

Figure 4.9. Radial profiles of average cooling time, normalized by the Hubble time at $z \sim 12$, for halos in bins of virial mass and dominant cooling type within R_{1000}. The top and middle rows show profiles for halos that cool primarily though metals and H_2, respectively, while the bottom row shows profiles for all cooling halos, regardless of which coolant is dominant. The columns separate halos into mass bins, with mass increasing from left to right. The text in the plot denotes the mass of halos within a given bin. Atomic cooling rates are shown in red, metal cooling rates are shown in green, H_2 cooling rates are shown in blue, and the total cooling rates are shown in black. The regions filled in with grey extend out to 1 standard deviation in log space from of the total cooling rate curve. The gas in the most massive halos is, on average, cooling at all radii.

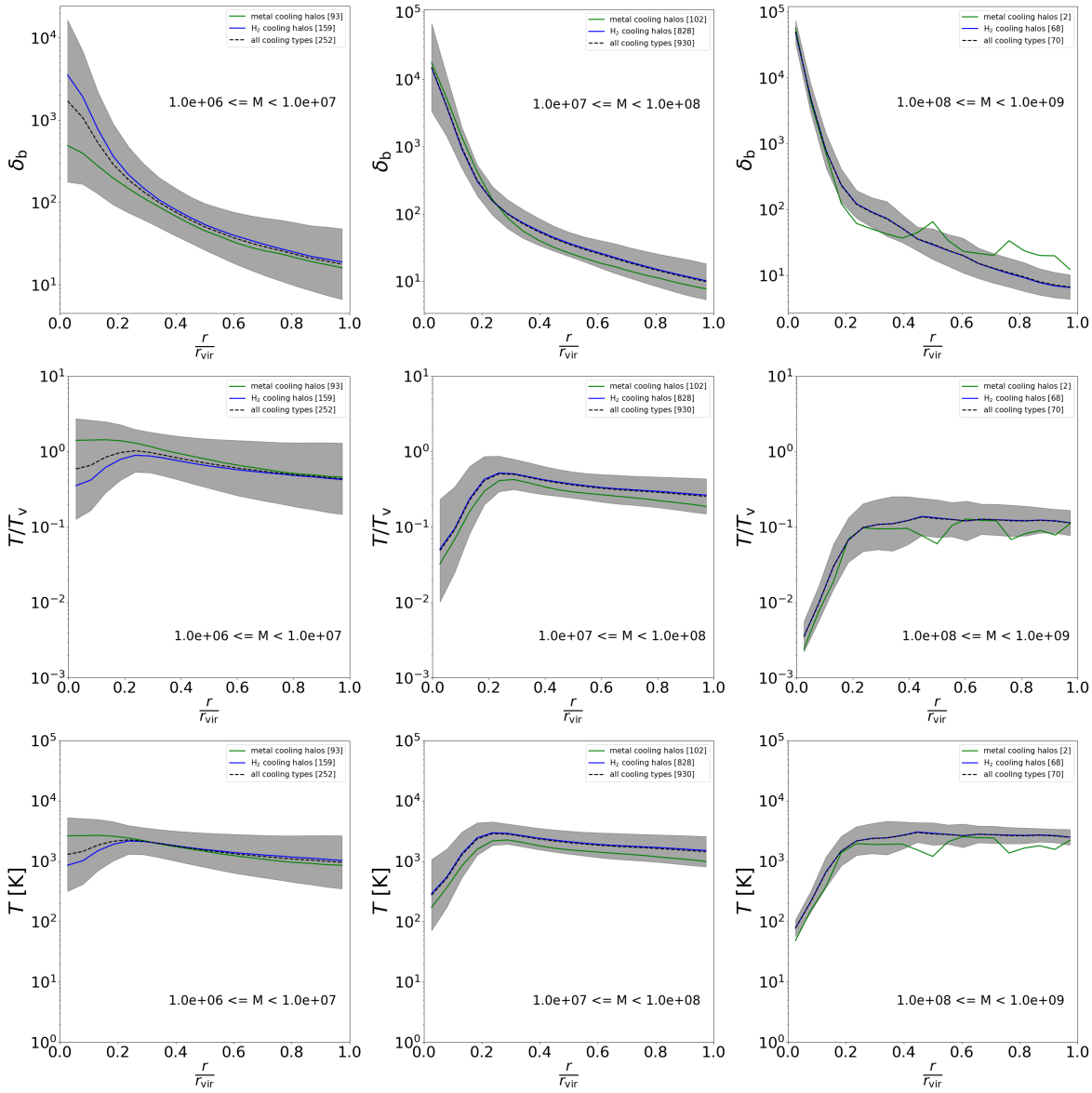

Figure 4.10. Average radial profiles of various gas properties for halos, binned by cooling type and virial mass. Each row shows a different gas property, and each column corresponds to halos in a given mass range. Metal cooling halos are shown in green, H_2 cooling halos are shown in blue, and the combined sample of cooling halos is shown in black. From top to bottom, profiles are plotted for baryon overdensity, normalized gas temperature, and un-normalized gas temperature, metallicity. The grey filled region extends out to 1 standard deviation in log space for the "all cooling halos" sample.

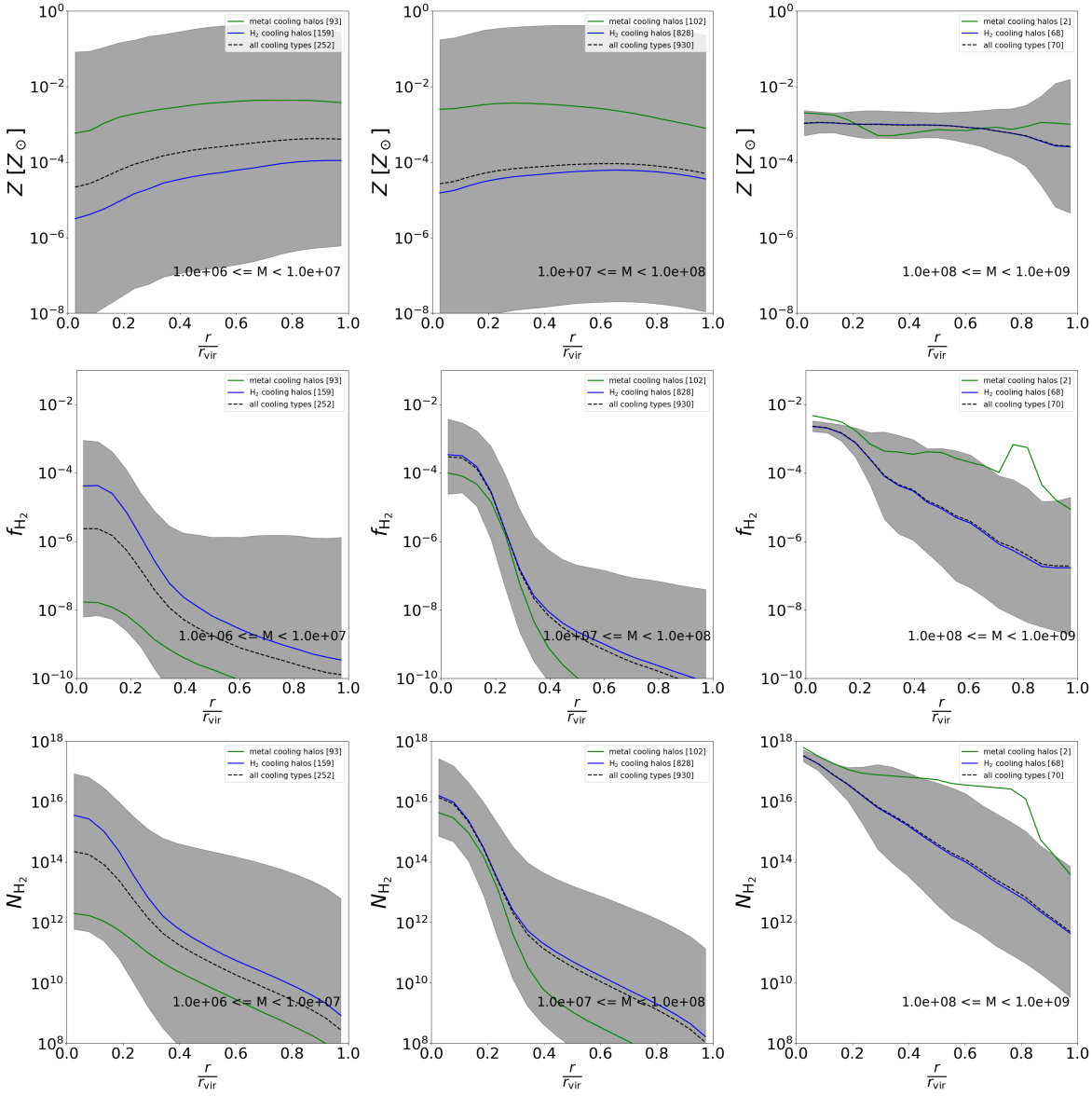

Figure 4.11. Same as Figure 4.10, but showing profiles for metallicity, H_2 fraction, and H_2 column density.

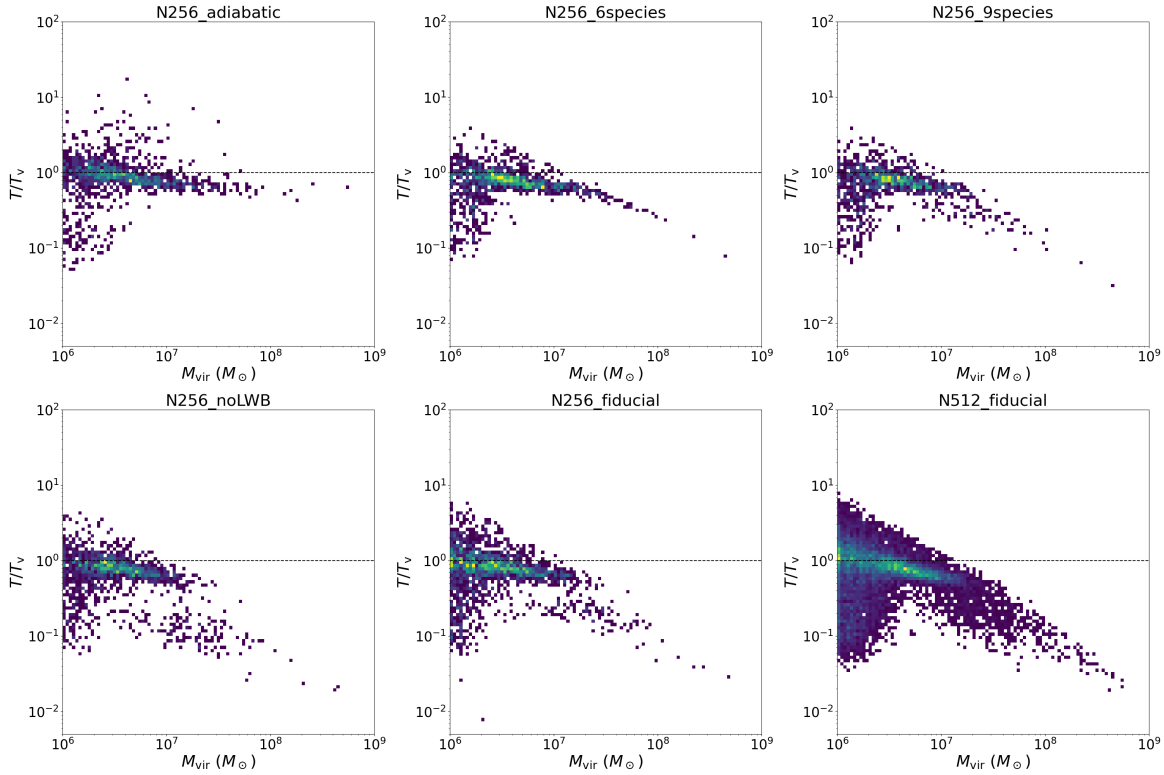

Figure 4.12. Normalized gas temperature within the virial radius for all halos in the simulations listed in Table 4.1. An ideal virialized halo would have $T/T_{\rm vir} \approx 1$.

are cooling within R_{1000}.

Figure 4.7 shows fractional inflow rates for gas at the virial radius that is cooling ($t_{\rm cool} < t_{\rm Hubble}$, red points), has $T < T_{\rm vir}$ (green points), and has $T < 10^3$ K (blue points). Fractional inflow rates are computed for each halo in the `N512_fiducial` simulation. Total inflow rates are calculated in the same way as accretion rates with Equation 4.5, except that only gas flowing inwards (i.e. cells with $\mathbf{p}_i \cdot \hat{r} < 0$) contributes to the summation in the numerator. The inflow rates for gas satisfying each of the three conditions listed above are then calculated and normalized by the total. An immediate takeaway from this figure is that for most halos, the inflowing gas is non-cooling. For halos with $M_{\rm vir} \gtrsim 3 \times 10^7\ M_\odot$ that we observe, most of the gas flowing in has 10^3 K $< T < T_{\rm vir}$. For most halos below this mass, the gas flows in with $T < 10^3$ K, though there is more scatter as halo mass decreases.

Figure 4.8 shows halo mass functions for cooling halos of various types. Cooling halos account for 12% of halos in the sample. The most striking result from Figure 4.8 is the complete absence of atomic cooling halos. Halos with $T_{\rm vir} > 10^4$ K are often colloquially referred to as "atomic cooling halos", as it is

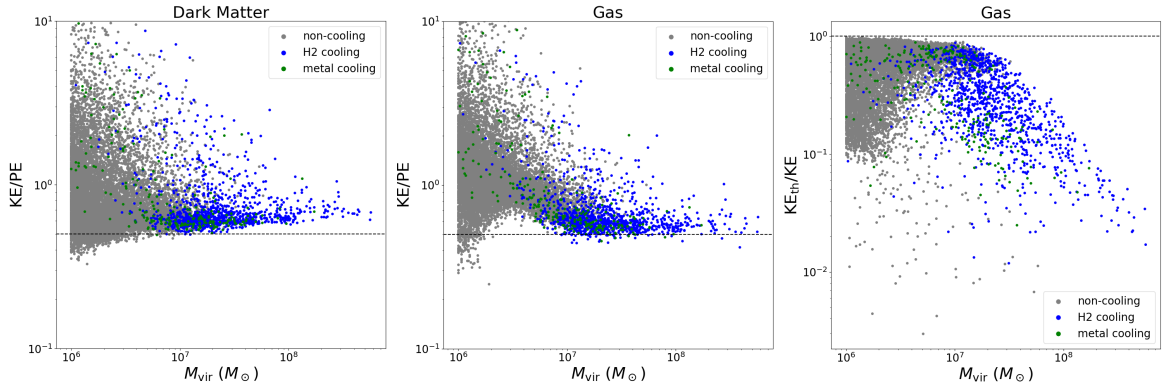

Figure 4.13. *Left:* Ratio of total kinetic to total potential energy for dark matter particles within the virial radius. The horizontal dashed line corresponds to KE/PE=0.5, which is the value corresponding to an ideally virialized halo. *Middle:* Ratio of total kinetic, including thermal and bulk motions, to total potential energy for gas within the virial radius. *Right:* Ratio of thermal energy to total kinetic energy. For each panel, grey points represent non-cooling halos, blue points represent H_2 cooling halos, and green points represent metal cooling halos.

typically assumed that gas at the center of these will cool primarily through atomic line transitions of H and He; however we do not observe this behavior in any of our halos, even those that are not yet metal enriched by supernovae. Instead, we observe that H_2 cooling is overall dominant for halos with $M_{\rm vir} > 10^4$ K. H_2 cooling halos account for 82% of all cooling halos. The remaining 18% of halos are dominated by metal-line cooling. 20% of cooling halos have average metal and H_2 cooling rates that are within a factor of 2 of each other, meaning that there are significant contributions from both metal and H_2 cooling.

While the most massive halos tend to be dominated by H_2 cooling within R_{1000}, metal cooling tends to exceed H_2 cooling further in towards the center. This can be seen in the third column of Figure 4.9, which shows average profiles of cooling time, normalized by the Hubble time, for halos of each cooling type across three mass ranges. For metal cooling halos with $M_{\rm vir} < 10^8\ M_\odot$, metal cooling is dominant at all radii. For H_2 cooling halos in this mass range, metal cooling times, while lower than H_2 cooling times at large radii, generally do not drop below the Hubble time. The H_2 cooling times for these halos drop below the Hubble time for $r/R_{\rm vir} < 0.2$.

Cooling halos with virial mass between $10^6\ M_\odot$ and $10^7\ M_\odot$ tend to have flat cooling time profiles, with $t_{\rm cool} < t_{\rm H}$ at all radii. As halo mass increases, the average profiles steepen for $r/R_{\rm vir} < 0.3$. For metal cooling halos with $M_{\rm vir} > 10^7\ M_\odot$, gas within within R_{1000} is still able to cool in less than a Hubble time through H_2 cooling alone.

Figures 4.10 and 4.11 show average radial profiles for a variety of physical properties of the gas within cooling halos of different mass ranges. The baryon overdensity profiles generally steepen towards the center as halo mass increases, as can be expected, with metal and H_2 cooling halos reaching similar overdensities on average. In regards to the temperature of the gas, the average temperature at the virial radius does not change significantly as virial mass increases. When normalized by $T_{\rm vir}$, then, the temperature profiles generally shift downwards as virial mass increases. One would naïvely expect that the average gas temperature within a virialized halo will be equal to the virial temperature, corresponding to $T/T_{\rm vir} = 1$ within the virial radius. This is approximately true for the lowest mass bin; however, the two higher mass bins show average values of $T/T_{\rm vir} < 1$ for all radii. At face value, this suggests that halos with $10^7\,M_\odot < M_{\rm vir} < 10^8\,M_\odot$ have not yet reached virial equilibrium at $z \sim 12$, and are actively accreting gas that is not shock heated to the virial temperature.

The presence of a strong LWB serves to photodissociate H_2. Intuitively, one would expect H_2 cooling to be suppressed by the LWB. This is generally true in low-density environments; however, we do not observe suppressed H_2 cooling in dense cores. This is primarily due to H_2 self-shielding. The bottom two rows of Figure 4.11 show average profiles for H_2 fraction ($f_{\rm H_2}$) and H_2 column density ($N_{\rm H_2}$). At large radii, $f_{\rm H_2}$ is generally low, with values $\leq 10^{-8}$ for the central mass bin. At $r/R_{\rm vir} \approx 0.3$, the $f_{\rm H_2}$ and $N_{\rm H_2}$ curves both sharply increase. H_2 self-shielding becomes non-negligible at $N_{\rm H_2} \approx 5 \times 10^{14}$ cm^{-2} for the self-shielding model used in our simulation (Wolcott-Green & Haiman, 2019).

4.3.4 Cooling vs. Incomplete Virialization

The temperature profiles in Figure 4.10 suggest that the halos in the `N512_fiducial` simulation are generally not in true virial equilibrium, using the virial temperature as a metric. Lochhaas et al. (2021) shows that the virial temperature is not an accurate description of virialized gas, as bulk flows at the center of the halo provides a non-negligible contribution of non-thermal kinetic energy to the system, which is not taken into account in the formal definition of the virial temperature. Using a set of cosmological zoom-in simulations of star-forming galaxies, they find that the true mean temperature within a "virialized" halo is typically lower than $T_{\rm vir}$ by a factor of ~ 2. It should be noted that the simulations in Lochhaas et al. (2021) include thermal energy injection due to various forms of Pop II stellar feedback, thus providing efficient means of heating the gas to offset radiative cooling, while our simulations do not. The most

massive halos in our simulations experience runaway cooling at their center, which drives the mean halo gas temperature down to values $\sim 50\times$ smaller than $T_{\rm vir}$. This can be seen in Figure 4.12, which shows the mean gas temperature within the virial radius, scaled by $T_{\rm vir}$, for every halo across all of our simulations. In each case, there is a large scatter for halos with $M_{\rm vir} \lesssim 5 \times 10^6\,M_\odot$. The scatter then decreases for $M_{\rm vir} \gtrsim 10^7\,M_\odot$. Beyond this point, the values either level out as $M_{\rm vir}$ increases, as is the case in the `N256_adiabatic` simulation, or steadily drop as gas cooling becomes more efficient at the halo centers. In the adiabatic case, the values level out at $T/T_{\rm vir} \sim 0.6$, which is in agreement with the findings in Lochhaas et al. (2021). For the `N256_6species` simulation, the temperatures drop smoothly with very little spread as $M_{\rm vir}$ increases. The `N256_9species`, `N256_fiducial`, and `N512_fiducial` values have more scatter at high masses because there is more complexity in the physics contributing to cooling, and reach values of $T/T_{\rm vir}$ as low as 10^{-2}.

As a direct measure of virialization, we show the ratio of the total kinetic energy to total potential energy separately for dark matter and gas for each halo in Figure 4.13. For the gas, the kinetic energy is taken to be the sum of both the thermal and non-thermal components, where the non-thermal component is computed as

$$\mathrm{KE} = \sum_{i=0}^{N_{\rm cells}} \frac{1}{2} M_i v_i^2, \tag{4.6}$$

where i loops over cells within the virial radius. The dark matter KE is computed in the same way as the gas, except instead of looping over cells in Equation 4.6, i loops over dark matter particles. Potential energies are computed pairwise. The dark matter potential energy takes into account DM-DM gravitational interactions, as well as DM-gas, and vice versa for the gas potential energy. Specifically,

$$\mathrm{PE}_{\rm gas} = -\frac{1}{2}\left[\sum_{j=0}^{N_{\rm cells}}\sum_{i=0}^{N_{\rm cells}} \delta_{ij} + \sum_{j=0}^{N_{\rm dm}}\sum_{i=0}^{N_{\rm cells}}\right] G\frac{M_i M_j}{r_{ij}} \tag{4.7}$$

for the gas, and

$$\mathrm{PE}_{\rm dm} = -\frac{1}{2}\left[\sum_{j=0}^{N_{\rm dm}}\sum_{i=0}^{N_{\rm dm}} \delta_{ij} + \sum_{j=0}^{N_{\rm cells}}\sum_{i=0}^{N_{\rm dm}}\right] G\frac{M_i M_j}{r_{ij}} \tag{4.8}$$

for the dark matter. Here, $r_{ij} = \mathtt{max}\left(\left|\mathbf{r}_{\rm i} - \mathbf{r}_{\rm j}\right|,\, \varepsilon\right)$, where $\varepsilon = 1$ kpccm (0.08 kpc at $z = 12$, which is roughly equal to 3 cell widths at the highest AMR refinement level). δ_{ij} evaluates to zero if $i = j$. The summations are multiplied by a factor of 1/2 to avoid double-counting.

For an ideal virialized halo, the magnitude of the time-averaged ratio of kinetic to potential energy should equal 0.5, as denoted by the dashed lines in the left and middle panel of Figure 4.13. We see in Figure 4.13 that there is a lot of scatter in KE/PE at the low virial mass, but values concentrate at the high mass end around KE/PE ≈ 0.6 for both the dark matter and the gas, suggesting that both the dark matter and gas are in a dynamical equilibrium consistent with virialization. We show the ratio between the thermal energy and total kinetic energy of the gas in the right panel of Figure 4.13. As halo mass increases, we observe that the gas KE becomes increasingly dominated by the non-thermal component. This is related to the runaway cooling effect that we discuss above. The shape of the gas profile mirrors that of the temperature profile in the `N512_fiducial` panel of Figure 4.12. From this, we can infer that while the gas is virialized for $M_{\rm vir} \gtrsim 10^7\ M_\odot$, virialization is supported by bulk turbulent flows, and not by thermal motions. For this reason, we describe these halos as being in a state of "incomplete virialization". If the gas KE was instead dominated by the thermal component, we would expect the halo-averaged gas temperatures in Figure 4.12 to be roughly equal to the virial temperature.

Due to the low gas temperatures in halos with $M_{\rm vir} \gtrsim 10^7\ M_\odot$, internal flows become increasingly supersonic on average as halo mass increases. This is shown in Figure 4.14, which plots mean Mach number within the virial radius versus virial mass for all halos in the `N512_fiducial` simulation. At the high mass end, mean Mach numbers have values of $\mathscr{M} > 10$. The shocks that result from colliding supersonic flows within the virial radius drive the turbulence that supports the virialization state of the gas.

4.3.5 The Cosmic Web at Redshift 12 Consists of Warm Filaments

We now take a short detour to discuss the properties of the medium that connects our dark matter halos together. We have seen that the majority of gas flowing into these halos flows in through filaments with temperatures between 10^2 K and 10^4 K at $z \sim 12$, with 10^3 K being typical (Fig. 4.10). It is not unsurprising, then, that this is the temperature range that generally describes the entire network of filaments at this redshift. Figure 4.15 shows a projection of temperature for the `N512_fiducial` simulation, as well as a global phase diagram of temperature versus overdensity. To accompany this, Figure 4.16 shows 1D profiles of baryon overdensity and temperature. Baryon overdensities typical of filaments are $\delta_{\rm b} \simeq 3 - 10$.

Table 4.2. Properties of the five most massive halos in the `N512_fiducial` simulation. From left to right, columns show halo name, dark matter virial mass, total baryon mass within $R_{\rm vir}$, predicted Pop II stellar mass (see Sec. 4.3.7), virial radius in proper kpc, mean metallicity within R_{1000}, the ratio of mean metal cooling rate to mean H_2 cooling rate within R_{1000}, the number of `popIII_remnant` particles within $R_{\rm vir}$, and the total number of computational cells within $R_{\rm vir}$.

Halo Properties								
Name	$M_{\rm vir}$ $[M_\odot]$	$M_{\rm b}$ $[M_\odot]$	$M^*_{\rm II}$ $[M_\odot]$	$R_{\rm vir}$ [kpc]	$\langle Z \rangle_{1000}$ $[Z_\odot]$	Λ_Z/Λ_{H_2}	$N_{\rm remnants}$	$N_{\rm cells}$
`Halo_0`	5.67×10^8	1.21×10^8	1.44×10^6	2.08	7.19×10^{-4}	0.97	20	993,088
`Halo_1`	5.57×10^8	1.09×10^8	1.80×10^6	2.06	1.25×10^{-3}	0.93	13	821,874
`Halo_2`	4.43×10^8	7.76×10^7	1.02×10^6	1.91	1.74×10^{-3}	0.96	13	451,572
`Halo_3`	4.35×10^8	8.22×10^7	8.24×10^5	1.90	9.31×10^{-4}	0.37	10	675,178
`Halo_4`	4.26×10^8	8.17×10^7	8.90×10^5	1.89	9.90×10^{-4}	0.69	12	820,252

The mean temperature of the IGM at a given redshift is given by

$$T(z) = \frac{T_0}{1+200}(1+z)^2, \tag{4.9}$$

where $T_0 = 2.73$ K is the IGM temperature at $z = 0$ (Anninos & Norman, 1996). At $z = 12$, Equation 4.9 evaluates to 2.3 K, which is consistent with the peak temperature value in the right panel of Figure 4.16.

At $z > 10$, the IGM has not yet been heated and ionized by the buildup of a UV background. Because of the low temperatures, and thus low sound speeds, gas flows in the IGM are highly supersonic, with Mach numbers of $\mathscr{M} > 100$. Since $\mathscr{M} \gg 1$, a flow encountering a filament from the outside will be strongly shocked. We have previously seen in Figure 4.7 the gas flowing through filaments into the most massive halos generally has cooling times greater than a Hubble time when it reaches the virial radius. As such, it is reasonable to assume that the shock will be adiabatic. For a strong shock in neutral gas, the post-shock temperature can be written as

$$T_{\rm post} \approx \frac{2(\gamma-1)}{(\gamma+1)^2}\mathscr{M}^2_{\rm pre}T_{\rm pre} \tag{4.10}$$

(Draine, 2011), where $\mathscr{M}_{\rm pre}$ and $T_{\rm pre}$ are the pre-shock Mach number and temperature, respectively. For $\mathscr{M}_{\rm pre} = 100$, $T_{\rm pre} = 2.3$ K, and $\gamma = 5/3$, Equation 4.10 evaluates to 5×10^3 K. This temperature is roughly the maximum temperature observed at the baryon overdensities consistent with filaments in Figure 4.15.

4.3.6 The Five Most Massive Halos

This study is ultimately motivated by the topic of high redshift galaxy formation, which would take place preferentially in the most massive halos. In this section, we analyze the five most massive halos in the `N512_fiducial` simulation, and discuss their potential for galaxy formation. Table 4.2 lists some basic properties of these 5 halos, which have virial masses between $4 \times 10^8\ M_\odot$ and $6 \times 10^8\ M_\odot$. All 5 halos contain metal-enriched gas from > 10 Pop III remnants, yet H_2 cooling rates exceed metal cooling rates within R_{1000}, though halos 0, 1, 2, and 4 have metal cooling rates that are within a factor of 2 of the H_2 cooling rates. For halos 0, 1, and 2, the fraction of mean central metal cooling rates to H_2 cooling rates 0.97, 0.93, and 0.96, respectively, meaning that metal cooling rates are on par with H_2 cooling rates at the centers of these halos.

We show zoomed-in projections of dark matter, baryon number density, H_2 fraction, metallicity, and temperature for the 5 most massive halos in Figure 4.17. In the dark matter projections, much substructure can be seen. The halos look to be in various stages of merging with nearby halos. As a result, the baryon distributions have highly irregular morphologies. Halos 0 and 1 in particular are undergoing major mergers, as is evident by the strong tidal disruption in both the dark matter and the baryon density projections. Halo 2 is perhaps the most stable system of the batch, with a quasi-spherical distribution of particles at the center, and multiple satellite halos. H_2 flows in through filaments, and gas with $n_\mathrm{b} \gtrsim 5 \times 10^{-1}\ \mathrm{cm}^{-3}$ is self-shielded to H_2 photodissociation by the LWB, resulting in large H_2 fractions within the halos.

Projections of atomic, metal, H_2, and total cooling rates for the five most massive halos are shown in Figure 4.18. The H_2 cooling rates are visibly very similar to the total cooling rates, which again demonstrates the importance of H_2 cooling. The regions where metal cooling is important appear to be more concentrated towards the halo centers. Atomic cooling rates appear to be non-zero along the filament boundaries, where some amount of shock heating has taken place. However, atomic cooling does not make any significant contribution to cooling when compared with the total cooling rates.

Figure 4.19 shows phase diagrams of H_2 fraction, metallicity, volumetric cooling rate, and temperature versus baryon number density for the gas within each of the five most massive halos. The images look very similar for each of the chosen halos. The effects of H_2 self-shielding can be observed in the H_2 fraction diagrams (leftmost column), where the distribution for $n \gtrsim 10^{-1}\ \mathrm{cm}^{-3}$ becomes bimodal,

with values tending towards $f_{H_2} = 10^{-3}$ at large densities. Metallicities (second column from the left) tend towards $Z = 10^{-3}\ Z_\odot$ at large densities. This tendency of metallicities towards $10^{-3} Z_\odot$ also shows up in the halo-averaged metallicities of Figure 4.5, where the mean metallicities of gas within high mass halos are also concentrated around $10^{-3}\ Z_\odot$.

4.3.7 Estimates Of Pop II Star Formation

We estimate the mass of Pop II stars, $M^*_{\rm II}$, that would potentially form in the most massive halos if a model for explicit Pop II star formation was included in the `N512_fiducial` simulation. To do this, we apply the following set of set of star-forming criteria in post to identify potential star-forming cells:

1. *gas flow is converging:* $\nabla \cdot \mathbf{v} < 0$
2. *gas is self-gravitating:* $\frac{\varepsilon}{\varphi} < 1$, where ε is the specific total energy of the gas, and φ is the gravitational potential. The ratio of these two quantities is akin to the virial parameter described in Hopkins et al. (2018a).
3. *cell mass is above a Jeans mass:* $M_{\rm cell} > M_{\rm Jeans}$
4. *gas is enriched:* $Z_{\rm cell} > Z_{\rm crit}$, where we take $Z_{\rm crit} = 10^{-5.5}\ Z_\odot$

The set of star formation criteria is inspired by the set used in Hopkins et al. (2022), and are those we will use in a followup study that will include an explicit recipe for Pop II star formation and feedback in a re-run of `N512_fiducial`. We have verified that the inclusion of a criterion enforcing a minimum gas density for star formation is not necessary, as gas density is implicitly taken into account in the Jeans mass and self-gravitating criteria (items 2 and 3, respectively). The flagged star-forming cells typically have baryon overdensities between 10^4 and 10^5, which is consistent with the central overdensities seen in Figure 4.10. We assume a conversion fraction of gas into stars of 0.05, and multiply the gas mass within a cell that satisfies all criteria by this value to obtain an estimate of the Pop II stellar mass. We then compute the Pop II SFR as

$$\mathrm{SFR} = \frac{\eta_{sf} M_{\rm b}}{t_{\rm ff}}, \tag{4.11}$$

where $\eta_{\rm s} = 0.05$ is the conversion fraction of gas into stars, $M_{\rm b}$ and $t_{\rm ff}$ are the baryon mass and freefall time of the star forming cell, respectively. If multiple cells are flagged as star-forming in a halo, we report

the total stellar mass and SFR summed over all flagged cells.

The Pop II stellar mass estimates for the 5 most massive halos are listed in Table 4.2. It should be stressed that the true stellar masses for these halos would be affected by feedback. Additionally, star formation will happen continuously, as opposed to at one instant, which could likely result in more the 5% of the gas being converted into stars. Nevertheless, this analysis provides us with a value for the *amount* of gas that has collected within the halos by $z \sim 12$ that is currently available for star formation. The stellar masses for the top 5 most massive halos are of order $10^6\ M_\odot$. Extending this analysis to all halos yields Figure 4.20, which shows a scatter plot of the estimated Pop II stellar mass versus virial mass. Stellar masses range from as low as $5 \times 10^2\ M_\odot$ to as high as $2 \times 10^6\ M_\odot$. The stellar masses are in good agreement with those obtained in O'Shea et al. (2015) using the *Renaissance Simulations*. Figure 4.20 also shows Pop II SFR versus stellar mass. Specific SFRs for galaxies formed in the *Renaissance Simulations* are shown in Figure 4 of McCaffrey et al. (2023). This is to be expected since we have ignored feedback effects. Our sSFRs are slightly higher than those observed in the *Renaissance Simulations*, of which $1 \times 10^7\ \mathrm{yr}^{-1}$ is the largest sSFR observed. The specific SFRs obtained by our analysis are between $1 \times 10^{-7}\ \mathrm{yr}^{-1}$ and $6 \times 10^{-7}\ \mathrm{yr}^{-1}$.

4.3.8 Sensitivity to Variations in Feedback and Chemistry Prescriptions

To investigate how gas cooling is effected by varying feedback and chemistry prescriptions, we show phase diagrams of cooling time, normalized by the Hubble time ($t_{\mathrm{cool}}/t_{\mathrm{H}}$), versus baryon number density for the most massive halo in each of the 256^3 simulations with gas cooling in Figure 4.22; the virial mass for each is listed in Table 4.1. These simulations have identical initial conditions, so Figure 4.22 shows the same halo under different conditions for chemistry and cooling. In each of the panels in Figure 4.22, gas that is able to cool has $t_{\mathrm{cool}}/t_{\mathrm{H}} \leq 1$. This is generally true for gas with $n_{\mathrm{b}} > 10^0\ \mathrm{cm}^{-3}$ in three of the four simulations plotted, with `N256_6species` being the exception. It can be seen in the second column that $t_{\mathrm{cool}}/t_{\mathrm{H}} = 1$ is the approximate lower limit for atomic cooling, meaning that atomic cooling is effectively inactive for this halo. In support of Figure 4.9, we can see that H_2 and metal cooling dominate in the densest gas for `N256_fiducial` and `N256_noLWB`. Interestingly, the `N256_9species` case, which employs a metallicity floor of $Z_{\mathrm{floor}} = 10^{-5.5}\ Z_\odot$, seems to under-predict the effects of metal cooling in dense gas, while over-predicting metal cooling in low-density gas (fourth column of Figure

4.22). The effects of the LWB can be seen in the H_2 cooling times (third column), where introducing a LWB increases H_2 cooling times by ~ 5 orders of magnitude in low-density gas.

Slices of baryon number density, temperature, electron fraction, and entropy through the most massive halo in each of the 256^3 simulations are shown in Figure 4.21. The conventional wisdom is that gas that spherically accretes onto the halo (i.e. hot mode accretion) will shock heat to the virial temperature near the virial radius, whereas gas that flows in through filaments (i.e. cold mode accretion) will heat further in towards the center (Kereš et al., 2005) by weak shocks and compressional heating. The gas at the shock boundary will experience a sharp increase in entropy. This can be observed in the entropy slices of Figure 4.21, most clearly in the adiabatic case. The shock boundary in the adiabatic case occurs at $r \approx R_{\rm vir}$, which is inline with the conventional wisdom. For all other cases, the shock boundary is notably less pronounced and is located at roughly $r = 0.3\,R_{\rm vir} - 0.5\,R_{\rm vir}$, in agreement with the early findings of Wise & Abel (2007). For the non-adiabatic cases, the shock boundaries coincide with increased electron fractions due to collisional ionization. As more types of cooling are introduced (moving downward in Figure 4.21), accretion flows onto the central region increase, and fragmentation can be observed.

Figure 4.23 shows a comparison between average profiles for all halos (i.e. not just cooling halos) in the 256^3 simulations for temperature and Mach number. Central temperatures are highest for the `N256_adiabatic` and `N256_6species` cases across all mass ranges, as expected. These two cases are characterized by subsonic central flows. The lowest central temperatures are for `N256_fiducial` and `N256_noLWB`, which have supersonic central flows due to the low sound speed in the cold gas. The `N256_9species` curves deviate from the rest at $r/r_{\rm vir} < 0.2$ because the inclusion of a metallicity floor allows all halos access to metal-line cooling, even those that would otherwise be pristine.

4.4 Discussion

4.4.1 Cold Mode Accretion At High Redshifts

Accretion histories of galaxies at $z \lesssim 4$ are studied in detail in Kereš et al. (2005) and Kereš et al. (2009) (K05 and K09 hereafter), where it is found that there are two distinct modes of accretion: a "hot mode" and a "cold mode". Hot mode accretion is typically experienced in high mass halos ($M_{\rm vir} \sim 10^{12}\,M_\odot$), and is the case where gas accretes spherically into the halo, and gets shock-heated to the virial temperature in the process. Halos of lower masses tend to experience cold mode accretion,

which is the case where gas flows into the halo smoothly through filaments. Because the accretion is smooth in the cold mode case, the inflowing gas is not shock-heated to the virial temperature during the process of accretion. The majority of the gas that ultimately coalesces in Milky Way-like galaxies by $z = 0$ enters through cold mode accretion.

Our simulations probe accretion and cooling in galaxies during an entirely different phase of the universe than the simulations in K05 and K09. For one, we simulate a universe before reionization, when the IGM has not yet been heated to temperatures above the atomic cooling limit of 10^4 K by the buildup of a global UV background. Additionally, the halos we resolve have lower masses, with values ranging between $10^6\ M_\odot$ and $10^9\ M_\odot$, as opposed to the $10^{10}\ M_\odot$ to $10^{14}\ M_\odot$ halos in K05 and K09. Regardless, cold mode accretion best describes the case that we observe in our simulations. In fact, the lack of shock-heated gas can also partially explain why we do not observe atomic cooling halos in our simulations, even though we resolve hundreds of halos with virial temperatures above the atomic cooling limit.

Greif et al. (2008) tracks the accretion history of a $5 \times 10^7\ M_\odot$ halo at $z \sim 10$ within a ~ 700 kpccm cosmological box. They do not include models for stellar feedback, yet allow the gas to undergo atomic and H_2 cooling. This is similar to our model, though we include Pop III feedback and subsequent metal cooling. In their study, they examine hot versus cold accretion in the halo's history, and find that there is an initial phase of hot accretion, with cold accretion taking over soon after. The hot accretion does manage to shock-heat a small amount of gas to $T \approx 10^4$ K at the virial radius, but the gas quickly cools to $T \approx 10^2$ K as it flows into the center, at which point the flows become supersonic and turbulent. This is consistent with our observations in Figures 4.10, 4.14, 4.19, and 4.23. Figure 7 in Greif et al. (2008) shows phase diagrams of gas temperature and H_2 fraction for the $5 \times 10^7\ M_\odot$ halo, which can be compared with the gas phase diagrams for our five most massive halos in Figure 4.19. There are some differences in the H_2 fractions at low densities due to the effects of the LWB in our simulation, but in both cases, H_2 fractions approach 10^{-3} in dense gas.

4.4.2 Population III Star Formation Histories

Trenti et al. (2009) derives the following equation that describes the minimum virial mass for a

pristine minihalo to be able to cool in less than a Hubble time via H_2 cooling:

$$M_{t_H - cool} \approx 1.54 \times 10^5 \, M_\odot \left(\frac{1+z}{31} \right)^{-2.074}. \tag{4.12}$$

At $z = 11.92$, Equation 4.12 evaluates to $9.5 \times 10^5 \, M_\odot$, which is approximately equal to our minimum resolved halo mass of $10^6 \, M_\odot$. From Figure 4.8, we can see that there are a few H_2 cooling halos around $10^6 \, M_\odot$, which is in good agreement with the prediction of Equation 4.12. Most of the cooling halos that we observe with $M_{\rm vir} \lesssim 3 \times 10^6 \, M_\odot$ actually cool via metals. These low mass metal cooling halos are primarily enriched externally (Fig. 4.4), though we do see some internal Pop III star formation in a few of these halos (Fig. 4.3).

Visbal et al. (2020) uses semianalytic models to compute Pop III star formation histories for a set of dark matter halos extracteed from dark matter-only simulations of comparable mass resolution to our own, including a variety of different feedback effects. Specifically, they consider the effects of the LWB, internal and external metal enrichment, and reionization feedback. We do not include radiative feedback explicitly, meaning that our model is most comparable to the "LW+M($Z_{\rm crit} = 10^{-6} \, Z_\odot$)" case in Visbal et al. (2020), where $Z_{\rm crit}$ is the chosen metallicity that distinguishes Pop III star formation from metal enriched Pop II star formation. They find Pop III star formation occuring in halos with virial masses as low as $2 \times 10^6 \, M_\odot$, which is consistent with our results in Figure 4.3, as well as with the minimum H_2 cooling mass computed using Equation 4.12. Our computed Pop III SFRD in Figure 4.2 is generally in good agreement with those in Visbal et al. (2020), though our rates are higher than the "LW+M" rates by a factor of 2-3 by the final output. Due to the many differences between our models and implementations, it is hard to say exactly where the deviation in our derived SFRDs originates, but the most likely reason is that we take into account H_2 self-shielding, while Visbal et al. (2020) does not. H_2 self-shielding works against the H_2 photodissociating LWB, which works to suppress Pop III star formation. The inclusion of H_2 self-shielding therefore increases Pop III SFRs. They cite inhomogeneous reionization and pollution of pristine halos by metal-enriched winds from nearby galaxies for the general flattening of their Pop III SFRD below z=15. We do not include these effects in our simulations, which is an additional explanation for why our SFRD overshoots theirs at lower redshifts.

4.4.3 The Role of Primordial Chemical Enrichment

Primordial chemical enrichment is an essential ingredient for galaxy formation. After all, all main-sequence stars that have been observed have nonzero metallicity, so it stands to reason that the gas in which they formed was metal enriched. We have replicated previous results that suggest that the primary mechanism for halo enrichment in the early universe is external enrichment, which is the case where metals are sourced from supernovae occuring outside the virial radius (Hicks et al., 2021; Smith et al., 2015b).

As a part of the *Birth of a Galaxy* series, Wise et al. (2014) (hereafter W14) simulates chemical enrichment by Pop III stars explicitly, and finds a population of low mass halos ($10^6\ M_\odot < M_{\rm vir} < 10^8\ M_\odot$) that are able to form metal enriched stars despite the fact that their virial temperatures are below the atomic cooling limit. These halos are directly comparable to the population of metal cooling halos that we identify in our `N512_fiducial` simulation. W14 performs a similar cooling analysis to the one we describe in Section 4.3.3, and finds a clean transition from H_2 cooling to metal cooling at $M_{\rm vir} \gtrsim 10^7\ M_\odot$, and another transition from metal cooling to atomic cooling at $T_{\rm vir} = 10^4$ K (see Figure 2 of W14). In contrast, we find that H_2 cooling is overall dominant for halos with $M_{\rm vir} > 10^7\ M_\odot$, and do not find any atomic cooling halos in the sample.

The main reason for our differing results with W14 is likely that W14 includes a full physics suite with Pop II star formation and feedback, including radiative feedback. This suggests that the relative importance of the three cooling rates we consider is modulated by stellar feedback from metal enriched stars. Since we do not observe any atomic cooling halos in our sample, it is possible that stellar feedback from metal enriched stars is actually a requirement for atomic cooling halos to exist. This is contrary to the usual story, which is typically recited in the literature in a way that suggests the opposite—that metal enriched star formation is not a cause, but a consequence of efficient atomic cooling in halos with $T_{\rm vir} > 10^4$ K (e.g., Greif (2015)).

4.4.4 H_2 Cooling and Self-Shielding

Ahvazi et al. (2023) computes occupation fractions for halos of a given mass to form a dwarf galaxy, and find that H_2 cooling is the essential ingredient for the occupation fractions to match up with predictions (see Figure 2 in Ahvazi et al. (2023)). The analysis used in the study takes the gas metallicity

to be uniform throughout the box. Our results corroborate with this key finding. We have found that H_2 cooling tends to dominate over metal cooling within R_{1000} for the majority of halos in our sample.

The strength of H_2 cooling is partially reliant on H_2 self-shielding, which protects the innermost regions of a halo from H_2 photodissociation by the LWB in halos with H_2 column densities greater than 10^{14} cm^{-2} (Draine & Bertoldi, 1996). We have seen in Figure 4.11 that the vast majority of cooling halos with $M_{\rm vir} > 10^7\ M_\odot$ in the `N512_fiducial` simulation have $N_{H_2} > 10^{14}$ cm^{-2}. The effect of H_2 self-shielding can be seen more explicitly when comparing the H_2 cooling times for the most massive halos in the `N256_fiducial` and `N256_noLWB` simulations in Figure 4.22. The impact of H_2 self-shielding on Pop III star formation are studied in Skinner & Wise (2020), where it is found that self-shielding lowers the minimum halo mass necessary for Pop III star formation to values as low as $3 \times 10^5\ M_\odot$. As a result, primordial chemical enrichment can occur at earlier redshifts, which is the precursor to metal enriched star formation.

4.4.5 Implications for Galaxy Formation Models

Cooling is a driver for star formation within a halo. The different cooling processes considered in this study operate efficiently at different gas temperatures. H atomic line cooling is effective at cooling gas down to 10^4 K. Below this temperature, atomic cooling quickly becomes inefficient as collisional excitations become rare, and H_2 cooling is required to cool the gas further (Abel et al., 2000; Bromm & Larson, 2004). H_2 cooling will cool the gas down to ~ 200 K. In pristine gas, this minimum temperature of ~ 200 K will result in a large Jeans mass, and will thus produce high mass Pop III stars (Abel et al., 2002). If metals are present, the gas will cool and condense further before reaching stellar densities. Semianalytic models for galaxy formation in the early universe are often applied to pure dark-matter-only simulations, and thus do not have the ability to directly measure the various cooling rates in the way that we have in this study. Instead, the virial temperature is typically used as a metric to label halos as atomic cooling or otherwise. Even in hydrodynamical simulations that do include explicit chemistry and cooling, it is common practice to identify halos as atomic cooling if $T_{\rm vir} > 10^4$ K.

Chen et al. (2014) derives a series of scaling relations for galaxies formed in the *Renaissance Simulations*, specifically in the "Rarepeak" region at $z = 15$. Most notably, the relationship between SFR and dark matter virial mass is piecewise, with a different slope on either side of $10^8\ M_\odot$ (see Fig. 3 in

Chen et al. 2014). All measured relationships in the study that depend on the SFR also have this feature. It is erroneously stated in the study that the discontinuity at $M_{\rm vir} \simeq 10^8\ M_\odot$ corresponds to $T_{\rm vir} \simeq 10^4$ K, when the virial mass corresponding to $T_{\rm vir} \simeq 10^4$ K at $z = 15$ is actually $M_{\rm vir} \simeq 2 \times 10^7\ M_\odot$. We speculate that the observed star formation efficiency at $M_{\rm vir} \simeq 10^8\ M_\odot$ is the result of self-enrichment of the halo by Pop II supernova feedback. Regardless, it is clear that the $10^7\ M_\odot - 10^9\ M_\odot$ mass range marks a transition from discrete star-forming events separated by quenching due to stellar feedback to sustained Pop II star formation. This is demonstrated in Figure 22 of Xu et al. (2016c), which shows the fraction of halos in the *Renaissance Simulations* that are actively forming stars at the final redshift for each simulated region. The curve is discontinuous, showing increased active star formation in halos with $M_{\rm vir} \gtrsim 10^8\ M_\odot$. It is clear from our results that while atomic cooling likely plays a role in counteracting gas heating from feedback, atomic cooling alone is not strong enough to mark a transition to efficient star formation in halos. It can be observed in Figure 4.4 that virtually all halos with $T_{\rm vir} > 10^4$ K are chemically enriched by $z \sim 12$, and are thus all candidates for Pop II star formation. These halos are generally massive enough to be able to contain outflows generated by Pop II supernovae through gravity, which could lead to the sustained star formation that has been observed in the *Renaissance Simulations*. For now, this is left as a point of speculation. We will explore this topic further in a followup study.

We have shown that the virial temperature is not an accurate indicator of gas temperature for halos in the early universe with virial masses between $10^6\ M_\odot$ and $10^9\ M_\odot$, and as such, semianalytic arguments that rely on the virial theorem for assessing the state of the gas in the regime we study should be made with caution. Furthermore, defining an atomic cooling halo as a halo with a virial temperature of $T_{\rm vir} > 10^4$ K is potentially misleading, as it is not at all guaranteed that the gas within such a halo would cool primarily through atomic H and He transitions. Our results suggest that gas heating from stellar feedback must be taken into account for efficient atomic cooling to take place in any capacity.

4.4.6 Caveats

There are a few shortcomings in our analysis that should be noted. As mentioned throughout the text, we do not include Pop II stellar feedback in our simulation. Pop II supernovae within a star-forming halo would dramatically impact the dynamics of the gas within R_{1000}. The relative importance of atomic, H_2, and metal cooling within star-forming halos would also be affected, though exactly how is not clear.

Atomic cooling rates would definitely become non-negligible due to the sharp increase in temperature in the wake of a supernova, though the energy injected into the gas would also induce collisional ionization of atomic hydrogen and helium, which would work against the increase in atomic cooling. The increased electron fractions that result from the collisional ionization of hydrogen and helium combined with the increased metal fractions due to stellar winds and metal ejection during supernovae would also serve to increase metal cooling rates. H_2 cooling rates would similarly be affected.

We also do not include the effects of radiative feedback. Radiation from young massive stars will ionize atomic hydrogen and helium, as well as heat the gas. In particular, local radiation from Pop II stars in the Lyman-Werner bands will photodissociate H_2 in star-forming halos. As a result, we expect that H_2 cooling will become less important for the cooling of the gas once a halo has achieved Pop II star formation.

The statistics for primordial stellar populations predicted by `StarNet` (number of Pop III stars, stellar masses, etc.) are randomly pulled from distribution functions derived from the *Phoenix Simulations*. While this approach is sound for the sake of global statistics, the properties of individual stellar populations do not directly depend on the state of the alleged star-forming gas. While topics related to the Pop III stellar IMF and primordial stellar populations remain highly uncertain in the literature, it should be noted that this is also point of uncertainty in our model. Regardless, good agreement for a variety of halo-averaged properties were shown in Wells & Norman (2022) between simulations that directly resolve Pop III star formation and feedback, and simulations that use `StarNet` to predict its effects.

4.5 Conclusion

We have studied the chemical history and dynamics of gas within a large sample of dark matter halos with virial masses on the range $10^6\ M_\odot < M_{\rm vir} < 10^9\ M_\odot$ in the absence of Pop II star formation and feedback at high redshifts. The halos are generated in a $(5.12\ \mathrm{cMpc})^3$ volume using a large `Enzo-E` AMR cosmology simulation that includes models for gravity, multispecies hydrodynamics, gas chemistry and cooling, an H_2 photodissociating LWB, and Pop III chemical enrichment. The simulation is run down to $z = 11.92$. The Pop III chemical enrichment is handled using the machine learning surrogate model, `StarNet`, which is called inline with the simulation. `StarNet` deposits metals from one or more Pop III supernovae in a composite supernova remnant near its terminal stage of expansion. This novel approach

allows us to simulate larger volumes for improved halo statistics by bypassing the early expansion phase of Pop III remnants.

We find that 16% of halos are chemically enriched by the final output, and thus have access to metal-line cooling. We then calculate average cooling rates for gas within R_{1000} for each halo, determine which halos contain a significant amount of gas that is able to cool in less than a Hubble time, and classify these halos as either (1) atomic cooling halos, (2) H_2 cooling halos, or (3) metal-cooling halos based on which cooling process is dominant. 12% of halos in our sample are able to cool by any means. The main conclusions from our analysis are:

1. H_2 is the dominant coolant for halos in our resolved mass range of $10^6\,M_\odot < M_{\rm vir} < 10^9\,M_\odot$, even for halos that are metal enriched. Metal cooling also makes a significant contribution; however, only 18% of the cooling halos are identified as "metal cooling" at the final redshift. For the most massive halos, it is typical for H_2 and metal cooling to contribute roughly equal amounts to the total cooling within R_{1000}.

2. True atomic cooling halos (cooling by H and He line excitation) are exceedingly rare for halos in our resolved mass range, even for halos with $T_{\rm vir} > 10^4$ K. In fact, we find that there are no atomic cooling halos in our sample at all. What little atomic cooling that is present is insufficient to induce the gravitational collapse of the first Pop II stars in a halo. Rather, it is likely that feedback from Pop II stars is actually required to heat the gas to temperatures sufficient for radiative transitions in atomic hydrogen and helium to take place. We will explore this topic in a followup study.

3. For the majority of halos with $M_{\rm vir} < 10^9\,M_\odot$, the gas contained within the virial radius is not thermally virialized. Rather, consistent with earlier findings, (Wise & Abel, 2007; Greif et al., 2008), we find that virial equilibrium is achieved by the additional kinetic energy of bulk flows and turbulence within the virial radius. Thanks to our large sample of halos, we find that the relative contribution of bulk kinetic energy to thermal energy of the gas systematically increases with virial mass (see Fig. 4.13), independent of the cooling properties of the halo. In addition, the mean temperature within the virial radius for halos with $M_{\rm vir} > 10^7\,M_\odot$ is typically much less than the virial temperature due to runaway cooling near the center. In the absence of gas cooling, mean temperatures are still less than the virial temperature by a factor of ~ 2.

4. Gas accretes onto halos primarily by cold mode accretion along filaments. Gaseous filaments at $z \sim 12$ have temperatures between 10^2 K and 5×10^3 K due to strong adiabatic shocks bounding the filaments.

5. H_2 self-shielding from the LWB is active for halos across our entire resolved mass range. The effectiveness of H_2 self-shielding generally increases as halo mass increases. For halos with $M_{\rm vir} > 10^8\,M_\odot$, gas generally flows in with larger H_2 fractions than for lower mass halos. As a result, the average radial profile of H_2 fraction for $M_{\rm vir} > 10^8\,M_\odot$ lacks the sharp increase at $r/R_{\rm vir} \approx 0.2$ that is typical for the lower mass halos, yet still reach values at the centers that are an order of magnitude higher than the lower mass halos.

6. Assuming an homogeneous metallicity floor of $Z_{\rm floor} = 10^{-5.5}\,Z_\odot$ in place of a model for Pop III star formation and feedback leads to over-estimated metal cooling in low density gas and under-estimated metal cooling in high density gas. Additionally, it gives all halos access to some amount of metal cooling, while, according to our fiducial simulation, only 16% of halos are chemically enriched by $z \sim 12$.

7. Through a post-processing approach, we estimate Pop II stellar masses and SFRs for our sample of halos in our fiducial simulation and obtain values that are in good agreement with those seen in the *Renaissance Simulations*. Whether a halo is an H_2 cooling or a metal cooling halo appears to have no effect on stellar mass or SFR.

We have found that the commonly assumed progression of halos from H_2 cooling to metal cooling to atomic cooling needs to be analyzed further at high redshifts, and is likely not reflective of the truth. In reality, things are much more complicated. Caution should be taken when relying on the virial theorem to assess the thermal state of the gas within halos at $z \gtrsim 10$, as it is not at all guaranteed that the gas within a given halo of $M_{\rm vir} < 10^9\,M_\odot$ is thermalized. Rather, we have found that kinetic motion of the gas (i.e. turbulence) contributes increasingly to the virial energy budget as halo mass increases. In a followup study, we will re-do our analysis in the presence of Pop II star formation and feedback to see what results change and what stays the same. We will place a focus on the properties of the galaxies that form, and will discuss any connections that can be made with recently observed JWST galaxies at $z > 10$.

4.6 Acknowledgements

This research was partially supported by National Science Foundation grant AST-2108076 to M.L.N. and via NASA grant 80NSSC21K1053, P.I. Molly Peeples, through a subaward to M.L.N. The simulations were carried out on the Frontera supercomputer operated by the Texas Advanced Computing Center with LRAC allocation AST20007. Simulations were performed with `Enzo-E` (https://github.com/enzo-project/enzo-e) coupled to `Grackle` (Smith et al., 2017). Analysis and plot generation was done using `YT` (Turk et al., 2011). `Enzo-E`, `Grackle`, and `YT` are all collaborative open source codes representing efforts from many independent scientists around the world.

Chapter 4, in full, has been submitted for publication of the material as it may appear in Hicks, Norman, Wells, & Bordner (2024), "Galaxies and Their Environment at $z \gtrsim 10$—I: Primordial Chemical Enrichment, Accretion, Cooling, and Virialization of Gas in Dark Matter Halos", *The Astrophysical Journal*. The dissertation author was the primary investigator and author of this paper.

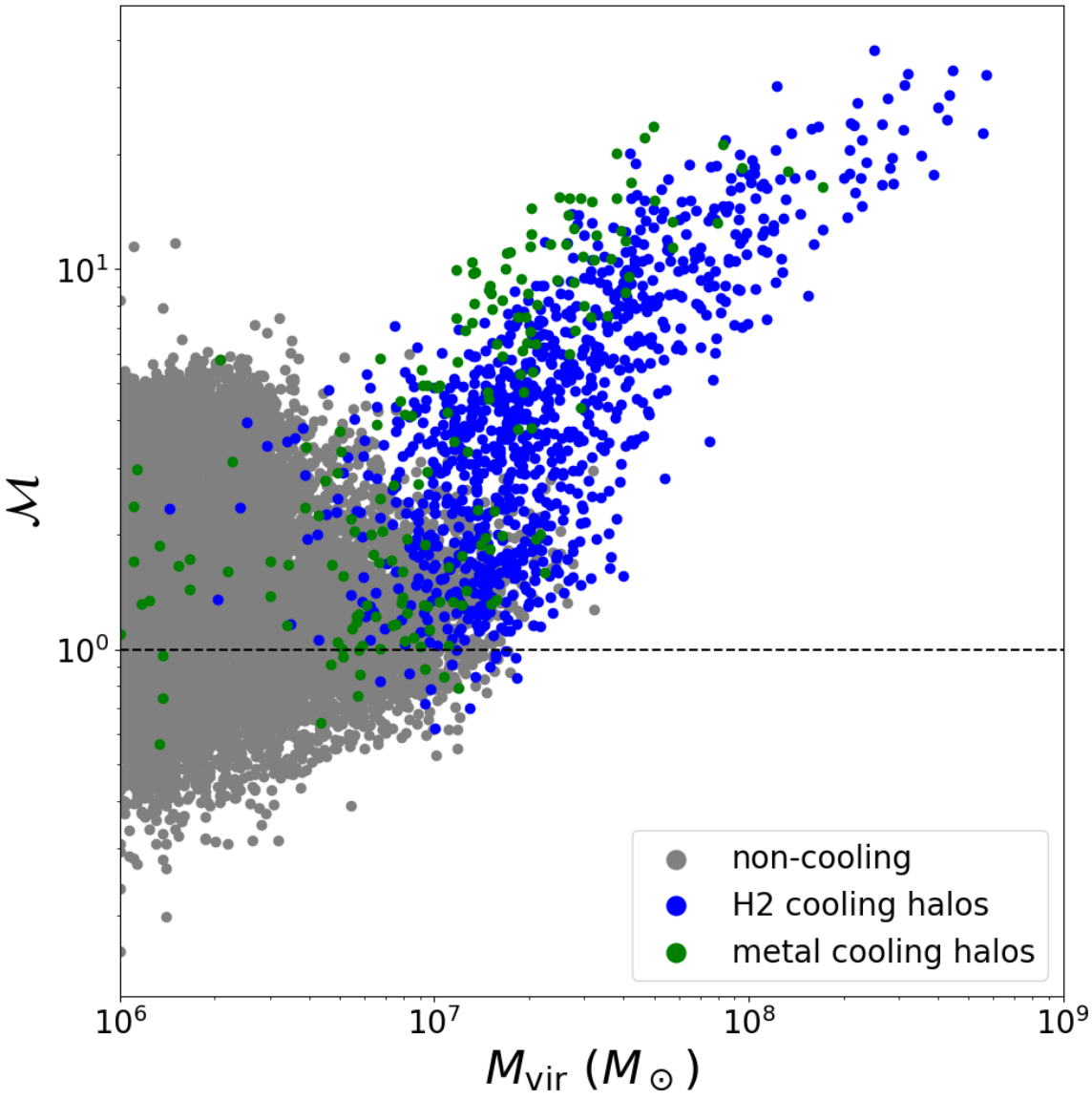

Figure 4.14. Mass-weighted average Mach number within the virial radius vs. virial mass for halos in the `N512_fiducial` simulation. Flows become increasingly supersonic for $M_{\rm vir} \gtrsim 10^7\ M_\odot$ as halo mass increases.

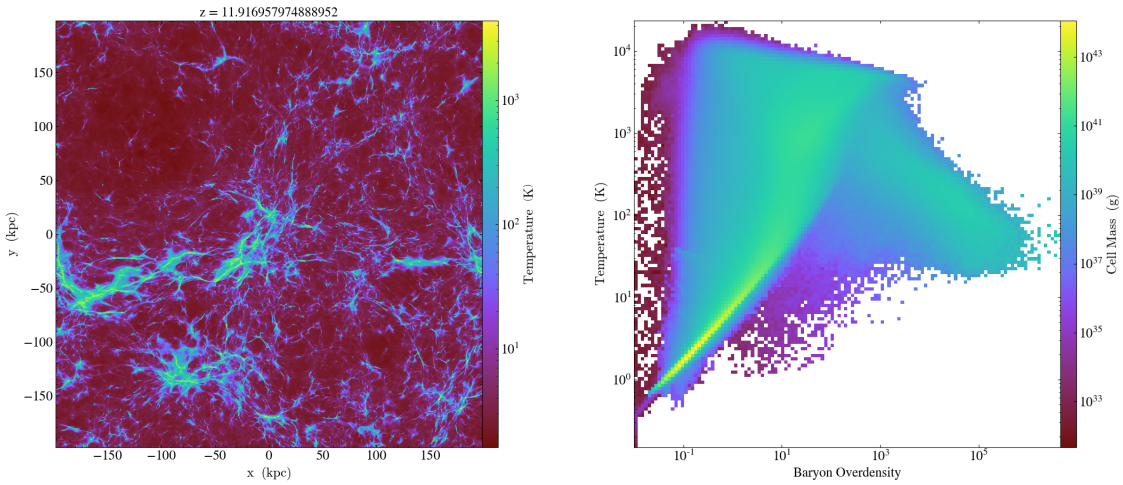

Figure 4.15. *Left:* Full-box temperature projection for the `N512_fiducial` simulation. Typical temperatures of gaseous filaments can be observed to be between 10^2 K and 10^4 K. *Right:* Temperature vs. baryon overdensity phase diagram for all gas in the `N512_fiducial` simulation. Overdensities between 10^1 and 10^2 correspond to gas in filaments.

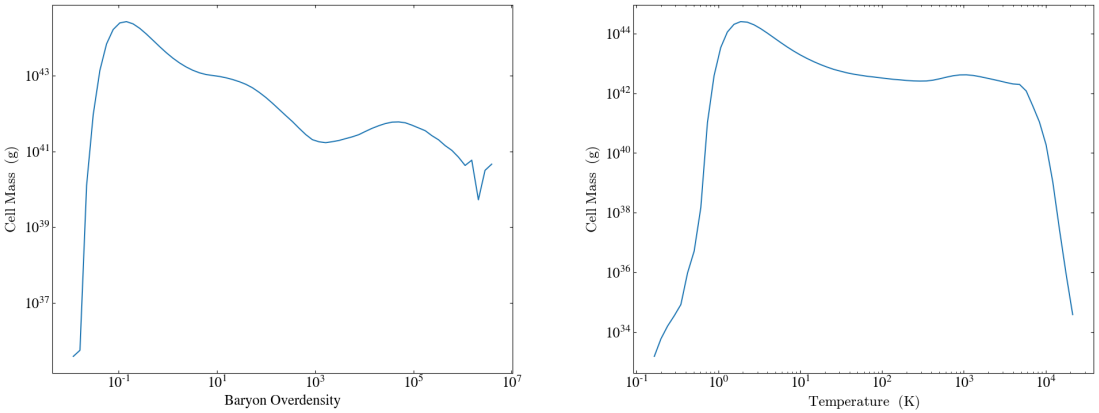

Figure 4.16. 1D profiles for baryon overdensity (*left*) and temperature (*right*) over the full volume of the `N512_fiducial` simulation.

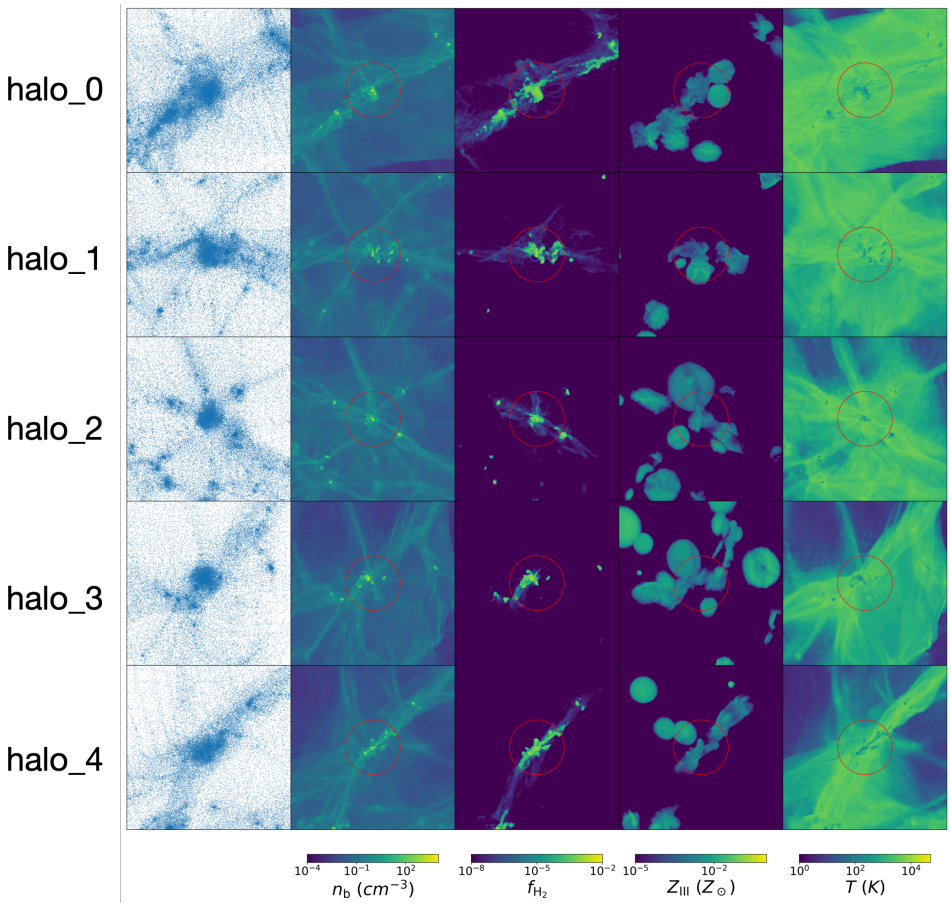

Figure 4.17. Projections of various quantities around the five most massive halos in the `N512_fiducial` simulation. The red circles extend out to the virial radius, where each halo has a virial radius of approximately 2 proper kpc. From left to right, the images show dark matter particles, baryon density, H_2 fraction, metallicity, and temperature.

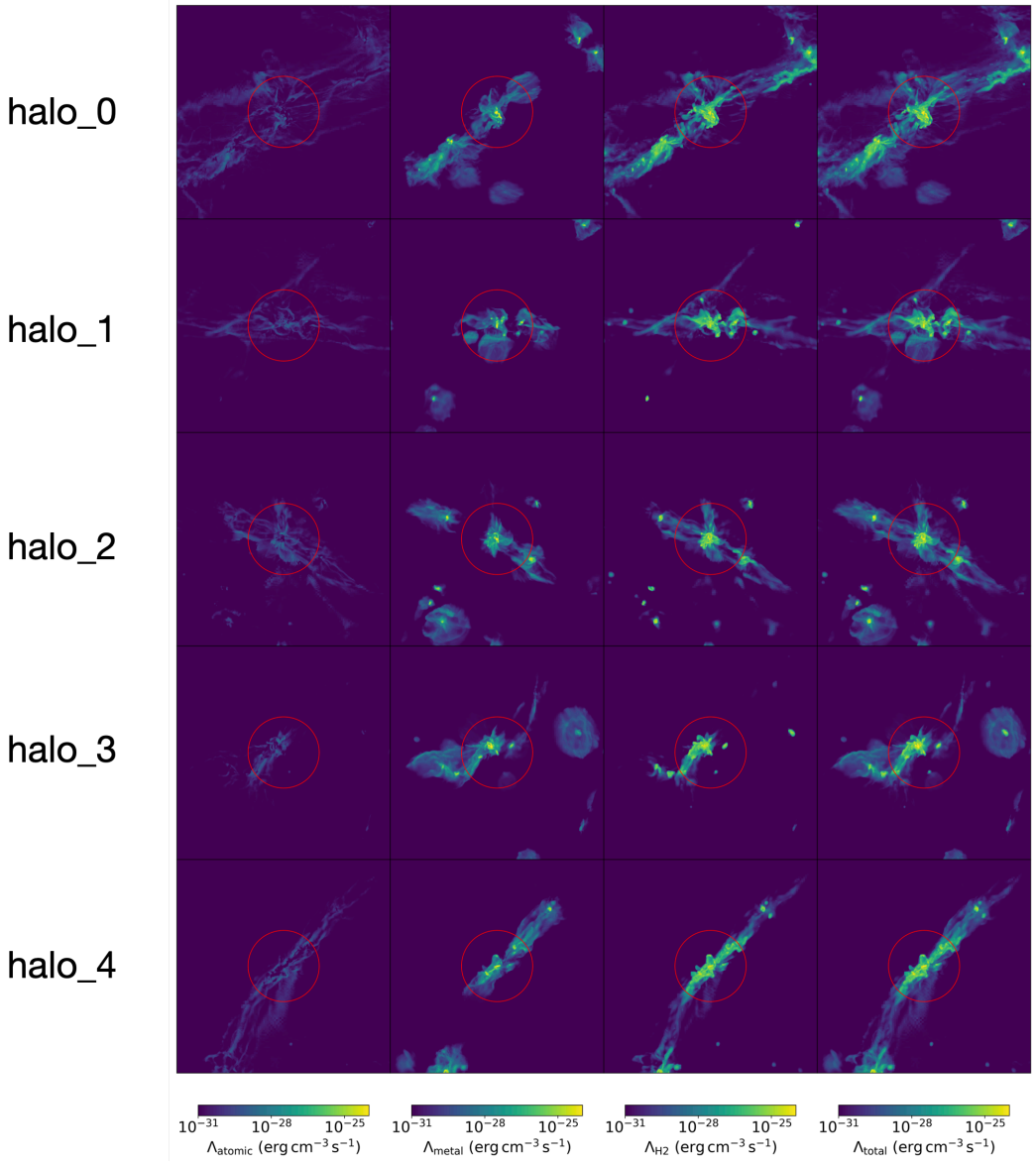

Figure 4.18. Projections of volumetric cooling rates for the five most massive halos in the `N512_fiducial` simulation. From left to right, the images show atomic cooling rate, H_2 cooling rate, metal cooling rate, and total cooling rate. The similarities between H_2 cooling rates and total cooling rates demonstrate that H_2 cooling is overall dominant for these halos. The red circles extend out to the virial radius, where each halo has a virial radius of approximately 2 proper kpc.

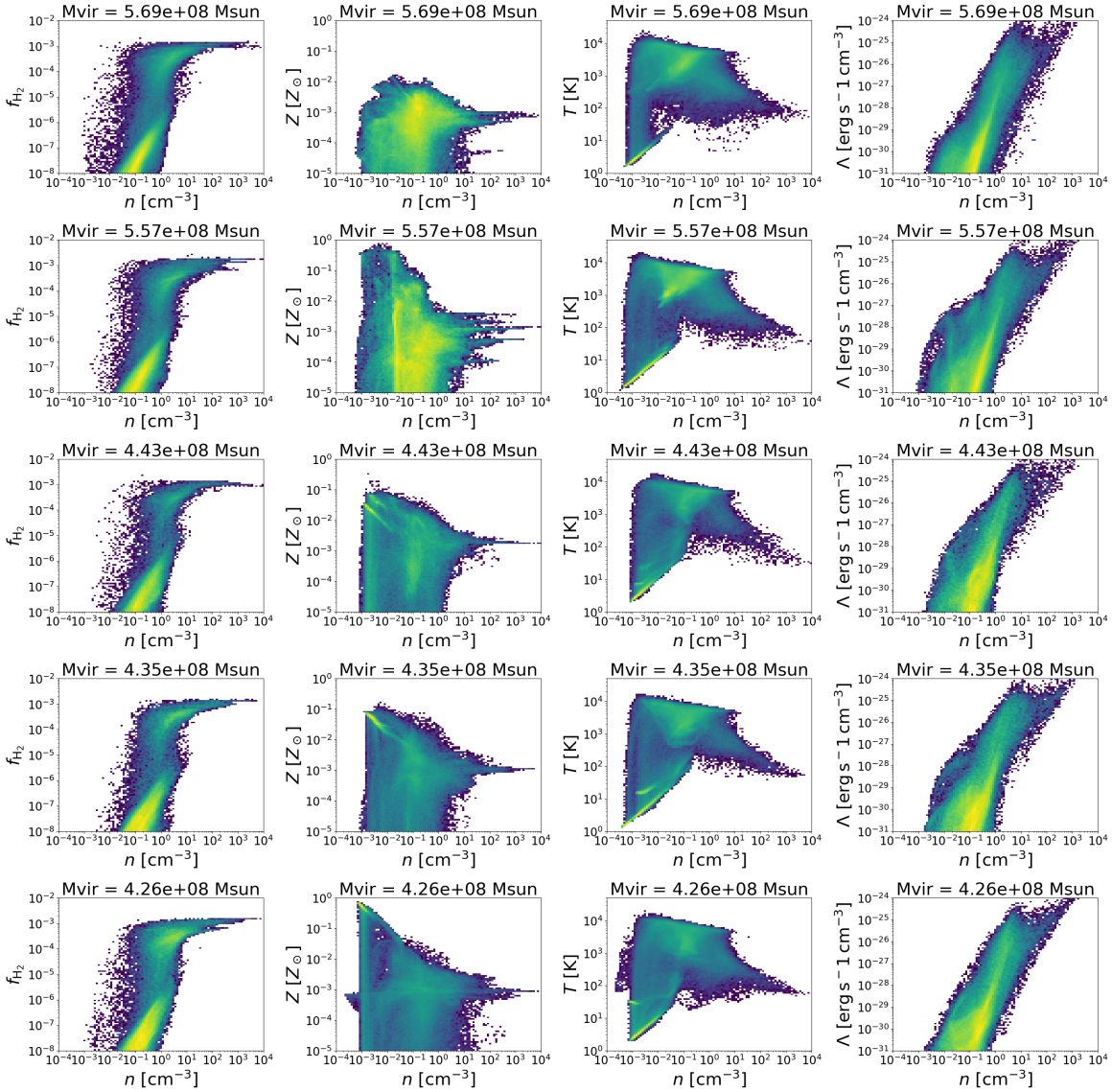

Figure 4.19. Phase diagrams of various properties of the gas within the five most massive halos vs. baryon number density. From left to right, diagrams are shown for H_2 fraction, metallicity, volumetric cooling rate, and temperature. Each row corresponds to a different halo. From top to bottom, the diagrams correspond to halos 0, 1, 2, 3, and 4. The distributions of the chosen properties look very similar for each of the halos.

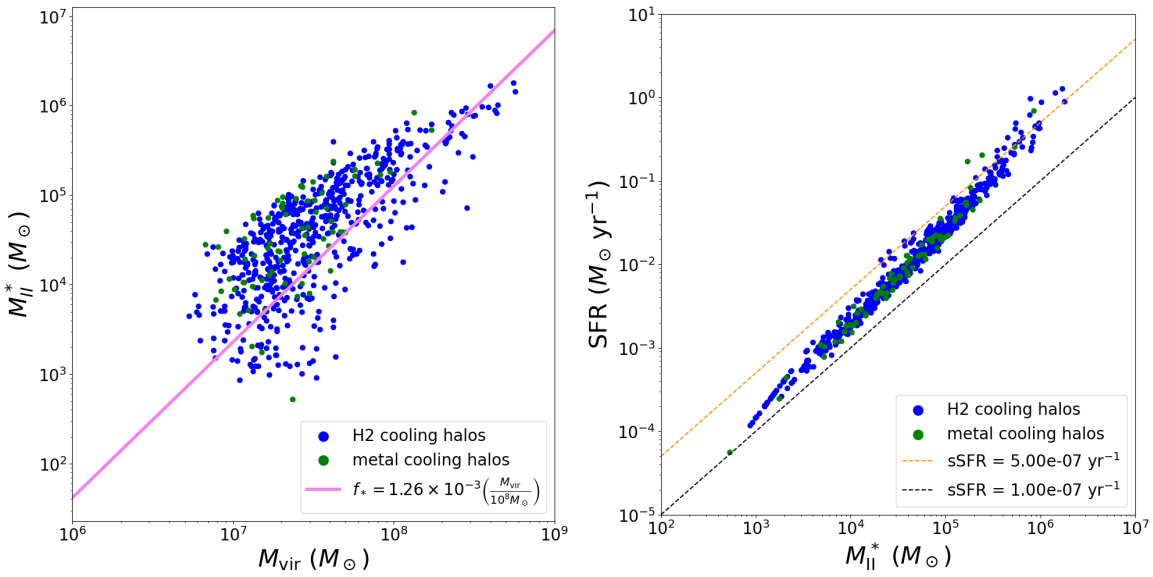

Figure 4.20. *Left:* Predicted Pop II stellar mass vs. virial mass. Blue points correspond to H_2 cooling halos, and green points correspond to metal cooling halos. The pink line shows a fit derived in O'Shea et al. (2015) using the *Renaissance Simulations*. *Right:* Predicted SFR vs. predicted Pop II stellar mass for H_2 cooling and metal cooling halos. The dashed lines show the expected values given a constant specific SFR.

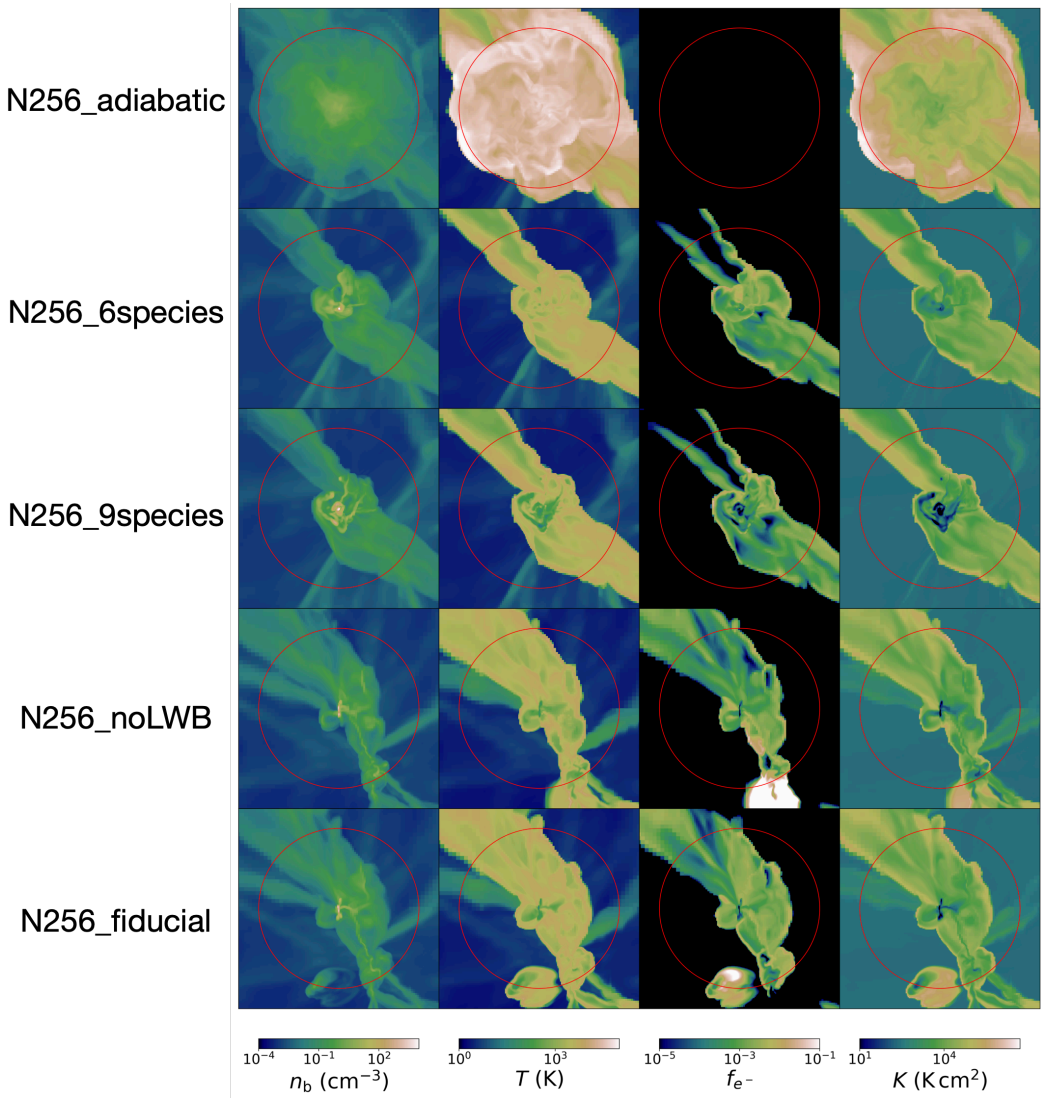

Figure 4.21. Slices of various quantities through the center the most massive halo in each of the 256^3 simulations. From top to bottom, images are shown for `N256_adiabatic`, `N256_6species`, `N256_9species`, `N256_noLWB`, and `N256_fiducial`. From left to right, slices are of the baryon number density, temperature, electron fraction, and entropy ($K = T/n_b^{2/3}$) fields. The red circles denote the virial radius of each halo. Similarities and differences between the gas morphologies can be observed here, with the most drastic differences coming from the `N256_adiabatic`.

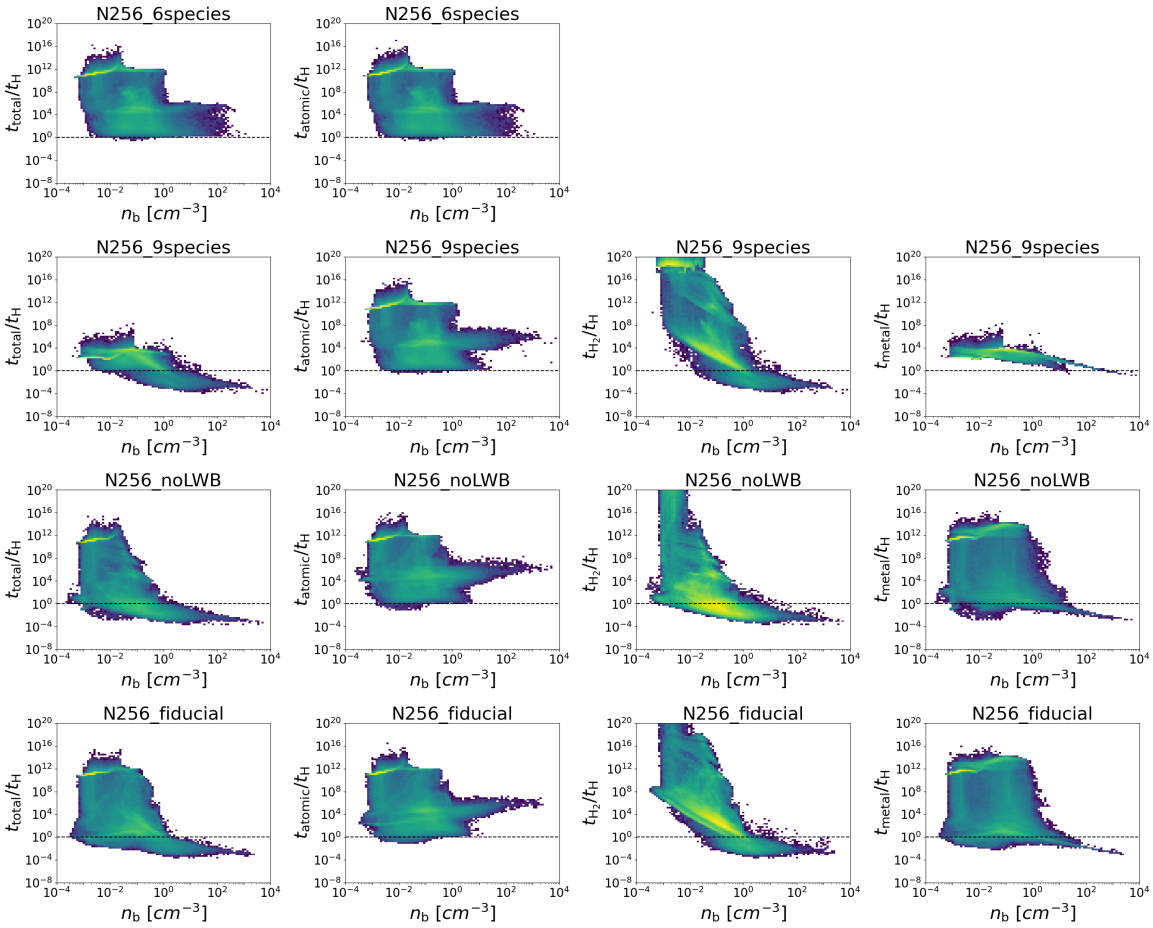

Figure 4.22. Comparison of diagrams of cooling time vs. baryon number density for the most massive halo in each of the 256^3 simulations, except for `N256_adiabatic`, which does not have gas cooling enabled. The 256^3 simulations have the same initial conditions, so this is effectively a comparison of the same halo under different physical conditions. From left to right, total cooling time, atomic cooling time, H_2 cooling time, and metal cooling time are shown. Cooling times are normalized by the Hubble time at the final redshift.

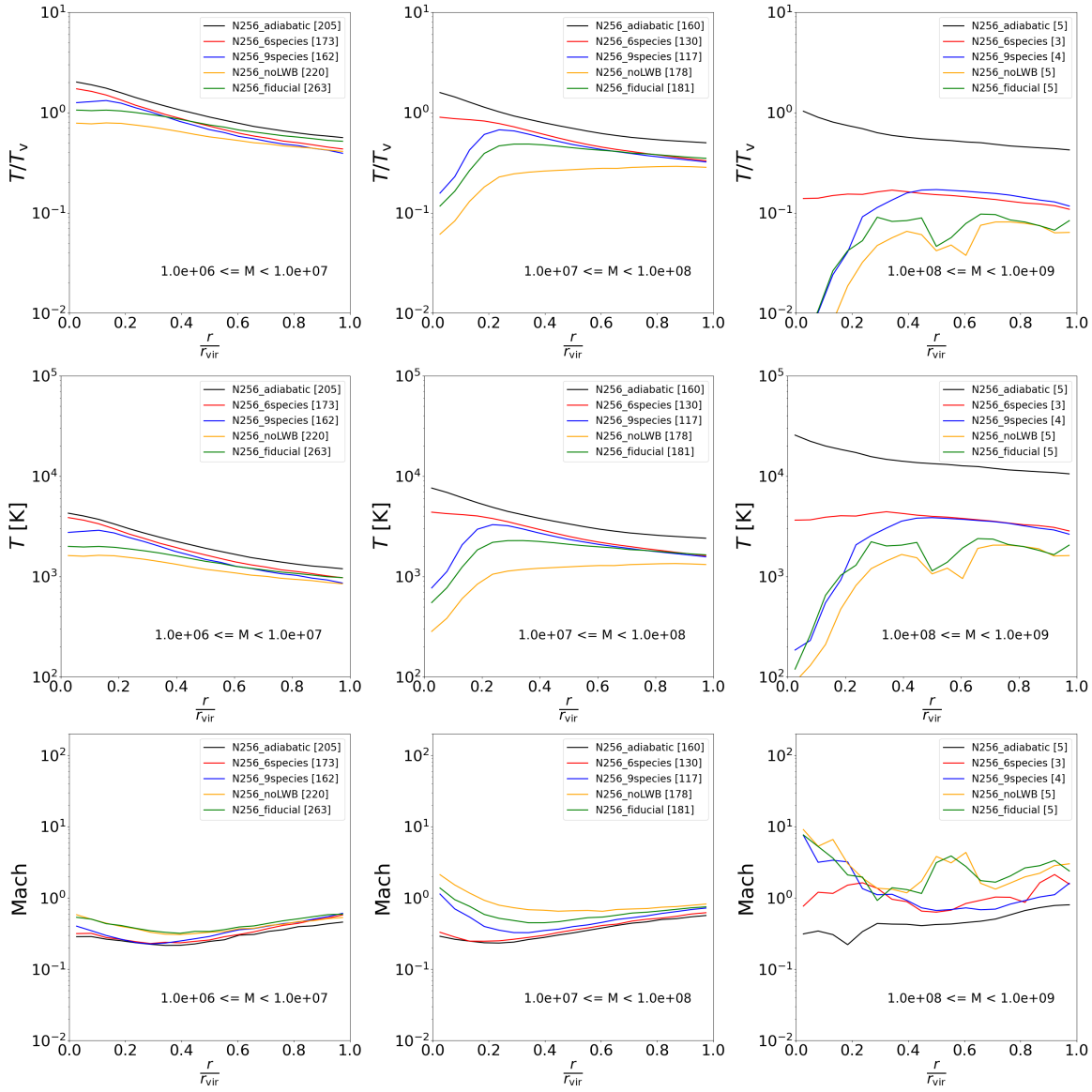

Figure 4.23. Average radial profiles for all halos in separate mass bins in the series of 256^3 simulations. The top row shows gas temperature, normalized by the virial temperature. The middle row shows the un-normalized gas temperature. The bottom row shows mach number. The effect of using a uniform metallicity floor can be seen in the sharp drop in temperatures below $r/R_{\rm vir} = 0.2$ in the blue temperature curves, which correspond to the `N256_9species` simulation. Note that the halos samples for this figure include both cooling and non-cooling halos.

Chapter 5

Galaxies and Their Environment at $z \gtrsim 10$ — II: The Role of Radiative and Kinetic Feedback in Protogalaxy Formation

Inspired by recent observations of high redshift galaxies made using the *James Webb Space Telescope*, this study is the second installment in a series that aims to tell the story of galaxy formation at $z \gtrsim 10$ using large-scale adaptive mesh refinement cosmological simulations. Here, we add the effects of metal-enriched star formation and feedback to our physics suite, and examine how radiative and supernova feedback impact the thermal, mechanical, and chemical state of the gas within low-mass dark matter halos. We limit our analysis to only the most massive halo formed in each simulation ($M_{\rm vir} \simeq 3 \times 10^7\ M_\odot$ at $z \sim 18$). We find that radiative feedback controls the star formation history of a halo early in its lifetime, and confirm that ionizing radiation from stars leads to both the creation and destruction of H_2. Strong H_2 formation in relic HII regions enhances H_2 cooling within a star-forming halo, and we find that H_2 cooling dominates over atomic and metal cooling by the final output because of this effect. We then find that the virial temperature does not accurately describe the thermal state of the gas at any point in the halo's lifetime that we simulate here. In a future study, we will test whether our precursory results hold for a statistical sample of protogalaxy-forming halos.

5.1 Introduction

The term "stellar feedback" encapsulates the many ways in which stars interact with their environment. In this chapter, we place a focus on radiative and supernova feedback. In nature, each of the two feedback mechanisms impacts the thermal, mechanical, and chemical evolution of gas in the

vicinity of the star in different ways. Radiation does so continuously through photoheating (thermal), radiation pressure (mechanical), and photoionization (chemical). Unlike the continuous energy release by radiative feedback, supernovae release energy in discrete bursts. The energy released changes form between thermal and mechanical kinetic energy as the supernova remnant expands and gas is "swept up" into a dense shell. Supernovae enrich the gaseous environment with metals and induce collisional ionization of shock-heated gas in the wake of the expanding remnant.

In Chapter 4, we performed a large-scale statistical study of potential protogalaxy-forming dark matter halos. We focused specifically on the physics of accretion, cooling, and virialization of gas in these halos in the absence of Population II (hereafter Pop II) star formation and feedback. The study raised a number of important questions:

1. How does gas virialize in low-mass star-forming halos?
2. Can we use the virial temperature to estimate the mean gas temperature in a halo?
3. Do classical atomic cooling halos (i.e. halos with $T_{\rm vir} \gtrsim 10^4$ K) actually cool primarily through atomic hydrogen and helium transition?
4. How does stellar feedback modulate the relative importance of atomic, H_2, and metal cooling?
5. How do the answers to these questions relate to the star formation history of a halo?

Concerning the first question, gas within low-mass halos is sensitive to disruption by stellar feedback, particularly radiative feedback. Radiation from the first luminous objects is sufficient to drive photoevaporative outflows that completely clear out gas from the host halo (Abel et al., 2007; Whalen et al., 2004).

The virial temperature is often used to predict the mean gas temperature within a halo, and the classical calculation of the virial temperature assumes that the gas is fully thermalized. In Chapter 4, we found that without Pop II star formation and feedback, the mean gas temperature within the halo is well below the virial temperature due to runaway cooling at the center. In this case, the gas still achieves a steady virial equilibrium that is supported by bulk turbulent flows as opposed to thermal motions. Lochhaas et al. (2021) finds that even in Milky Way-mass halos that experience Pop II star formation and feedback, support from nonthermal motions are a requirement for the gaseous component of the halo

to achieve virial equilibrium. As a result, the virial temperature over-predicts the mean gas temperature within the virial radius by roughly a factor of 2. In the context of low-mass halos, various heating effects may offset the overcooling observed in Chapter 4. If heating and cooling balance perfectly with each other, mean gas temperatures may be comparable to the virial temperature. This assumes, however, that the gas is still able to achieve a steady virial equilibrium.

A related topic is the fact that halos with a virial temperature above 10^4 K are typically referred to as "atomic cooling halos" (ACHs) in the literature. This is because cooling through collisional excitation of atomic hydrogen and helium is possible in 10^4 K gas, and gas in a halo with $T_{\rm vir} = 10^4$ K is typically assumed to reach this temperature. Efficient atomic cooling in a halo is often used as the explanation for increased star forming efficiencies in halos with $M_{\rm vir} > 10^8\ M_{\odot}{}^1$ (e.g. Wise et al., 2014; Chen et al., 2014). In order to tell a cohesive story of protogalaxy formation, it is imperative that we understand the dynamics of cooling processes in a halo, and how those processes are impacted by stellar feedback.

Taking the results from Chapter 4 as a point of comparison, we are poised to understand how exactly stellar feedback would impact our findings. Due to technical limitations, we do not obtain a statistical sample of star-forming halos here, and instead focus our analysis on the evolution of a single halo within a cosmological simulation under different prescriptions for stellar feedback. As such, this chapter is meant to serve as a precursor to a more fleshed-out study that will have results supplemented by statistics. Section 5.2 briefly describes the simulations that were run and the relevant physics methods included. Section 5.2.1 walks through the major events that occur during a given Pop II star particle's lifetime under our star formation and feedback algorithm. In Section 5.3, we present our results. Section 5.3.1 is concerned with Pop II star formation and feedback histories, accretion physics, and the evolution of various physical quantities over time. Section 5.3.2 examines gas virialization and thermal history of the halo under different feedback prescriptions. Section 5.3.3 then presents radial profiles of atomic, H_2, and metal cooling rates, and discusses the relative importance of each coolant. In Section 5.4, we discuss our results and make comparisons with the literature. Section 5.4.4 discusses some caveats to our analysis. Finally, Section 5.5 summarizes our main conclusions.

Table 5.1. List of relevant parameters for each of the simulations run for this study. From left to right, columns show simulation name, root grid dimension, box length in comoving Mpc, relevant physics included, and final redshift. All simulations start from identical cosmological intitial conditions, have a maximum AMR level of 5, and reach the same maximum spatial resolution of 312.5 comoving pc (26 proper pc at z=11). All simulations utilize nine-species chemistry and cooling (H, He, H_2, e^-, plus ions) via `Grackle`. In the `N256_noSNe` simulation, Pop II star particles only emit radiative feedback (i.e. no SNe or stellar winds). The `N256_noPopII` simulation is the fiducial 256^3 run from Chapter 4, which has only Pop III star formation and feedback (i.e. no Pop II). We use a dark matter particle mass of $3.34 \times 10^4\ M_\odot$.

Simulations				
Name	Root	$L_{\rm box}$ [cMpc]	Physics	$z_{\rm final}$
`N256_fiducial`	256^3	2.56	Pop III + Pop II + RT	17.54
`N256_noSNe`	256^3	2.56	Pop III + Pop II (SF only) + RT	18.09
`N256_noRad`	256^3	2.56	Pop III + Pop II	17.90
`N256_noPopII`	256^3	2.56	Pop III	11.34

Table 5.2. Multigroup setup for the M1 Closure RT solver in the `N256_fiducial` and `N256_noSNe` simulations. From left to right, columns show group number, lower and upper bounds on the energy, and the mean energy for each bin. The "SED" column lists the energy multiple of the computed ionizing luminosity placed into each group. Note that ionizing luminosity corresponds to $E > 13.6\,e$V, so the fractions for groups 1, 2, and 3 sum to 1.0. The mean energies and SED for these groups is computed using fits from Schaerer (2003). The Lyman-Werner luminosity (group 0) is computed as 1.288 times the H-ionizing luminosity (group 1), assuming a 2×10^4 K blackbody spectrum.

Radiation Groups				
Group	$E_{\rm low}$ (eV)	$E_{\rm high}$ (eV)	$E_{\rm mean}$ (eV)	SED
0	11.18	13.60	12.80	0.9075
1	13.60	24.59	21.62	0.7046
2	24.59	54.42	30.0	0.2951
3	54.42	100.0	60.0	2.818×10^{-4}

5.2 Methodology

In total, we run 4 cosmological simulations using the `Enzo-E` code. These simulations use identical initial conditions and simulation parameters as the fiducial 256^3 simulation from Chapter 4, but with additional physics included. A summary of relevant parameters for each simulation are listed in Table 5.1. The `N256_fiducial` simulation (not be confused with the `N256_fiducial` simulation in Chapter 4) has a root grid dimension of 256^3 with 5 levels of AMR, a box length of 2.56 comoving Mpc, and includes both Pop III and Pop II star formation and feedback (SF+FB). Pop III SF+FB is handled using the machine-learning surrogate model, `StarNet` (Sec. 3.1, Wells & Norman 2022, Wells & Norman 2022, Wells & Norman 2021). `StarNet` makes predictions during the running simulation every ~ 5 Myr on subvolumes of size 10 proper kpc. Just as in the simulations of Chapter 4, if a star-forming region is predicted, a spherical metal bubble of radius 1 to 3 proper kpc is deposited at the center-of-mass of the star-forming region. The total deposited metal mass is computed assuming randomized population statistics based on the *Phoenix Simulations* (Wells & Norman, 2022). Pop II SF+FB is handled using the STARSS subgrid model (Sec. 3.2, Wells & Norman 2022), using the following star-formation criteria:

1. *Velocity divergence:* $\nabla \cdot \mathbf{v}_\mathrm{b} < 0$.
2. *Virial parameter:* $\alpha < 1$, where $\alpha \equiv \frac{\text{gravitational potential}}{\text{specific energy}}$.
3. *Jeans mass:* $M_\mathrm{b} > M_\mathrm{Jeans}$, where $M_\mathrm{J} \equiv \frac{\pi}{6} \frac{c_s^3}{G^{\frac{3}{2}} \rho^{\frac{1}{2}}}$.
4. *Cooling time:* $t_\mathrm{cool} < t_\mathrm{ff}$, where $t_\mathrm{ff} \equiv \sqrt{\frac{3\pi}{32G\rho}}$.

When these criteria are met in a cell, the prospective star particle's mass is computed assuming a gas conversion fraction of 0.05. The minimum and maximum allowed particle masses are 1000 $M_\odot$ and 3000 $M_\odot$, respectively. If all criteria are met, but $M_* = 0.05 M_\mathrm{b} < 1000\, M_\odot$ in the cell, a star particle is not formed. If, instead, $M_* = 0.05 M_\mathrm{b} \geq 3000\, M_\odot$, only 3000 $M_\odot$ of gas is converted into a star particle. Stellar feedback in the STARSS model includes Type Ia SNe, Type II SNe, stellar winds, and ionizing radiation, and is handled as described in Section 3.2.2. Radiative transport is performed using the M1 closure method in `Enzo-e` using a reduced speed of light fraction of 10^{-2} (Sec. 3.3.2). Photochemistry and photoheating are handled by `Grackle`. We evolve 4 radiation groups, with energies listed in Table 5.2.

[1] $M_\mathrm{vir} = 10^8\, M_\odot$ is the virial mass corresponding to $T_\mathrm{vir} = 10^4$ K at $z \simeq 8$.

We include ionizing radiation from Pop II star particles as well as recombination radiation. We subcycle radiative transfer and chemistry with respect to hydrodynamics (see Sec. 3.3.2), and further subcycle all physics methods with respect to gravity. Subcycling with respect to gravity is allowed because the gravitational time scale is typically much longer than the hydrodynamic time scale. This is especially true with stellar feedback heating the gas, as the hydrodynamic time scale decreases with increasing gas temperature due to the Courant condition (Courant et al., 1928).

To disentangle the effects of radiative and chemical feedback, we run two simulations that exclude either one form of feedback or the other. `N256_noSNe` is a re-run of `N256_fiducial` that excludes Pop II supernova feedback but retains radiative feedback. Similarly, `N256_noRad` is a re-run of `N256_fiducial` that instead excludes radiative feedback, as well as recombination radiation but retains supernova feedback. We additionally include the fiducial 256^3 simulation from Chapter 4 in our simulation suite, which is identical to `N256_fiducial`, except that it excludes Pop II SF+FB altogether. We refer to this simulation as `N256_noPopII` here.

5.2.1 Algorithmic Timeline of a Pop II Star Particle

To set the stage for the following results, it is useful to walk through the major events that occur during a given Pop II star particle's lifetime under the STARSS algorithm. Immediately following formation, the particle emits ionizing radiation with luminosity given by Equation 3.19. There is a time delay of 3.401 Myr following formation before the particle is allowed to emit Type II SNe. For ages between 3.401 Myr and 10.37 Myr, the particle emits SNe at a rate of 5.408×10^{-4} Myr$^{-1}\,M_{\odot}^{-1}$. For ages between 10.37 Myr and 37.53 Myr, the Type II SNe event rate is changed to 2.516×10^{-4} Myr$^{-1}\,M_{\odot}^{-1}$. Once the Pop II star particle reaches an age of 25 Myr, its ionizing luminosity is set to zero as the more massive stars in the population that are strong emitters of ionizing radiation are assumed to have died (see Eq. 3.19). After an age of 37.53 Myr, the Type II SNe event rate is set to zero, and the particle is allowed to emit Type Ia SNe at a low rate in perpetuity.

5.3 Results

For each simulation, dark matter halos are identified using the `Rockstar` halo finder (Behroozi et al., 2013), and the most massive halo in each is tracked over time. Because all simulations start from

identical initial conditions, halos between simulations can be directly compared with one another. We refer to the most massive halo in each simulation as `MMH_<sim_name>` (e.g. `MMH_fiducial`, `MMH_noSNe`, etc.). Any differences in the halos' evolution are purely due to differences in baryonic physics. It should be noted that there are stochastic elements to the star formation and feedback algorithms employed here, so some differences in stellar mass and metal enrichment are to be expected between runs with identical parameters. Nevertheless, the qualitative evolution of the halo is set by the physics suite. In the results that follow, a general trend can be observed where the overall behavior of the simulation is largely determined by whether or not radiative feedback is included. In other words, `MMH_fiducial` and `MMH_noSNe` evolve similarly to one another, but differently than `MMH_noRad` and `MMH_noPopII`.

5.3.1 Pop II Star Formation and Feedback Histories

Figure 5.1 shows the evolution of various quantities over time. For each star-forming halo, the first Pop II star particle forms around $t = 155$ Myr ($z \sim 22$). In `MMH_noRad`, stellar mass grows uninhibited from this point onwards, reaching a final value of $6 \times 10^5\ M_\odot$. Because of the relatively shallow potential well at the center of the halo, photoheating in `MMH_fiducial` and `MMH_noSNe` drives outflows from the halo centers. Within R_{1000}, the mean baryon number density drops from $\sim 10^1$ cm^{-3} to as low as $\sim 10^{-2}$ cm^{-3} in `MMH_fiducial` and `MMH_noSNe`. The HII region extends outwards to a radius of ~ 5 kpc, far beyond the virial radius. Star formation is suppressed in `MMH_fiducial` and `MMH_noSNe` until gas is able to re-collapse into a star-forming core. This occurs approximately 20 Myr after the Pop II star particles stop emitting ionizing radiation at $t \approx 165$ Myr. The flow of gas back into the halo occurs mainly through a single filament, through which gas flows at a speed of roughly 3×10^6 cm s^{-1}. The virial radius of the halo is $R_{\rm vir} \approx 0.5$ kpc. The time it takes for a parcel of gas flowing at a speed of 3×10^6 cm s^{-1} to travel a distance of $R_{\rm vir} \approx 0.5$ kpc is about 16 Myr, which, to first order, explains the 20 Myr time delay before star formation resumes that we observe. As before, ionizing radiation from the newly formed star particles again suppresses further star formation, though for a shorter time period of ~ 5 Myr. From there, star-forming events occur on a 1-5 Myr cadence until the final output at $t \approx 220$ Myr. With this, the early stages of star formation within a halo in the presence of radiative feedback can be characterized as bursty. In the runs that do not include radiation, the mean baryon density within R_{1000} stays roughly constant at $\sim 10^1$ cm^{-3}, and star formation occurs continuously at a rate of $10^{-2}\ M_\odot\,{\rm yr}^{-1}$ to $10^{-1}\ M_\odot\,{\rm yr}^{-1}$.

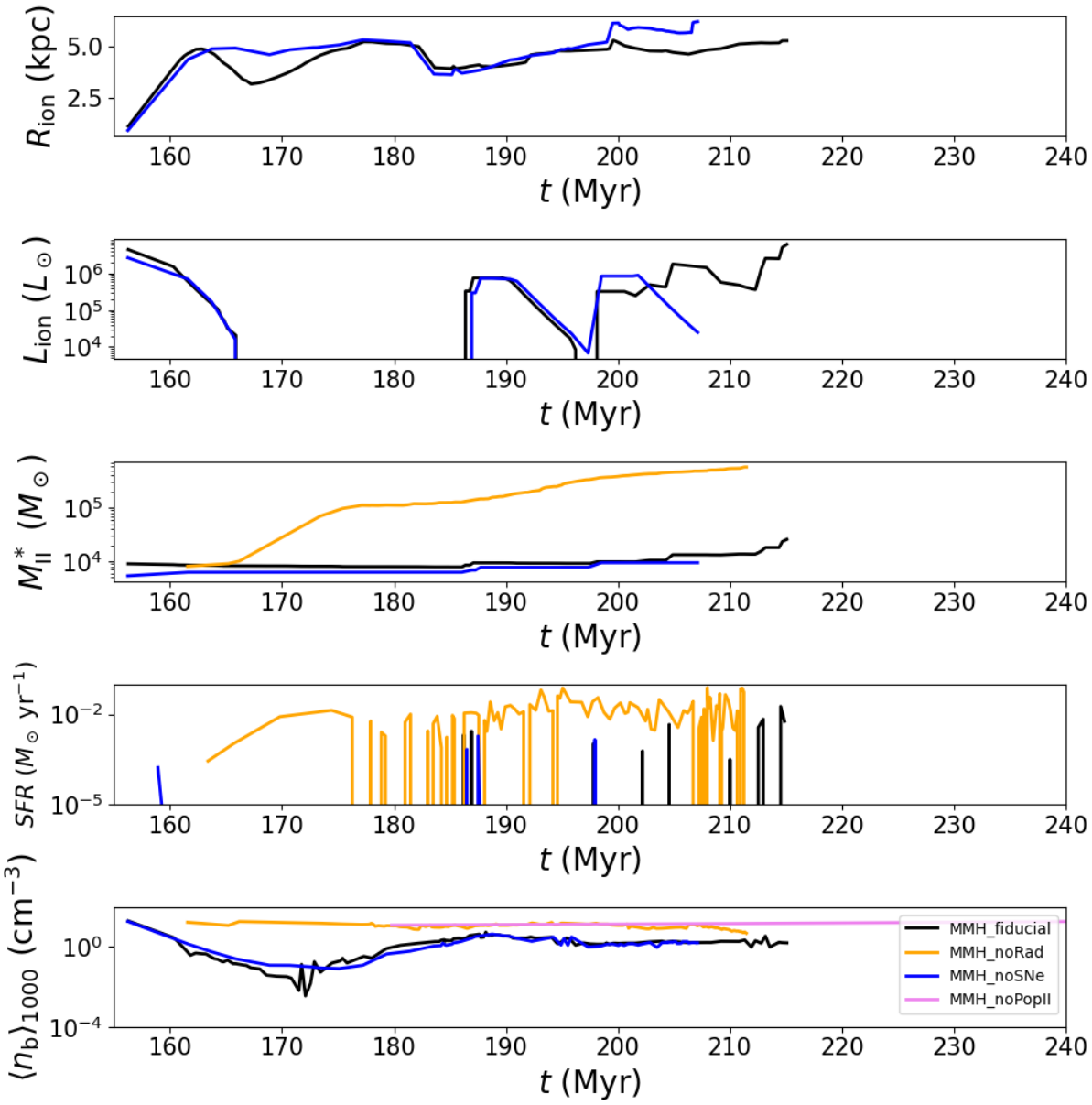

Figure 5.1. Time evolution of various quantities for each halo. From top to bottom, I-front radius, total ionizing luminosity from Pop II stars, Pop II stellar mass, star formation rate, and mean baryon density within R_{1000} are plotted versus time. The I-front radius is computed as the mean distance from the center that has an HII fraction between 0.1 and 0.2. `MMH_noRad` is not reflected in the I-front radius and ionizing luminosity panels because radiative feedback is inactive in the halo. Similarly, `MMH_noPopII` is reflected only in the mean baryon density panel because Pop II star formation and feedback is inactive for that particular halo altogether.

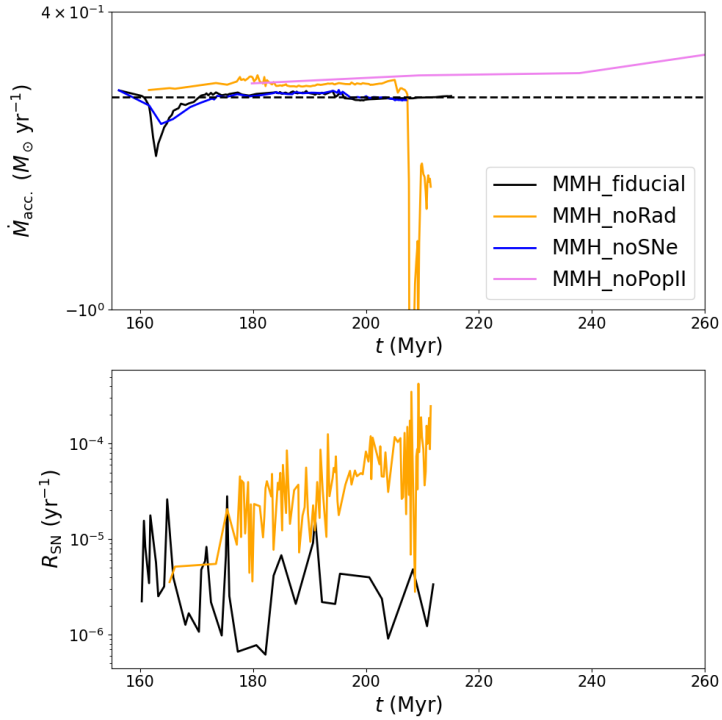

Figure 5.2. *Top:* Accretion rate through the virial radius vs. time for the most massive halo in each simulation. Positive values correspond to net inflow, while negative values correspond to net outflow. The black dashed line corresponds to $\dot{M}_{\rm acc} = 0$. Accretion rates for runs with radiative feedback are characteristically different from those without radiative feedback. *Bottom:* Supernova rate, computed as $N_{\rm SN}/\Delta t_{\rm out}$, where $N_{\rm SN}$ is the number of supernovae that occur in the halo between adjecent data outputs, and $\Delta t_{\rm out}$ is the time difference between the outputs. `MMH_noSNe` and `MMH_noPopII` are not shown because supernova feedback is turned off for both halos.

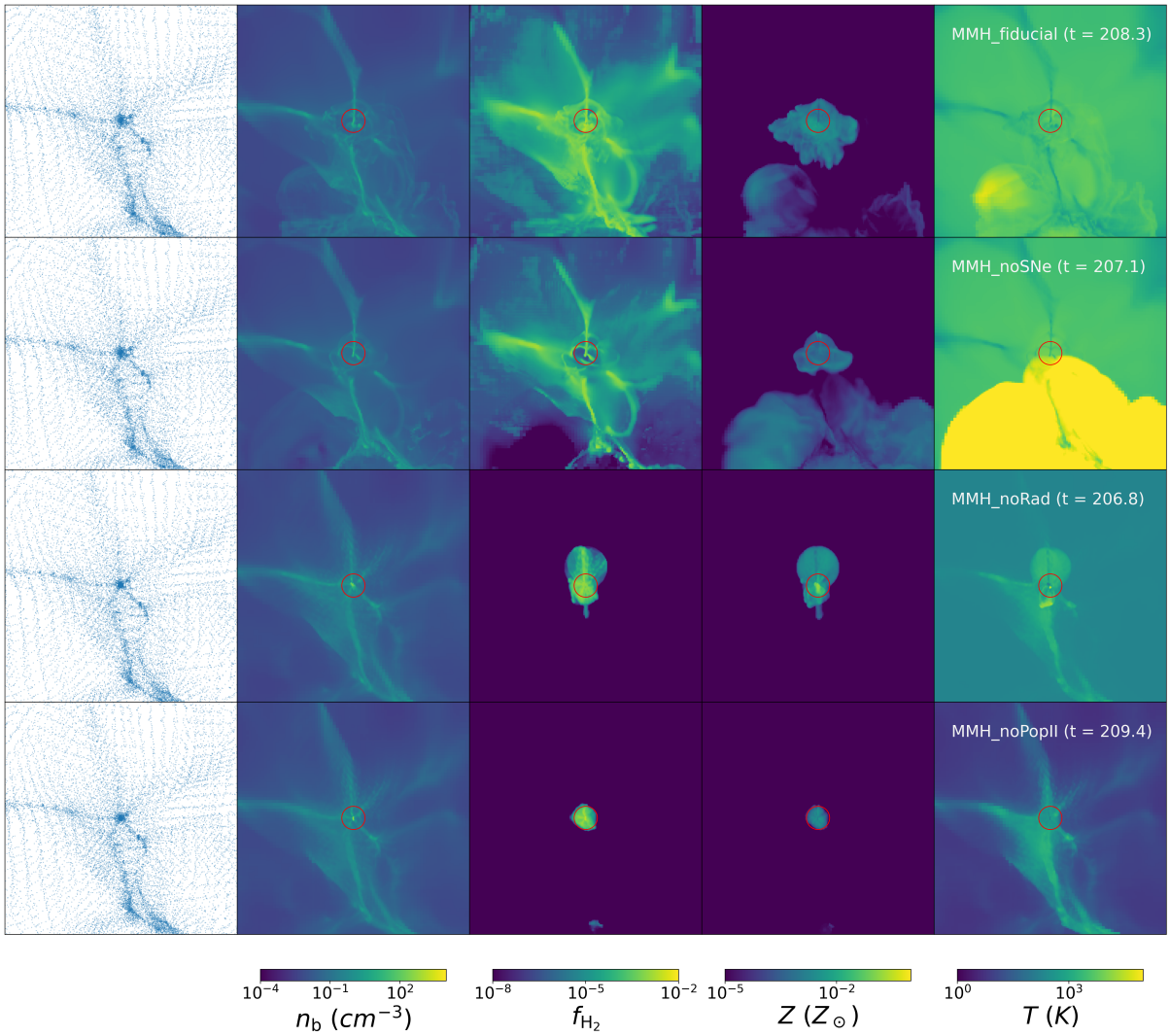

Figure 5.3. From left to right, projections of dark matter particles, baryon number density, H_2 fraction, metallicity, and temperature. From top to bottom, projections are shown for `MMH_fiducial`, `MMH_noSNe`, `MMH_noRad`, and `MMH_noPopII` at $z \sim 18$.

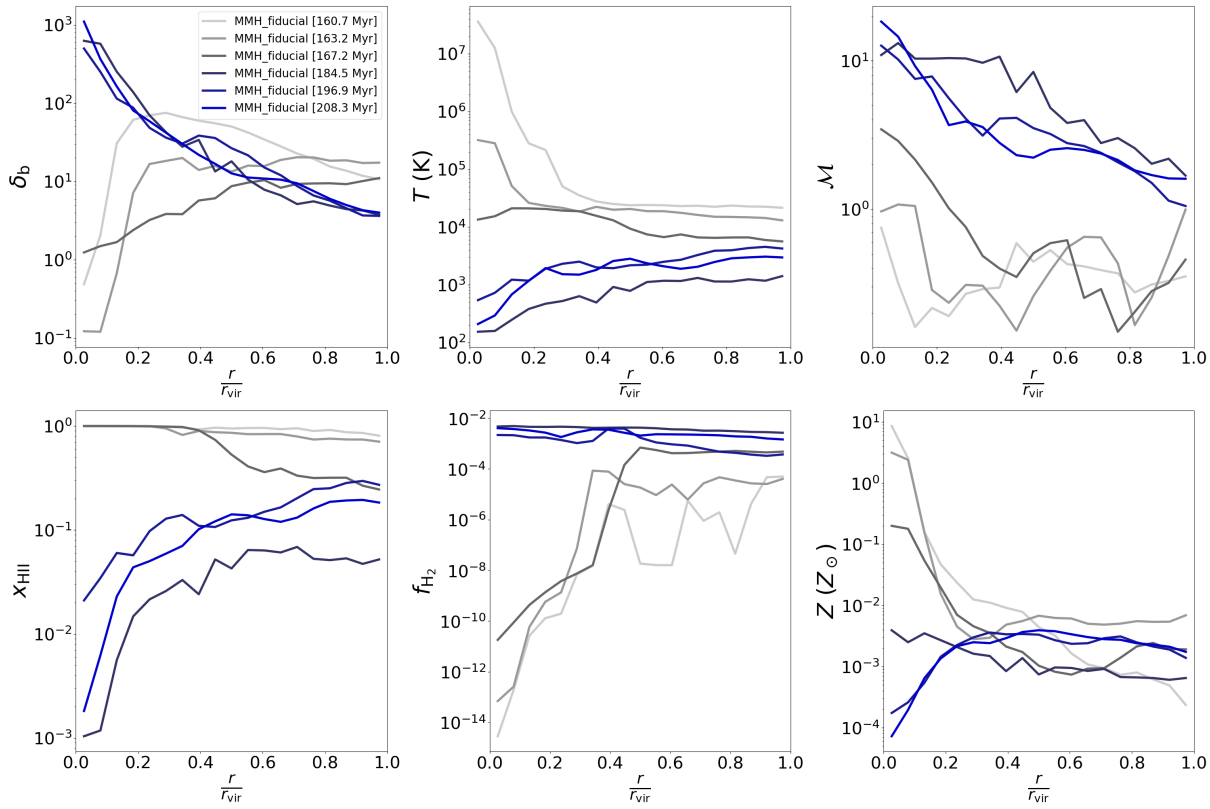

Figure 5.4. Radial profiles of baryon overdensity, temperature, mach number, HII fraction, H_2 fraction, and metallicity for `MMH_fiducial` at a number of different times. Profiles during the initial radiative phase are shown as shades of grey, while profiles after ionizing radiation from the first set of Pop II stars is shut off are shown as shades of blue.

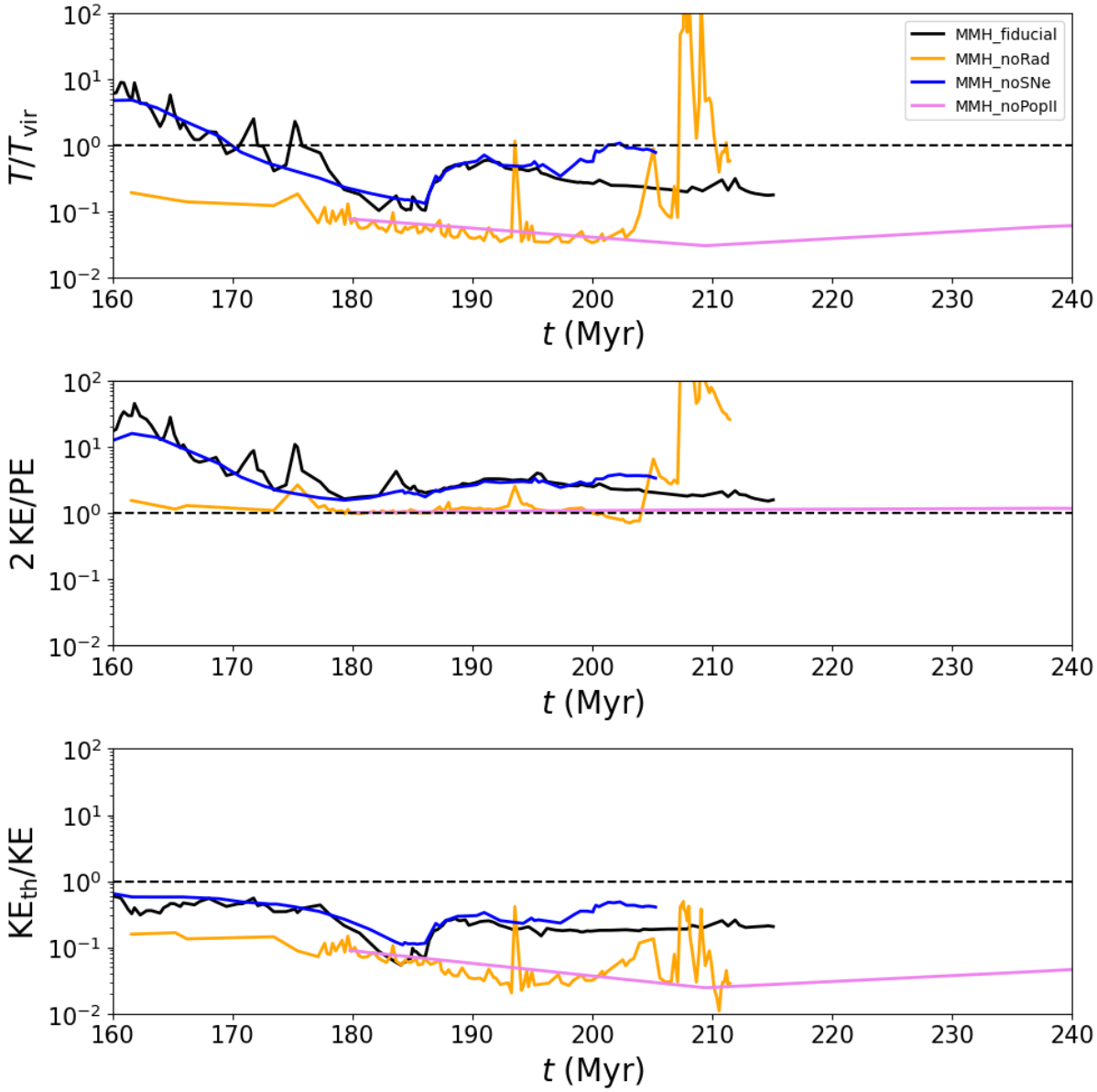

Figure 5.5. Time evolution of three quantities relevant to gas virialization. *Top:* Mean gas temperature within $R_{\rm vir}$, normalized by the virial temperature. *Middle:* Ratio between gas kinetic energy, including both mechanical and thermal components, and the potential energy. By definition, a virialized halo would have KE/PE=0.5. *Bottom:* Ratio between thermal energy and total kinetic energy within $R_{\rm vir}$.

Accretion rate through the virial radius is plotted versus time for each halo in the top panel of Figure 5.2. Accretion rates for MMH_fiducial and MMH_noSNe evolve similarly to one another. Photoevaporative outflows are clearly seen in downwards spikes in MMH_fiducial and MMH_noSNe (black and blue curves) at $t \approx 165$ Myr. Once radiation shuts off and photoheating is inactive, accretion onto the halo resumes. For the runs without radiation, accretion rates evolve similarly between MMH_noRad and MMH_noPopII (orange and violet curves) until $t \approx 205$ Myr. After this point, an uptick in supernova activity in MMH_noRad drives strong galactic winds, which shows up as a sharp downward spike in the top panel of Figure 5.2. The bottom panel of Figure 5.2 shows the occurrence rate of Pop II supernovae for MMH_fiducial and MMH_noRad. By the final output, MMH_fiducial has supernovae occuring at a rate of approximately 3×10^{-6} yr^{-1}, while the rate for MMH_noRad is approximately 10^{-4} yr^{-1}. The nearly two orders of magnitude difference in supernova rate is proportional to the difference in stellar mass between the two halos.

Figure 5.3 shows projections of baryon number density, H_2 fraction, metallicity, and temperature for a ~ 5 kpc box centered on the most massive halo in each simulation at $z \sim 18$. Also shown in each figure is the projected dark matter particle distribution around the halo. Since these are all effectively the same halo subject to different baryonic physics, the dark matter distribution looks more-or-less identical between the halos. MMH_noRad shows the effects of strong supernova-driven galactic winds, which result in a hot, asymmetrical bubble that extends beyond the virial radius. While supernovae are very energetic events, a stellar population will emit more energy during its early stages in the form of radiation[2]. Because of this, galactic winds in MMH_fiducial and MMH_noSNe are instead primarily driven by radiative feedback, and baryon distributions look very similar visually to one another. In each case, radiation carves out a cavity within the halo. Gas inflows occur through the filament that extends vertically northward of the halo as viewed in the baryon density projections. A flow of hot, enriched gas encroaching onto the halo from outside can be seen in MMH_fiducial and MMH_noSNe. This flow originates from a nearby halo that has also formed Pop II stars by this redshift. In each case, the metal content of the flow is almost entirely Pop III metals that have been driven outwards by radiative feedback.

Radial profiles of baryon overdensity, temperature, mach number, ionized fraction, H_2 fraction,

[2]For a stellar population with a total ionizing luminosity of $10^5\ L_\odot$, the total energy radiated over a time period of 25 Myr is 3×10^{53} erg, which is roughly equal to the energy released by 300 Type II supernovae. We see that strong supernova-driven outflows in MMH_noRad do not take place until the supernova event rate reaches $\sim 5 \times 10^{-5}$ yr^{-1} (50 Myr^{-1}). At this event rate, supernovae inject 3×10^{53} erg into the gas in bursts over the course of 6 Myr.

and metallicity for `MMH_fiducial` at a number of different times are shown in figure 5.4. During the initial radiative phase, the baryon overdensty at the center has values between 10^{-1} and 10^{0}. The gas is hot, ionized, metal-enriched, and has low H_2 fractions during this phase. Energy from supernovae occuring in the diffuse gas at the center is deposited by our feedback model as primarily thermal energy, leading to temperatures as high as 4×10^7 K at the center. The large temperatures, and thus large sound speeds at the center result in subsonic flows. The gas has a large metal component at the center, with metallicities as high as $Z = 10^1\ Z_\odot$. Because the photoevaporative flows from Pop II stars have pushed Pop III metals to outside the virial radius, the metallicity of the halo is dominated by Pop II metals. After the radiative phase, baryon overdensity recovers to $\delta_b \simeq 10^3$ at the center, the gas cools to $T = 10^2 - 10^3$ K, and flows become supersonic. Hydrogen recombination occurs from the inside-out, with ionized fraction increasing with radius. Along with hydrogen recombination comes stimulated H_2 formation, resulting in approximately flat profiles of H_2 fraction with values between 10^{-3} and 10^{-2}. The metallicity profile also changes shape. The five orders of magnitude reduction in metallicity at the center over time is due to the cycling of hydrogen and helium, which had originally been pushed out of the halo by the radiative feedback, back towards the center of the halo. By the final output, metallicities range from $Z \simeq 10^{-4}\ Z_\odot$ at the center to $Z \simeq 3 \times 10^{-3}$ beyond $r/R_{\rm vir} = 0.2$.

Recall that the function of the STARSS feedback algorithm is to use physical arguments to determine the phase of evolution for a supernova remnant by the time it expands to a radius of a cell width, Δx, and compute the fraction of the total kinetic energy to be deposited as thermal energy versus mechanical energy. We take the total energy released by a Type II supernova to be 10^{51} erg. To better understand the effects of supernova feedback we have seen so far, we take a short detour to walk through how our feedback algorithm deposits supernova remnants for exemplary densities and temperatures. During the initial radiative phase in `MMH_fiducial`, densities at the center of the halo drop to $n_b \simeq 10^{-2}$ cm^{-3}. At this time, the free expansion radius computed using Equation 3.11 is $R_{\rm free} = 19.4$ pc, and the proper cell width is $\Delta x = 15.6$ pc. Because $\Delta x < R_{\rm free}$, the remnant will be deposited in the free expansion phase. In this case, the energy makeup of the remnant is roughly 50% thermal at deposition (see Eq. 3.17). Thermal energy scales with density and temperature (i.e. $E_{\rm th} \sim n_b T$). At such a low density as 10^{-2} cm^{-3}, the temperature needed to give a thermal energy of 5×10^{50} erg is very large. This is why temperatures at the center of the halo exceed 10^7 K at early times (Fig. 5.4). Later on, densities at the center recover to

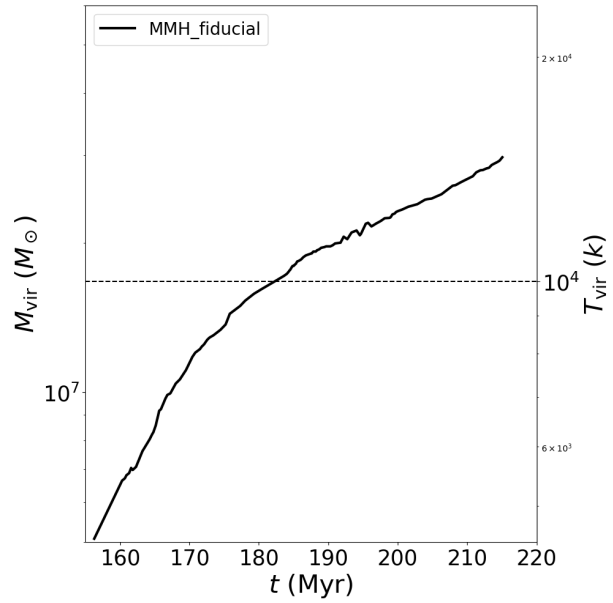

Figure 5.6. Virial mass versus time for `MMH_fiducial`. The vertical axis on the right shows the corresponding virial temperature. The horizontal dashed line indicates $T_{\rm vir} = 10^4$ K.

$n_{\rm b} \simeq 10^2$ cm^{-3}. For this new density, $R_{\rm free} = 0.90$ pc, $R_{\rm cool} = 4.0$ pc, and $R_{\rm fade} = 30.2$ pc (assuming a sound speed of 10^5 cm s^{-1}). Because $R_{\rm cool} < \Delta x < R_{\rm fade}$, the remnant will be deposited in the terminal phase. In this case, Equation 3.17 gives an energy makeup of roughly 75% thermal and 25% mechanical. Now that the gas density is 4 orders of magnitude larger than the low-density case, the temperature required to give the same thermal energy is roughly 4 orders of magnitude smaller. This is why supernova feedback appears to have little effect on accretion rates and the overall thermodynamics of gas in the halo for most of its lifetime. Once the gaseous core has been restored in `MMH_fiducial`, supernovae exploding within the core do not create significant temperature gradients to impact gas dynamics on scales larger than a cell width.

5.3.2 Incomplete Virialization and Gas Thermalization

In Chapter 4, it was found that in the absence of Pop II SF+FB, virialization of gas within a halo is supported by turbulence instead of by thermal motions. We again assess the virialization state of the gas within the most massive halo for each simulation in Figure 5.5, which shows the time evolution of mean gas temperature, the ratio between kinetic and potential energies, and the ratio of thermal kinetic energy to total kinetic energy for gas within the halo. Kinetic and potential energies are computed using

Equations 4.6, 4.8, and 4.7. To compute the virial temperature, we use the following definition from Trenti & Stiavelli (2009):

$$T_{\rm vir}(M_{\rm vir}, z) = 2554\ {\rm K} \left(\frac{M_{\rm vir}}{10^6\ M_\odot} \right)^{2/3} \left(\frac{1+z}{31} \right). \tag{5.1}$$

An ideal, virialized halo will have $2\,{\rm KE}/{\rm PE} = 1$. If the gas within the halo is fully thermalized, it will have $T/T_{\rm vir} = {\rm KE_{th}}/{\rm KE} = 1$. For reference, the virial mass versus time is plotted for `MMH_fiducial` in Figure 5.6.

Starting from $t = 160$ Myr, `MMH_fiducial` (black curves) has $T/T_{\rm vir} \simeq 6$, $2\,{\rm KE}/{\rm PE} \simeq 20$, and ${\rm KE_{th}}/{\rm KE} \simeq 0.6$. Photoheating is responsible for the relatively high temperature and energy fraction at this time. By $t = 165$ Myr, the total ionizing luminosity of the stellar population has reduced to zero. For a period of roughly 20 Myr after this point, the gas is allowed to cool in the absence of strong sources of photoheating. By $t = 185$ Myr, all quantities have reduced. Specifically, $T/T_{\rm vir} \simeq 0.2$, $2\,{\rm KE}/{\rm PE} \simeq 3$, and ${\rm KE_{th}}/{\rm KE} \simeq 0.1$. With star formation resuming after $t = 185$ Myr, the gas is quickly photoheated to $T/T_{\rm vir} \simeq 0.6$. After this point, $T/T_{\rm vir}$ and $2\,{\rm KE}/{\rm PE}$ gradually decline to 0.3 and 2, respectively, and ${\rm KE_{th}}/{\rm KE}$ remains roughly constant at a value of 0.3.

`MMH_noSNe` (blue curves) evolves similarly to `MMH_fiducial` in Figure 5.5, minus the small deviations during Pop II SNe that are present in `MMH_fiducial`. $2\,{\rm KE}/{\rm PE} > 1$ for both halos at all times. Due to slight differences in Pop II SFRs at $t \simeq 195$, `MMH_noSNe` deviates somewhat from `MMH_fiducial`, and the mean gas temperature is close to the virial temperature by the final output. It should be noted that photoheating, not shock heating, is responsible for bringing the gas to the virial temperature in this case, meaning that the fact that the gas is at the virial temperature is more-or-less coincidental.

In `MMH_noRad` (orange curves) and `MMH_noPopII` (violet curves), thermal energy accounts for only a small fraction of the total gas KE. In both cases, virialization is supported by non-thermal bulk flows. In `MMH_noRad`, the gas is temporarily thrown out of virial equilibrium during periods of heavy supernova feedback, though it seems to recover quickly. Because the curves for `N256_fiducial` and `N256_noSNe` follow similar trends, we can say that the thermal history of gas during the early stages of the halo's lifetime is primarily modulated by radiative feedback. This is perhaps the key takeaway from Figure 5.5.

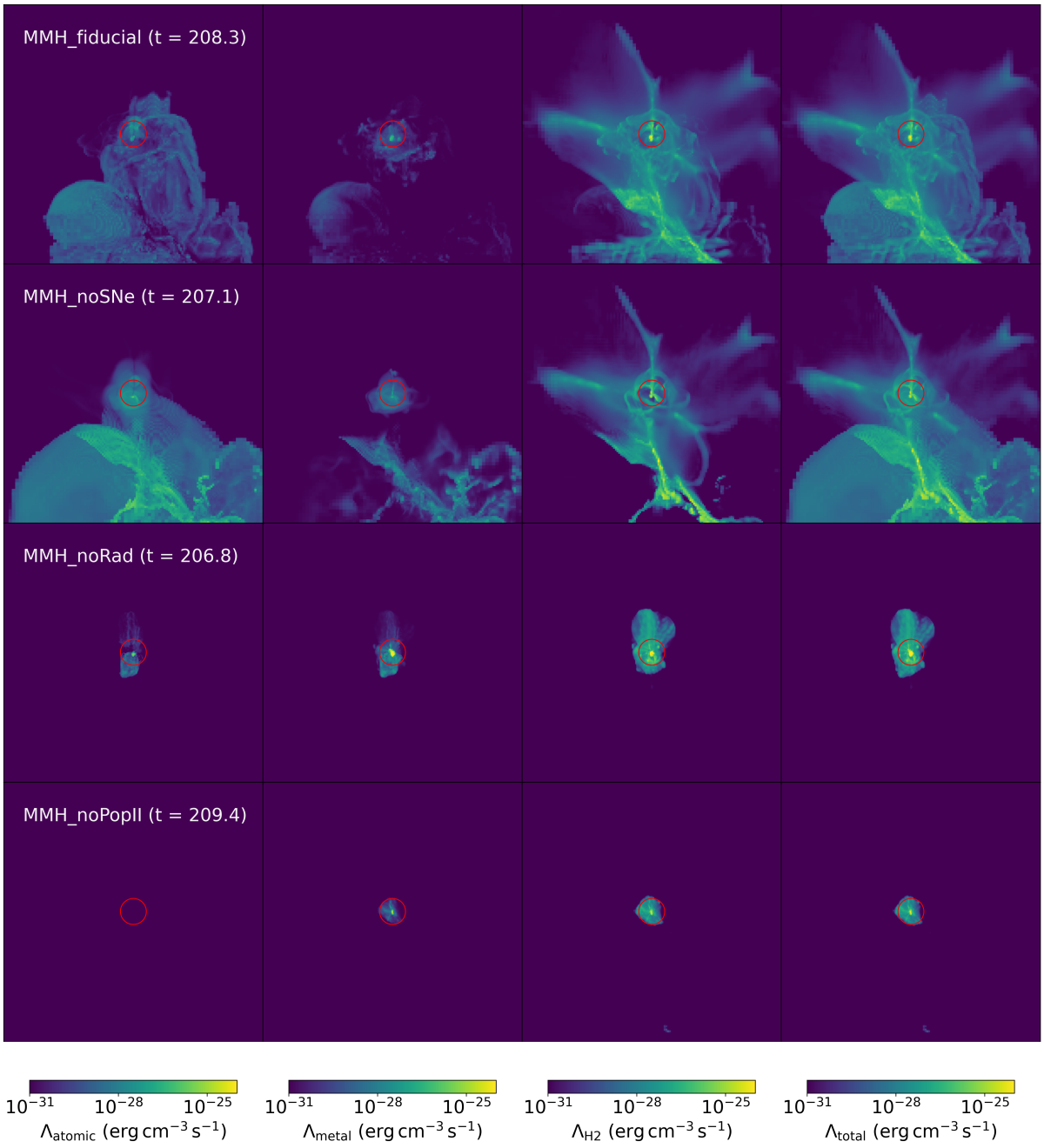

Figure 5.7. From left to right, projections of atomic, metal, H_2, and total cooling rates. From top to bottom, projections are shown for `MMH_fiducial`, `MMH_noSNe`, `MMH_noRad`, and `MMH_noPopII` at $z \sim 18$.

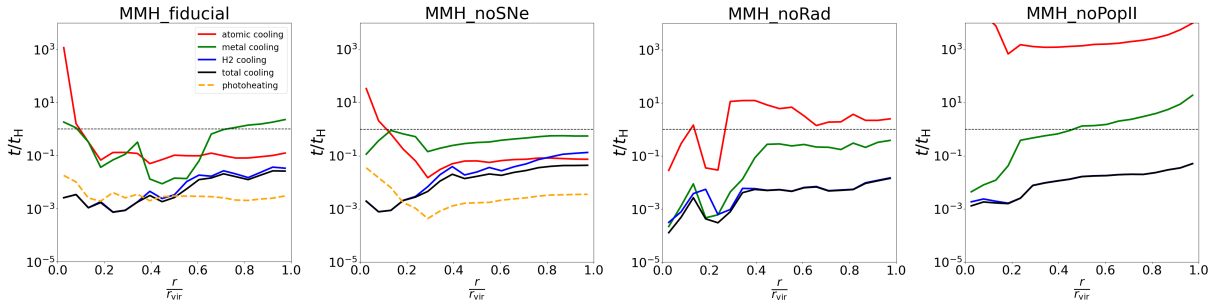

Figure 5.8. Radial profiles of atomic, metal, H_2, and total cooling time for each simulation, normalized by the Hubble time, at $z \simeq 18$. For `MMH_fiducial` and `MMH_noSNe`, and additional profile of photoheating time is overplotted. While photoheating is clearly active in each halo, gas is net cooling at the center.

5.3.3 Chemistry and Cooling

Of particular importance is the notable increase in H_2 fraction in the halo's environment in the `N256_fiducial` and `N256_noSNe` simulations. This can be clearly seen in the third column of Figure 5.3. While Pop II stars are actively emitting ionizing radiation in these simulations, gas within a ~ 5 kpc radius around the halo is fully ionized. When the stellar population reaches an age of 25 Myr, ionizing radiation, including radiation in the LW band, is shut off, and gas is able to recombine in the vicinity of the halo. During this recombination phase, the now partially ionized gas is a breeding ground for H_2 via the associative attachment reaction channel:

$$H + e^- \rightarrow H^- + h\nu \tag{5.2}$$

$$H^- + H \rightarrow H_2 + e^-. \tag{5.3}$$

As the newly formed H_2 falls back towards the center of the halo, H_2 becomes the dominant coolant.

Just as in Chapter 4, we compute atomic (H and He), H_2, and metal cooling rates using the python extension of `Grackle`, `PyGrackle`[3]. Projections of each of the aforementioned cooling rates, as well as the total cooling rate are shown for each halo in Figure 5.7. In Chapter 4, we saw that in the absence of Pop II SF+FB, H_2 was overall the dominant coolant for most halos with $M_{vir} < 10^9\ M_\odot$, with metal cooling also playing a role. This appears to be true for the halos analyzed here, though atomic cooling is also relevant now that additional heating sources can bring gas to $T > 10^4$ K. However, atomic cooling remains subdominant to H_2 cooling by the final output, even though the halo surpasses a virial temperature

[3] https://grackle.readthedocs.io/en/grackle-3.1.1/Python.html

of 10^4 K by $t = 175$ Myr. This can be seen in Figure 5.8, which shows radial profiles of atomic, metal, and H_2 cooling times, normalized by the Hubble time, for each simulation at $z \sim 18$. In all cases, H_2 cooling remains the dominant cooling channel for gas in the halo. Metal cooling rates are slightly higher than H_2 cooling rates at the center of `MMH_noRad` due to its higher stellar mass, and thus higher supernova rates (Fig. 5.2).

The fact that H_2 cooling remains vital for cooling in `MMH_fiducial` in the presence of multiple forms of stellar feedback is interesting for a number of reasons. For one, the halo has a virial temperature above 10^4 K, and is also metal-enriched. Conventional wisdom would imply that the halo would either be atomic cooling ($T_{\rm vir} > 10^4$ K) or metal cooling (halo is enriched). On top of this, we include both local LW radiation from Pop II stars, as well as a LWB, each of which acts to photodissociate H_2. During the radiative phase of a stellar population's lifetime, local LW radiation is stronger than the LWB. Once local radiation is turned off and H_2 formation begins in the partially recombined gas, the halo achieves an H_2 column density of $N_{\rm H_2} \approx 3 \times 10^{16}$ cm^{-2} at the center by the final output. For H_2 self-shielding from the LWB to be important, gas must have an H_2 column density of $N_{\rm H_2} \gtrsim 5 \times 10^{14}$ cm^{-2}. `MMH_fiducial` has achieved such a value, which means that self-shielding is partially responsible for allowing H_2 cooling to remain the primary cooling channel for the halo.

5.4 Discussion

5.4.1 Bursty Star Formation In Young Halos

Star formation in young halos has long been understood to be episodic in nature. This feature in a halo's star-forming history can be attributed to a combination of chemical dynamics and mechanical motions of the gas. On the chemistry side, the dynamics of H_2 formation and destruction in the vicinity of the first luminous objects was first studied in Ricotti et al. (2002), where the authors distinguish between "positive" and "negative" feedback. In the case of positive feedback, H_2 formation takes place ahead of the I-front during the radiative phase, and then within the HII region that is left behind once the stellar population stops emitting ionizing radiation. In the case of negative feedback, local LW radiation during the radiative phase photodissociates H_2 near the source. The authors find that this destruction and subsequent reformation of H_2 in low-mass star formation halos leads to bursty star-formation rates.

Our simulations directly resolve positive and negative radiative feedback (Figs. 5.3 and 5.4) as

defined by Ricotti et al. (2002), and confirm that H_2 remains the dominant coolant during the reassembly of the star-forming core in the low-mass halos analyzed here (Fig. 5.8). In fact, H_2 is the *only* coolant that is able to overcome photoheating from recombination radiation at the center of the halos in the simulations that include radiative feedback, which implies that the positive feedback seen in these particular simulations is partially responsible for the second burst of star formation we observe.

Along with the chemical dynamics, the mechanical motions of the gas in a halo (i.e. inflows and outflows) are partially responsible for the bursty star formation we observe. The relationship between mechanical gas flows and star formation are studied in detail in Muratov et al. (2015) in low-to-moderate redshift contexts ($z \simeq 0-4$), where they find that the transition to continuous, non-episodic star formation does not take place until a halo mass of $M_{\rm vir} \approx 10^{12}\,M_{\odot}$ is reached. The halos analyzed here are not anywhere near as massive as $10^{12}\,M_{\odot}$, meaning that episodic star formation is to be expected.

5.4.2 $T_{\rm vir} > 10^4$ K as a Marker for Atomic Cooling Halos

A virial temperature of 10^4 K has long been used as a dividing line for whether or not a halo is an atomic cooling halo (ACH). This is because gas with $T > 10^4$ K is able to cool via collisional excitations and subsequent de-excitations in atomic hydrogen and helium. In Chapter 4, we found that in the absence of Pop II star formation and feedback, runaway cooling at the centers of halos prevents gas from ever reaching the virial temperature, thus rendering atomic cooling irrelevant to the dynamics of the gas. In this case, virialization is supported by bulk flows instead of by thermal motions. If gas in a halo is fully thermalized, its temperature in a virialized halo should be equal to the virial temperature. In this study, we allow thermal energy injection from both radiative and supernova feedback from Pop II stars. With this, it is now possible for gas in a halo to be heated to $T > 10^4$ K; however, the mean temperature of the gaseous component is not equal to the virial temperature, due to a combination of cooling and various feedback effects (see Fig. 5.5). Because of this, the virial temperature cannot be used as a reliable predictor for gas temperature in a halo with $M_{\rm v} \lesssim 10^8\,M_{\odot}$. It should be noted that we do not analyze a statistical sample of halos with $T_{\rm vir} \sim 10^4$ K here, and we therefore can not make a definitive statement about whether or not we should expect gas in *any* $M_{\rm vir} \lesssim 10^8\,M_{\odot}$ halo to match with the virial temperature. Nevertheless, we predict that our observations here will generally hold for any low-mass halo whose internal structure is sensitive to disruption by stellar feedback.

If virial temperature is indeed not indicative of a shift towards atomic cooling in a halo, then what measure should be used? Wise et al. (2014) performs a similar breakdown of the relative strengths of atomic, H_2, and metal cooling rates as we perform here (see Fig. 2 in the cited study) in a cosmological simulation of a 1 comoving Mpc box. In the study, the authors do observe a transition to atomic cooling at $T_{\rm vir} = 10^4$ K; however, there are no 10^4 K halos in the sample before $t \approx 500$ Myr ($z \approx 10$), at which point $T_{\rm vir} = 10^4$ K corresponds to a virial mass of $M_{\rm vir} \approx 4 \times 10^7\ M_\odot$. This means that the atomic cooling halos identified in Wise et al. (2014) had virial masses generally above $4 \times 10^7\ M_\odot$. Our simulations are not run far past $t = 200$ Myr ($z \approx 18$), yet we do form a 10^4 K halo at a virial mass of $M_{\rm vir} = 2 \times 10^7\ M_\odot$.

A number of scaling relations derived from a larger sample of halos in the *Renaissance Simulations* are presented in Chen et al. (2014). In particular, the obtained relationship between SFR and virial mass is piecewise, with a shift to increased SFRs that occurs at $M_{\rm vir} = 10^8\ M_\odot$ (see Fig. 3 in cited study). Wise et al. (2014) finds a similar relationship, albeit with a much smaller sample of halos with $M_{\rm vir} \gtrsim 10^8\ M_\odot$. In both cases, the respective authors attribute the increased SFRs to efficient atomic cooling in these halos. It should be noted that in both studies, the halo sample is comprised of halos at a number of redshifts—$18.43 \leq z \leq 15$ for Chen et al. (2014) and $17 \lesssim z \leq 7.3$. While the two samples are obtained over different redshift ranges, both observe an increase in SFR at $M_{\rm vir} \approx 10^8\ M_\odot$, which suggests that the physics that causes the increase is redshift-independent (note that virial temperature scales with redshift). If the effect is indeed caused by efficient atomic cooling, then $M_{\rm vir} > 10^8\ M_\odot$ should be taken as the marker for a true atomic cooling halo instead of $T_{\rm vir} > 10^4$ K.

5.4.3 Interplay Between Radiative and Supernova Feedback

We have seen that radiative feedback causes bursty star formation in a protogalaxy, resulting in a much lower stellar mass after ~ 50 Myr of evolution than otherwise. Because chemical feedback is tightly coupled to star formation, the metal mass in `MMH_noRad` is an order of magnitude larger than that in `MMH_fiducial`. Somewhat counter-intuitively, radiative feedback helps metals spread further earlier despite the drastic reduction in supernova feedback. This is possible because of the time delay between star formation and supernova feedback, during which time a photoevaporative flow is able to propagate. A supernova remnant expanding in the wake of the photoevaporative flow will experience free expansion through the warm, diffuse medium until it reaches the photoevaporative front, which may be outside the

virial radius for a halo with $M_{\rm vir} \lesssim 10^8\ M_\odot$. In the absence of radiative feedback, the first supernovae would instead go off in a cold, dense medium, and the metals would remain trapped in the core until a period of heavy supernova feedback is able to drive outflows to outside the virial radius. The no-radiation case is artificial though, as stars emit radiative feedback in nature.

5.4.4 Caveats

We now note a few shortcomings to our analysis that may impact our results. The most significant shortcoming is that our findings are based on the analysis of individual halos. We do not obtain a statistical sample of star-forming halos, and can therefore not conclusively comment on whether our findings are indicative of general trends for halos with $M_{\rm vir} \lesssim 10^8\ M_\odot$. Analyzing a larger simulation based on the 512^3 simulation of Chapter 4 with Pop II star formation and feedback would be highly informative. Another shortcoming is that we often do not resolve the Sedov-Taylor phase expansion for Pop II supernova remants. As mentioned in Section 5.3.1, supernovae exploding in dense gas are often identified to be well into the terminal phase by the time the remnant expands to a cell width in radius. While our feedback algorithm is designed to be physically accurate over a wide range of grid resolutions, nature has effectively infinite resolution. In reality, the ISM within the central cells would be turbulent, and running with sufficient resolution to simulate the dynamics of gas heated by supernovae in the turbulent ISM may impact star formation rates. On the topic of stellar feedback, while we include thermal radiative feedback in the form of photoheating, we do not include mechanical radiative feedback in the form of radiation pressure. Including radiation pressure would increase photoevaporative outflows, which would likely lead to longer time delays between star-forming events, and would decrease star formation rates as a whole (Wise et al., 2012a).

5.5 Conclusion

Using the AMR cosmology code, `Enzo-E`, we have simulated the evolution of the gas within a dark matter halo of mass $M_{\rm vir} \simeq 3 \times 10^7\ M_\odot$ subject to four different Pop II feedback prescriptions: (1) supernova and radiative feedback, (2) radiative feedback only, (3) supernova feedback only, and (4) no Pop II star formation and feedback. The halo is identified as the most massive halo within a comoving volume of $(2.56\ {\rm Mpc})^3$ at $z \sim 18$. These simulations were based on the 256^3 series of simulations in

Chapter 4, which do not include Pop II star formation and feedback. We have obtained a number of key results:

1. Radiative feedback alone is sufficient to drive outflows and suppress star formation during the early stages of a halo's lifetime, leading to bursty star formation histories (Figs. 5.1 and 5.2). Radiation injects energy into its environment much more efficiently than supernova feedback. Excluding radiative feedback from the physics suite leads to artificially large star formation rates, which, in turn, leads to an overproduction of metals.

2. Radiation both reduces and promotes H_2 cooling. The reduction occurs through H_2 photodissociation by Lyman-Werner radiation. The promotion occurs through enhanced H_2 formation in the partially recombined gas of relic HII regions. The two effects do not cancel each other out. Rather, the net effect is dramatically increased production of H_2 both in and around the halo (Figs. 5.3 and 5.4).

3. H_2 remains the dominant coolant in the simulated halo, even in the presence of photoheating and metal enrichment from Pop II stars. Atomic cooling, while made relevant by photoheating, is subdominant to H_2 and metal cooling, even after the halo reaches a virial temperature of $T_{\rm vir} = 10^4$ K (Fig. 5.8).

4. The virial temperature is not a reliable measure of the gas temperature in a halo with $M_{\rm vir} \lesssim 10^8\ M_\odot$. A halo of such a low mass is sensitive to disruption by stellar feedback effects. On top of this, interactions between heating and cooling processes in the halo are complicated, and heating does not generally balance with cooling (Fig. 5.5).

These results serve as a preview of what is to come. In the complete version of this study, we will test whether our findings here hold for a statistical sample of halos in the mass range $10^6\ M_\odot < M_{\rm vir} < 10^9\ M_\odot$. The larger sample will also allow us to probe the evolution of large-scale quantities over time, such as Pop III/II star formation rates, luminosity functions, and two-point correlation functions. From there, we will draw connections with observed high redshift galaxies where possible.

5.6 Acknowledgements

This research was partially supported by National Science Foundation grant AST-2108076 to M.L.N. and via NASA grant 80NSSC21K1053, P.I. Molly Peeples, through a subaward to M.L.N. The simulations were carried out on the Frontera supercomputer operated by the Texas Advanced Computing Center with LRAC allocation AST20007. Simulations were performed with `Enzo-E` (https://github.com/enzo-project/enzo-e) coupled to `Grackle` (Smith et al., 2017). Analysis and plot generation was done using `YT` (Turk et al., 2011). `Enzo-E`, `Grackle`, and `YT` are all collaborative open source codes representing efforts from many independent scientists around the world.

Chapter 5, in part, is currently being prepared for submission for publication of the material as it may appear in Hicks, Norman, Wells, & Bordner (2024), "Galaxies and Their Environment at $z \gtrsim 10$—II: The Role of Radiative and Kinetic Feedback in Protogalaxy Formation", *The Astrophysical Journal*. The dissertation author was the primary investigator and author of this paper.

Bibliography

Abel T, P Anninos, Y Zhang, & ML Norman 1997 'Modeling primordial gas in numerical cosmology' *New Astronomy* 2(3):181–207 doi: 10.1016/s1384-1076(97)00010-9 URL http://dx.doi.org/10.1016/S1384-1076(97)00010-9.

Abel T, GL Bryan, & ML Norman 2000 'The Formation and Fragmentation of Primordial Molecular Clouds' 540(1):39–44 doi: 10.1086/309295.

Abel T, GL Bryan, & ML Norman 2002 'The Formation of the First Star in the Universe' *Science* 295(5552):93–98 doi: 10.1126/science.295.5552.93.

Abel T, JH Wise, & GL Bryan 2007 'The h ii region of a primordial star' *The Astrophysical Journal* 659(2):L87–L90 doi: 10.1086/516820 URL http://dx.doi.org/10.1086/516820.

Abohalima A & A Frebel 2018 'Jinabase—a database for chemical abundances of metal-poor stars' *The Astrophysical Journal Supplement Series* 238(2):36 doi: 10.3847/1538-4365/aadfe9 URL http://dx.doi.org/10.3847/1538-4365/aadfe9.

Adamo A, H Atek, MB Bagley, E Bañados, KSS Barrow, DA Berg, R Bezanson, M Bradač, G Brammer, AC Carnall, J Chisholm, D Coe, P Dayal, DJ Eisenstein, JJ Eldridge, A Ferrara, S Fujimoto, A de Graaff, M Habouzit, TA Hutchison, JS Kartaltepe, SA Kassin, M Kriek, I Labbé, R Maiolino, R Marques-Chaves, MV Maseda, C Mason, J Matthee, KBW McQuinn, G Meynet, RP Naidu, PA Oesch, L Pentericci, PG Pérez-González, JR Rigby, G Roberts-Borsani, D Schaerer, AE Shapley, DP Stark, M Stiavelli, AL Strom, E Vanzella, F Wang, SM Wilkins, CC Williams, CJ Willott, D Wylezalek, & A Nota 2024 'The First Billion Years, According to JWST' *arXiv e-prints* :arXiv:2405.21054doi: 10.48550/arXiv.2405.21054.

Adamo A, H Atek, MB Bagley, E Bañados, KSS Barrow, DA Berg, R Bezanson, M Bradač, G Brammer, AC Carnall, J Chisholm, D Coe, P Dayal, DJ Eisenstein, JJ Eldridge, A Ferrara, S Fujimoto, A de Graaff, M Habouzit, TA Hutchison, JS Kartaltepe, SA Kassin, M Kriek, I Labbé, R Maiolino, R Marques-Chaves, MV Maseda, C Mason, J Matthee, KBW McQuinn, G Meynet, RP Naidu, PA Oesch, L Pentericci, PG Pérez-González, JR Rigby, G Roberts-Borsani, D Schaerer, AE Shapley, DP Stark, M Stiavelli, AL Strom, E Vanzella, F Wang, SM Wilkins, CC Williams, CJ Willott, D Wylezalek, & A Nota 2024 'The first billion years, according to jwst' .

Ade PAR, N Aghanim, C Armitage-Caplan, M Arnaud, M Ashdown, F Atrio-Barandela, J Aumont, C Baccigalupi, AJ Banday, & et al 2014 'Planck2013 results. xvi. cosmological parameters' *Astronomy & Astrophysics* 571:A16 doi: 10.1051/0004-6361/201321591 URL http://dx.doi.org/10.1051/0004-6361/

201321591.

Ahvazi N, A Benson, LV Sales, EO Nadler, S Weerasooriya, X Du, & MS Bovill 2023 'A comprehensive model for the formation and evolution of the faintest milky way dwarf satellites' .

Anninos P & ML Norman 1996 'The Role of Hydrogen Molecules in the Radiative Cooling and Fragmentation of Cosmological Sheets' 460:556 doi: 10.1086/176992.

Bañados E, M Rauch, R Decarli, EP Farina, JF Hennawi, C Mazzucchelli, BP Venemans, F Walter, RA Simcoe, JX Prochaska, T Cooper, FB Davies, & SFS Chen 2019 'A metal-poor damped ly system at redshift 6.4' *The Astrophysical Journal* 885(1):59 doi: 10.3847/1538-4357/ab4129 URL https://doi.org/10.3847%2F1538-4357%2Fab4129.

Behroozi PS, RH Wechsler, & HY Wu 2013 'The rockstar phase-space temporal halo finder and the velocity offsets of cluster cores' *The Astrophysical Journal* 762(2):109 URL http://stacks.iop.org/0004-637X/762/i=2/a=109.

Behroozi PS, RH Wechsler, HY Wu, MT Busha, AA Klypin, & JR Primack 2013 'Gravitationally Consistent Halo Catalogs and Merger Trees for Precision Cosmology' 763(1):18 doi: 10.1088/0004-637X/763/1/18.

Berger MJ & P Colella 1989a 'Local Adaptive Mesh Refinement for Shock Hydrodynamics' *Journal of Computational Physics* 82(1):64–84 doi: 10.1016/0021-9991(89)90035-1.

Berger MJ & P Colella 1989b 'Local Adaptive Mesh Refinement for Shock Hydrodynamics' *Journal of Computational Physics* 82(1):64–84 doi: 10.1016/0021-9991(89)90035-1.

Bettinelli M, SL Hidalgo, S Cassisi, A Aparicio, & G Piotto 2018 'The star formation history of the Sextans dwarf spheroidal galaxy: a true fossil of the pre-reionization era' *Monthly Notices of the Royal Astronomical Society* 476(1):71–79 doi: 10.1093/mnras/sty226 URL https://doi.org/10.1093/mnras/sty226.

Bolton JS & MG Haehnelt 2007 'The observed ionization rate of the intergalactic medium and the ionizing emissivity at z ¿= 5: evidence for a photon-starved and extended epoch of reionization' 382(1):325–341 doi: 10.1111/j.1365-2966.2007.12372.x.

Bordner J & ML Norman 2018 'Computational Cosmology and Astrophysics on Adaptive Meshes using Charm++' *arXiv e-prints* :arXiv:1810.01319doi: 10.48550/arXiv.1810.01319.

Bordner J & ML Norman 2018 'Computational cosmology and astrophysics on adaptive meshes using charm++' .

Bromm V & RB Larson 2004 'The First Stars' 42(1):79–118 doi: 10.1146/annurev.astro.42.053102.134034.

Bromm V & A Loeb 2003 'The formation of the first low-mass stars from gas with low carbon and oxygen

abundances' 425(6960):812–814 doi: 10.1038/nature02071.

Brummel-Smith C, G Bryan, I Butsky, L Corlies, A Emerick, J Forbes, Y Fujimoto, NJ Goldbaum, P Grete, CB Hummels, J hoon Kim, D Koh, M Li, Y Li, X Li, B OShea, MS Peeples, JA Regan, M Salem, W Schmidt, CM Simpson, BD Smith, J Tumlinson, MJ Turk, JH Wise, T Abel, J Bordner, R Cen, DC Collins, B Crosby, P Edelmann, O Hahn, R Harkness, E Harper-Clark, S Kong, AG Kritsuk, M Kuhlen, J Larrue, E Lee, G Meece, ML Norman, JS Oishi, P Paschos, C Peruta, A Razoumov, DR Reynolds, D Silvia, SW Skillman, S Skory, GC So, E Tasker, R Wagner, P Wang, H Xu, & F Zhao 2019 'Enzo: An adaptive mesh refinement code for astrophysics (version 2.6)' *Journal of Open Source Software* 4(42):1636 doi: 10.21105/joss.01636 URL https://doi.org/10.21105/joss.01636.

Bryan GL, ML Norman, JM Stone, R Cen, & JP Ostriker 1995 'A piecewise parabolic method for cosmological hydrodynamics' *Computer Physics Communications* 89(1):149–168 doi: https://doi.org/10.1016/0010-4655(94)00191-4 URL https://www.sciencedirect.com/science/article/pii/0010465594001914 numerical Methods in Astrophysical Hydrodynamics.

Bryan GL, ML Norman, BW O'Shea, T Abel, JH Wise, MJ Turk, DR Reynolds, DC Collins, P Wang, SW Skillman, B Smith, RP Harkness, J Bordner, J hoon Kim, M Kuhlen, H Xu, N Goldbaum, C Hummels, AG Kritsuk, E Tasker, S Skory, CM Simpson, O Hahn, JS Oishi, GC So, F Zhao, R Cen, Y Li, & TE Collaboration 2014 'Enzo: An adaptive mesh refinement code for astrophysics' 211(2):19 URL http://stacks.iop.org/0067-0049/211/i=2/a=19.

Burstedde C, LC Wilcox, & O Ghattas 2011 'p4est: Scalable algorithms for parallel adaptive mesh refinement on forests of octrees' *SIAM Journal on Scientific Computing* 33(3):1103–1133 doi: 10.1137/100791634 URL https://doi.org/10.1137/100791634.

Carrera R, A Aparicio, D Martínez-Delgado, & J Alonso-García 2002 'The star formation history and spatial distribution of stellar populations in the ursa minor dwarf spheroidal galaxy' *The Astronomical Journal* 123(6):3199–3209 doi: 10.1086/340702 URL https://doi.org/10.1086%2F340702.

Cen R & MA Riquelme 2008 'Lower metal enrichment of virialized gas in minihalos' *The Astrophysical Journal* 674(2):644–652 doi: 10.1086/524724 URL https://doi.org/10.1086%2F524724.

Chen KJ, DJ Whalen, KMJ Wollenberg, SCO Glover, & RS Klessen 2017 'How the first stars regulated star formation. II. enrichment by nearby supernovae' *The Astrophysical Journal* 844(2):111 doi: 10.3847/1538-4357/aa7b34 URL https://doi.org/10.3847%2F1538-4357%2Faa7b34.

Chen P, JH Wise, ML Norman, H Xu, & BW O'Shea 2014 'Scaling relations for galaxies prior to reionization' 795(2):144 URL http://stacks.iop.org/0004-637X/795/i=2/a=144.

Colella P & PR Woodward 1984 'The piecewise parabolic method (ppm) for gas-dynamical simulations' *Journal of Computational Physics* 54(1):174–201 doi: https://doi.org/10.1016/0021-9991(84)90143-8 URL https://www.sciencedirect.com/science/article/pii/0021999184901438.

Cooke RJ, M Pettini, & CC Steidel 2017 'Discovery of the most metal-poor damped Lyman system' *Monthly Notices of the Royal Astronomical Society* 467(1):802–811 doi: 10.1093/mnras/stx037 URL

https://doi.org/10.1093/mnras/stx037.

Courant R, K Friedrichs, & H Lewy 1928 'Über die partiellen Differenzengleichungen der mathematischen Physik' *Mathematische Annalen* 100:32–74 doi: 10.1007/BF01448839.

Draine BT 2011 *Physics of the Interstellar and Intergalactic Medium*.

Draine BT & F Bertoldi 1996 'Structure of Stationary Photodissociation Fronts' 468:269 doi: 10.1086/177689.

Eisenstein DJ & P Hut 1998 'HOP: A New Group-Finding Algorithm for N-Body Simulations' 498(1):137–142 doi: 10.1086/305535.

Feltzing S & M Chiba 2013 'Elemental abundances in the milky way stellar disk(s), bulge, and halo' *New Astronomy Reviews* 57(3):80 – 99 doi: https://doi.org/10.1016/j.newar.2013.06.001 URL http://www.sciencedirect.com/science/article/pii/S1387647313000055.

Frebel A & JE Norris 2015 'Near-field cosmology with extremely metal-poor stars' *Annual Review of Astronomy and Astrophysics* 53(1):631–688 doi: 10.1146/annurev-astro-082214-122423 URL https://doi.org/10.1146/annurev-astro-082214-122423.

Gnedin NY 2016 'On the proper use of the reduced speed of light approximation' *The Astrophysical Journal* 833(1):66 doi: 10.3847/1538-4357/833/1/66 URL http://dx.doi.org/10.3847/1538-4357/833/1/66.

Gnedin NY & T Abel 2001 'Multi-dimensional cosmological radiative transfer with a Variable Eddington Tensor formalism' 6(7):437–455 doi: 10.1016/S1384-1076(01)00068-9.

Gnedin NY & P Madau 2022 'Modeling cosmic reionization' .

Greif TH 2015 'The numerical frontier of the high-redshift Universe' *Computational Astrophysics and Cosmology* 2:3 doi: 10.1186/s40668-014-0006-2.

Greif TH, JL Johnson, V Bromm, & RS Klessen 2007 'The First Supernova Explosions: Energetics, Feedback, and Chemical Enrichment' 670(1):1–14 doi: 10.1086/522028.

Greif TH, JL Johnson, RS Klessen, & V Bromm 2008 'The first galaxies: assembly, cooling and the onset of turbulence' 387(3):1021–1036 doi: 10.1111/j.1365-2966.2008.13326.x.

Hahn O & T Abel 2011 'Multi-scale initial conditions for cosmological simulations' 415(3):2101–2121 doi: 10.1111/j.1365-2966.2011.18820.x.

Harikane Y, M Ouchi, M Oguri, Y Ono, K Nakajima, Y Isobe, H Umeda, K Mawatari, & Y Zhang 2023 'A comprehensive study of galaxies at z 9–16 found in the early jwst data: Ultraviolet luminosity functions and cosmic star formation history at the pre-reionization epoch' *The Astrophysical Journal Supplement Series* 265(1):5 doi: 10.3847/1538-4365/acaaa9 URL http://dx.doi.org/10.3847/1538-4365/acaaa9.

Harten A, PD Lax, & Bv Leer 1983 'On upstream differencing and godunov-type schemes for hyperbolic conservation laws' *SIAM Review* 25(1):35–61 doi: 10.1137/1025002 URL https://doi.org/10.1137/1025002.

Heger A & SE Woosley 2002 'The Nucleosynthetic Signature of Population III' 567:532–543 doi: 10.1086/338487.

Hernández JIG, DS Aguado, CA Prieto, AJ Burgasser, & R Rebolo 2020 'The extreme CNO-enhanced composition of the primitive iron-poor dwarf star j08154729' *The Astrophysical Journal* 889(1):L13 doi: 10.3847/2041-8213/ab62ae URL https://doi.org/10.3847%2F2041-8213%2Fab62ae.

Hicks WM, A Wells, ML Norman, JH Wise, BD Smith, & BW O'Shea 2021 'External enrichment of mini halos by the first supernovae' *The Astrophysical Journal* 909(1):70 doi: 10.3847/1538-4357/abda3a URL https://doi.org/10.3847%2F1538-4357%2Fabda3a.

Hicks WM, ML Norman, AI Wells, & JO Bordner 2024 'Galaxies and their environment at $z \gtrsim 10$ – i: Primordial chemical enrichment, accretion, cooling, and virialization of gas in dark matter halos' URL https://arxiv.org/abs/2407.20429.

Hopkins PF, A Wetzel, D Kereš, CA Faucher-Giguère, E Quataert, M Boylan-Kolchin, N Murray, CC Hayward, & K El-Badry 2018a 'How to model supernovae in simulations of star and galaxy formation' *Monthly Notices of the Royal Astronomical Society* 477(2):1578–1603 doi: 10.1093/mnras/sty674 URL https://doi.org/10.1093/mnras/sty674.

Hopkins PF, A Wetzel, D Kereš, CA Faucher-Giguère, E Quataert, M Boylan-Kolchin, N Murray, CC Hayward, S Garrison-Kimmel, C Hummels, R Feldmann, P Torrey, X Ma, D Anglés-Alcázar, KY Su, M Orr, D Schmitz, I Escala, R Sanderson, MY Grudić, Z Hafen, JH Kim, A Fitts, JS Bullock, C Wheeler, TK Chan, OD Elbert, & D Narayanan 2018b 'FIRE-2 simulations: physics versus numerics in galaxy formation' *Monthly Notices of the Royal Astronomical Society* 480(1):800–863 doi: 10.1093/mnras/sty1690 URL https://doi.org/10.1093/mnras/sty1690.

Hopkins PF, A Wetzel, C Wheeler, R Sanderson, MY Grudić , O Sameie, M Boylan-Kolchin, M Orr, X Ma, CA Faucher-Giguère, D Kereš, E Quataert, KY Su, J Moreno, R Feldmann, JS Bullock, SR Loebman, D Anglés-Alcázar, J Stern, L Necib, CR Choban, & CC Hayward 2022 'FIRE-3: updated stellar evolution models, yields, and microphysics and fitting functions for applications in galaxy simulations' *Monthly Notices of the Royal Astronomical Society* 519(2):3154–3181 doi: 10.1093/mnras/stac3489 URL https://doi.org/10.1093%2Fmnras%2Fstac3489.

Iliev IT, B Ciardi, MA Alvarez, A Maselli, A Ferrara, NY Gnedin, G Mellema, T Nakamoto, ML Norman, AO Razoumov, EJ Rijkhorst, J Ritzerveld, PR Shapiro, H Susa, M Umemura, & DJ Whalen 2006 'Cosmological radiative transfer codes comparison project – I. The static density field tests' *Monthly Notices of the Royal Astronomical Society* 371(3):1057–1086 doi: 10.1111/j.1365-2966.2006.10775.x URL https://doi.org/10.1111/j.1365-2966.2006.10775.x.

Iliev IT, D Whalen, G Mellema, K Ahn, S Baek, NY Gnedin, AV Kravtsov, M Norman, M Raicevic, DR Reynolds, D Sato, PR Shapiro, B Semelin, J Smidt, H Susa, T Theuns, & M Umemura 2009

'Cosmological radiative transfer comparison project â ii. the radiation-hydrodynamic tests' *Monthly Notices of the Royal Astronomical Society* 400(3):1283–1316 doi: 10.1111/j.1365-2966.2009.15558.x URL http://dx.doi.org/10.1111/j.1365-2966.2009.15558.x.

Incatasciato A, S Khochfar, & J Oñorbe 2023 'Modelling the cosmological Lyman–Werner background radiation field in the early Universe' *Monthly Notices of the Royal Astronomical Society* 522(1):330–349 doi: 10.1093/mnras/stad1008 URL https://doi.org/10.1093/mnras/stad1008.

Jeon M, G Besla, & V Bromm 2017 'Connecting the first galaxies with ultrafaint dwarfs in the local group: Chemical signatures of population iii stars' 848(2):85 URL http://stacks.iop.org/0004-637X/848/i=2/a=85.

Kalé LV 2011 *Charm++* Boston, MA: Springer US pp. 256–264 doi: 10.1007/978-0-387-09766-4_242 URL https://doi.org/10.1007/978-0-387-09766-4_242.

Keller SC, MS Bessell, A Frebel, AR Casey, M Asplund, HR Jacobson, K Lind, JE Norris, D Yong, A Heger, Z Magic, GS da Costa, BP Schmidt, & P Tisserand 2014 'A single low-energy, iron-poor supernova as the source of metals in the star SMSS J031300.36-670839.3' 506:463–466 doi: 10.1038/nature12990.

Kereš D, N Katz, DH Weinberg, & R Davé 2005 'How do galaxies get their gas?' 363(1):2–28 doi: 10.1111/j.1365-2966.2005.09451.x.

Kereš D, N Katz, M Fardal, R Davé, & DH Weinberg 2009 'Galaxies in a simulated CDM Universe – I. Cold mode and hot cores' *Monthly Notices of the Royal Astronomical Society* 395(1):160–179 doi: 10.1111/j.1365-2966.2009.14541.x URL https://doi.org/10.1111/j.1365-2966.2009.14541.x.

Kim CG & EC Ostriker 2015 'Momentum Injection by Supernovae in the Interstellar Medium' 802(2):99 doi: 10.1088/0004-637X/802/2/99.

Kirby EN, JG Cohen, P Guhathakurta, L Cheng, JS Bullock, & A Gallazzi 2013 'The Universal Stellar Mass-Stellar Metallicity Relation for Dwarf Galaxies' 779(2):102 doi: 10.1088/0004-637X/779/2/102.

Krumholz MR & NY Gnedin 2011 'A comparison of methods for determining the molecular content of model galaxies' *The Astrophysical Journal* 729(1):36 doi: 10.1088/0004-637X/729/1/36 URL https://dx.doi.org/10.1088/0004-637X/729/1/36.

Labbé I, P van Dokkum, E Nelson, R Bezanson, KA Suess, J Leja, G Brammer, K Whitaker, E Mathews, M Stefanon, & B Wang 2023 'A population of red candidate massive galaxies 600 Myr after the Big Bang' 616(7956):266–269 doi: 10.1038/s41586-023-05786-2.

Lochhaas C, J Tumlinson, BW O'Shea, MS Peeples, BD Smith, JK Werk, R Augustin, & RC Simons 2021 'Figuring out gas amp; galaxies in enzo (foggie). v. the virial temperature does not describe gas in a virialized galaxy halo' *The Astrophysical Journal* 922(2):121 doi: 10.3847/1538-4357/ac2496 URL http://dx.doi.org/10.3847/1538-4357/ac2496.

McCaffrey J, S Hardin, JH Wise, & JA Regan 2023 'No tension: Jwst galaxies at zgt;10 consistent with cosmological simulations' *The Open Journal of Astrophysics* 6 doi: 10.21105/astro.2304.13755 URL http://dx.doi.org/10.21105/astro.2304.13755.

Muratov AL, D Kereš, CA Faucher-Giguère, PF Hopkins, E Quataert, & N Murray 2015 'Gusty, gaseous flows of FIRE: galactic winds in cosmological simulations with explicit stellar feedback' 454(3):2691–2713 doi: 10.1093/mnras/stv2126.

Nomoto K, N Tominaga, H Umeda, C Kobayashi, & K Maeda 2006 'Nucleosynthesis yields of core-collapse supernovae and hypernovae, and galactic chemical evolution' *Nuclear Physics A* 777:424 – 458 doi: https://doi.org/10.1016/j.nuclphysa.2006.05.008 URL http://www.sciencedirect.com/science/article/pii/S0375947406001953 special Isseu on Nuclear Astrophysics.

Omukai K 2001 'Primordial star formation under far-ultraviolet radiation' *The Astrophysical Journal* 546(2):635 doi: 10.1086/318296 URL https://dx.doi.org/10.1086/318296.

O'Shea BW, JH Wise, H Xu, & ML Norman 2015 'Probing the Ultraviolet Luminosity Function of the Earliest Galaxies with the Renaissance Simulations' 807:L12 doi: 10.1088/2041-8205/807/1/L12.

O'Shea BW, JH Wise, H Xu, & ML Norman 2015 'Probing the ultraviolet luminosity function of the earliest galaxies with the renaissance simulations' */apj* 807(1):L12 URL http://stacks.iop.org/2041-8205/807/i=1/a=L12.

Puchwein E, F Haardt, MG Haehnelt, & P Madau 2019 'Consistent modelling of the meta-galactic UV background and the thermal/ionization history of the intergalactic medium' *Monthly Notices of the Royal Astronomical Society* 485(1):47–68 doi: 10.1093/mnras/stz222 URL https://doi.org/10.1093%2Fmnras%2Fstz222.

Ricotti M, NY Gnedin, & JM Shull 2002 'The fate of the first galaxies. ii. effects of radiative feedback' *The Astrophysical Journal* 575(1):49–67 doi: 10.1086/341256 URL http://dx.doi.org/10.1086/341256.

Rosdahl J, J Blaizot, D Aubert, T Stranex, & R Teyssier 2013 'ramses-rt: radiation hydrodynamics in the cosmological context' *Monthly Notices of the Royal Astronomical Society* 436(3):2188–2231 doi: 10.1093/mnras/stt1722 URL https://doi.org/10.1093%2Fmnras%2Fstt1722.

Schaerer D 2003 'The transition from Population III to normal galaxies: Lyalpha and He II emission and the ionising properties of high redshift starburst galaxies' 397:527–538 doi: 10.1051/0004-6361:20021525.

Shapiro PR 1986 'Cosmological h ii regions and the photoionization of the intergalactic medium' *Publications of the Astronomical Society of the Pacific* 98(608):1014–1017 URL http://www.jstor.org/stable/40678804.

Skinner D & JH Wise 2020 'Cradles of the first stars: self-shielding, halo masses, and multiplicity' *Monthly Notices of the Royal Astronomical Society* 492(3):4386–4397 doi: 10.1093/mnras/staa139 URL https://doi.org/10.1093/mnras/staa139.

Smith BD & M Lang 2019 'ytree: A python package for analyzing merger trees' *Journal of Open Source Software* 4(44):1881 doi: 10.21105/joss.01881 URL https://doi.org/10.21105/joss.01881.

Smith BD, JH Wise, BW O'Shea, ML Norman, & S Khochfar 2015a 'The first population ii stars formed in externally enriched mini-haloes' 452(3):2822–2836 doi: 10.1093/mnras/stv1509 URL +http://dx.doi.org/10.1093/mnras/stv1509.

Smith BD, JH Wise, BW O'Shea, ML Norman, & S Khochfar 2015b 'The first population ii stars formed in externally enriched mini-haloes' 452(3):2822–2836 doi: 10.1093/mnras/stv1509 URL +http://dx.doi.org/10.1093/mnras/stv1509.

Smith BD, GL Bryan, SCO Glover, NJ Goldbaum, MJ Turk, J Regan, JH Wise, HY Schive, T Abel, A Emerick, BW O'Shea, P Anninos, CB Hummels, & S Khochfar 2017 'GRACKLE: a chemistry and cooling library for astrophysics' 466(2):2217–2234 doi: 10.1093/mnras/stw3291.

Stecher TP & DA Williams 1967 'Photodestruction of Hydrogen Molecules in H I Regions' 149:L29 doi: 10.1086/180047.

Thornton K, M Gaudlitz, HT Janka, & M Steinmetz 1998 'Energy Input and Mass Redistribution by Supernovae in the Interstellar Medium' 500(1):95–119 doi: 10.1086/305704.

Trenti M & M Stiavelli 2009 'Formation rates of population iii stars and chemical enrichment of halos during the reionization era' *The Astrophysical Journal* 694(2):879–892 doi: 10.1088/0004-637x/694/2/879 URL http://dx.doi.org/10.1088/0004-637X/694/2/879.

Trenti M, M Stiavelli, & J Michael Shull 2009 'Metal-free gas supply at the edge of reionization: Late-epoch population iii star formation' *The Astrophysical Journal* 700(2):1672–1679 doi: 10.1088/0004-637x/700/2/1672 URL http://dx.doi.org/10.1088/0004-637X/700/2/1672.

Turk MJ, BD Smith, JS Oishi, S Skory, SW Skillman, T Abel, & ML Norman 2011 'yt: A Multi-code Analysis Toolkit for Astrophysical Simulation Data' 192:9 doi: 10.1088/0067-0049/192/1/9.

Visbal E, GL Bryan, & Z Haiman 2020 'Self-consistent semianalytic modeling of feedback during primordial star formation and reionization' *The Astrophysical Journal* 897(1):95 doi: 10.3847/1538-4357/ab994e URL http://dx.doi.org/10.3847/1538-4357/ab994e.

Wells AI & ML Norman 2021 'Predicting localized primordial star formation with deep convolutional neural networks' *The Astrophysical Journal Supplement Series* 254(2):41 doi: 10.3847/1538-4365/abfa17 URL https://doi.org/10.3847%2F1538-4365%2Fabfa17.

Wells AI & ML Norman 2022 'Connecting primordial star-forming regions and second-generation star formation in the phoenix simulations' *The Astrophysical Journal* 932(1):71 doi: 10.3847/1538-4357/ac6c87 URL https://dx.doi.org/10.3847/1538-4357/ac6c87.

Wells AI & ML Norman 2022 'The First Galaxies and the Effect of Heterogeneous Enrichment from Primordial Stars' *arXiv e-prints* :arXiv:2210.14805doi: 10.48550/arXiv.2210.14805.

Welsh L, R Cooke, & M Fumagalli 2019 'Modelling the chemical enrichment of Population III supernovae: the origin of the metals in near-pristine gas clouds' *Monthly Notices of the Royal Astronomical Society* 487(3):3363–3376 doi: 10.1093/mnras/stz1526 URL https://doi.org/10.1093/mnras/stz1526.

Whalen D, T Abel, & ML Norman 2004 'Radiation hydrodynamic evolution of primordial h¡scp¿ii¡/scp¿regions' *The Astrophysical Journal* 610(1):14–22 doi: 10.1086/421548 URL http://dx.doi.org/10.1086/421548.

Whalen D, B van Veelen, BW O'Shea, & ML Norman 2008 'The destruction of cosmological minihalos by primordial supernovae' *The Astrophysical Journal* 682(1):49–67 doi: 10.1086/589643 URL https://doi.org/10.1086%2F589643.

Whalen D, B van Veelen, BW O'Shea, & ML Norman 2008 'The Destruction of Cosmological Minihalos by Primordial Supernovae' 682(1):49–67 doi: 10.1086/589643.

Wise JH & T Abel 2007 'Resolving the Formation of Protogalaxies. I. Virialization' 665(2):899–910 doi: 10.1086/520036.

Wise JH & T Abel 2008 'Resolving the Formation of Protogalaxies. III. Feedback from the First Stars' 685(1):40–56 doi: 10.1086/590417.

Wise JH & T Abel 2011a 'enzo+moray: radiation hydrodynamics adaptive mesh refinement simulations with adaptive ray tracing' 414(4):3458–3491 doi: 10.1111/j.1365-2966.2011.18646.x URL +http://dx.doi.org/10.1111/j.1365-2966.2011.18646.x.

Wise JH & T Abel 2011b 'enzo+moray: radiation hydrodynamics adaptive mesh refinement simulations with adaptive ray tracing' *Monthly Notices of the Royal Astronomical Society* 414(4):3458–3491 doi: 10.1111/j.1365-2966.2011.18646.x URL https://doi.org/10.1111/j.1365-2966.2011.18646.x.

Wise JH & R Cen 2009 'Ionizing Photon Escape Fractions From High-Redshift Dwarf Galaxies' 693(1):984–999 doi: 10.1088/0004-637X/693/1/984.

Wise JH, T Abel, MJ Turk, ML Norman, & BD Smith 2012a 'The birth of a galaxy – ii. the role of radiation pressure' *Monthly Notices of the Royal Astronomical Society* 427(1):311–326 doi: 10.1111/j.1365-2966.2012.21809.x URL http://dx.doi.org/10.1111/j.1365-2966.2012.21809.x.

Wise JH, MJ Turk, ML Norman, & T Abel 2012b 'The birth of a galaxy: Primordial metal enrichment and stellar populations' 745(1):50 URL http://stacks.iop.org/0004-637X/745/i=1/a=50.

Wise JH, VG Demchenko, MT Halicek, ML Norman, MJ Turk, T Abel, & BD Smith 2014 'The birth of a galaxy – III. Propelling reionization with the faintest galaxies' *Monthly Notices of the Royal Astronomical Society* 442(3):2560–2579 doi: 10.1093/mnras/stu979 URL https://doi.org/10.1093/mnras/stu979.

Wolcott-Green J & Z Haiman 2019 'H2 self-shielding with non-LTE rovibrational populations: implications for cooling in protogalaxies' *Monthly Notices of the Royal Astronomical Society* 484(2):2467–2473

doi: 10.1093/mnras/sty3280 URL https://doi.org/10.1093/mnras/sty3280.

Xu H, JH Wise, & ML Norman 2013 'Population III Stars and Remnants in High-redshift Galaxies' 773:83 doi: 10.1088/0004-637X/773/2/83.

Xu H, K Ahn, JH Wise, ML Norman, & BW O'Shea 2014 'Heating the Intergalactic Medium by X-Rays from Population III Binaries in High-redshift Galaxies' 791:110 doi: 10.1088/0004-637X/791/2/110.

Xu H, K Ahn, ML Norman, JH Wise, & BW O'Shea 2016a 'X-Ray Background at High Redshifts from Pop III Remnants: Results from Pop III Star Formation Rates in the Renaissance Simulations' 832:L5 doi: 10.3847/2041-8205/832/1/L5.

Xu H, ML Norman, BW O'Shea, & JH Wise 2016b 'Late Pop III Star Formation During the Epoch of Reionization: Results from the Renaissance Simulations' 823:140 doi: 10.3847/0004-637X/823/2/140.

Xu H, JH Wise, ML Norman, K Ahn, & BW O'Shea 2016c 'Galaxy Properties and UV Escape Fractions during the Epoch of Reionization: Results from the Renaissance Simulations' 833:84 doi: 10.3847/1538-4357/833/1/84.